

Algorithms and Resources for Quantum Technology, Sensing and Random Number Generation

Von der Fakultät Mathematik und Physik der Universität
Stuttgart zur Erlangung der Würde eines Doktors der
Naturwissenschaften (Dr. rer. nat.) genehmigte Abhandlung

vorgelegt von
Johannes Nikolaus Greiner
aus Backnang

Hauptberichter: Prof. Dr. Jörg Wrachtrup

Mitberichter: Prof. Dr. Eric Lutz

Tag der mündlichen Prüfung: 28.05.2020

3. Physikalisches Institut der Universität Stuttgart

2020

Contents

| | |
|--|-----------|
| List of Abbreviations | 9 |
| Abstract | 13 |
| Zusammenfassung | 15 |
| List of Figures | 23 |
| List of Tables | 25 |
| Introduction: Resources for Quantum Technology | 27 |
| 1 Quantum Sensing | 31 |
| 1.1 Improving Sensitivity by Indirect Sensing using NV-Centers | 32 |
| 1.1.1 Strongly Coupled Nuclear Spins as Indirect Sensors | 35 |
| 1.1.2 Standard Sequence for Direct Detection | 36 |
| 1.1.3 Novel Pulse Sequences for Indirect Sensing using the Inherent Nitrogen Nuclear Spin | 38 |
| 1.1.4 Advantages of the Indirectly Sensing Nuclear Spin under NV Electron De- coherence | 42 |
| 1.2 Indirect Signal Transmission by an Asymmetric Sequence | 43 |
| 1.2.1 Performance of the Asymmetric Sequence under Decoherence | 45 |

Contents

| | | |
|----------|--|-----------|
| 1.2.2 | Effects of treating the Ancillary Spin as Spin 1 with additional Decoherence | 46 |
| 1.2.3 | Decoherence under Periodic Reinitializations | 51 |
| 1.3 | A Quantum Derivative? | 53 |
| 1.4 | Conclusion: Quantum Sensing | 55 |
| 2 | Quantum State Engineering | 57 |
| 2.1 | Effective Hamiltonians by repeated measurements | 58 |
| 2.2 | Purification by controlled non-unitary evolution | 59 |
| 2.2.1 | Repeated measurement of a central spin | 60 |
| 2.2.2 | Purification Mechanism | 63 |
| 2.2.3 | Derivation of the effective Quantum Dynamics on the bath | 65 |
| 2.2.4 | Optimization of External Parameters for Specific Target States | 67 |
| 2.3 | Specific Target States and their Applications | 69 |
| 2.3.1 | Pairwise Entangled Singlet States | 70 |
| 2.3.2 | Advantages for Quantum Sensing | 71 |
| 2.4 | Results for Different Geometries of Surrounding Spins | 74 |
| 2.4.1 | Three-dimensional Geometries of Surrounding Spins | 75 |
| 2.5 | Methods for Correlation of a large Number of Bath Spins | 78 |
| 2.5.1 | Specific Separable One-Qubit Operations and their Permutations introduced by Power Expansion | 78 |
| 2.5.2 | Relation of the Involved Permutations to Binary Numbers | 80 |
| 2.5.3 | Partial Trace of a Large Pure State | 81 |
| 2.5.4 | Results: Simulating Pairwise Entanglement among up to Twenty Spins | 82 |
| 2.5.5 | Twenty Spin (Qubits) Case | 84 |
| 2.5.6 | Eight Spin Case with Maximal Total Correlation | 88 |
| 2.5.7 | Consequences and Possible Improvements | 89 |
| 2.6 | Experimental Implementations using NV-Centers | 90 |
| 2.6.1 | Existing Purification Experiment using NVs | 91 |

| | | |
|----------|--|------------|
| 2.6.2 | Open Questions addressable in further Purifications Experiments using NV-Centers | 92 |
| 2.7 | Application of Repetitive Projections to Superconducting Qubits | 93 |
| 2.8 | Squeezed Spin States | 96 |
| 2.8.1 | Heisenberg's Uncertainty Relation | 96 |
| 2.8.2 | General Dynamics for Generation of Spin Squeezed States | 99 |
| 2.8.3 | Nuclear Spin Squeezed States in Diamond | 107 |
| 2.8.4 | The Squeezed Nuclear Spin Register as a Coprocessor for the Electron Spin Sensor | 114 |
| 2.8.5 | Robustness of the Nuclear Spin Squeezed State against Decoherence | 117 |
| 2.8.6 | Analytical Model of Nuclear Spin Squeezing in Fock Basis | 119 |
| 2.8.7 | Outlook and Possible Improvements for Nuclear Spin Squeezing | 121 |
| 2.8.8 | Spin Squeezing with NV Ensembles | 122 |
| 2.8.9 | Diamond Samples and Coupling Geometries Suitable for NV Ensemble Spin Squeezing | 126 |
| 2.9 | Conclusion: Quantum State Engineering | 130 |
| 3 | Multiple Quantum levels or Qudits | 131 |
| 3.1 | Bound Entanglement | 132 |
| 3.2 | Measuring Bound Entanglement in two-Qutrit Systems | 134 |
| 3.3 | Quantum Contextuality | 139 |
| 3.3.1 | The Peres-Mermin Square | 140 |
| 3.4 | The KCBS inequality | 142 |
| 3.5 | Experimental KCBS Inequality Violation | 145 |
| 3.5.1 | Proposal for an Implementation with NV centers | 145 |
| 3.5.2 | The Problem of Maintaining Coherence in Quantum Measurements | 147 |
| 3.5.3 | Measurement of One-dimensional projectors | 149 |
| 3.5.4 | Operations and Measurements to violate the KCBS inequality | 151 |

Contents

| | | |
|----------|--|------------|
| 3.6 | Conclusion: Qudits | 158 |
| 4 | Quantum Random Number Generation | 159 |
| 4.1 | Certified Quantum Random Number Generation | 160 |
| 4.1.1 | Quantum Indeterminism and Bell-like Inequalities | 160 |
| 4.2 | QRNG Certified by Quantum Contextuality | 163 |
| 4.3 | The NV-Center as Single-Photon Emitter for QRNG | 165 |
| 4.4 | Unambiguous QRNG by Optical Parametric Oscillators | 170 |
| 4.4.1 | The Optical Parametric Oscillator and Period Doubling | 171 |
| 4.4.2 | Unambiguous all-optical Random Number Generation with OPOs | 172 |
| 4.5 | Analysis of Random Numbers | 174 |
| 4.5.1 | Feller's Coin Tossing Constants | 175 |
| 4.5.2 | Conditional Entropy Analysis of Random Numbers | 180 |
| 4.6 | Conclusion: QRNG | 184 |
| | Appendix | 185 |
| A.1 | Non-unitary Sum of two Unitaries | 185 |
| A.2 | Selected Mathematica Code | 186 |
| A.2.1 | Correlation of Twenty Spins by Repetitive Measurements of a Central Spin | 186 |
| A.2.2 | Purification Measurement Scheme Illustration | 187 |
| A.2.3 | Spin Squeezing Uncertainty Spherical Plot | 190 |
| | Acknowledgements | 191 |
| | Publications and Patents | 195 |
| | Publications | 195 |
| | News and Views Articles with Reference to our Work | 196 |
| | Patents and Inventions | 197 |

| | |
|-------------------------|------------|
| Bibliography | 199 |
| Curriculum Vitae | 230 |

List of Abbreviations

List of Abbreviations

| | |
|----------------------|---|
| APD | Avalanche Photodiode |
| Bath Spin | An external spin entity individually coupled to a Central Spin. C.f. abbreviations ‘Central Spin’ and ‘Nuclear Spin’ below. |
| Central Spin | A spin entity – typically an electron spin – coupled individually to several external spins, generally assumed to have no additional couplings among themselves |
| CNOT | Controlled NOT Quantum Gate |
| CPU | Central Processing Unit of a computer |
| Electron Spin | Spin of a negatively charged Nitrogen-Vacancy Center in diamond, unless otherwise indicated |
| GHZ States | Fully entangled states introduced by Greenberger, Horne and Zeilinger in 1990 [1]. |
| IBM | International Business Machines Corporation |
| IT | Information Technology |
| KCBS | Klyachko, Can, Binicioğlu and Shumovsky. Derived an Inequality as an experimentally accessible test of Quantum Contextuality [2]. |
| LIGO | Laser Interferometer Gravitational-Wave Observatory |
| NMR | Nuclear Magnetic Resonance |

List of Abbreviations

| | |
|---------------------|--|
| Nuclear Spin | Non-spinless nuclear spin entity, typically a ^{13}C or ^{14}N nuclear spin surrounding the electron spin of a negatively charged Nitrogen-Vacancy Center in diamond, unless otherwise indicated |
| NV | Nitrogen-Vacancy Center in diamond |
| NV-Center | Nitrogen-Vacancy Center in diamond |
| OPO | Optical Parametric Oscillator |
| P2 | Period-Doubling |
| PPT | Positive Partial Transpose |
| PRNG | Pseudo Random Number Generators |
| QC | Quantum Computing |
| QPD | Quasiprobability Distribution |
| Qubit | Quantum Bit or two-level quantum system |
| Qutrit | Three-level quantum system |
| Qudit | n-level quantum system |
| QRNG | Quantum Random Number Generator |
| QUBO | Quadratic unconstrained binary optimization |
| RAM | Random-Access Memory |
| RNG | Random Number Generator |
| SNR | Signal to Noise Ratio |
| SQUID | Superconducting Quantum Interference Device |
| T_1 | Longitudinal relaxation time |

- T_2 Transverse relaxation time
- TRNG** True Random Number Generators
- W.l.o.g.** Without loss of generality

Abstract

Abstract

This dissertation presents theoretical results as well as proposed and conducted experiments in the areas of Quantum Sensing, Quantum State Engineering, Bound Entanglement, Quantum Contextuality and Quantum Random Number Generation. A novel detection scheme to improve Quantum Sensing by indirect sensing with the help of an ancillary quantum system is introduced. Sensing information is shown to be obtainable both by direct and indirect sensors, even though their quantum states are not cloned or explicitly transferred. The steps of sensing an external signal and the transfer of information to an ancillary Qubit are combined in one asymmetric pulse sequence. Squeezed spin states, which are a well-known resource for Quantum Sensing due to their robustness to Decoherence, are also discussed. Particularly, their creation in systems of Nitrogen-Vacancy Centers (NVs) in diamond and surrounding nuclear spins, as well as ensembles of such NVs is implemented with specifically tailored sequences. In terms of Quantum State Engineering, a method to purify unpolarized Qubits surrounding and coupled to a central spin is introduced. Repeated projective measurements are used to instil a Zeno-like effect, extendable to a general unpolarized spin bath. Given a suitable trajectory of measurement outcomes, whose crucial role is explored, said projections are shown to enable driving the quantum states of the surrounding nuclear spins towards pure entangled states. Sufficient generality of the approach is shown by applying it to both NVs and superconducting qubits as physical systems. A wide range of target states of the environmental spins can be reached, including pairwise correlated Singlet states, while maximal entanglement is reachable. Advantages for Quantum Sensing granted by specific states obtained by the introduced Purification method are described. Concerning Qudits or quantum systems with

Abstract

arbitrarily high dimensionality as a resource, the possibility for generation and measurement of Bound Entanglement with NVs is investigated and an experimental implementation is proposed. Additionally, an experimental violation of a KCBS Inequality, in order to demonstrate Quantum Contextuality with NVs is proposed and details of an implementation are discussed. It is moreover shown how Contextuality can be used as a resource towards Certified Quantum Random Number generation with NVs. Other approaches to Quantum Random Number Generation are also introduced, including a standard single-photon Ansatz using NVs as well as a scheme utilizing the period-doubling state of an Optical Parametric Oscillator.

Zusammenfassung

Diese Dissertation präsentiert theoretische Ergebnisse und sowohl vorgeschlagene als auch bereits durchgeführte Experimente in den Bereichen Quantensensorik, Erzeugung bestimmter Quantenzustände, Gebundene Verschränkung, Quantenkontextualität und Quantenzufall. Ein neues Detektionsschema zur Verbesserung von Quantensensorik durch indirekte Sensorik mithilfe von zusätzlichen quantenmechanischen Hilfssystemen, wie z.B. ein zusätzliches Qubit, wird vorgestellt. Weiterhin wird aufgezeigt, dass sensorische Information sowohl durch direkte als auch durch indirekte Sensoren verfügbar gemacht werden kann – obwohl deren Quantenzustände weder geklont noch explizit transferiert werden. Die Schritte der Erfassung eines externen Signals und des Transfers von Information zu einem Hilfsqubit, werden kombiniert in einer einzelnen asymmetrischen Pulssequenz. Gequetschte Spinzustände, die dank ihrer Robustheit gegenüber Dekohärenz eine bekannte Ressource für Quantensensorik sind, werden ebenfalls diskutiert. Insbesondere deren Erzeugung in Systemen aus Stickstofffehlstellenzentren in Diamant (NV-Zentren) und umgebenden Kernspins, sowie Ensembles solcher NV-Zentren wird mit speziell dafür zugeschnittenen Sequenzen implementiert. Im Bereich der Quantenzustandserzeugung wird eine Methode zur Bereinigung unpolarisierter Qubits vorgestellt, die einen zentralen Spin umgeben und an diesen gekoppelt sind. Wiederholte projektive Messungen werden benutzt, um einen Effekt ähnlich des Quanten-Zeno-Effekts zu erzeugen, der bis hin zu einem allgemeinen unpolarisierten Spinbad verallgemeinert werden kann. Wenn eine passende Trajektorie von Messergebnissen gegeben ist, deren zentrale Rolle ebenfalls untersucht wird, sind diese Projektionen nachweislich in der Lage, die Quantenzustände der umgebenden Kernspins in reine, verschränkte Zustände umzuwandeln. Hinreichende

Zusammenfassung

Allgemeingültigkeit wird gezeigt, indem der Ansatz sowohl auf NV-Zentren als auch auf supraleitende Qubits als physikalische Systeme angewandt wird. Eine Vielzahl von Zielzuständen der Umgebungsspins sind zugänglich, inklusive paarweise korrelierter Singulett-Zustände, während maximale Verschränkung ebenso erreichbar ist. Vorteile für Quantensensorik, die aufgrund von spezifischen, durch die vorgestellte Bereinigungsmethode hervorgebrachten Zuständen gewährt werden, werden ebenfalls herausgestellt. Qudits oder Quantensysteme von beliebig hoher Dimensionalität als Ressource betreffend, wird die Möglichkeit der Herstellung und Messung gebundener verschränkter Zustände mit NV-Zentren untersucht und eine experimentelle Umsetzung vorgeschlagen. Zusätzlich wird die Vorgehensweise für die experimentelle Verletzung einer KCBS Ungleichung aufgezeigt, um Quantenkontextualität mit NV-Zentren zu demonstrieren, und die Details einer möglichen Umsetzung werden beschrieben. Weiterhin wird dargestellt wie Quantenkontextualität als Ressource zur Erzeugung von quantenmechanisch zertifizierten Zufallszahlen mit NV-Zentren genutzt werden kann. Andere Ansätze zur Quantenzufallszahlenerzeugung werden ebenfalls vorgestellt, inklusive des bekannten Einzelphotonenansatzes mit NV-Zentren sowie ein Schema, das den periodenverdoppelten Zustand eines Optischen Parametrischen Oszillators verwendet.

List of Figures

| | | |
|-----|--|----|
| 1.1 | 3D model of an NV defect in a diamond lattice. | 34 |
| 1.2 | Standard sequence for direct detection of external spins [3]. | 36 |
| 1.3 | Sensing of the coupling frequency J of an external spin coupled directly to the electron spin of a Nitrogen-Vacancy Center. | 37 |
| 1.4 | Sensing of multiple coupling frequencies J, J_1 of external spins directly by the NV electron spin. | 38 |
| 1.5 | Modified sequence for indirect detection of external spins [3,4]. | 39 |
| 1.6 | Comparison of the expectation values on the NV electron spin $\langle S_x \rangle$ and on the strongly coupled Nitrogen nuclear spin $\langle F_x \rangle$ both in presence (solid lines) and in absence (dotted lines) of the mapping sequence of Figure 1.5. | 40 |
| 1.7 | Pulse sequences for mapping information to the strongly coupled Nitrogen nuclear spin (D_F), compared to the same sequence with the electron spin as active sensor (D_S). | 41 |
| 1.8 | Comparison of direct detection of an external nuclear spin on the NV electron spin when using the sequence D_S (Figure 1.7) with the indirect detection on the strongly coupled nuclear spin when performing the pulse sequence D_F | 41 |
| 1.9 | When applying depolarization solely on the NV electron spin – related to the observable S_x – both the direct signal on the electron spin and the indirect signal observed on the nuclear spin by the observable F_x are affected. | 43 |

List of Figures

| | | |
|------|---|----|
| 1.10 | The portrayed asymmetric sequence with unitary operations limited to the electron spin alone can replace both sequences in Figure 1.7, which includes unitary operations on the electron spin as well as the strongly coupled nuclear spin. | 44 |
| 1.11 | Using the asymmetric sequence D_{SF} (Figure 1.10) in both cases, the direct detection of an external nuclear spin on the NV electron spin is compared with the indirect detection on the strongly coupled nuclear spin. | 45 |
| 1.12 | Performance of the asymmetric sequence D_{SF} (Figure 1.10) under decoherence. . . | 46 |
| 1.13 | Zoom-in at the minima of the amplitudes of the expectation values in Figure 1.11 in order to prove that the signals are not exactly identical. | 47 |
| 1.14 | Fidelity between the density matrices of the central electron spin (ρ_1) and the strongly coupled nuclear spin (ρ_2). | 48 |
| 1.15 | Expectation values of the X -Operator when using the same parameters as before in Figure 1.11, besides elevating the strongly coupled nuclear spin from a Spin 1/2 to a realistic Spin 1 entity. | 50 |
| 1.16 | Signals on the electron spin and nuclear spin in the presence of decoherence on both spins. | 51 |
| 1.17 | Effect of periodic reinitializations on the Contrast in the Signal Amplitude with increasing decoherence. | 52 |
| 1.18 | The amplitude series on the strongly coupled nuclear spin resembles the envelope of the derivative of the direct detection signal on the central electron spin. | 54 |
| 2.1 | Mathematica illustration of the proposed purification experiment. | 62 |
| 2.2 | Proposed Measurement Sequence for Purification and results from simulation. . . . | 63 |
| 2.3 | Probabilities for selected sequences or trajectories of measurement results, resulting from repeated projections of a central spin. | 64 |
| 2.4 | Effects of different choices of the external field (ω) and the free evolution time (τ). | 68 |
| 2.5 | In an exemplary two-dimensional configuration of spins distributed on a plane, four different Singlet pairs are forming within a set-up of eight spins. | 71 |

| | | |
|------|--|----|
| 2.6 | Three-dimensional scenario for a simple demonstration of benefits to Quantum Sensing by Quantum State Engineering. | 72 |
| 2.7 | Larmor frequencies of three external spins in the setting of Figure 2.6 sensed by a central electron spin. | 73 |
| 2.8 | Three-dimensional configuration of nuclear spins (blue dots) used for the Purification simulation below. | 76 |
| 2.9 | Plot of the populations of the involved 64x64 density matrices from simulation of the $N = 6$ nuclear spins after one repetition (left image) and after 300 repetitions (right image) of the measurement sequence in Figure 2.2. | 76 |
| 2.10 | Pairwise Entanglement of the spins involved in a three-dimensional Purification setting. | 77 |
| 2.11 | Development of the sum of all pairwise Concurrences, using the introduced repeated central spin projection, when scaling up the number of involved external spins (Qubits) from four to twenty. | 83 |
| 2.12 | Simulated evolution of the density matrices of the first ten out of twenty spins, correlated by repetitive measurement of a central spin. | 85 |
| 2.13 | Pairwise Concurrences (a, left image) and Overlap with Singlet State $ S\rangle = 1/\sqrt{2} 0, 1, -1, 0\rangle$ (b, right image) among the first ten out of twenty spins, correlated by repetitive measurement of a central spin. | 86 |
| 2.14 | Plot of the absolute values of the final density matrix of the last ten out of twenty spins, correlated by repetitive measurement of a central spin. | 87 |
| 2.15 | Density matrix absolute values of the final state of simulated repeated central spin measurements and their effects on eight external spins. | 88 |
| 2.16 | Pairwise Concurrence (a,left) and Singlet State Overlap (b,right) within the final state of an eight external spin simulation of repeated central spin projections. . . . | 89 |
| 2.17 | Experimental results from the Purification experiment using NV-Centers at low temperature in [5]. | 91 |

List of Figures

| | | |
|------|--|-----|
| 2.18 | Probability of consecutively obtaining the same measurement result after n identical measurement results in a low-temperature Purification experiment using NV-Centers. | 92 |
| 2.19 | Coupling topology of the simulated five-Qubit system provided by the IBM Quantum Experience in early 2017. | 94 |
| 2.20 | Results of simulated central-spin projections within a five-Qubit system provided by the IBM Quantum Experience in 2017. | 95 |
| 2.21 | Time Evolution of the Squeezing Parameter ξ_R , calculated according to equation (2.65), in the case of the state in equation (2.55), stemming from a One-Axis Twisting Hamiltonian (2.54). | 100 |
| 2.22 | Evolved Quasiprobability Distribution constructed as overlap of the evolved state resulting from a One-Axis Twisting Hamiltonian for Spin Squeezing with the reference state in (2.56). | 101 |
| 2.23 | Entanglement among the Qubits subjected to a One-Axis Twisting Hamiltonian (2.54) over time is analysed by the measure of Entanglement Entropy $S(t)$, defined in (2.58). | 102 |
| 2.24 | QPD of the exemplary state in equation (2.60), a superposition state evolved by a Two-Axis Countertwisting Hamiltonian. | 103 |
| 2.25 | Evolution of the Spin Squeezing parameter $\xi(t)$ (left image) and the Entanglement Entropy $S(t)$ (right image) in a Two-Axes Countertwisting Hamiltonian two-qubit example. | 104 |
| 2.26 | Evolution of the Squeezing Parameter $\widetilde{\xi}_q$ (2.65) in the case of simple z-z coupling between spins in different coupling geometries, for the case of four spins (top) and nine spins (bottom). | 106 |
| 2.27 | Sequence to create Spin Squeezing among nuclear spins in diamond. | 108 |

2.28 3D Plots of Spin Squeezing (left image) among seven nuclear spins and the associated total angular momentum $\langle I_x \rangle$ expectation value (right image) under variation of both free parameters α and ϕ in two iterations of the sequence in Figure 2.27. 110

2.29 Parameters obtained from numerical optimization for different numbers of nuclear spins involved in a Spin Squeezing sequence mediated by the central NV electron spin. 111

2.30 Optimized Squeezing over the number of involved nuclear spins, where all involved free parameters have been numerically optimized. 111

2.31 Results of numerical optimization within the Squeezing Scheme (2.63) when minimizing the Squeezing Parameter ξ_R defined by Wineland (2.53). 112

2.32 Direct comparison between the Squeezing Parameters ξ_R defined by Wineland (2.53) and ξ_q defined by Kitagawa and Ueda (2.52) in a specific numeric example ($n = 4$ spins, $p = 2$ iterations) following the introduced sequence in (2.63). 113

2.33 Quantum Circuit to illustrate the mapping of a phase collected by the electron spin onto a single nuclear spin. 114

2.34 Sequential mapping of phases collected individually by the NV electron spin, onto nuclear spins. 115

2.35 Proposed total operation in Quantum Gate notation for squeezing of nuclear spins surrounding an NV-Center. 115

2.36 Numerical Optimization of the benefit factor b introduced in (2.72) for up to eight nuclear spins. 117

2.37 Sensitivity of a Nuclear Spin Squeezed state composed of $n = 4$ nuclear spins, compared to the shot-noise limit and the Heisenberg limit. 118

2.38 Comparison of different squeezing mechanism, as defined in (2.78) with analytical expression in a Fock basis for up to twenty spins. 120

2.39 A GHZ state and a squeezed state are compared under dephasing by (2.79) in terms of the Sensitivity in (2.75). 121

List of Figures

| | | |
|------|---|-----|
| 2.40 | Illustration of the proposed coupled NV electron system with surrounding nuclear spins for Interferometry with nuclear spin squeezed states. | 122 |
| 2.41 | Decoupling sequences for Spin Squeezing of NV ensembles introduced by Cappellaro and Lukin in [6]. | 124 |
| 2.42 | Conditions for Spin Squeezing with NV ensembles as proposed by Cappellaro and Lukin in [6]. | 125 |
| 2.43 | Schematic Illustration of the method used to calculate coupling frequencies between NV centers in diamond, with diamond unit cells arranged in a spherical manner. | 127 |
| 2.44 | Possible occurrences of coupling frequencies within an ensemble of NV centers distributed in three dimensions, for all possible orientations and lattice sites in a distance of up to 1024 diamond unit cells from a central NV. | 128 |
| 2.45 | Exemplary three-dimensional geometries of NV Centers and resulting total dipolar coupling D as proposed for experiments to investigate possibilities of Spin Squeezing with NV ensembles. | 129 |
| 3.1 | Illustration of the ball of states with radius r (3.7) in terms of the Hilbert-Schmidt norm $\ X\ _2 = \sqrt{\text{Tr}(X^\dagger X)}$, in order to identify bound-entangled states, starting from a well-defined family of states (3.6). | 136 |
| 3.2 | The Peres-Mermin Square, defining sets of commuting operators in its rows and columns which are jointly measured in projective measurements and thus define contexts for a test of Quantum Contextuality. | 141 |
| 3.3 | KCBS pentagram. | 144 |
| 3.4 | An NV^- center consisting of two spin-1 entities in a modified diamond lattice, namely the inherent electron spin of the Vacancy (blue), as well as the adjacent ^{14}N nuclear spin (orange); both spins can in principle be used for KCBS inequality violations by projective readouts. | 146 |
| 3.5 | General procedure for a measurement of operators U and V in one context. | 151 |

| | | |
|-----|---|-----|
| 3.6 | Explicit construction of the involved unitaries U_1 to U_5 in Jerger et al [7]. | 153 |
| 3.7 | All possible choices of pentagram states according the operations described in Um et al [8]. | 155 |
| 4.1 | Schematic illustration of a Bell-like inequality violation based on deterministic assumptions and a priori assignment of values. | 161 |
| 4.2 | Experimental Setup for Random Number Generation with single photons originat- ing from a NV-Center, by using a beam splitter with detectors on each path. | 167 |
| 4.3 | Experimental data (in thousand counts per second) recorded of the single-photon QRNG based on an NV-Center in a 24/7 operation at ambient conditions. | 168 |
| 4.4 | Correlation data obtained from the NV-Center based single-photon Random Num- ber Generator. | 170 |
| 4.5 | Simplified schematic illustration of a Period-Doubling Fibre-Feedback Optical Parametric Oscillator (OPO), featuring the experimental setup used (a) and a de- scription of period-doubling (P2-state) by plotting Pulse Energy of the equilibrated OPO against Power of the pump laser (b). | 172 |
| 4.6 | Transient process for Equilibration of a Period-Doubling Fibre-Feedback OPO (a) and method to obtain random numbers (b) by comparison of the OPO pulse-train with a reference signal. | 173 |
| 4.7 | Generalized Fibonacci numbers $F_{n+k}^{(k)}$ used in (4.15) to calculate the probabilities associated to Feller's Coin Tossing Constants [9], displayed up to order $k = 20$. . . | 176 |
| 4.8 | Shannon Entropies and Min Entropies calculated from the sequence of random bits produced by our OPO experiment in [10]. | 182 |

List of Tables

List of Tables

| | | |
|-----|---|-----|
| 2.1 | Numerical parameters used in simulations of large spin numbers, using the introduced repeated central spin projection. | 84 |
| 2.2 | Absolute values (in kHz) of the coupling parameters between the five superconducting Qubits publicly available on the IBM Quantum Experience. | 94 |
| 3.1 | Pentagram states used by Um et al [8] for an experimental test of Contextuality by KCBS-inequality violation. | 154 |
| 3.2 | A corrected set of Pentagram states, published by Um et al in [11]. | 156 |
| 4.1 | The ideal probabilities $p(n, k)$ related to Feller's Coin Tossing Constants, and occurrences of associated sequences in the measurement data from the OPO operated as a Random Number Generator. | 178 |
| 4.2 | Feller's Coin Tossing Constants (second column) compared to the constants extracted from measurement data provided by the OPO experiment (third column). | 179 |

Introduction: Resources for Quantum Technology

Introduction: Resources for Quantum Technology

“Quantum mechanics was, and continues to be, revolutionary, primarily because it demands the introduction of radically new concepts to better describe the world. In addition we have argued that conceptual quantum revolutions in turn enable technological quantum revolutions.”

-Alain Aspect-

Quantum Technology is emerging as one of the most important advances of the 21st century. It promises potential technological improvements in sensing, random number generation, cryptography, optimization, machine learning, computing and hacking. Big IT companies have recognized this potential by investing millions and billions into research and development, in particular in the area of quantum computing. Within Europe, the European Commission has answered by funding a billion-euro quantum technology flagship program and big companies are examining the possibilities of further development. As an example of Quantum Technology, sensing can be enhanced by using effects at the level of single quanta such as electrons and photons. Quantum mechanical couplings and correlations – mainly quantum entanglement – enable sensitivities that were previously unreachable. A prime example is the Nobel-prize winning LIGO interferometer which uses squeezed light in order to enable gravitational wave detection [12]. Practical applications such as highly sensitive water sensors or detection of other very weak magnetic signals coming from brain waves, biological structures or single spins are also surfacing. Random Number Generation

is greatly enhanced by the inherent non-deterministic structure of Quantum Mechanics. Einstein famously exclaimed: “God does not play dice.” when confronted with the uncertainties and probabilities of quantum mechanics. Nowadays, after decades of research and in particular due to the important results of Bell and others, we understand quantum mechanics to be indeed probabilistic and provably non-deterministic. In Random Number Generation, this leads to quantum mechanical phenomena being a great resource of entropy. Moreover, the violation of a Bell-like inequality provides a continuous test of the non-deterministic nature of a number-generating device, which is infeasible with classical, non-quantum mechanical approaches. In Cryptography, quantum key distribution systems are already commercially available and quantum information is shared over great length scales through optical fibers or even via satellite communication [13, 14]. Quantum Algorithms such as Shor’s algorithm – based on Quantum Fourier Transformation – are proven to introduce great improvements in number factoring and thus in breaking certain methods of encryption. Therefore, classical encryption algorithms are being changed to care for potential attacks by Quantum Computers. Certain optimization problems – in particular QUBOs (Quadratic unconstrained binary optimization) have been shown to be very suitable for Quantum Annealers such as those provided by a well-known Quantum Optimization company. First advances in pattern recognition and improved machine learning have also been made. Yet, these machines are still lacking one dimension in coupling to be considered adiabatic quantum computers [15]. Quantum Computing itself has seen impressive progress by scaling up the number of error-corrected qubits. In particular, approaches with superconducting qubits and trapped ions have been successful and are promising to reach three-digit numbers of coherent qubits soon [15–17]. Yet, the quest to outperform classical (super)computers in solving practical every-day problems seems to be rather far away in the future. This is despite the fact that a specific sampling problem has been successfully engineered in order to show one example of such an out-performance, named Quantum Supremacy [18]. In general, it is difficult to demonstrate exactly what kind of tasks can be uniquely solved by Quantum Computers. Still, Quantum Technologies already enable important technological progress in Sensing, Cryptography and Data Science.

With all the excitement about Quantum Technology, it should not be forgotten that there are also important open questions in fundamental research. Is our interpretation of Quantum Mechanics correct? What role does gravity play in the end? Are extended theories like Quantum Gravity, String Theory or Supersymmetry necessary for a proper understanding of Quantum Mechanics? On a much more basic and technical level, multipartite entanglement is not well understood in the sense that notions of entanglement are not uniquely defined in systems of large Hilbert spaces [19–21]. Even the use of Hilbert spaces as a proper description of quantum mechanical degrees of freedom is under criticism by parts of the scientific community [22]. One symptom of the possible unsuitability of Hilbert spaces may be the mentioned uncertainties in multipartite entanglement definition, as well as the fact that some quantum correlations are not represented by entanglement – or, in other words, by the separability of Hilbert spaces – at all and must be instead described by Quantum Discord and other generalized measures which may still present a resource for certain protocols or applications such as sensing.

Both fundamental properties of Quantum Mechanics – such as Bound Entanglement and Quantum Contextuality – and applications to Quantum Technology such as Sensing and Random Number Generation are discussed in this thesis. In particular, the certification of random numbers by Quantum Contextuality unifies both of these aspects. The prime physical system considered is the NV Center, a color defect in diamond. Moreover, applications utilizing superconducting Transmon qubits and optical parametric oscillators (OPOs) are also presented.

Introduction: Resources for Quantum Technology

1 Quantum Sensing

“Very simply, normal computers work, either there’s power going through a wire, or not. It’s 1, or a 0, they’re binary systems. What quantum states allow for is much more complex information to be encoded into a single bit.”

-Justin Trudeau-

The area of Quantum Technology which is likely the closest to an industrial application is Quantum Sensing. In Quantum Computing, even though the academic exercise of demonstrating Quantum Supremacy in an experiment has been performed [18] – accompanied by profound scepticism [23] – a viable improvement of a practical problem that cannot be solved by classical computers is still not in sight. Quantum Sensors, however, promise a range of practical applications in the near future. Resources such as coherent Superposition [24], Quantum Memory [25], Entanglement and Spin Squeezing [26] are mainly used to enable sensing of weak electromagnetic fields [27] down to the level of single spins [24, 28, 29]. This enables applications in Material Science due to the detection of spin and ion compositions, in Medicine and Biology due to better detection of signals and markers [29] and in industrial processes by quality control of involved magnetic fields [30] or gyroscopic rotations [31, 32]. This short list of possible applications is indeed far from complete. Specific review papers have been written to address the exciting possibilities of this emerging technology [24, 28]. In this work, a contribution is made towards the detection of single spins by using correlations of a central sensor spin to ancillary spins and measurement back-action [4, 5].

1.1 Improving Sensitivity by Indirect Sensing using Nitrogen-Vacancy Centers

Nitrogen-Vacancy (NV) centers in diamond have been established as very good candidates for a practical implementation of quantum computing. Indeed, some of the early theoretical predictions like quantum entanglement can now be demonstrated in the laboratory using these diamond impurities. As can be deduced from their name, NV centers consist of a vacancy replacing one of the carbon atoms of a diamond. Additionally, one of its nearest-neighbour carbon atoms is replaced by a Nitrogen atom. The spin of this vacancy can be controlled by microwave-radiation whereas the nuclear spins of the neighbouring atoms can be addressed by radio-frequency pulses [33]. Thus, the vacancy, as well as the surrounding nuclear spins can be used as Qubits for the purposes of Quantum Computing, Quantum Sensing and other Quantum Technologies. The involved nuclear spins of the isotopes ^{13}C and ^{14}N display comparatively long coherence times such that the information about the quantum state is not lost as quickly as in other systems and is long enough to initialize the qubits, perform quantum gates and read out the resulting state [34, 35]

Utilizing Nuclear Spins for Sensing Purposes. It is a well-known property in the case of NV centers, that coherence times of the nuclear spins surrounding the defect are potentially much longer than the coherence time of the inherent electron spin. This is largely due to the fact that the magnetic moment of the electron spin is larger than the magnetic moment of, e.g. the inherent nitrogen nuclear spin by a factor of roughly 3000. Thus, the electron spin couples much more strongly to external magnetic fields and to the spin bath by dipole-dipole coupling [33]. This is the main reason why it is beneficial to consider mapping information obtained during active sensing by the electron spin directly to the nitrogen nuclear spin as an ancillary spin. While storing and classically correlating information such as the phase collected during sensing on the nuclear spin state is no novelty [36], a pure quantum mechanical treatment of the combined electron spin nuclear spin system and the mapping of quantum information therein was previously missing. A

1.1 Improving Sensitivity by Indirect Sensing using NV-Centers

proposal in which the coupled nuclear spin takes over the role of the sensor spin and extends the detection volume was therefore published and extended by ideas on direct mapping with asymmetric sequences, as well as considerations of improvements to sensing under decoherence [4]. In particular, it was demonstrated that the utilization of the presented scheme allows for the detection of very weakly coupled carbon nuclear spins in the diamond lattice. A similar experiment focusing on the nitrogen nuclear spin as an entangled memory qubit was subsequently carried out and published by our institute [25], moreover an experiment directly following our proposal was performed later on [5].

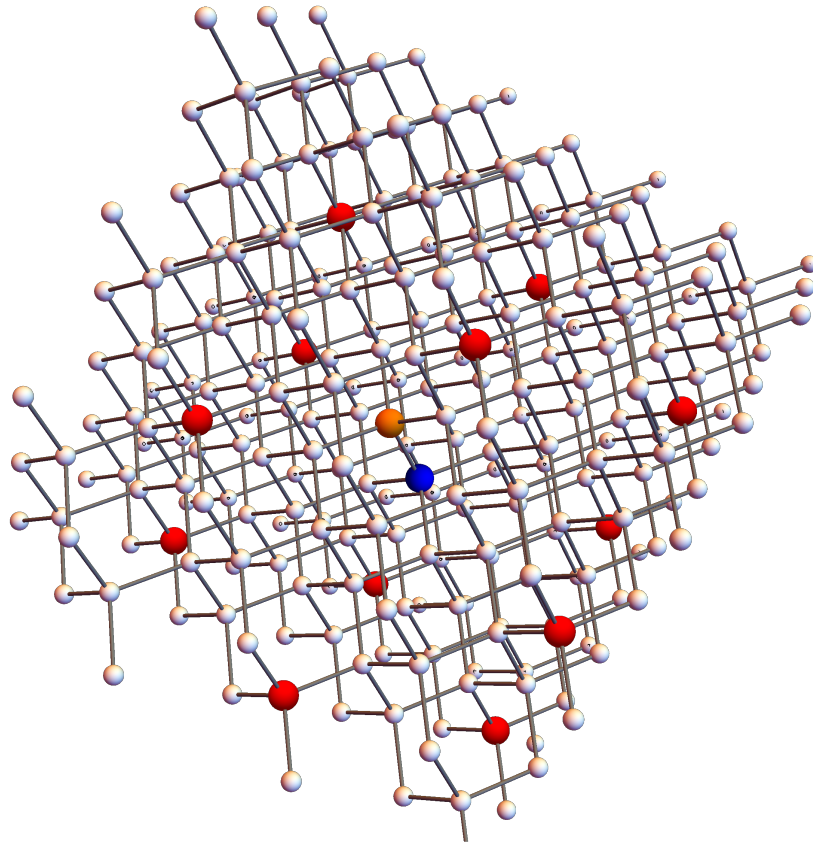


Figure 1.1: 3D model of an NV defect in a diamond lattice. Surrounding ^{13}C nuclear spins are symbolized as red spheres, while the NV is portrayed as a Nitrogen atom (orange sphere) with adjacent vacancy. Note that this model lattice only consists of adjacent cells. In reality, ^{13}C atoms are less abundant (1.1% natural abundance) and are more likely to be found further away from a given defect. The most abundant carbon isotope is ^{14}C which is spin-less and can therefore not be coupled by dipole-dipole interaction, unlike ^{13}C which possesses nuclear spin $I = -1/2$. [33]. In the following, the mapping of spin signals to the NV's nitrogen nuclear spin is considered, while the spins to sense are the surrounding ^{13}C nuclear spins.

1.1.1 Strongly Coupled Nuclear Spins as Indirect Sensors

In order to improve the detection of spins which are weakly coupled, we propose new mapping sequences between the sensor spin and the ancillary nuclear spin. The initial signal can then be inferred by reading out the nuclear spin state, a method which we call Indirect Sensing here. The electron spin interacts directly with a weakly coupled sample spin, while the nuclear spin's magnetic moment is negligible in comparison and is assumed to interact only with the sensor spin. In particular, by mapping to the ancillary spin, the T_1 relaxation time of the sensor spin is no longer the limiting factor [4]. An increased volume of detection is indeed beneficial, not only for detection and control of far away and very weakly coupled nuclear spins within the diamond lattice such as the described ^{13}C carbon spins, but also for the detection of spin species outside the diamond crystal [37], even up to using these detected spins as a resource for molecular qubit-based quantum registers [29] and for quantum simulations at room temperature [38].

Detection Sequences used. In order to achieve this magnified detection, we modify existing detection sequences [3] and tune the occurring waiting times to the coupling frequency of the sensor spin and the ancillary nuclear spins as follows. Let us first define the Hamiltonian that determines the dynamics between the sensing electron spin S , the strongly coupled ancillary nuclear spin F and the sample spin I .

$$H = gS^zF^z + JS^z(\cos\theta I^z + \sin\theta I^x) + \omega_L I^z - \gamma_e B_z S_z + DS_z^2 \quad (1.1)$$

Here, g is the mentioned coupling frequency between the sensor S and the ancillary F . In the case of the NV center and its inherent nitrogen nuclear spin, this is necessarily a z-z coupling due to the symmetry of the defect [33]. The second term describes the coupling between the sensor S and the sample spin I . The sample spin is assumed to be described by polar coordinates r and θ and J is the suitable coupling frequency. An external magnetic field B is applied and aligned along the z-axis of the electron spin with gyromagnetic ratio γ_e . This external field which causes the sample nuclear spin to precess with Larmor frequency ω_L . D is the standard NV zero-field

1 Quantum Sensing

splitting, which causes the electron $| -1 \rangle$ and $| 1 \rangle$ levels to split. We focus on the case of a single sample spin I here, while the model can be easily extended to a principally unlimited number of external spins which are sensed.

1.1.2 Standard Sequence for Direct Detection

In the following, we focus on the most relevant part of the Hamiltonian above, namely the interaction part combined with the applied external field

$$H_{int} = gS^z F^z + JS^z (\cos \theta I^z + \sin \theta I^x) + \omega_L I^z \quad (1.2)$$

A standard sequence for the detection of external spins has been introduced by Taminiau et al [3]. In particular, quantum operations are given as non-continuous microwave pulses on the NV electron spin, combined with unitary evolutions – according to the standard quantum time evolution from the Schrödinger equation $U = e^{-i/\hbar Ht}$ – of the interaction Hamiltonian H_{int} in units of a set time τ . The sequence introduced is specified as in the following figure: When applying this se-

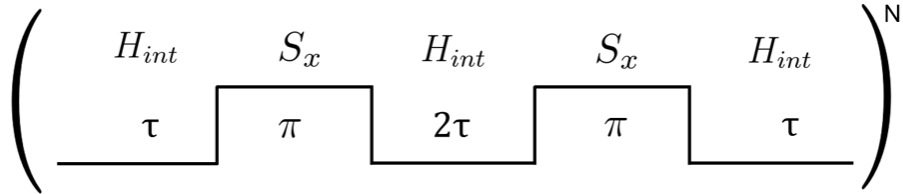


Figure 1.2: Standard sequence for direct detection of external spins [3]. A free time evolution of the Hamiltonian H_{int} for a duration τ is combined with applications of a microwave π pulse on the NV electron spin (S_x operator). The sequence is repeated N times. [4]

quence, the dynamics on the electron spin are governed by the coupling to the external spin with coupling strength J . For simplification, we assume $g = 0$ here, such that the clear dependence of the peak position on J is visible. When monitoring the expectation value $\langle S_x \rangle$, i.e. the expectation

1.1 Improving Sensitivity by Indirect Sensing using NV-Centers

value of the NV electron spin in x-direction, a sharp transition related to the coupling frequency J is observed. Namely, when varying the time τ in the sequence, a sharp transition is observed at $\tau = \pi/(2\omega_L + J \cos(\theta))$ as in Figure 1.3 below.

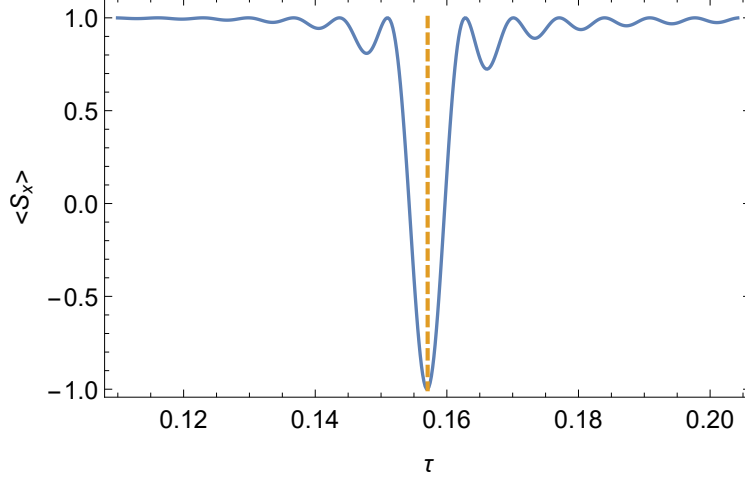


Figure 1.3: Sensing of the coupling frequency J of an external spin coupled directly to the electron spin of a Nitrogen-Vacancy Center. Here the sequence in Figure 1.2 is repeated with varying τ for each sequence. The number of repetitions is set to $N = 23$. Further numerical parameters of the simulation are $J = 1$, $\theta = \pi/4$, $\omega = 10 - J \cos(\theta)$, $g = 0$. The expectation value of the NV electron in x-direction shows a transition at $\tau = \pi/(2\omega_L + J \cos(\theta))$ (dotted line). [4]

If several external spins are present, the resulting expectation value will show multiple transitions, if all parameters are chosen appropriately. Adding another spin to the simulation as well as a further J -coupling term to the Hamiltonian results in two visible dips in the signal. Then, the Hamiltonian reads as

$$H_{int} = gS^z F^z + JS^z (\cos \theta I^z + \sin \theta I^x) + J_1 S^z (\cos \theta_1 I_1^z + \sin \theta_1 I_1^x) + \omega_L I^z I_1^z. \quad (1.3)$$

The expected resolution of both involved coupling frequencies can be observed in the simulation

1 Quantum Sensing

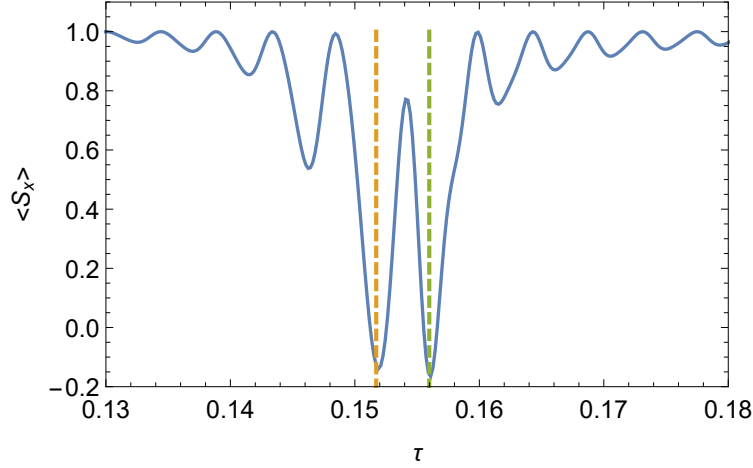


Figure 1.4: Sensing of multiple coupling frequencies J, J_1 of external spins directly by the NV electron spin. The numerical parameters of the simulation are $N = 35, J = 1, J_1 = 1/5, \theta = \theta_1 = \pi/4, \omega = 10, g = 0$. Two dips in the signal are visible at $\tau = \pi/(2\omega_L + J \cos(\theta))$ and $\tau_1 = \pi/(2\omega_L + J_1 \cos(\theta))$ (dotted lines).

as in Figure 1.4, as confirmed by experiments [3, 25]. Conclusively, external spins can be detected directly by the NV electron spin. However, the overall time for any given sequence, including the necessary (N) repetitions of the sequence, are limited by the coherence time of the NV electron spin, T_1 [36, 39]. In order to surpass this limitation, we turn to an indirect detection which includes the longer-lived Nitrogen nuclear spin.

1.1.3 Novel Pulse Sequences for Indirect Sensing using the Inherent Nitrogen Nuclear Spin

In the following, we include the Nitrogen nuclear spin more actively into the simulation. Having in mind that the peak position with relevance to the time τ in the expectation value of S_x depends directly on the coupling, we can motivate the choice of now setting

$$\tau \propto \frac{\pi}{g}, \quad (1.4)$$

1.1 Improving Sensitivity by Indirect Sensing using NV-Centers

which is central for the following sequences to work since the time of the free evolution τ is then adapted to the coupling of the strongly coupled spin, to which the signal is to be mapped. When using a slightly modified standard sequence, the dynamics of the electron spin become visible on the strongly coupled nuclear spin.

However, as visible in Figure 1.6, the dynamics do not necessarily agree, i.e. they show different

$$\left(\begin{array}{ccccc} H_{int} & S_x & H_{int} & S_x & H_{int} \\ \tau & \frac{\pi}{2} & 2\tau & \frac{\pi}{2} & \tau \end{array} \right)^N$$

Figure 1.5: Modified sequence for indirect detection of external spins [3, 4]. Note that the microwave pulse length is reduced by a factor of two compared to the previous sequence in Figure 1.2. [4]

frequencies and amplitudes of the signal. In order to map as much of the sensing information from the electron spin to the nuclear spin as possible, further adaptation of the used sequence may be in order, including operations with radio frequency waves on the strongly coupled nuclear spin.

Consequently, we introduce a more sophisticated version of the sequences above, in which firstly, each free evolution by H_{int} is replaced by another sequence, and secondly, unitary operations are performed on both the electron spin and the strongly coupled nuclear spin. In the case of reading out the signal on the electron spin, π -pulses are performed on the electron spin (D_S sequence), while in the other case when the nuclear spin is read out, π -pulses are also performed on the nuclear spin (D_F sequence). The explicit sequences are composed as in Figure 1.7.

When tuning the experimental parameters appropriately, these sequences lead to very similar expectation values on both the electron spin and the strongly coupled Nitrogen nuclear spin of an NV center. This is a remarkable result, since the information is transferred from the NV electron spin, which is an active sensor, to the nuclear spin, which is passive. Moreover, this is achieved without explicit two-qubit or multiple-spin gates, but by single spin rotations combined with well-timed

1 Quantum Sensing

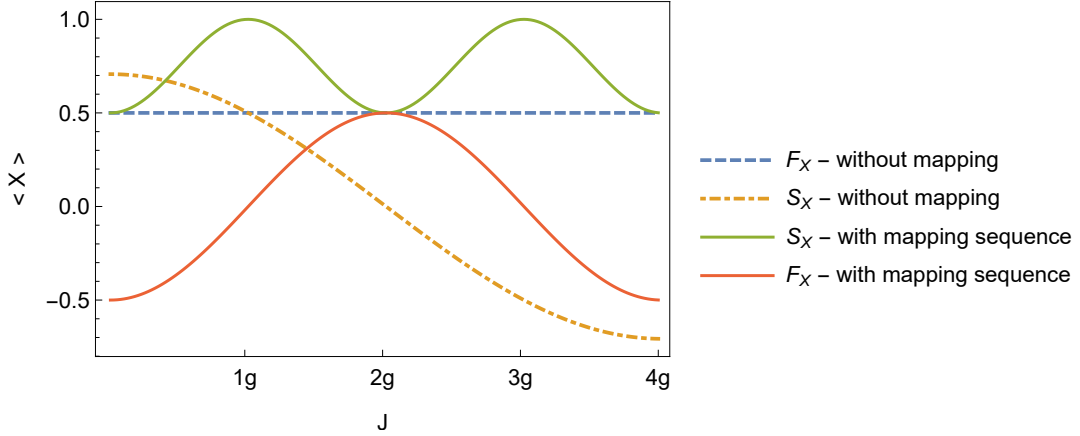


Figure 1.6: Comparison of the expectation values on the NV electron spin $\langle S_x \rangle$ and on the strongly coupled Nitrogen nuclear spin $\langle F_x \rangle$ both in presence (solid lines) and in absence (dotted lines) of the mapping sequence of Figure 1.5. The following parameters were used for the simulation: $g = 40$, $\tau = \pi/(2g)$, $J \in \{0, 4g\}$. The mapping sequence introduces dynamics on the nuclear spin which reflect the dynamics of the electron spin.

free evolutions which make use of the inherent dipole-dipole coupling. This leads to the possibility of overcoming the electron spin's limitation defined by its decoherence time T_1 . However, it is also worthwhile to note that the expectation values of the nuclear spin and the electron spin show very similar dynamics when the parameters are well-tuned, however they do not agree exactly for all parameters, which also signifies that the states have not been cloned, which would violate the non-cloning theorem. This can be observed from Figure 1.8, in which the side peaks of the direct and the indirect detection are slightly varied. Moreover it should also be noted that different sequences and measurements are performed in both cases, such that cloning is principally excluded and the situation is better compared with a cut-and-paste situation such as in Quantum Teleportation [40].

1.1 Improving Sensitivity by Indirect Sensing using NV-Centers

$$D_F = \left(\begin{array}{c} \text{---} U_M \text{---} \pi \text{---} U_M^2 \text{---} \pi \text{---} U_M \text{---} \\ \text{---} F_x \text{---} \end{array} \right)^N ; \quad U_M = \left(\begin{array}{c} \text{---} H_{int} \text{---} S_x \text{---} H_{int} \text{---} S_x \text{---} H_{int} \text{---} \\ \text{---} \tau \text{---} \frac{\pi}{2} \text{---} 2\tau \text{---} \frac{\pi}{2} \text{---} \tau \text{---} \end{array} \right)$$

$$D_S = \left(\begin{array}{c} \text{---} U_M \text{---} \pi \text{---} U_M^2 \text{---} \pi \text{---} U_M \text{---} \\ \text{---} S_x \text{---} \end{array} \right)^N ; \quad U_M = \left(\begin{array}{c} \text{---} H_{int} \text{---} S_x \text{---} H_{int} \text{---} S_x \text{---} H_{int} \text{---} \\ \text{---} \tau \text{---} \frac{\pi}{2} \text{---} 2\tau \text{---} \frac{\pi}{2} \text{---} \tau \text{---} \end{array} \right)$$

Figure 1.7: Pulse sequences for mapping information to the strongly coupled Nitrogen nuclear spin (D_F), compared to the same sequence with the electron spin as active sensor (D_S). Note that in each repetition of D_F or D_S , a single repetition of the mapping sequence U_M is also performed. U_M is the sequence introduced before in Figure 1.5. F_x is the operator in x-direction associated with a strongly coupled nuclear spin, while S_x denotes the same for the electron spin.

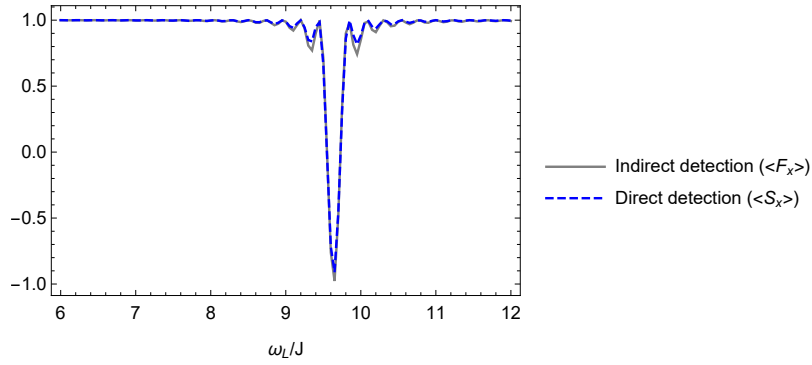


Figure 1.8: Comparison of direct detection of an external nuclear spin on the NV electron spin when using the sequence D_S (Figure 1.7) with the indirect detection on the strongly coupled nuclear spin when performing the pulse sequence D_F . The resulting expectation values agree very well and the peaks show full resolution from the expectation value +1 to -1. Slight variations of the side peaks show that the expectation values are not necessarily exactly identical, however the peaks are found at the same frequencies. Simulation parameters include $N = 44$, $g = 80$, $J = 1$, $\tau = \pi/g$, $\theta = \pi/4$. Here, the frequency ω_L of the external field on the external spin is varied in units of the coupling J of the NV electron spin to the sensed external spin. [4]

1.1.4 Advantages of the Indirectly Sensing Nuclear Spin under NV Electron Decoherence

In order to verify the benefit of mapping the sensing information of the electron spin to the nuclear spin, we now investigate the behaviour of the coupled system under decoherence. Note that we first assume decoherence effects to only affect the NV electron spin. This assumption is justified by the fact that the gyromagnetic ratio of the NV electron spin is larger than the gyromagnetic ratio of the nuclear spin by a factor of roughly 3000 [33]. In other words, since the NV electron is a much better sensor, it is also much more sensitive to the decohering influence of external fields and external spins. This is also the main reason why the T_1 time of the surrounding nuclear spins is significantly longer than the coherence time of the NV's inherent electron spin [33]. We therefore introduce the following simple decoherence model, which only affects the NV electron spin.

$$\rho_{dec} = p \left(\frac{\mathbb{1}}{2} \otimes \text{Tr}_1(\rho) \right) + (1 - p)\rho \quad (1.5)$$

Here, a portion p with $0 \leq p \leq 1$ of the electron spin – the first spin in the model – is replaced by the completely dephased state, the normalized identity. The remaining part of the density matrix is left intact by tracing out the first spin through the application of the partial trace Tr_1 . Moreover, the portion $(1 - p)$ of the original density matrix is left completely intact. This represents a partial depolarizing channel [41], which is applied each time after the mapping sequence U_M , as in Figure 1.7.

Under the influence of decoherence on the actively sensing electron spin, the main advantage of the presented scheme becomes visible, namely the non-vanishing contrast of the signal on the ancillary strongly coupled nuclear spin.

1.2 Indirect Signal Transmission by an Asymmetric Sequence

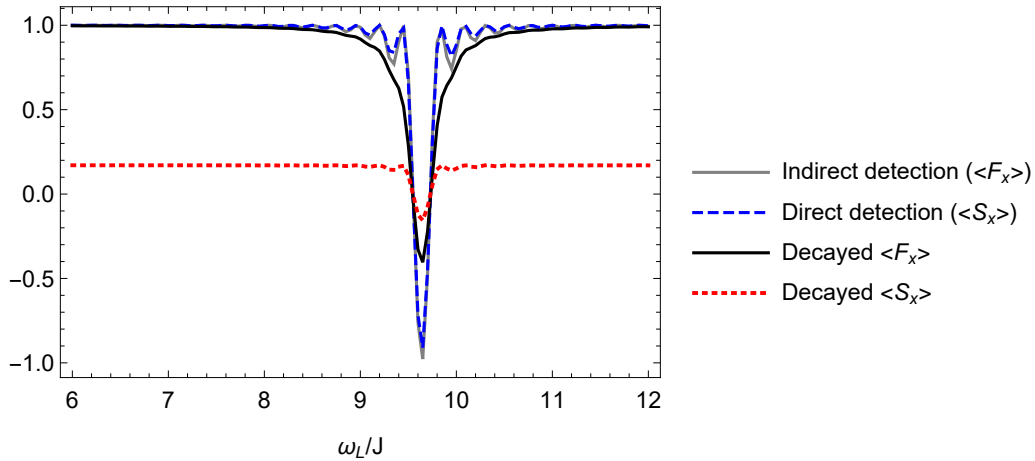


Figure 1.9: When applying depolarization solely on the NV electron spin – related to the observable S_x – both the direct signal on the electron spin and the indirect signal observed on the nuclear spin by the observable F_x are affected. Yet, the contrast of the peak at the detected coupling frequency of the external spin is clearly higher in the case of the nuclear spin. The chosen parameters are equal to the parameter set in Figure 1.8, apart from the introduced decoherence parameter which is here set to $p = 10^{-2}$.

1.2 Immediate Indirect Signal Transmission by an Asymmetric Sequence

A surprising find while performing the related simulations was the fact that it is sufficient to perform operations on the actively sensing NV electron spin in an asymmetric manner in order to map the sensing information to the ancillary Nitrogen nuclear spin. Before, the sequence in Figure 1.7 included pulses on each spin, from which the signal is to be read out. However, we now turn to a single sequence which only includes unitary operations on the central electron spin, regardless of whether the signal is read off from the nuclear spin or the electron. In this sequence, the first π -pulse of the previous sequences is replaced by a $\pi/2$ -pulse, while the second pulse is left unvaried. This is a central result of our paper [4], indeed also a central result of this thesis. Note that here,

1 Quantum Sensing

$$D_{SF} = \left(\underbrace{U_M}_{\tau} \underbrace{\left[\frac{S_x}{\frac{\pi}{2}} \right]}_{\frac{\pi}{2}} \underbrace{U_M^2}_{\pi} \underbrace{\left[\frac{S_x}{\pi} \right]}_{\pi} \underbrace{U_M}_{\tau} \right)^N ; \quad U_M = \left(\underbrace{H_{int}}_{\tau} \underbrace{\left[\frac{S_x}{\frac{\pi}{2}} \right]}_{\frac{\pi}{2}} \underbrace{H_{int}}_{2\tau} \underbrace{\left[\frac{S_x}{\frac{\pi}{2}} \right]}_{\frac{\pi}{2}} \underbrace{H_{int}}_{\tau} \right)$$

Figure 1.10: The portrayed asymmetric sequence with unitary operations limited to the electron spin alone can replace both sequences in Figure 1.7, which includes unitary operations on the electron spin as well as the strongly coupled nuclear spin. The signal can still be read out from both the actively sensing electron spin and the passive ancillary nuclear spin.

the indirect nature of the sensing enhancement mechanism becomes fully apparent. While manipulations are only carried out on the central electron spin, its sensitivity is enhanced by the interplay with the coupled nuclear spin. This is done by constructing a suitable Quantum Algorithm on the electron spin, in which the free interaction time $\tau = \pi/g$ crucially mirrors the coupling strength g of the two involved spin entities.

As seen in figure 1.11, the contrast of the detection is somewhat reduced, i.e. here, the expectation value does not display the full range between +1 and -1, even though the number of repetitions is quadrupled compared to the previous image in Figure 1.8. The full contrast can however be restored by performing even more repetitions of the sequence ($N \approx 8*44$). This illustrated that using the sequence on the electron spin above, the sensing information is distributed equally between the electron spin and the coupled nuclear spin. While this does not seem an advantage on first sight, it has to be kept in mind that the behaviour under decoherence is more beneficial when including the nuclear spin due to its long coherence time. Moreover, the electron spin state is destroyed during optical readout of an NV [33] while the nuclear spin can repeatedly be read out when using single-shot readout [42].

1.2 Indirect Signal Transmission by an Asymmetric Sequence

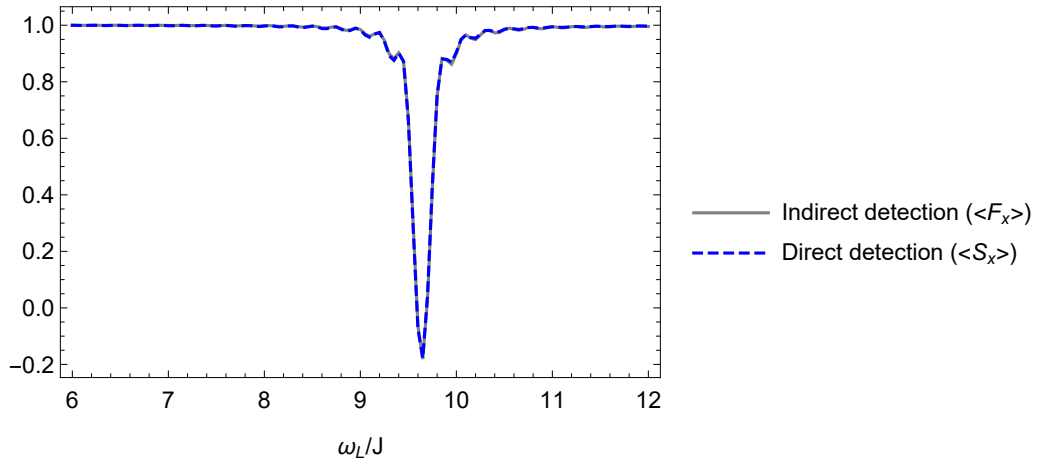


Figure 1.11: Using the asymmetric sequence D_{SF} (Figure 1.10) in both cases, the direct detection of an external nuclear spin on the NV electron spin is compared with the indirect detection on the strongly coupled nuclear spin. The resulting expectation values agree even better than when performing separate sequences on the different spins as in Figure 1.8. Simulation parameters include $N = 4 * 44$, $g = 80$, $J = 1$, $\tau = \pi/g$, $\theta = \pi/4$. The frequency ω_L of the external field on the external spin is again varied in units of the coupling J of the NV electron spin to the sensed external spin. [4]

1.2.1 Performance of the Asymmetric Sequence under Decoherence

This advantage becomes visible as we introduce decoherence by a partial depolarizing channel [41] again according to the model in equation (1.5). The resulting amplitude signals (Figure 1.12) show a clear advantage when reading out the signal from the nuclear spin, unsurprisingly, as the depolarization is carried out directly on the electron spin while the nuclear spin only suffers decoherence effects indirectly by transmission through coupling to the central spin.

1 Quantum Sensing

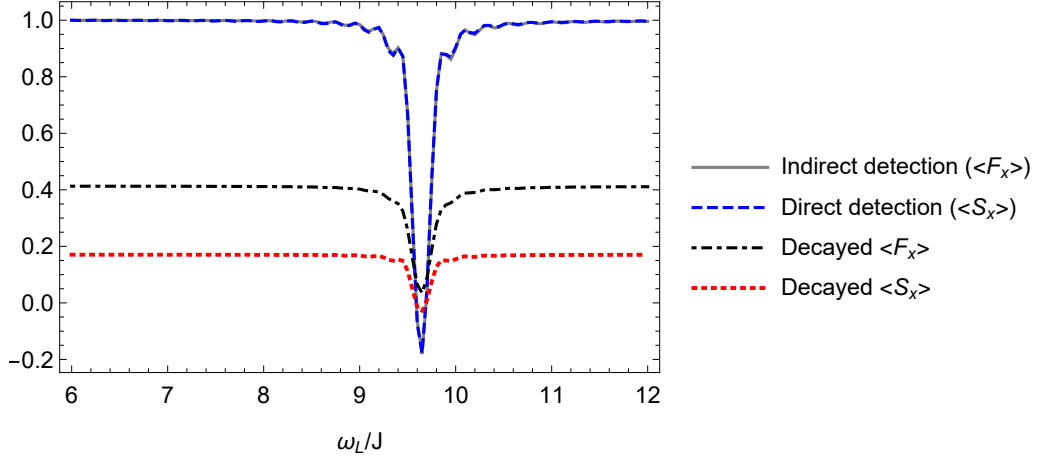


Figure 1.12: Performance of the asymmetric sequence D_{SF} (Figure 1.10) under decoherence. Simulation parameters are defined in Figure 1.11 above, with the addition of the decoherence parameter $p = 10^{-2}$ in eq (1.5). A better contrast of the nuclear spin observable $\langle F_x \rangle$ as opposed to the electron spin observable $\langle S_x \rangle$ is clearly visible.

1.2.2 Effects of treating the Ancillary Spin as Spin 1 with additional Decoherence

Upon publication of the results introduced in the section above in [4], resonance from the scientific community lead to further investigations on our side. Namely, Professor Jiangfeng Du from the University of Science and Technology of China and his institute took interest and questioned whether our introduced Quantum Algorithm violates the No-Cloning Theorem of Quantum Mechanics due to the surprising overlap of amplitudes that can be produced as in Figure 1.11. Our reaction was twofold, firstly we show that neither the signal amplitudes nor the quantum states of the two involved spins are exactly equal. Secondly, given that the spins were not even of the same dimensionality in our calculations, we show that the No-Cloning propositions and the presented results still hold in the case when both involved spins are Spin 1 entities.

No-Cloning Theorem is not violated

In order to proof that the No-Cloning Theorem is not violated, we firstly zoom in at the minimum of the signal in Figure 1.11 in order to show that the amplitudes are not exactly identical. Indeed, it becomes obvious that there is a discrepancy between the expectation values of the two different spins.

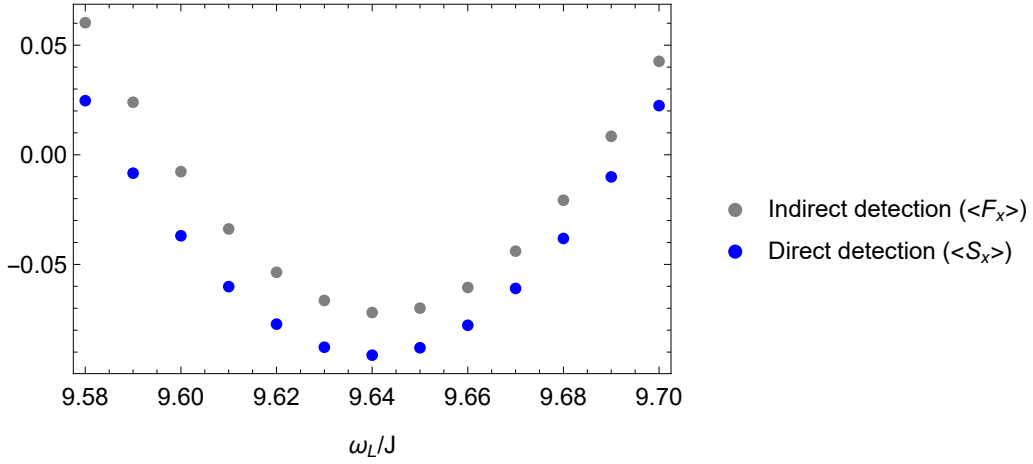


Figure 1.13: Zoom-in at the minima of the amplitudes of the expectation values in Figure 1.11 in order to prove that the signals are not exactly identical. Simulation parameters are as in the referenced figure.

Definition of the Entanglement Measure Fidelity. Moreover, we portray the fidelity F of the reduced density matrices of the specific spins, given by the formula [41]

$$F(\rho_1, \rho_2) = \left(\text{Tr} \left(\sqrt{\sqrt{\rho_1} \cdot \rho_2 \cdot \sqrt{\rho_1}} \right) \right)^2, \quad (1.6)$$

for two density matrices ρ_1 and ρ_2 , where the square root is defined as the Matrix Square Root. Here, ρ_1 and ρ_2 are the reduced density matrices of the electron spin and the nuclear spin, respectively.

1 Quantum Sensing

Note that the electron spin is treated as a Spin 1, however we only work in the $m_s = 0$ and $m_s = 1$ subspace. The nuclear spin is still treated as a Spin 1/2 system. When visualizing the overlap between the respective density matrices, it is visible that the states differ, especially in the decisive region, in which the Fidelity between the relevant states drops along with the signal amplitudes in the figures before. Being initialized in the same state,

$$|\Psi_{initial}\rangle_{el,ns} = \frac{1}{\sqrt{2}} (|0\rangle + |1\rangle) \quad (1.7)$$

the Fidelity is always close to unity, but never reaches 1 during the course of the algorithm, such that it is obvious that the density matrices of the electron spin and nuclear spin are very similar, albeit never exactly the same. Therefore, there is no cloning between the spin states or subspaces thereof.

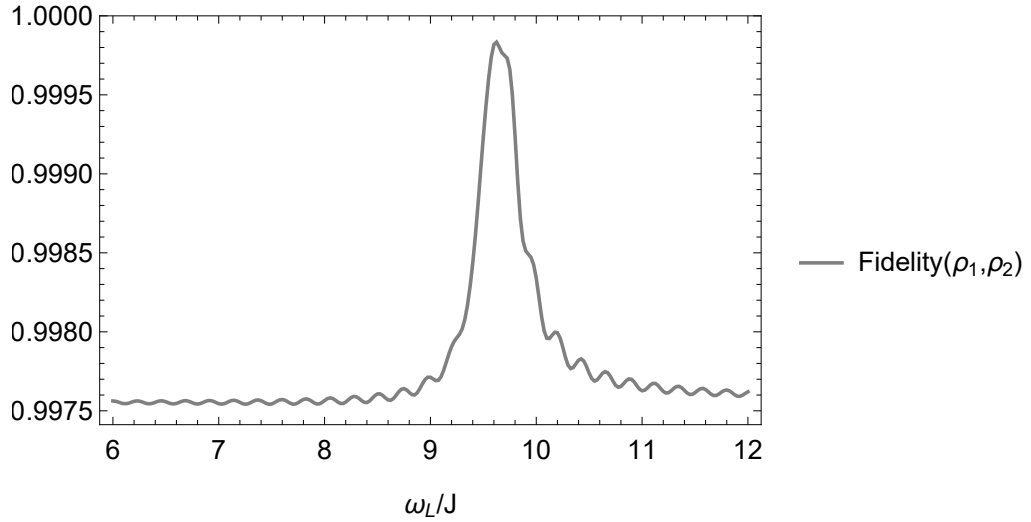


Figure 1.14: Fidelity between the density matrices of the central electron spin (ρ_1) and the strongly coupled nuclear spin (ρ_2). Simulation parameters are defined as before in Figure 1.11 and the Fidelity is given in equation (1.6). Most significantly, this figure signifies that the No-Cloning Theorem of Quantum Information Processing [41] is not violated as the Fidelity between the two reduced density matrices does not reach unity.

Treating the nuclear spin as Spin 1

In the previous sections, the central electron spin was continuously treated as a Spin 1 entity, by either using the full spin operator

$$S_z^{\text{Spin1}} = \begin{pmatrix} 1 & 0 & 0 \\ 0 & 0 & 0 \\ 0 & 0 & -1 \end{pmatrix} \quad (1.8)$$

or the reduced spin operator acting on the $m_s = +1$ and $m_s = 0$ subspace

$$S_z^{\text{Spin1,red.}} = \begin{pmatrix} 1 & 0 \\ 0 & 0 \end{pmatrix}. \quad (1.9)$$

By using this operator, the electron Qutrit (Spin 1) is effectively reduced to a Qubit (Spin 1/2). The nuclear spin, however was implicitly treated as a Spin 1/2 entity, mainly for simplicity of calculations and since the introduced model is generally valid for any dimension of spin subspaces. In the scenario of the NV-center, both Spin 1/2 and Spin 1 entities are present among the nuclear spins, namely the isotopes ^{13}C and ^{14}N [33].

We now treat the nuclear spin used as an ancillary for indirect detection explicitly as a Spin 1 system, as in the realistic case when the strongest coupling to the NV's electron spin is the coupling to the inherent nitrogen nuclear spin ^{14}N . We will demonstrate that the results above still hold and this case and moreover, that a direct cloning between the involved two Qutrits can be excluded. As visible in Figure 1.15, the results of being able to detect the coupling frequency of a third spin and a good agreement between the signals of the direct sensor and indirect ancillary still hold. As the dimensionality of the involved spins is different, the signal of the electron spin has a slightly different shape than before in Figure 1.11 with the same simulation parameters, besides the Spin dimensionality. The depth of the peaks suggests that more information about the recorded signal is transferred to the nuclear spin (Indirect Detection Signal($\langle F_x \rangle$)) with increasing dimensionality of the same. Most significantly, it is clearly visible that the amplitudes do not exactly agree, but the peaks are present and indirect sensing still increases the visibility.

1 Quantum Sensing

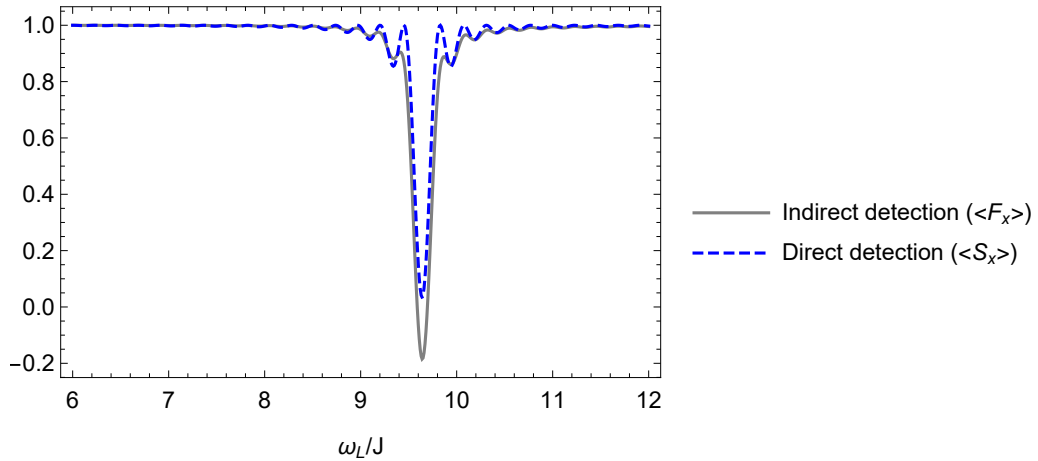


Figure 1.15: Expectation values of the X-Operator when using the same parameters as before in Figure 1.11, besides elevating the strongly coupled nuclear spin from a Spin 1/2 to a realistic Spin 1 entity. The peak of the Indirect Detection on the nuclear spin becomes enhanced and the signal amplitude of the electron spin shows slight variation in comparison with the previous amplitude series while the overall effect is maintained.

Introducing additional Decoherence on the Nuclear Spin

Motivated by the realistic scenario in the case of the Nitrogen-Vacancy center, we previously introduced decoherence effects solely on the electron spin, which are still affecting the nuclear spin signal due to the strong coupling between the spins, as in Figure 1.9 where the decoherence model is given by Equation (1.5). A justified scientific question was what happens to the enhanced signal on the nuclear spin if additional dephasing is introduced. Will the effect on the strongly coupled spin still remain? Indeed, we find that when introducing a weak decoherence the benefits of indirect sensing still remain. On the ancillary nuclear spin, we use a decoherence factor 100 times smaller than on the electron spin, which is still a much stronger decoherence than in the realistic scenario in which the nuclear spin dipole moment is smaller by a factor of roughly 3000 [33].

1.2 Indirect Signal Transmission by an Asymmetric Sequence

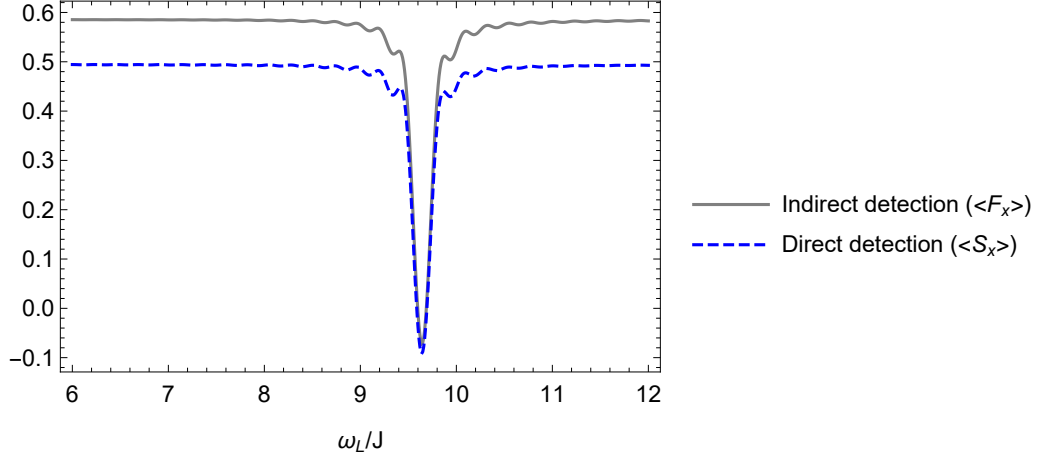


Figure 1.16: Signals on the electron spin and nuclear spin in the presence of decoherence on both spins. The decoherence factor p in equation (1.5) is 10^{-3} on the electron and 10^{-5} on the nuclear spin. Expectedly, the signal amplitude of the nuclear spin remains more visible with a more distinct peak.

1.2.3 Decoherence under Periodic Reinitializations

In the presented scheme so far, all manipulations on the spins were unitary gates or regular Quantum Algorithms, in other words. We now turn to a scenario in which these Quantum Gates are complemented by another operation, namely a reset, more technically a reinitialization of the central electron spin. This means that whichever – possibly mixed – state the electron spin may have evolved to is replaced again by a pure initial state $|\Psi_{initial}\rangle_{el}$. This state is defined by the physical initialization process of populating the energy level $|m_s = 0\rangle$ through the known optical pumping process of the NV-center [33], followed by defined local operations that allow for initial superposition states. Experimentally, it is hard – though possible – to perform those reinitializations without destroying the quantum states of neighbouring nuclear spins [43]. In a simulation however, the reinitialization of part of a composed quantum system is easily performed by setting

$$\rho_{reinit} = |\Psi_{initial,1}\rangle \langle \Psi_{initial,1}| \otimes \text{Tr}_1(\rho(t)) \quad (1.10)$$

1 Quantum Sensing

which means that in a time-evolved collective state $\rho(t)$, the first spin is traced out by the partial trace Tr_1 , replaced by an initial pure state and recombined with the remaining part of the density matrix.

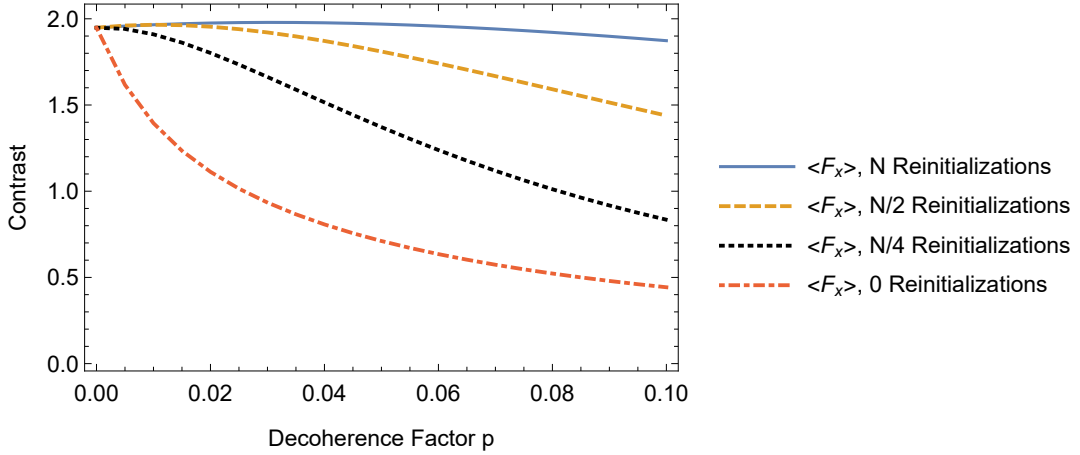


Figure 1.17: Effect of periodic reinitializations on the Contrast in the Signal Amplitude with increasing decoherence. Simulations were performed with $N = 32$ repetitions of the sequence D_F on the strongly coupled nuclear spin (see Figure 1.7). The number of reinitializations is varied from N (solid blue curve) to 0 (dash-dotted red curve). The performance of a larger number of reinitializations is clearly better, while additional realistic side-effects of the physical reinitialization mechanism are not considered.

Simulations were performed including reinitializations according to equation (1.10). The number of reinitializations was varied between a reset at every repetition of the sequence to no reinitializations at all. As a result, the maximum contrast is calculated, i.e. the depth of the peak in the signal as in the amplitude plots before, e.g. Figure 1.16. Being the simple difference between Maximum and Minimum of the signal, this contrast can maximally reach the number 2, as the maximum and minimum of the expectation value are 1 and -1 , respectively. By plotting this contrast over the decoherence parameter p introduced above in (1.5) for different numbers of reinitializations, a clear positive effect of said reinitializations in terms of a better contrast with increasing decoherence is

seen in Figure 1.17.

From a Quantum Information Processing perspective, this is a somewhat surprising consideration. In a standard sensing scenario, in which one spin detects an external spin, reinitializations hardly make sense, since they destroy any correlations, especially entanglement, between a sensor spin and an external spin. Here, with the help of an ancillary spin which is used to enhance sensing, there is also a possibility of mapping correlations between the sensor spin and external spin to the ancillary spin. Thus, the ancillary spin can maintain correlations, even when the active sensor spin is reinitialized. As the sensor spin is also the most active source of decoherence, reinitializations in our indirect scheme turn out to reduce the effects of decoherence.

1.3 A Quantum Derivative?

A second surprising result during the course of the simulations performed – besides the information mapping performance of the asymmetric sequence in section 1.2 – is the fact that the amplitude signal found on the strongly coupled nuclear spin can indeed resemble the derivative of the amplitude signal on the central electron spin.

We use the asymmetric sequence D_{SF} defined above in Figure 1.10, with the difference that instead of using an even number of sequence repetitions, as before, we now use an odd number of repetitions. The response signal on the strongly coupled nuclear spin changes significantly in the sense that it no longer resembles the same peak as the signal from direct detection on the electron spin, but actually resembles a derivative of this signal. More particularly, the amplitude series coming from indirect detection portrays as the envelope of a numerically constructed derivative of the signal. This curious observation was not added to our publication in [4]. Even though the puzzling effect is reproducible in the simulation and only occurs while a third spin is present, which is sensed, we do not yet have an explanation of the observation of this Quantum Deriva-

1 Quantum Sensing

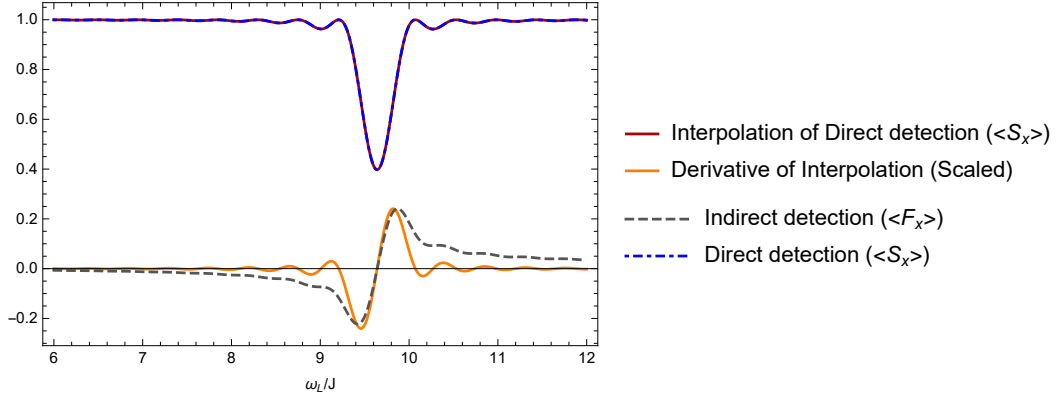


Figure 1.18: The amplitude series on the strongly coupled nuclear spin resembles the envelope of the derivative of the direct detection signal on the central electron spin. The asymmetric sequence D_{SF} (Figure 1.10) was used with an odd ($N = 89$) number of repetitions, which presents the only difference in simulation parameters compared to the standard set in Figure 1.11. The expectation values on the electron spin $\langle S_x \rangle$ from numerical simulation (blue dot-dashed line) are interpolated (red solid line). The derivative of this interpolation (orange solid line) with respect to ω_L is scaled to fit the maximum of the indirect detection signal $\langle F_x \rangle$ from simulation. However it is not shifted on the horizontal axis (parameter ω_L) and shows surprisingly good agreement with the numerical Derivative.

tive. Therefore, the simulative observation is included here in order to inspire further theoretical research, i.e. as an open scientific question alike an experimental measurement that still lacks finding of a deeper mechanism. An explanation of this effect may have implications even in Quantum Computing, as the possibility of a physically inherent Derivation and Integration is very appealing to any Computational System. This may therefore present a very interesting topic to be studied further by future theoretically inclined students and Scientists.

1.4 Conclusion: Quantum Sensing

Improvements to Quantum Sensing using single Nitrogen-Vacancy Centers in diamond were shown in this chapter. A protocol to make use of the long coherence time of nuclear spins surrounding the NV was introduced in section 1.1, in particular by making full use of the dynamics of the collective Hilbert space of the involved spins, rather than treating ancillary spins as a memory. An Asymmetric Sequence acting directly on the NV electron spin was introduced (1.2, Figure 1.10) and found to be able to replace the previous novel sequence acting on both the electron and the ancillary, strongly coupled nuclear spin (1.1.3, Figure 1.7). In both cases, an advantage of the introduced Indirect Sensing protocols was shown when subjecting the NV electron spin to decoherence (sections 1.1.4, 1.2.1), as opposed to direct sensing. The effects of treating the ancillary nuclear spin as a Qutrit, rather than a Qubit were also analysed (1.2.2) as well as the effect of periodic reinitializations of the sensing electron spin (1.2.3). Finally, a curious observation relating signals on the electron spin and the strongly coupled nuclear spin to the application of a mathematical derivative operation (1.3) was presented as a phenomenon to inspire future studies.

Here, the focus on entities to be sensed was on the signals of other external spins, such as nuclear spins passively occurring in the diamond lattice. In the following chapter, Quantum Sensing of external spin entities will still be addressed – when discussing the benefits of pairwise entangled Singlet States, generated by the methods introduced therein. The focus then also shifts to Quantum Sensing of Magnetic Fields and Electrical Fields. These can be sensed more effectively by the aid of correlated nuclear spin states and, more canonically, by ensembles containing between hundreds up to millions of NV spins, particularly when those NVs can be brought into a collective Spin Squeezed State. In general, several methods involving measurement techniques such as repeated Projections and the generation of effective Hamiltonians will be portrayed with the aim to create special quantum states as useful resources. This applies again to Quantum Sensing but also to further protocols in Quantum Information Processing.

1 Quantum Sensing

2 Quantum State Engineering

“Basically, quantum mechanics is the operating system that other physical theories run on as application software (with the exception of general relativity...). There’s even a word for taking a physical theory and porting it to this OS: ‘to quantize’.”

-Scott Aaronson-

An aspect of Quantum Technology which is crucial for different applications such as Sensing, Error Correction or Computing, is the engineering of specific quantum states. Some states such as highly entangled states have specific non-classical properties and can also be used for counter-intuitive protocols such as Quantum Teleportation [40,44]. Other states such as squeezed states are particularly robust to noise and can thus enhance practical Quantum Sensing applications [6, 12]. Creating such states in the laboratory is often a daunting task due to the general instability of correlated states under decoherence [45], imperfections in the implementation of quantum gates and resulting unsatisfactory fidelities. In order to avoid the problem of accumulating gate errors and infidelities, we follow a different approach. Instead of following the usual steps of a prior initialization and subsequent application of quantum gates, our approach allows to combine these two separate steps into one. Specifically, by repeated measurement of one central qubit, that is coupled to all other qubits in our case, the whole remaining quantum system is projected into a purified state and specific target states can be addressed. The possible target states include squeezed states and specific pairwise entangled states [46], depending on the initial parameters, external fields and the timing between different sequential measurements.

2.1 Creation of effective Hamiltonians by repeated measurements

The effect of measurements in Quantum Mechanics have been very surprising in their discovery and subject to many debates during the formative years of the theory [47]. Here we focus on the property of quantum mechanical measurements to change the measured state, especially in the case when only a subsystem (A) of a bigger composite state ($A \otimes B$) is measured such that the measurement operator M_A acts as

$$\langle M_A \rangle = \langle \Psi_{A,B} | M_A \otimes \mathbb{1}_B | \Psi_{A,B} \rangle \quad (2.1)$$

In particular, following the Ansatz of Nakazato et al. [48] we focus on systems evolving under a composite Hamiltonian, while one subsystem (say A) is repeatedly projected to its initial state. Then,

$$H_{A,B} = H_A + H_B + H_{int} \quad (2.2)$$

where H_{int} is the interaction Hamiltonian. Let ρ_0 be the initial state of the total system with the property

$$\rho_0 = |\Phi\rangle_A \langle \Phi|_A \otimes \rho_B \quad (2.3)$$

Moreover let ρ be subject to repeated projections of system A to its initial state by the partial projection operator

$$O = |\Phi\rangle_A \langle \Phi|_A \otimes \mathbb{1}_B \quad (2.4)$$

such that for each projection

$$V_{B,\Phi}(\tau) \equiv \langle \Phi|_A e^{iH_{A,B}\tau} |\Phi\rangle_A \quad (2.5)$$

is the non-unitary operator acting on the environmental system ρ_B . The most relevant finding of Nakazato et al. [48] for our interests is that the undefined state ρ_B is driven towards a well-defined pure state by the repetition of the projection measurements. Indeed, their 2003 paper finds that

2.2 Purification by controlled non-unitary evolution

with a large number of repetitions N , any initial environmental (ρ_B) state is guaranteed to be driven to

$$\rho_B(N) \xrightarrow{N \text{ large}} \frac{|u_{max}\rangle \langle u_{max}|}{\langle u_{max}|u_{max}\rangle} \quad (2.6)$$

where $|u_{max}\rangle$ is the eigenstate with the property

$$V_{B,\Phi}(\tau) |u_{max}\rangle = \lambda_{max} |u_{max}\rangle, \text{ with } \lambda_{max} > \dots > \lambda_{min} \quad (2.7)$$

under the assumption that λ_{max} exists as a unique, discrete and maximal eigenvalue of $V_{B,\Phi}(\tau)$, such that

$$V_{B,\Phi}(\tau)^N \xrightarrow{N \text{ large}} \lambda_{max}^N |u_{max}\rangle \langle u_{max}|. \quad (2.8)$$

Remarkably then, a repeated projection of one part of the quantum system leads to the purification of the other part, even towards a calculable, well defined final target state.

2.2 Purification of an unpolarized spin-bath by controlled non-unitary evolution

Before we apply the introduced method to our specific scenario, let us briefly review and illustrate the mechanism of Purification at a fundamental level. Consider the following standard example of purification. Let two qubits be entangled in the Bell state

$$|\Phi^+\rangle = \frac{1}{\sqrt{2}} (|\uparrow\uparrow\rangle + |\downarrow\downarrow\rangle) \quad (2.9)$$

Then obviously, since the two qubits are not separable, a reduced state of one of the qubits is always mixed. In particular, tracing out yields a fully mixed state in this case

$$Tr_1 (|\Phi^+\rangle \langle \Phi^+|) = \frac{\mathbb{1}_2}{2} \quad (2.10)$$

which clearly fulfils the condition $Tr(\rho^2) < 1$ as required for a mixed state. However, when one of the qubits is measured, the combined state is projected into one of the two the separable pure

2 Quantum State Engineering

states

$$|\Psi_{res}\rangle = |\uparrow\uparrow\rangle \text{ XOR } |\Psi_{res}\rangle = |\downarrow\downarrow\rangle \quad (2.11)$$

with equal probability. XOR signifies the logical exclusive OR. For both of these states, the partial trace yields pure states as

$$Tr_1(|\Psi_{res}\rangle\langle\Psi_{res}|) = |\uparrow\rangle\langle\uparrow| \text{ XOR } Tr_1(|\Psi_{res}\rangle\langle\Psi_{res}|) = |\downarrow\rangle\langle\downarrow|. \quad (2.12)$$

At the single qubit level, the individual states have thus changed from a mixed state to a pure state with the property $\rho^2 = \rho$. Therefore, the effect of a local measurement within a combined system can be the Purification of a coupled qubit. This can also be generalized to higher-level subsystems or qudits.

We apply the introduced method and propose an implementation using an NV center and surrounding nuclear spins [46]. A heralded optical readout of the NV spin at low temperature [43] allows for repeated sequential measurements. Depending on the detected outcome, the sequence of measurements is continued or discontinued. The measurement result signifies whether the central NV spin has been successfully projected into a target spin state. We focus mainly on the case of repeated successful projection. When choosing suitable target states, it is found by numerical simulations that the surrounding nuclear spins are purified as expected, even when a fully mixed state is the initial condition.

2.2.1 Repeated measurement of a central spin

In order to approach the realistic situation of an NV spin coupled to surrounding nuclear spins, we consider a central spin geometry. In the NV case, the direct couplings between neighbouring nuclear spins can be neglected. The magnetic moment of the central NV electron spin is much greater than the magnetic moment of the C^{13} nuclear spins, by a factor of about 3000 [33]. The interaction is thus dominated by the coupling of the central spin to the individual nuclear spins. In

2.2 Purification by controlled non-unitary evolution

practice, the dipole-dipole coupling between NV and nuclear spins is three-dimensional. However, we begin by assuming dominating z-z coupling and a one-dimensional geometry. We generalize to two-dimensional and three-dimensional coupling geometries later. The symmetry axis of the NV center defines a quantization axis and thereby the z-direction. The general Hamiltonian of the problem is given by

$$H = S_z \sum_k \vec{g}_k \cdot \vec{I}_k + \omega \sum_k I_z^{(k)}. \quad (2.13)$$

Here, S_z is the NV electron spin operator, while \vec{I}_k contains the spin operators of the k -th nuclear spin. The coupling strength in each direction is given by the elements of the respective coupling vector \vec{g}_k . An external magnetic field is applied to the nuclear spins in z-direction with strength ω . While the external magnetic field is homogeneous for all nuclear spins and introduces a common preferred direction, the different coupling strengths introduce inhomogeneities that have the important purpose to perturb the dynamics of preferred directions or symmetries [46]. By tuning the strength of the external field, the significance of these inhomogeneities can thus be controlled.

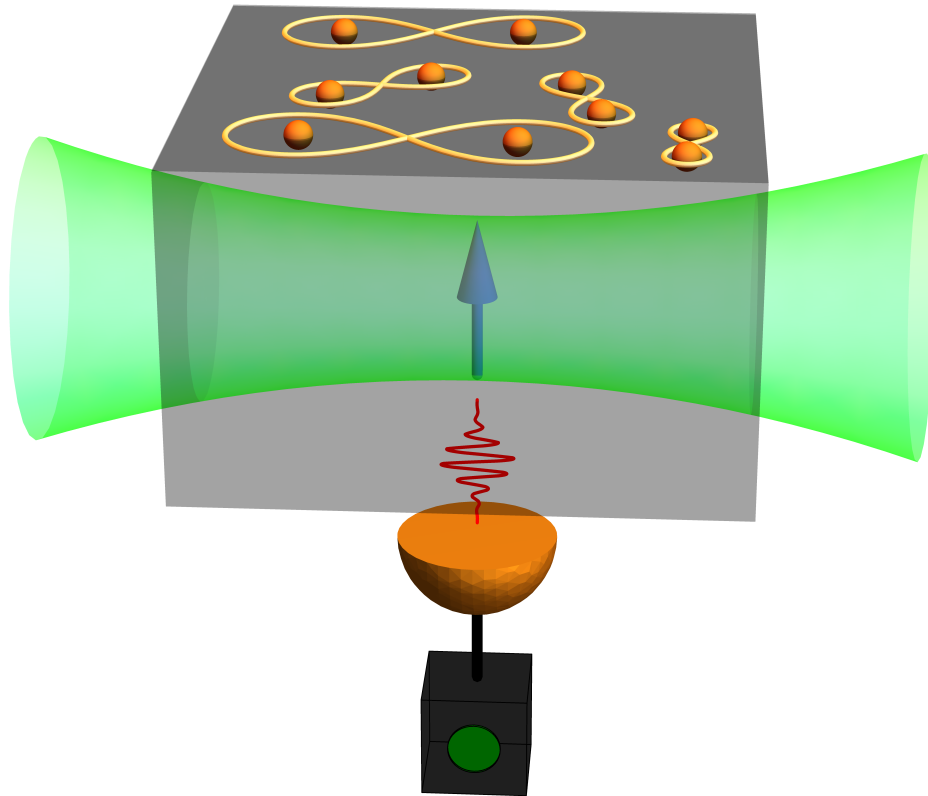


Figure 2.1: Mathematica illustration of the proposed purification experiment. The NV spin (solid blue arrow) is repeatedly projectively measured – aided by the inherent Nitrogen nuclear spin – by illumination with green laser light and subsequent detected emission of single photons (red sinusoid). Nuclear spins (orange spheres) experience coupling mediated by the NV spin. In the illustrated scenario, the result is a pairwise entangled state, as symbolized by the figure-eight curves (lemniscate of Gerono), see A.2.2, [46].

2.2.2 Purification Mechanism

In order to purify the nuclear spins around the NV electron spin, we thus need to develop a sequence of unitary operations and measurements on the NV electron spin. As we will see later on, any superposition state of the electron spin states $|+1\rangle$ and $|-1\rangle$ is suitable for purification. However, we first focus on a simple superposition resulting from a Hadamard gate or a $\pi/2$ - pulse, in other terms.

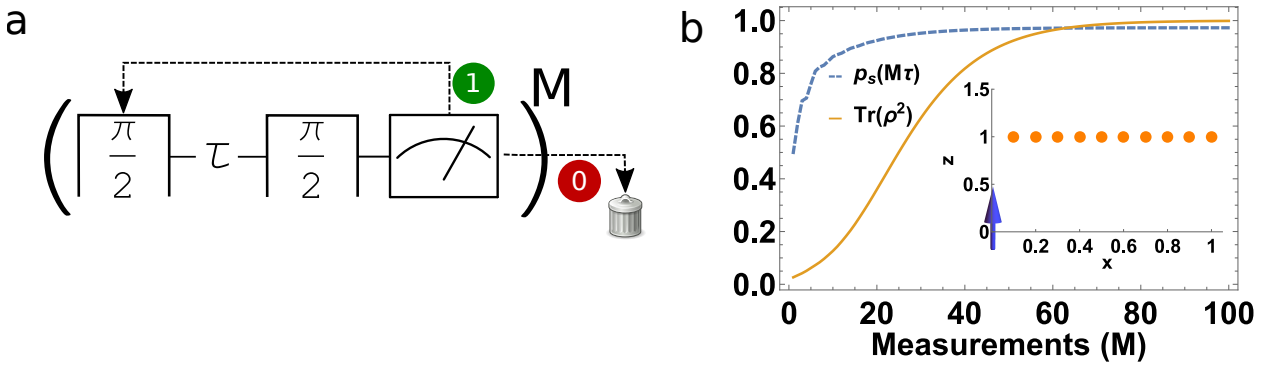


Figure 2.2: Proposed Measurement Sequence for Purification and results from simulation.

(a) Sequence for repeated projection of the central spin into a superposition state.

(b) Repeated Projective Measurements result in a purification of the surrounding nuclear spins (solid orange curve). Moreover, the probability p_s (dashed blue curve) of projecting the electron spin into the right state is increased with the number of measurements. The 1D scenario considered for this particular calculation is illustrated in the inset, with the blue arrow signifying the central electron spins whereas orange spheres symbolize nuclear spins, coupled to the central spin. The z position for all ancillary spins is equal in this case, while the x positions are distributed equidistantly. [46]

Figure 2.2a shows the sequence used to repeatedly prepare a superposition state of the central NV spin. The $\pi/2$ pulse serves the purpose to create a superposition state after an initialization of the spin. The system is then evolved freely for a time τ , followed by another pulse in order to map the

2 Quantum State Engineering

population of the superposition state back to an energy eigenstate for readout purposes. The NV fluorescence measured corresponds to the population of the eigenstate $|0\rangle$. If the projection was successful, the measurement result is “1” and the sequence can be repeated (M times). Crucially, in case of an unsuccessful projection, the whole experiment has to be aborted or corrected, since the purification has been interrupted, leading to ambiguity in the knowledge of the target state. Therefore, a high preparation and readout Fidelity is of high importance for this experiment.

Note that the probability of obtaining a whole sequence of successful measurements is still low a priori, as visible in Figure 2.3. However, a successful measurement increases the chance of another successful repetition in each step, as in Figure 2.2b. This can be interpreted as a non-Markovian memory effect in the environment surrounding the central spin, due to the described Purification.

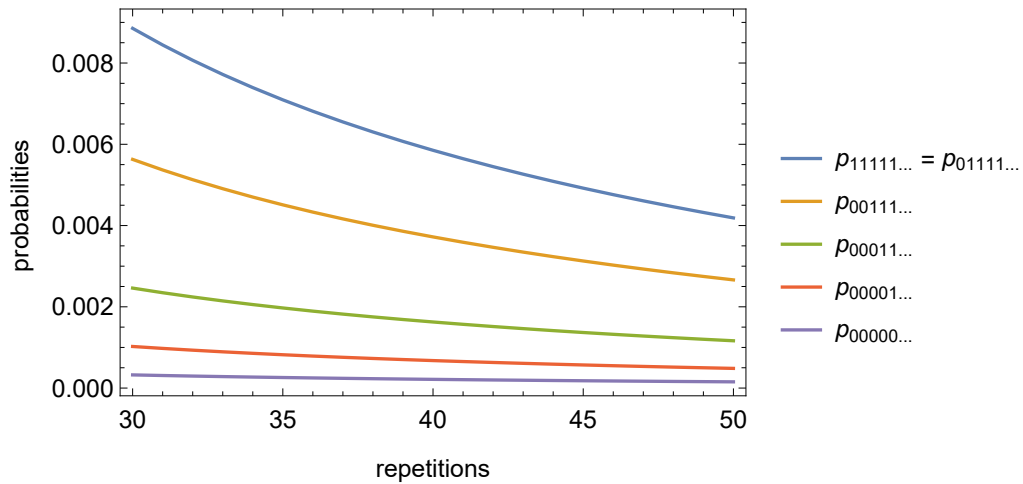


Figure 2.3: Probabilities for selected sequences or trajectories of measurement results, resulting from repeated projections of a central spin. The scenario considered in this chapter is a sequence of successful projections, i.e. the sequence corresponding to $p_{111...}$ above (solid blue line). It is important to keep in mind that the introduced method increases the success probability for a single measurement (cf. Figure 2.2). Yet the overall probability of obtaining the proper sequence is still low, even though the probability of obtaining other particular sequences is lower. This means that a high number of measurements may be necessary in order to prepare a well-defined bath spin state.

2.2.3 Derivation of the effective Quantum Dynamics on the bath

Let us now move on to investigate theoretically how these results from simulations can be understood and generalized. In brief, spectral decomposition of the Hamiltonian shows that the result of measuring a superposition state yields a well-defined non-unitary operation on the bath. In more detail, the Hamiltonian in (2.13) can be rewritten using spectral decomposition as

$$\begin{aligned}
 H &= \begin{pmatrix} 1 & 0 & 0 \\ 0 & 0 & 0 \\ 0 & 0 & -1 \end{pmatrix} \otimes \sum_k \vec{g}_k \cdot \vec{I}_k + \omega \sum_k \mathbb{1} \otimes I_z^{(k)} \\
 &= \begin{pmatrix} \sum_k \vec{g}_k \cdot \vec{I}_k + \omega \sum_k I_z^{(k)} & 0 & 0 \\ 0 & \omega \sum_k I_z^{(k)} & 0 \\ 0 & 0 & -(\sum_k \vec{g}_k \cdot \vec{I}_k) + \omega \sum_k I_z^{(k)} \end{pmatrix} \quad (2.14) \\
 &\equiv |1\rangle\langle 1| H_+ + |0\rangle\langle 0| H_0 + |-1\rangle\langle -1| H_-
 \end{aligned}$$

in block diagonal form such that the Hamiltonian is split into one part H_+ containing the coupling term with a positive sign while the other part H_- includes this term with a negative sign. The part of the Hamiltonian corresponding to the electronic level $m_s = 0$, i.e. H_0 , does not contain coupling terms, but only the contribution of the external field. For the dynamics this means that

$$\begin{aligned}
 U &= e^{iHt} = |1\rangle\langle 1| e^{iH_+t} + |0\rangle\langle 0| e^{iH_0t} + |-1\rangle\langle -1| e^{iH_-t} \\
 &\equiv |1\rangle\langle 1| U_+ + |0\rangle\langle 0| U_0 + |-1\rangle\langle -1| U_- .
 \end{aligned} \quad (2.15)$$

Notice that the remaining unitaries U_+ , U_0 and U_- only act on the nuclear spin states. The central electron NV spin is just represented by its spin states $|+1\rangle$, $|0\rangle$ and $|-1\rangle$ within the equation (2.15). Therefore, the action on the nuclear spins can be controlled by projecting the central spin into

2 Quantum State Engineering

specific states. As an illustrative example, let us chose the central NV spin to be prepared in the state

$$|\Psi_{el}\rangle = \frac{|1\rangle + |-1\rangle}{\sqrt{2}} \quad (2.16)$$

while the state of all surrounding nuclear spins $|\Psi_{ns}\rangle$ is arbitrary (here assumed to be pure for clarity w.l.o.g.). So, the action of the time evolution of the Hamiltonian is

$$U |\Psi_{el}\rangle \otimes |\Psi_{ns}\rangle \stackrel{(2.15)}{=} \frac{1}{\sqrt{2}} (|1\rangle U_+ + |-1\rangle U_-) |\Psi_{ns}\rangle \quad (2.17)$$

where the overlaps of the states represented in U in (2.15) with $|\Psi_{el}\rangle$ define the effective operation on the nuclear spins. For example, the part corresponding to electron state $|0\rangle$ is left out. In the next step, the electron state shall be projected back into the same state $|\Psi_{el}\rangle$ after the time evolution with time t .

$$\begin{aligned} (|\Psi_{el}\rangle \langle \Psi_{el}| \otimes \mathbb{1}) U (|\Psi_{el}\rangle \otimes |\Psi_{ns}\rangle) &= |\Psi_{el}\rangle \frac{U_+ + U_-}{2} |\Psi_{ns}\rangle \\ &\equiv |\Psi_{el}\rangle \otimes V |\Psi_{ns}\rangle. \end{aligned} \quad (2.18)$$

We see that the combination of unitary time evolution and projection can be rewritten as an operator V acting on the nuclear spins. Remarkably, this operator is given as the sum of two unitaries. As explicitly demonstrated in the appendix, section A.1, and as confirmed by Nakazato et al. [48], this means that the operator acting on the nuclear spins is in general non-unitary. Physically, it is not surprising that a non-unitary operation appears when the effect of a measurement is included. This property has the consequence that the operation has the potential to be an entangling operation since a non-unitary operation can never be written as product of local unitaries.

The above example can also be generalized to any superposition state. We still restrict to the qubit subspace $|-1\rangle, |1\rangle$ and find that

$$|\Psi_{el}\rangle = \frac{\alpha |1\rangle + \beta |-1\rangle}{\sqrt{|\alpha|^2 + |\beta|^2}} \quad (2.19)$$

with general $\{\alpha, \beta\} \in \mathbb{C}$ yields the operation on the nuclear spins as

$$V = |\alpha|^2 U_+ + |\beta|^2 U_- \quad (2.20)$$

2.2 Purification by controlled non-unitary evolution

such that these superposition parameters also represent degrees of freedom that can be chosen in order to fulfil requirements concerning the target state and the available time of evolution. In other words, two important resources in Quantum Information Processing are related by this method, namely superposition and entanglement. When choosing the parameters appropriately, the superposition of the initial central spin state is converted into entanglement of the surrounding spins by the use of time evolution and successful projective measurements.

2.2.4 Optimization of External Parameters for Specific Target States

Within the presented purification mechanism, there are a number of different parameters which influence the particular state obtained as a result of the purification. If the parameters are not inherently fixed, as the coupling parameters in a solid state scenario, they can thus be used to obtain different target states. In particular, these parameters are:

- The coupling parameters \vec{g}_k
- The strength of the external field ω
- The time(s) between different measurements τ
- The superposition weights α and β , as in equation (2.19)
- The number of involved spins N (and their dimensionality).

Tuning these parameters leads to very different results in terms of achieved purity, entanglement and success probability. Figure 2.4 shows contour plots obtained when varying the time τ and the external field strength ω numerically, as an example. In an experiment, the choice of parameters can obviously be optimized by simple trial and error. One more intelligent way is to previously simulate the full quantum mechanical system. This is often a computationally hard problem though, growing exponentially with the number of spins involved. However, there is a better numerical method in order to choose the parameters in an ideal way. As observed in 2.1, the

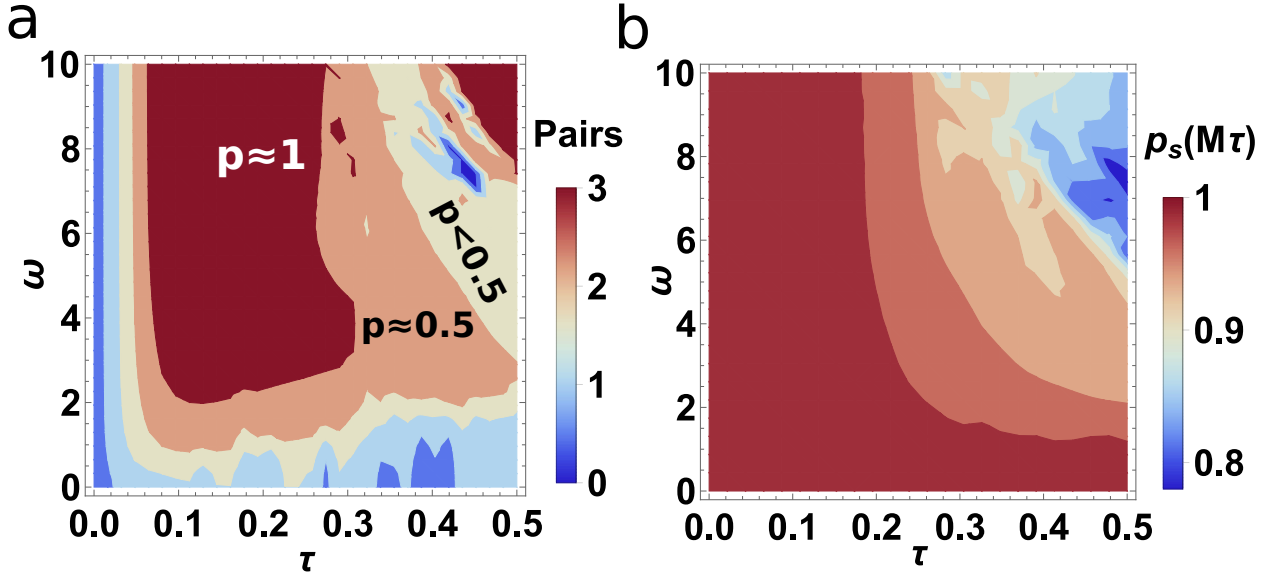


Figure 2.4: Effects of different choices of the external field (ω) and the free evolution time (τ). In (a), the focus is on the number of created entangled pairs. A darker (red) colour signifies more pairs, while a lighter (blue) colour means less entangled pairs. Moreover, the inset text shows the purity of the nuclear spin state. The scale is in units of the (inverse) effective coupling $g = \sqrt{1/N \sum_k |\vec{g}_k|^2}$. (b) shows the probability of obtaining the selected state in the M -th repetition of the sequence. Here, red is the optimal probability 1, while at the other end of the scale, blue signifies a probability value of 0.8. The coupling scenario considered is the 1D spin chain as in Figure 2.2. [46]

purified spins will evolve towards an eigenstate of the non-unitary operator V that describes the combined effect of projection and time evolution of the system, as in equation (2.18). In particular, in the limit of a large number of repetitions M , the bath spins will assume the eigenstate corresponding to the maximal eigenvalue of V .

We observed this theoretically in (2.6) but re-illustrate it with our concrete example when analysing the effect of many repetitions in the eigenbasis of V as

$$\rho_{res} = \frac{V^M \rho V^{\dagger M}}{N_{norm}^M} = \frac{(BDB^\dagger)^M \rho (B^\dagger DB)^M}{N_{norm}^M}, \quad (2.21)$$

2.3 Specific Target States and their Applications

where B is an operator consisting of the eigenstates of V , thus transforming V into a diagonal operator D . N_{norm} is the normalization constant necessary in each step due to the non-unitary nature of V . Since the eigenvalues $\{d_i\}$ fulfil the condition $0 \leq d_i \leq 1$ it becomes obvious that

$$V^M = \frac{BD^M B^\dagger}{N_{norm}^M} = B \begin{pmatrix} d_1 & 0 & \dots & 0 \\ 0 & d_2 & \ddots & \vdots \\ \vdots & \ddots & \ddots & 0 \\ 0 & \dots & 0 & d_N \end{pmatrix}^M B^\dagger / N_{norm}^M \quad (2.22)$$

$$\xrightarrow[\substack{M \rightarrow \infty \\ (d_1 > d_2 > \dots > d_N)}]{} B \begin{pmatrix} 1 & 0 & \dots & 0 \\ 0 & 0 & \ddots & \vdots \\ \vdots & \ddots & \ddots & 0 \\ 0 & \dots & 0 & 0 \end{pmatrix} B^\dagger = |d_1\rangle\langle d_1|$$

since the smaller eigenvalues vanish much quicker with $d_2^M \rightarrow 0 \dots d_N^M \rightarrow 0$ while d_1 dominates, such that V^M becomes a projection operator into the eigenstate $|d_1\rangle$ corresponding to the largest eigenvalue d_1 . From this, it also obvious to see that the gap $(d_1 - d_2)$ between d_1 and the other eigenvalues is important. In particular, less repetitions M are necessary when the gap is sufficiently large. On the other hand, if the gap is too small, there are several conflicting target states which results in the fact that the resulting state ρ_{res} is not fully purified. We also observe in numerical simulations that a larger gap leads to faster convergence of the system towards a pure target state.

2.3 Specific Target States and their Applications

Having established the mechanism of reaching a well defined pure state in a realistic scenario, we now turn our attention towards the question which particular states can be reached and what applications they may serve. While in general, the possibilities of reaching arbitrary target states is given, we focus here on pairwise entangled singlet states. These states are especially interesting due to the negligible interactivity of spins in this state with other spin entities. As their net angular

2 Quantum State Engineering

momentum is vanished and as the involved spins are ideally fully entangled, these states serve to decrease interactions to coupled spins as well as the environment [49]. Moreover, singlet states also serve applications in Quantum Simulations, such as excitations in spin models with exact dimer ground states [50]. However, the described methods are, in general, also suitable to create other states very useful for Quantum Technology, such as Spin Squeezed states and Multipartite Entangled States.

2.3.1 Pairwise Entangled Singlet States

In our publication [46] we focus especially on pairwise entangled singlet states of the form

$$|S\rangle = \frac{1}{\sqrt{2}} (|\uparrow\downarrow\rangle - |\downarrow\uparrow\rangle). \quad (2.23)$$

In particular, we demonstrate that in the case of the considered central spin system with inhomogeneous couplings and a high (even) number of spins, a repeated projective measurement of the central spin can remarkably result in a state in which all of the spins are paired up in identical singlet states as

$$|\Psi\rangle_{res} = \bigotimes_{i=1}^{N-1} |S_{i,i+1}\rangle. \quad (2.24)$$

Note that such a pairing can not occur if all spins are coupled with equal coupling strength to the central spin. It is indeed the dynamics of the interplay of the inhomogeneous couplings with the externally applied field that paradoxically leads to such a homogeneously distributed entangled state. However, it has to be stressed again, that this result is heavily dependent on the involved coupling parameters and the choice of external parameters, such that the number of spins pairing up in singlets is subject to change as well as the purity of the involved states (see Figure 2.4 above). However, we can find scenarios in the numerical simulation, in which the involved spins do pair up into singlets. We demonstrate this singlet formation by extracting the sub-matrix $\rho_{(i,i+1)}$ from the density matrix resulting from the measurement scheme at a given number of measurements according to equation (2.21) by partial tracing.

Note that the Fidelity is defined differently than the direct overlap of density matrices $\text{Tr}(\rho_1, \rho_2)$

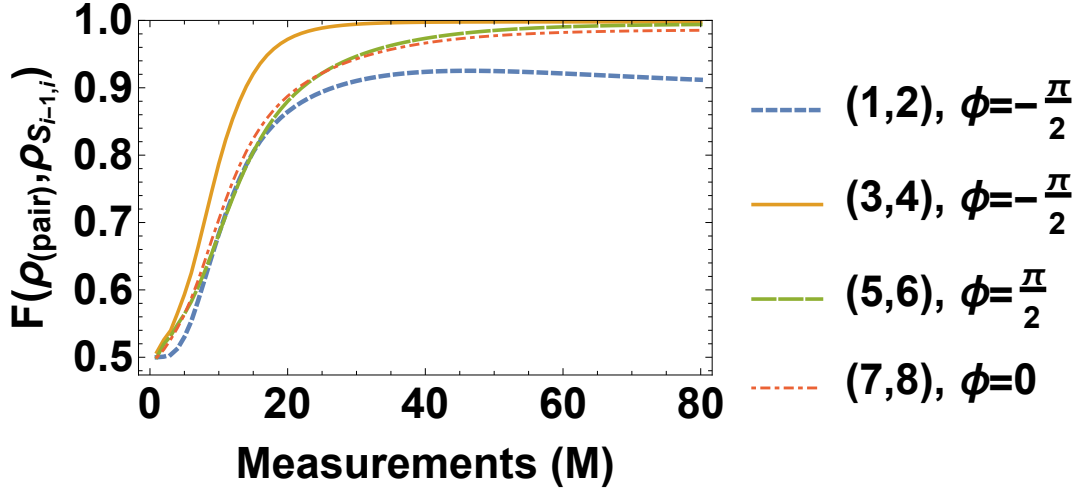


Figure 2.5: In an exemplary two-dimensional configuration of spins distributed on a plane, four different Singlet pairs are forming within a set-up of eight spins. With increasing number of measurements, the Fidelity, as defined in (1.6), is increasing towards unity, except for one pair, namely the pair indexed as (1, 2), blue dashed line, for which the Fidelity saturates. The plot legend includes the spin indices of the respective entangled pair of qubits, as well as the angle Φ within a family of Singlet states defined by $|\tilde{S}\rangle = \frac{1}{\sqrt{2}}(|\uparrow\downarrow\rangle - e^{i\Phi}|\downarrow\uparrow\rangle)$.

used in our publication [46]. The qualitative result is the same which confirms the findings of the publication while the Fidelity – as defined in equation (1.6) – is a better measure for possibly occurring mixed states.

2.3.2 Advantages for Quantum Sensing

As the central electron spin acts as a sensing spin, the state of the surrounding spins is of relevance for the sensing performance. In the case of the NV center, the dipole-dipole coupling to the surrounding nuclear spins introduces chaotic phases to the electron spin, if these are in a fully

2 Quantum State Engineering

mixed state. Intuitively, a well-defined nuclear spin state is thus beneficial. Moreover, due to the Monogamy of Entanglement [51], any spin can only be fully pairwise entangled with exactly one other spin. According to the well-established decoherence model by Zurek [52], decoherence basically means entanglement to an entity outside the desired quantum system. Here, decoherence on the central spin could be introduced by undesired entanglement to the nuclear spins. Therefore, pairwise entanglement of the nuclear spins contributes to protecting the information gathered by the central spin.

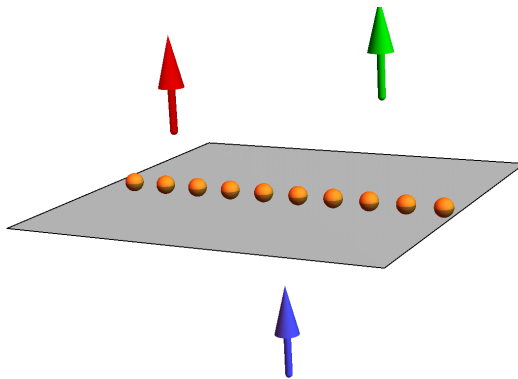


Figure 2.6: Three-dimensional scenario for a simple demonstration of benefits to Quantum Sensing by Quantum State Engineering. The sensor spin (blue) is surrounded by ancillary nuclear spins (orange spheres). Since these are coupled to the central spin, the nuclear spins may prohibit the detection of external spins (red, green arrows) or aid in detection, depending on their engineered quantum states. [46]

In the following, it is demonstrated how subjecting the spins surrounding the sensor spin to pairwise entangled singlet states aids in detecting external spins which may otherwise be unresolvable. We introduce three different external spin species with Larmor frequencies

$$\omega_0 = \omega, \quad \omega_1 = \omega + \frac{\omega}{10}, \quad \omega_2 = \omega - \frac{\omega}{10}. \quad (2.25)$$

2.3 Specific Target States and their Applications

In the Hamiltonian governing the system dynamics, (2.13), a linear spin chain containing a significant number ($N = 10$) of nuclear spins is assumed. The first two of these spins are precessing with Larmor frequency ω and are subjected to different states, namely paired as singlets, a pure but separable state and a completely mixed state. Two additional spins are situated above the linear chain and are subjected to Larmor frequencies ω_1 and ω_2 as defined above.

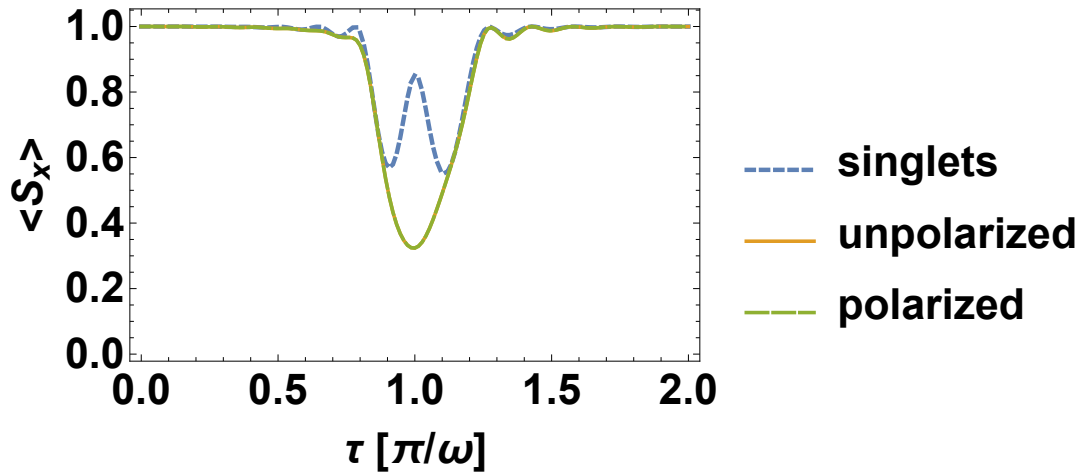


Figure 2.7: Larmor frequencies of three external spins in the setting of Figure 2.6 sensed by a central electron spin. Two of the Larmor frequencies, which are slightly shifted from the dominating frequency ω are only visible as beatings in the case when the surrounding nuclear spins are paired in singlet states (blue dashed line). On the contrary, these frequencies can not be observed when the external spins are shielded by the nuclear spins, which can entangle with the central electron spin. This is the case when the nuclear spins are not prepared in a pairwise entangled singlet state, but in a separable pure state (polarized, green solid line) or in a completely mixed state (unpolarized, solid orange line), respectively. The time scale of the free evolution time τ is given in inverse units of the dominating Larmor frequency ω . The dimensionless expectation value on the ordinate is the x -coordinate of the electron spin 1. [46]

Clearly, the benefit on engineering the most suitable quantum state in the environment for the task

at hand is visible. Being paired up as singlets, the nuclear spins can not pairwise entangle to the central electron spin. Moreover, their net angular momentum is zero such that the dipolar interaction is intuitively minimized in this state. We have thus shown that the obtained pairwise entangled states of environmental spins are beneficial for sensing external spin entities.

2.4 Results for Different Geometries of Surrounding Spins

Having looked at one-dimensional spin chains and spins distributed in a two-dimensional plane [46], we now turn to the more realistic scenario of a three-dimensional geometry of the nuclear spins surrounding an NV center. In order to further analyse the amount of Pairwise Entanglement in the resulting density matrices, let us introduce the concept of Concurrence [53].

Concurrence The basic idea of this Entanglement Measure defined by Wootters in 1997 is to compare a density matrix to its spin-flipped counterpart $\tilde{\rho}$ as [53]

$$\tilde{\rho} = (\sigma_y \otimes \sigma_y) \rho^* (\sigma_y \otimes \sigma_y). \quad (2.26)$$

Here, the asterisk (*) denotes a simple complex conjugate. The comparison is then carried out by looking at the Hermitian matrix R as by the equation

$$R = \sqrt{\sqrt{\rho} \cdot \tilde{\rho} \cdot \sqrt{\rho}}. \quad (2.27)$$

Note that the computation of the overlap is very similar to the Fidelity defined in equation (1.6). In the case of the Concurrence, however, computation of this matrix overlap is not followed by a Trace, but by an analysis of Eigenvalues. The Eigenvalues of R are equivalent to the Square Root of the Eigenvalues of the non-Hermitian overlap matrix $O = (\rho \cdot \tilde{\rho})$ [53], which is also the matrix used for the usual Trace overlap $\Omega = \text{Tr}(\rho \cdot \tilde{\rho})$. For the computation of Concurrence, the Eigenvalues of R are then sorted in decreasing order $\lambda_{R,1} \geq \lambda_{R,2} \geq \lambda_{R,3} \geq \lambda_{R,4}$. The dimension

2.4 Results for Different Geometries of Surrounding Spins

is fixed to four as we only introduce Concurrence as a measure of pairwise entanglement. The Concurrence is finally computed as

$$C(\rho) = \max(0, \lambda_{R,1} - \lambda_{R,2} - \lambda_{R,3} - \lambda_{R,4}). \quad (2.28)$$

2.4.1 Three-dimensional Geometries of Surrounding Spins

Note that the observation of pairwise singlet states or other entangled or correlated states depends heavily on the involved couplings and thus on the geometry of the coupled spins, and the tuning of all other free parameters. In an experimental setting with spins at fixed lattice sites, the observation of such states is therefore a very non-trivial task, besides the probabilistic nature of the measurement sequences in question. In a simulation however, the positions of the spins can be easily fixed and adapted to situations in which e.g. pairwise entanglement is favoured. Such a successfully engineered system is presented in the following with $N = 6$ spins occupying corners of a cuboid as in Figure 2.8. Both Purification and Pairwise Entanglement are observed in this scenario, when a sufficiently high number of repetitions of the measurement sequence is carried out. The results of the simulation are displayed and discussed in Figures 2.9 and 2.10.

2 Quantum State Engineering

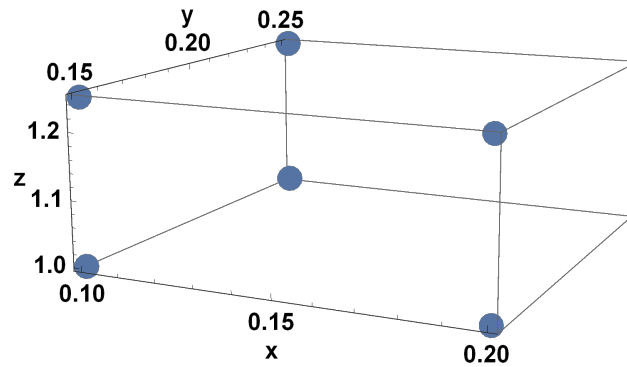


Figure 2.8: Three-dimensional configuration of nuclear spins (blue dots) used for the Purification simulation below. The central spin is situated at the origin while the nuclear spins are elevated in the z -direction and distributed in x and y in a pairwise grouping to increase the likelihood for singlet formation. The units are arbitrary but influence the coupling strength by the dipolar coupling $\vec{d} = \frac{\vec{r}/|\vec{r}|}{|\vec{r}|^3}$.

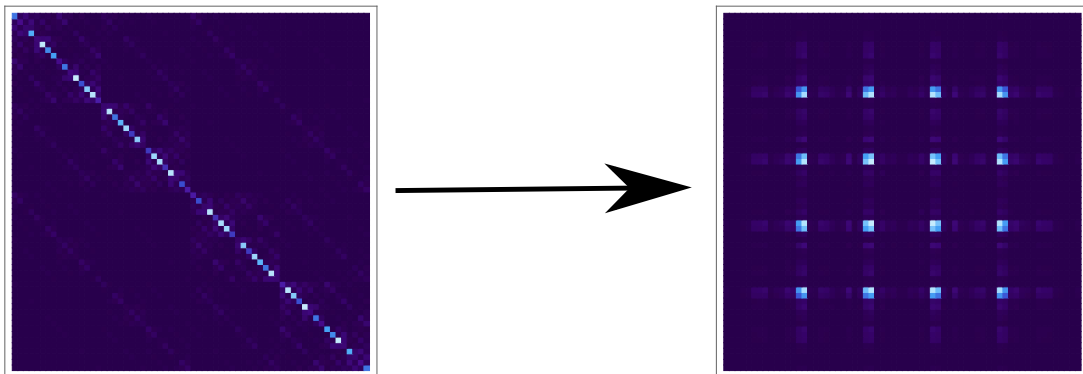


Figure 2.9: Plot of the populations of the involved 64×64 density matrices from simulation of the $N = 6$ nuclear spins after one repetition (left image) and after 300 repetitions (right image) of the measurement sequence in Figure 2.2. Dark areas signify entries with an absolute value close to 0, while bright areas show entries with maximal absolute values. Notably, the system develops from a nearly completely mixed state with almost only diagonal entries to a well-structured density matrix with clearly visible off-diagonal entries, stemming from correlated states.

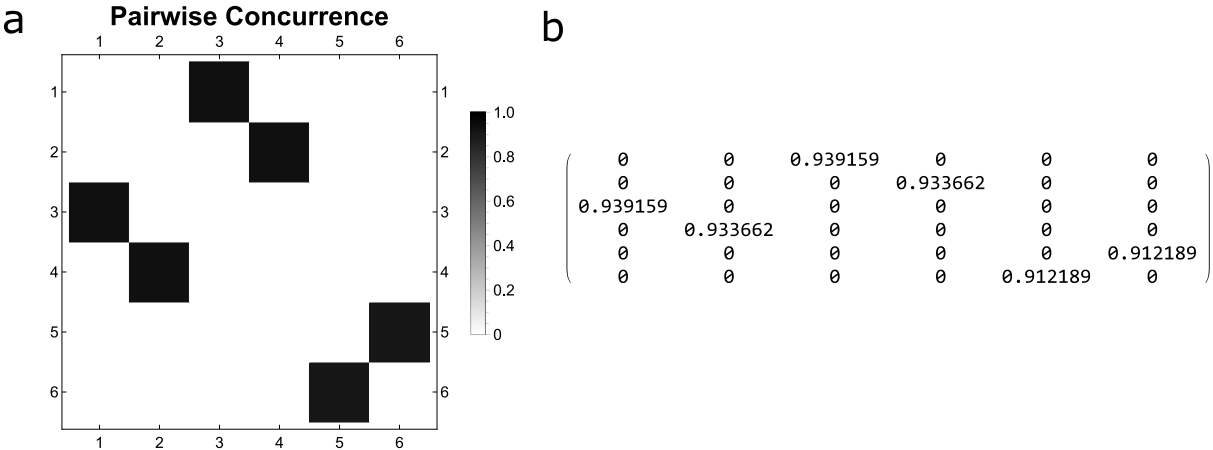


Figure 2.10: Pairwise Entanglement of the spins involved in a three-dimensional Purification setting. The Concurrence plot (a,left) is a visualisation of the occurring pairwise Concurrences, as defined in equation (2.28). The explicit values of the involved Concurrences are also given for comparison (b,right). The indices of the matrix, or the labels of the Concurrence plot are simply indices of the involved spins.

2.5 Methods for Correlation of a large Number of Bath

Spins

Remarkably, there is no upper limit per se on how many spins can be polarized and purified by the presented central spin projective measurements. We thus performed simulations with high numbers of nuclear spins, up to $N = 20$, on a multi-core IBM Server System. As the dimensions of the involved density matrices and unitary operations scale as $\dim(\rho) = 2^N \cdot 2^N$ with complex entries, so $2^N \cdot 2^N \cdot 2 = 2^{2N+1}$ real variables in total (e.g. $2^{41} = 2\,199\,023\,255\,552 \approx 2,2 \cdot 10^{12}$ real variables for the case $N = 20$), the involved matrix multiplications are very extensive, especially in terms of RAM, but also CPU-expensive. Methods were thus developed, specifically tailored to the involved operations, to enable Parallel Computing of the Algorithms in question.

2.5.1 Specific Separable One-Qubit Operations and their Permutations introduced by Power Expansion

The non-unitary operation V acting on the nuclear spins (Index I) as defined before, e.g. in (2.20), is now fixed to

$$V(\tau) = \frac{1}{2} (U_I^+ + U_I^-). \quad (2.29)$$

Remember that the sum of two unitaries is in general non-unitary as demonstrated in the appendix, section A.1 and confirmed by Nakazato et al. [48]. Two observations now help to simplify the dynamics. Firstly, the summed Unitaries acting on the nuclear spins can be rewritten as separable tensor products [46].

$$V^n = \frac{1}{2^n} (U^+ + U^-)^n = \frac{1}{2^n} \left(\bigotimes_i U_i^+ + \bigotimes_j U_j^- \right)^n. \quad (2.30)$$

Secondly, a successive application V^n , where n is the total number of repetitions of the sequence, can be rewritten in terms of Permutations. Here, V^n acts on an already pure, but separable input

2.5 Methods for Correlation of a large Number of Bath Spins

state $|\Psi_0\rangle$, for further simplicity of the involved calculations. The focus is thus shifted here from the mere Purification of the system to the question whether the repeated projection of the central spin leads to entanglement among the attached nuclear spins [46].

$$V^n |\Psi_0\rangle = \frac{1}{2^n} \sum_{n\text{Perm}_2} \bigotimes_k n\text{Perm}_2(U_k^+, U_k^-) |\Psi_{0,k}\rangle. \quad (2.31)$$

To better understand this somewhat involved equation, let us first define the terms, before we look at one illustrative example. The sum is taken over permutations. $n\text{Perm}_2(U_k^+, U_k^-)$ is a multiset-permutation of the simple set of the two operators $O = \{U_k^+, U_k^-\}$. [54] A multiset is, by definition [55], a modified set which allows for an element of the set to occur multiple times, e.g. the multiset $\tilde{S} = \{a, b, b, a\}$ has two elements which both have multiplicity 2. Whereas, in a regular set, only multiplicity 1 is allowed, such that the multiset \tilde{S} would have to be redefined as $S = \{a, b\}$, to obtain a regular set S . Here, the set of operators $O = \{U_k^+, U_k^-\}$ is thus elevated to a multiset

$$\tilde{O}_{k,n,m_+,m_-} = \underbrace{\{U_k^+, U_k^-, U_k^-, \dots, U_k^+, U_k^+, U_k^-\}}_{n \text{ entries}}, \quad (2.32)$$

where n is both the power applied to the operation V , but also the Cardinality of the multiset, which is the sum of the individual multiplicities m_+ (number of $\{U_k^+\}$ entries) and m_- , i.e.

$$|\tilde{O}_{k,n,m_+,m_-}| = n = m_+ + m_- \quad (2.33)$$

Successively, it is inherently understood in (2.31) that the multiset \tilde{O}_{k,n,m_+,m_-} originates from the different terms introduced by the matrix power V^n . Thus, each individual multiset is subsequently subjected to matrix multiplication, such that it defines a unitary operation $O_{k,n,m}$ by

$$\tilde{O}_{k,n,m_+,m_-} = \{U_k^+, U_k^-, U_k^-, \dots, U_k^+, U_k^+, U_k^-\} \rightarrow O_{k,n,m} = U_k^+ \cdot U_k^- \cdot U_k^-, \dots, U_k^+ \cdot U_k^+ \cdot U_k^-, \quad (2.34)$$

where m is a running index of the different multiset permutations occurring when the matrix power n is applied to the operator V .

We have thus introduced a formalism for a better description of the involved matrix powers, with the goal to simplify the involved calculations. Before we see how this is indeed related to counting

2 Quantum State Engineering

in binary numbers and thus very native to the way a classical computer ‘thinks’, let us first look at a simple example for the case of $N = 2$ nuclear spins and $n = 3$ repetitions.

$$\begin{aligned}
 V^3 |\Psi_0\rangle &= \frac{1}{2^3} \left(\bigotimes_{i=1}^{N=2} U_i^+ + \bigotimes_{j=1}^{N=2} U_j^- \right)^3 |\Psi_0\rangle = \\
 &U_1^- U_1^- U_1^- |\Psi_{0,1}\rangle \otimes U_2^- U_2^- U_2^- |\Psi_{0,2}\rangle + U_1^- U_1^- U_1^+ |\Psi_{0,1}\rangle \otimes U_2^- U_2^- U_2^+ |\Psi_{0,2}\rangle + \\
 &U_1^- U_1^+ U_1^- |\Psi_{0,1}\rangle \otimes U_2^- U_2^+ U_2^- |\Psi_{0,2}\rangle + U_1^- U_1^+ U_1^+ |\Psi_{0,1}\rangle \otimes U_2^- U_2^+ U_2^+ |\Psi_{0,2}\rangle + \\
 &U_1^+ U_1^- U_1^- |\Psi_{0,1}\rangle \otimes U_2^+ U_2^- U_2^- |\Psi_{0,2}\rangle + U_1^+ U_1^- U_1^+ |\Psi_{0,1}\rangle \otimes U_2^+ U_2^- U_2^+ |\Psi_{0,2}\rangle + \\
 &U_1^+ U_1^+ U_1^- |\Psi_{0,1}\rangle \otimes U_2^+ U_2^+ U_2^- |\Psi_{0,2}\rangle + U_1^+ U_1^+ U_1^+ |\Psi_{0,1}\rangle \otimes U_2^+ U_2^+ U_2^+ |\Psi_{0,2}\rangle
 \end{aligned} \tag{2.35}$$

This example illustrates the terms generated by $nPerm_2(U_k^+, U_k^-)$, indeed by $3Perm_2(U_k^+, U_k^-)$ ($n = 3$), in this case. These permutations are simply all possible permutations of three matrices consistent of U^+ and U^- for each involved qubit. Note that the permutations are the same for both qubits simultaneously in this case. In fact, since the entries are summed over, the position of each term is irrelevant, such that the order of the permutations can also be varied for each qubit separately, in principle.

2.5.2 Relation of the Involved Permutations to Binary Numbers

Note that the expression above in (2.35) has indeed been explicitly constructed by the use of binary numbers. Incidentally, the involved multiset permutations of a set of cardinality 2 are equal to counting in binary numbers. Unsurprisingly, binary numbers are just a multiset of the set $\{0, 1\}$. Thus, compare the expression above with the following expression

2.5 Methods for Correlation of a large Number of Bath Spins

$$\begin{aligned}
& 000 |\Psi_{0,1}\rangle \otimes 000 |\Psi_{0,2}\rangle + 001 |\Psi_{0,1}\rangle \otimes 001 |\Psi_{0,2}\rangle + \\
& 010 |\Psi_{0,1}\rangle \otimes 010 |\Psi_{0,2}\rangle + 011 |\Psi_{0,1}\rangle \otimes 011 |\Psi_{0,2}\rangle + \\
& 100 |\Psi_{0,1}\rangle \otimes 100 |\Psi_{0,2}\rangle + 101 |\Psi_{0,1}\rangle \otimes 101 |\Psi_{0,2}\rangle + \\
& 110 |\Psi_{0,1}\rangle \otimes 110 |\Psi_{0,2}\rangle + 111 |\Psi_{0,1}\rangle \otimes 111 |\Psi_{0,2}\rangle
\end{aligned} \tag{2.36}$$

Here, the complicated permutations are instead substituted by successive binary numbers from 000 to $(111)_2 = 8$. Note that it is enough to replace each 0 with the respective U^- and each 1 with the U^+ operations to reconstruct equation (2.35) above. This is generalizable to arbitrary numbers of spins and repetitions of the sequence. Conclusively, for this specific problem we have reduced the challenging task of a matrix power – and thus a diagonalization – of a $2^N \cdot 2^N$ complex matrix to a simple and easily parallelizable sum with binary indices and single-qubit operations.

2.5.3 Partial Trace of a Large Pure State

As the involved density matrices grow exponentially in size, a simple observation helps to still enable the calculation of a partial trace. While there may usually not be enough RAM space available for even containing a large enough density matrix, operations can still be applied to pure states in order to obtain the desired result. Starting from the usual definition of a partial trace [41]

$$\rho_B = \text{Tr}_A(\rho_{AB}) = \sum_i (\langle i|_A \otimes \mathbb{1}_B) \rho_{AB} (|i\rangle_A \otimes \mathbb{1}_B), \tag{2.37}$$

observe, that for a pure state $\rho_{AB} = |\psi\rangle_{AB}\langle\psi|_{AB} = |\psi\rangle_A \otimes |\psi\rangle_B \langle\psi|_A \otimes \langle\psi|_B$, such that the above equation can be rewritten

$$\text{Tr}_A(\rho_{AB}) = \sum_i \underbrace{(\langle i|\psi\rangle_A |\psi\rangle_B)}_{|\varphi\rangle_{B,i}} \underbrace{(\langle\psi|i\rangle_A \langle\psi|_B)}_{\langle\varphi|_{B,i}}, \tag{2.38}$$

which means that it is enough to calculate $|\varphi\rangle_{B,i} = \langle i|\psi\rangle_A |\psi\rangle_B = (\langle i|_A \otimes \mathbb{1}_B) |\psi\rangle_{AB}$ in each summation step, followed by complex conjugation and transposition to obtain $\langle\varphi|_{B,i}$. This enables the calculation of a partial trace from a pure state of high dimensionality, since it drastically lowers the RAM

requirements compared to calculations involving the full density matrices, and produces an easily parallelizable sum.

2.5.4 Results: Simulating Pairwise Entanglement among up to Twenty Spins

Using the methods described above, it is possible to scale up the simulation of correlating external spins by the repetitive projective measurement of a central spin to $N = 20$ external spins. A one-dimensional geometry is used in numerical simulations, in the sense that the central spin is assumed to be below the first spin of a linear chain of external spins. The resulting couplings can be specified as

$$\vec{J}_k = J \cdot \begin{pmatrix} d_k \\ 0 \\ 1 \end{pmatrix} / \left| \begin{pmatrix} d_k \\ 0 \\ 1 \end{pmatrix} \right|^4 \quad (2.39)$$

where J is a weight of the couplings and d_k is the distance in the linear chain spread out along the x-axis, varied for each spin. For the simulations of a large number of spins, an equidistant spacing was used. The exact involved parameters and the code for the twenty-spin simulation is given in the Appendix in A.2.1.

As expected, it was observed that with an increasing number of external spins, it gets increasingly harder to correlate the spins. See Figure 2.11. This observation has two main reasons. Firstly, with an increasing linear spin chain, each added spin is further away from the central spin and thus has lower coupling strength, scaling as $1/|\vec{r}_k|^3$, where \vec{r}_k is the position vector of the k -th external spin. Secondly, the Purification effect also gets decreased. Indeed, the ratio between the one central spin and the number of external spins is obviously diminishing. However, intuitively, the amount of information that spreads from the central spin remains the same. As an effect, a larger number of repetitions and a stronger external field is necessary when the number of involved spins

2.5 Methods for Correlation of a large Number of Bath Spins

increases, in order to still observe pairwise correlations between the involved spins. However, a larger number of repetitions results in significant increases of the duration of the parallel computation. For example, simulating twenty spins on two coupled IBM Server Systems x3850 X5 4x 8C Xeon X7560 2,26GHz 128GB (in total 64 cores, 256GB RAM), took 7h 55min for 22 repetitions of the measurement sequence, whereas simulating 23 repetitions used up a whole 13h 45min of calculation time on the IBM Server System.

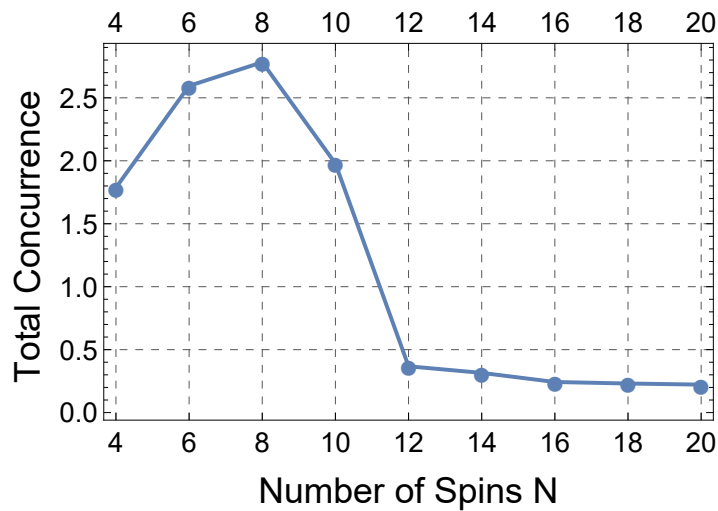


Figure 2.11: Development of the sum of all pairwise Concurrences, using the introduced repeated central spin projection, when scaling up the number of involved external spins (Qubits) from four to twenty. Note that the involved parameters were kept as constant as possible for comparison ($\tau = 0.3025, J = 20$), however at least one parameter (here ω) had to be optimized manually to fit the respective problem sizes (c.f. Table 2.1). It is clearly observable that the overall Concurrence drops rapidly from a problem size of ten spins and stabilizes afterwards. Notably, pairwise entanglement is still observable, even for $N = 20$ spins.

2.5.5 Twenty Spin (Qubits) Case

Let us elaborate a bit further on the results from the twenty spin simulation. Firstly, we list the parameters involved in Table 2.1 to stress that the parameters are comparable, but slightly adapted for each problem size. Secondly, in the figures below, excerpts from the involved $2^{20} \cdot 2^{20} \approx 10^6 \cdot 10^6$ matrices are plotted below. Note that loading the full matrix into RAM is already a huge challenge, due to roughly $2,2 \cdot 10^{12}$ real parameters. Thus, the Partial Trace methods outlined in 2.5.3 are applied and the analysis is focused on the first ten and the last ten involved spins, respectively.

| Number of Spins | External field strength ω | Waiting time τ | Coupling Weight J | Repetitions n |
|-----------------|----------------------------------|---------------------|---------------------|-----------------|
| 4 | 17 | 0.3025 | 20 | 23 |
| 6 | 16 | 0.3025 | 20 | 23 |
| 8 | 17 | 0.3025 | 20 | 23 |
| 10 | 19 | 0.3025 | 20 | 23 |
| 12 | 22 | 0.3025 | 20 | 23 |
| 14 | 22 | 0.3025 | 20 | 23 |
| 16 | 23 | 0.3025 | 20 | 23 |
| 18 | 23 | 0.3025 | 20 | 23 |
| 20 | 23 | 0.3025 | 20 | 23 |

Table 2.1: Numerical parameters used in simulations of large spin numbers, using the introduced repeated central spin projection. Note that, in order to obtain a qualitative result, the units are arbitrary, in terms of the (inverse) coupling, with the coupling specified in (2.39). It was aimed to keep all parameters constant for comparison, however at least the external field strength ω had to be adapted for higher spin numbers.

Using the parameters in the table above, we further analyse the reduced density matrices and the Correlations within the final state output from the simulation of the entire Hilbert space in the following Figures.

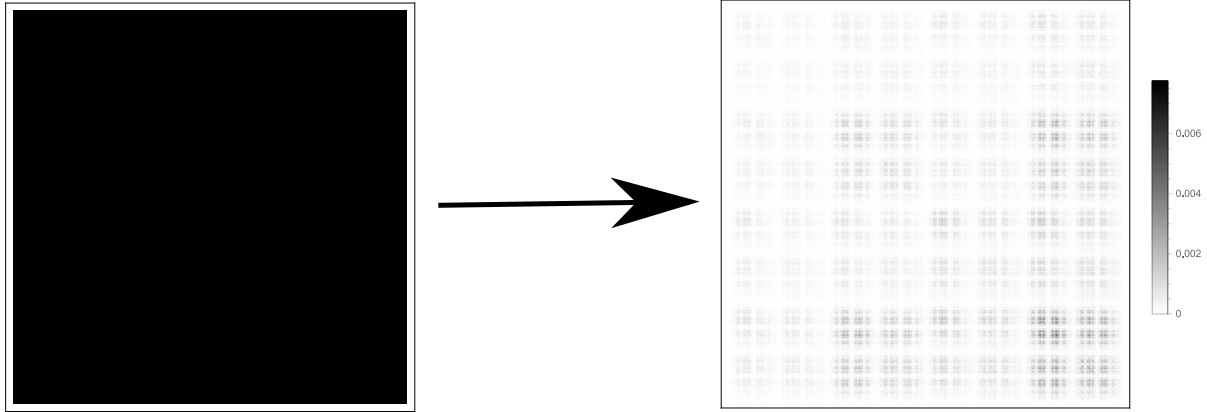


Figure 2.12: Simulated evolution of the density matrices of the first ten out of twenty spins, correlated by repetitive measurement of a central spin. The simulation starts with a pure initial state (left), where each of the spins is in a superposition state $1/\sqrt{2}(|0\rangle + |1\rangle)$. The focus of the simulation is thus on Correlation, not on Purification. Each entry of the initial density matrix, reduced to ten spins, is therefore exactly $1/2^{10}$, such that a colour-scaled plot of the density matrix is completely monochrome. Note that after several repetitions of the measurement sequence, the final $2^{10} \cdot 2^{10}$ density matrix (right) shows a distinct pattern of block-diagonal matrices with different individual weights (darker colours signify higher absolute values), indicating that correlations between different spins have occurred. Indeed, spins number four and five as well six and seven are showing non-zero Concurrence in this case. Simulation parameters include: Coupling weight $J = 20$, external field strength $\omega = 23$, waiting time $\tau = 0.3025$, in (inverse) units of the coupling J . Number of repetitions $n = 23$. These parameters were manually optimized to yield maximal Concurrence.

2 Quantum State Engineering

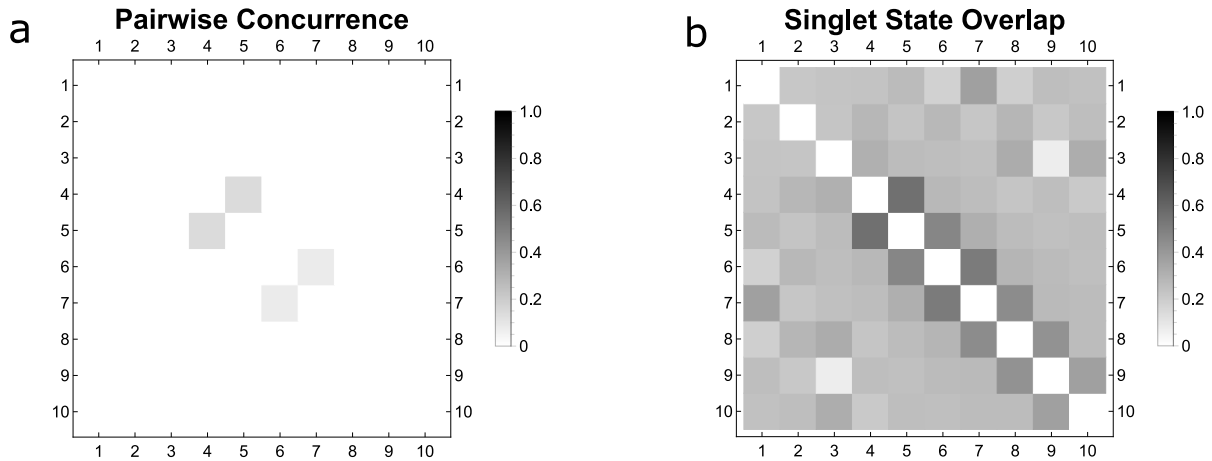


Figure 2.13: Pairwise Concurrences (a, left image) and Overlap with Singlet State $|S\rangle = \frac{1}{\sqrt{2}}|0, 1, -1, 0\rangle$ (b, right image) among the first ten out of twenty spins, correlated by repetitive measurement of a central spin. The labels indicate numbers of the involved spins. Darker colours signify higher values of Concurrence or Overlap, respectively. The overlap is calculated as $\text{Tr}(|S\rangle\langle S| \rho_{\text{reduced}})$. Note that the Concurrence as a measure for pairwise entanglement is only non-zero for two pairs (spins 4 and 5 as well as spins 6 and 7), while the Overlap, as a less ‘strict’ measure is non-zero for all pairs, but still shows the highest values for the entangled pairs.

2.5 Methods for Correlation of a large Number of Bath Spins

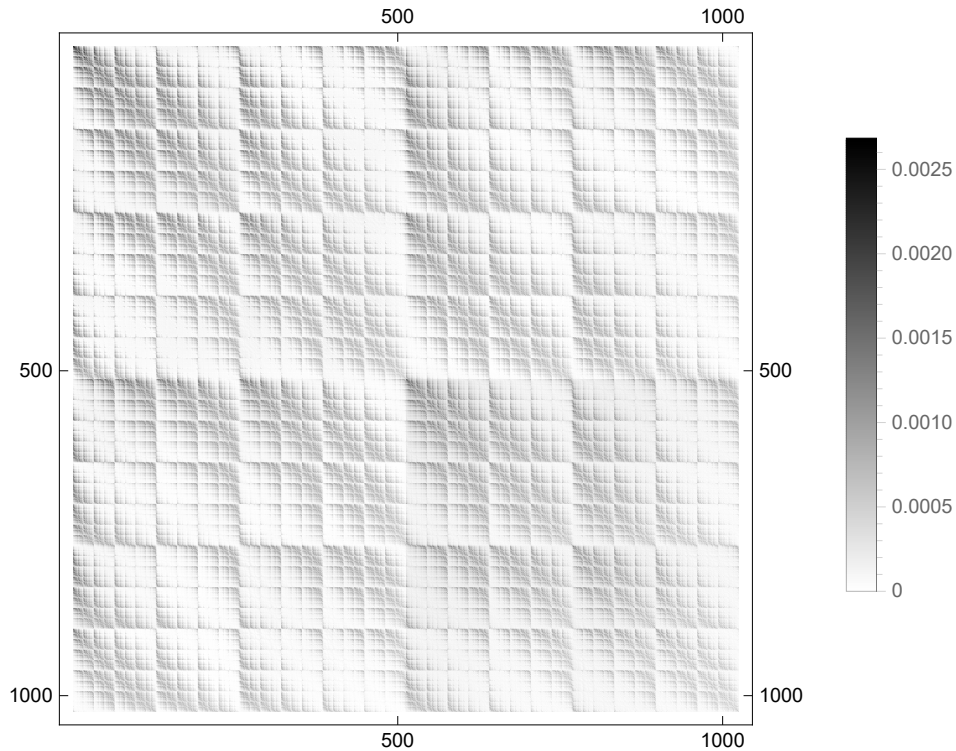


Figure 2.14: Plot of the absolute values of the final density matrix of the last ten out of twenty spins, correlated by repetitive measurement of a central spin. For completeness, we also show the density matrix plot of these remaining spins, completing the analysis in Figure 2.12 before. Note that the absolute values within the density matrix are significantly lower than those of the first ten spins. This signifies that, while starting from the same pure state, the dynamics have shifted spin population towards the spins which are most strongly coupled and affected by the central spin. While a clear repetitive pattern is observable in the structure of the density matrix, pairwise entanglement could not be observed for the final ten spins in this simulation. Note that the overall diagonal of the $1024 \cdot 1024$ matrix is quite pronounced, indicating only very weak correlations, visible as off-diagonal elements.

2.5.6 Eight Spin Case with Maximal Total Correlation

For comparison, the final state of the simulation involving eight spins is analysed in the following. While less spins are included, the build-up of entanglement is more readily observable, as the ratio between the actively projected central spin and the passive external nuclear spins is improved. Moreover the coupling of each individual spin to the central spin decreases with the spin number, as in equation (2.39). Results from the simulation in this case are displayed and discussed in the following Figures 2.15 and 2.16.

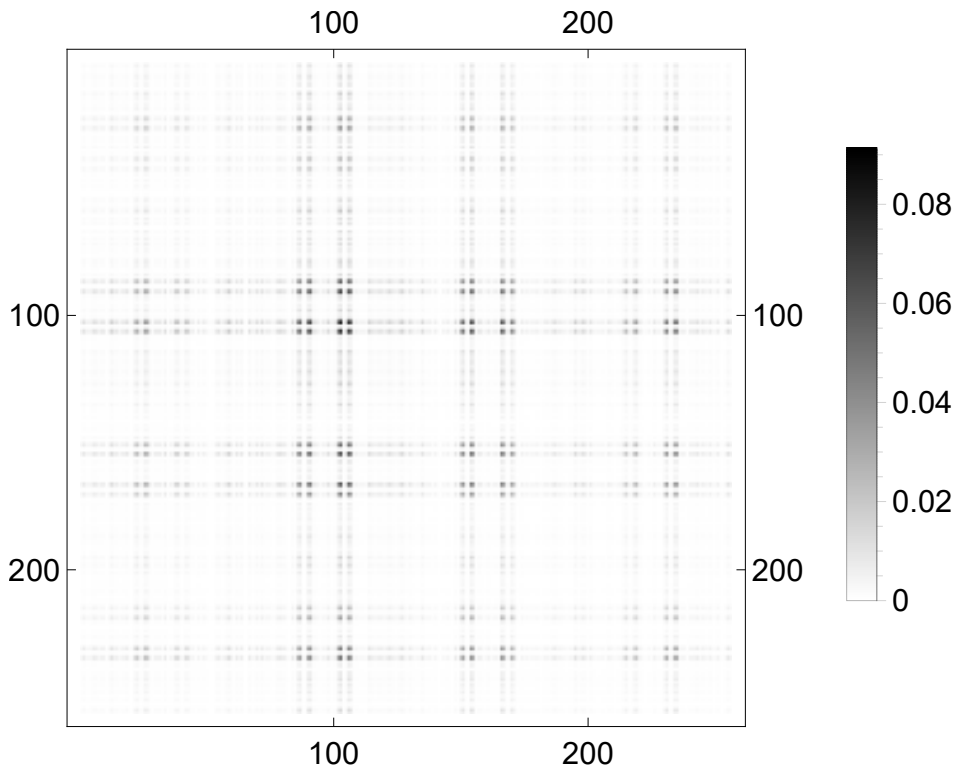


Figure 2.15: Density matrix absolute values of the final state of simulated repeated central spin measurements and their effects on eight external spins. Involved parameters are listed in Table 2.1. Labels indicate the position of elements in the matrix, while darker colours signify higher absolute values. Observe that there is a very clear structure within the density matrix with pronounced off-diagonal elements.

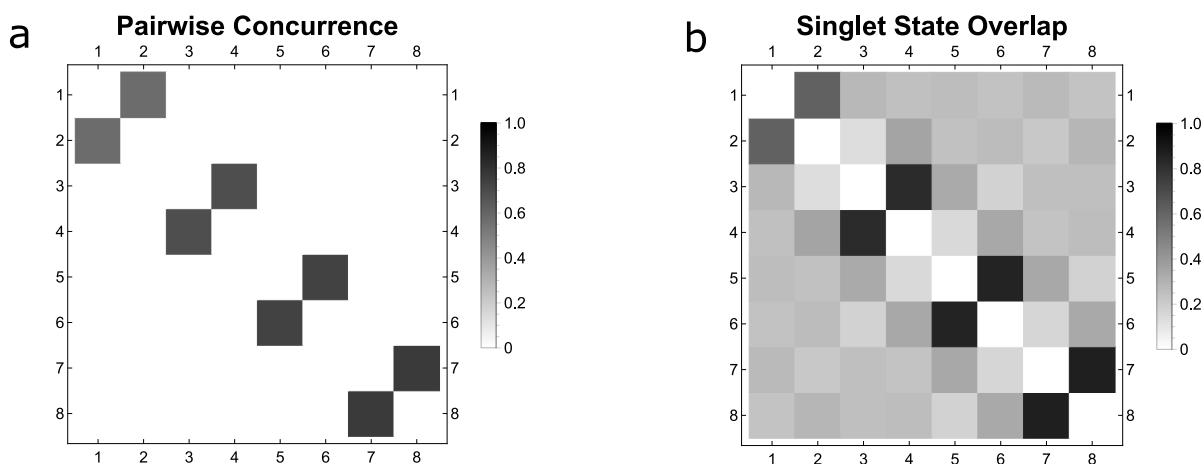


Figure 2.16: Pairwise Concurrence (a, left) and Singlet State Overlap (b, right) within the final state of an eight external spin simulation of repeated central spin projections. The values are obtained in the same way as before in the twenty-spin case (Figure 2.13). However, all involved spins are pairwise entangled with their next neighbour, as visible from high Concurrence values (dark colours) in (a). The Singlet State Overlap shows the same qualitative structure, while pairs other than nearest neighbours all show zero Concurrence.

2.5.7 Consequences and Possible Improvements

While it is surely remarkable that twenty spins could be simulated in this case, the insights gained diminish due to the lack of Correlations building up for higher numbers of spins. This could be corrected by simulating a much higher number of repetitions, which was beyond the scope of the presented calculations and the involved computational power. As a consequence of the observations, in an experimental case, the landscape of possibly involved nuclear spins will have to be mapped out carefully. If too many spins are involved, it will be very hard to observe correlations, except if the number of repetitions are scaled up, rendering the experiments very time intensive. Computationally, the number of involved spins could be further scaled up, obviously by involving

further computational resources, but also by computational methods avoiding the usage of RAM, instead using high-performance hard disks to stream and write the data directly.

2.6 Experimental Implementations using NV-Centers

We can summarize from the simulation results above that the experimental implementation of the described Purification procedure is surely a non-trivial task. Parameters such as the strength of the external field ω , the time τ between different measurements and the superposition state (2.19) have to be chosen carefully in order to observe Purification and possible Correlation. Moreover, the number of involved spins and the involved coupling parameters have to be mapped out carefully in order to enable a relevant simulation aiding the experimental effort. A pure trial-and-error strategy is not recommended due to the large parameter space and the dependence on the coupling geometry. It has to be noted again that a repeated projection of the central spin into a superposition state without affecting the associated nuclear spin states is most accessible at low temperature NV experiments [5, 43]. Many repetitions of the described measurements, including post-selection of the results depending on individual measurement outcomes, require a significant amount of measurement time. Both the spin-landscape and the parameter space should thus be analysed carefully and should be accompanied by simulations before aiming to show Correlations or even Singlet States arising among the spins coupled to an NV.

However, performing experiments with the introduced methods also presents many advantages. The achievable states are useful in Quantum Sensing and for the coherence time of the involved NV, as we have seen in the previous sections. Moreover, there is also a profound advantage in performing Quantum Simulations. While a simulation of a specific Hamiltonian on a regular Quantum Computer requires to first translate the dynamics into specific Quantum Gates, at the expense of a regular dynamic evolution, an effective Hamiltonian can here be generated by mere application of a suitable repeated projective measurement of just one central spin.

2.6.1 Existing Purification Experiment using NVs

An experiment using the methods described in our proposal paper [46] has already been performed using the described projective readout of an NV electron spin at low temperatures [5]. While the publication in [5] also provides interpretations of the results in terms of Quantum Random Walks, we focus on the Purification aspect, while providing a short summary of the experimental results and possible future experiments here.

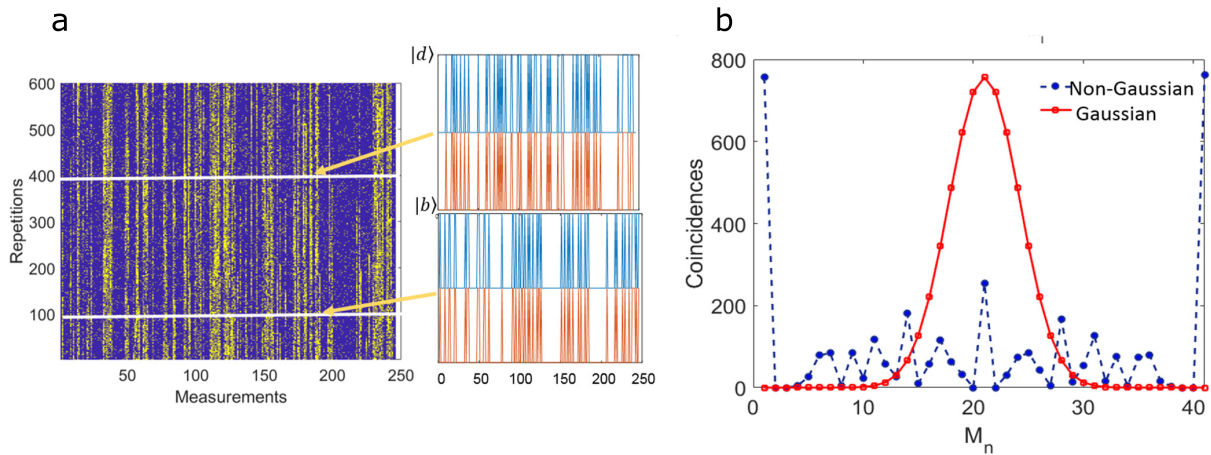


Figure 2.17: Experimental results from the Purification experiment using NV-Centers at low temperature in [5]. The left image (a) shows different traces from an experiment with $n = 246$ measurements (x-axis), repeated 600 times (y-axis). Violet colour signifies that at least one photon was detected in an individual measurement (bright state $|b\rangle$), while yellow colour means that no photon was detected (dark state $|d\rangle$) in the associated individual measurement. The analysis within the right image (b) demonstrates effects of the involved measurement back-action. Several cases of 40 consecutive measurements are extracted from the experimental data. The dashed blue curve shows occurrences of individual measurement strings from this experimental data. This is confirmed to differ from a Gaussian distribution (red curve), which would occur if there was no measurement back-action. Illustration directly adapted from [5].

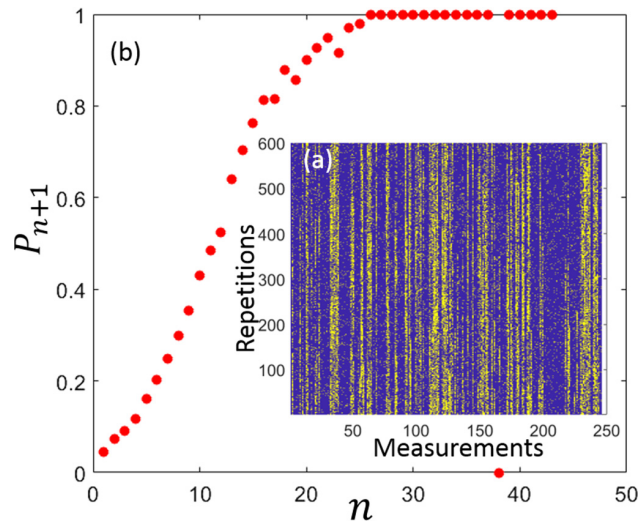


Figure 2.18: Probability of consecutively obtaining the same measurement result after n identical measurement results in a low-temperature Purification experiment using NV-Centers. The probability (red dots, y-axis) is clearly seen to rise with the number of measurements (x-axis) when extracting the cases of successive successful photon measurements, i.e. finding the system in the bright state $|b\rangle$, from the experimental data (inset (a), as in Figure 2.17). Note that the rise of the projection probability therefore experimentally confirms the observation in our proposal paper [46] and the qualitative results from the simulations above, e.g. in Figure 2.2. Illustration directly adapted from [5].

2.6.2 Open Questions addressable in further Purifications Experiments using NV-Centers

We have seen a clear confirmation of the measurement back-action instilled by the methods described above and laid out in our Purification proposal paper [46]. In particular, the probability of repeatedly projection the central NV spin into the selected superposition state increases with each successful repetition of the measurement sequence. This also hints towards a Purification of the associated nuclear spins [5]. However, the other central aspect of our proposal, namely

2.7 Application of Repetitive Projections to Superconducting Qubits

Correlation of the involved bath spins and even the observation of Entanglement or projection into Singlet states has not yet been directly observed. This would necessitate either a full density matrix tomography of the associated nuclear spins or, preferably, suitable measurements directly designed to detect entanglement within the spin bath – avoiding errors accumulating within the density matrix tomography and entanglement measure retrieved thereof [56, 57]. Such measurements have not yet been carried out, but are prepared at the time of writing. Moreover, the prepared states and effective dynamics can then be used for Quantum Simulation of specific relevant Hamiltonians [49, 50] as well as for the implementation of target states which would otherwise require complicated Quantum Algorithms. As discussed in section 2.3.2, a successful Purification measurement sequence can further be used as a starting point for successive Quantum Sensing measurements, which benefit from the Purification and Correlation of the bath spins.

2.7 Application of Repetitive Projections to Superconducting Qubits

The presented method of repetitive projections of a central spin can in principle be applied to any physical Quantum System, regardless of the specific ‘hardware’. In order to demonstrate this, a simulation was carried out of a Superconducting Transmon Qubit system with parameters available from the IBM Quantum Experience, on the second version of the first ever Quantum Computer available on a public cloud system [16]. However, since repetitive measurements were not available as a functionality at the time, these parameters were used for a simulation of the system on a classical machine. Yet, using realistic parameters, a build-up of pairwise entanglement, even formation of Singlet states, was observed for the two pairs of qubits which were not directly measured, starting from a completely mixed state of all qubits. As before, a central qubit, named Q_C here, was assumed to be repeatedly projected in a superposition state. Purification and Entanglement of the remaining qubits takes place by Measurement back-action alone.

2 Quantum State Engineering

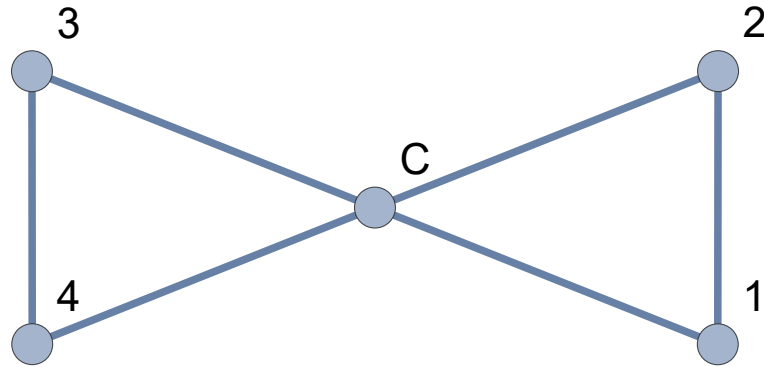


Figure 2.19: Coupling topology of the simulated five-Qubit system provided by the IBM Quantum Experience in early 2017. The central Qubit Q_C , coupled to all other Qubits, is repeatedly projected into a superposition state here. The remaining Qubits Q_1 to Q_4 are shown to be projected into a Singlet state by this mechanism. Lines indicate non-zero coupling between the Qubits, with coupling strengths provided in Table 2.2. Circles symbolize Qubits, labelled with Qubit indices.

| | Q_C | Q_1 | Q_2 | Q_3 | Q_4 |
|-------|-------|-------|-------|-------|-------|
| Q_C | 0 | 42.2 | 37.8 | 74.6 | 38.9 |
| Q_1 | 42.2 | 0 | 38.9 | 0 | 0 |
| Q_2 | 37.8 | 38.9 | 0 | 0 | 0 |
| Q_3 | 74.6 | 0 | 0 | 0 | 64. |
| Q_4 | 38.9 | 0 | 0 | 64. | 0 |

Table 2.2: Absolute values (in kHz) of the coupling parameters between the five superconducting Qubits publicly available on the IBM Quantum Experience. The values were adapted from the IBM Quantum Experience in early 2017 and used for simulation of repetitive projection and readout of the central Qubit Q_C , in order to correlate the remaining four Qubits.

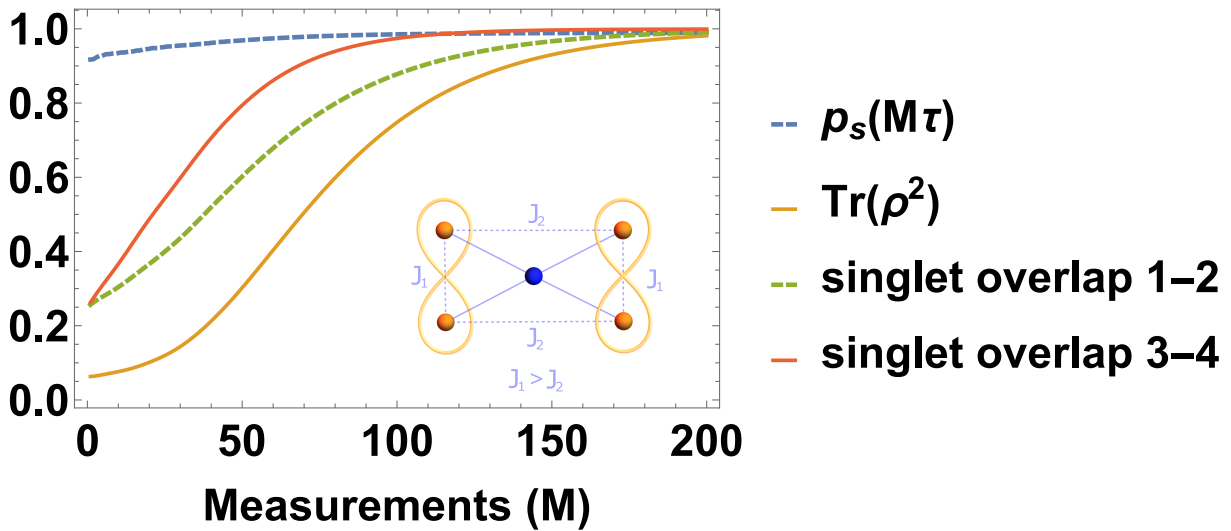


Figure 2.20: Results of simulated central-spin projections within a five-Qubit system provided by the IBM Quantum Experience in 2017. Parameters used include the free evolution time $\tau = 2\pi\mu s \approx 6.28\mu s$, external field strength $\omega = 200\text{kHz}$. The probability of measuring the central spin in a superposition state (blue dashed line) increases with each repetition of a Measurement. Moreover, the purity increases (orange solid line), starting from a completely mixed state. Two pairs of entangled Qubits build up, with both pairs constantly increasing the overlap with a Singlet state (green dashed line, red solid line). The numerical Concurrence (2.28) obtained for the pairs was 0.984 (1,2) and 0.999 (3,4) , respectively.

2.8 Squeezed Spin States

The properties that qualify spin squeezed states [58, 59] for applications in quantum metrology or quantum information [60] are the reduction of uncertainty in one component of angular momentum as well as their stability in presence of decoherence [6] in comparison with fully entangled states [45]. This leads to an improvement in sensitivity in realistic systems when an external field is measured as a phase Φ which is collected during the time evolution of the quantum system. Experimentally, the creation of spin squeezed states has been demonstrated in systems of high spin numbers and at low temperatures such as ensembles of cold atoms [61–64] or in Bose-Einstein condensates [64–66]. On the theoretical side, it has been shown that squeezing is well defined in an individually addressable multi-qubit system as opposed to the more frequently studied case of collective symmetric multi-particle states [67].

2.8.1 Heisenberg's Uncertainty Relation

Since Heisenberg's uncertainty relation is at the core of a certain understanding of squeezed states, we will review it briefly and give a quick derivation thereof. To do so, given the standard Hilbert space formalism of quantum mechanics, we only need to assume two theorems, namely the Cauchy-Schwarz inequality and the triangle inequality. Recall that for two Operators A and B acting on a Hilbert space such that a scalar product is defined as

$$\langle A, B \rangle \equiv \langle \Psi | A \cdot B | \Psi \rangle \quad ; | \Psi \rangle \in \mathcal{H}, \quad (2.40)$$

the Cauchy-Schwarz inequality reads

$$\langle A, A \rangle \cdot \langle B, B \rangle = \langle A^2 \rangle \cdot \langle B^2 \rangle \geq |\langle A, B \rangle|^2. \quad (2.41)$$

Secondly, due to the triangle inequality it is true that

$$\forall z \in \mathbb{C}, |z|^2 \equiv |\Re(z)^2 + \Im(z)^2| \geq |\Im(z)|^2 \quad (2.42)$$

where $\Re(z)$ and $\Im(z)$ are the Real and Imaginary parts of z , respectively. Now if we define $\langle A, B \rangle = c \in \mathbb{C}$ and assume A and B to be hermitian operators, we have

$$|\Im(c)| \equiv \left| \frac{1}{2i}(c - c^*) \right| = \frac{1}{2} |\langle A, B \rangle - \langle B, A \rangle| = \frac{1}{2} |\langle [A, B] \rangle|. \quad (2.43)$$

Therefore,

$$|\langle A, B \rangle|^2 \geq |\Im(\langle A, B \rangle)|^2 = \left| \frac{1}{2} \langle [A, B] \rangle \right|^2. \quad (2.44)$$

In combining the above inequalities we obtain

$$\langle A^2 \rangle \cdot \langle B^2 \rangle \geq |\langle A, B \rangle|^2 \geq \frac{1}{4} |\langle [A, B] \rangle|^2. \quad (2.45)$$

We finally set $A = C - \langle C \rangle \mathbb{1}$ and $B = D - \langle D \rangle \mathbb{1}$ which leaves the commutator invariant such that upon taking the square root, the resulting equation is the Heisenberg uncertainty relation

$$(\Delta C)(\Delta D) \geq \frac{1}{2} |\langle [C, D] \rangle| \quad (2.46)$$

with the standard deviation Δ defined as $(\Delta C)^2 \equiv \langle (C - \langle C \rangle)^2 \rangle = \langle C^2 \rangle - \langle C \rangle^2$.

Squeezed States defined by the Heisenberg Inequality

Squeezed states are collective quantum states $|\Psi\rangle \in \mathcal{H}$ of minimal Uncertainty, which means that for squeezed states, the above inequality is minimized to yield the equality

$$(\Delta C)(\Delta D) = \frac{1}{2} |\langle [C, D] \rangle|. \quad (2.47)$$

Moreover, uncertainties are unevenly distributed between the operators, such that

$$\Delta C \neq \Delta D \quad (2.48)$$

which distinguishes squeezed states from coherent quantum states for which the uncertainties concerned are equal. To quantify the squeezing given in a state, the squeezing parameter ξ is defined. However, different definitions of squeezing parameters exist depending on the context [68].

2 Quantum State Engineering

Usually in spin physics the operators of interest are angular momenta with commutation relation $[J_i, J_j] = i\epsilon_{ijk}J_k$ (where $i, j, k \in \{x, y, z\}$) and a possible definition of the squeezing parameter can be read off from the uncertainty relation

$$(\Delta J_i)(\Delta J_j) = \frac{1}{2}\langle J_k \rangle \xrightarrow{\Delta J_i = \Delta J_j} \Delta J_i = \sqrt{\frac{1}{2}\langle J_k \rangle}. \quad (2.49)$$

In the case of a squeezed state, the equality on the right of the above formula becomes an inequality since $\Delta J_i \neq \Delta J_j$. More particularly, it can be tested whether squeezing is persistent by checking whether

$$(\Delta J_i)^2 < \frac{\langle J_k \rangle}{2}. \quad (2.50)$$

Therefore, squeezing is given if

$$\xi_h = \frac{\Delta J_i}{\sqrt{\langle J_k \rangle/2}} \neq 1 \quad (2.51)$$

where usually the focus is on the component of lower uncertainty such that $\xi_h < 1$ constitutes squeezing.

A Coordinate-Independent Refinement of the Definition of Squeezed Spin States

It has been noticed by Kitagawa and Ueda [58] that the definition of squeezed states in the directions x, y and z is generally not coordinate independent. Specifically, a rotation of the coordinate system of a coherent state already leads to a squeezed state by means of the definition of ξ_h as in equation (2.51) above. In order to obtain a rigorous definition of spin squeezing, it is therefore necessary to refer to the quantization axis of the system and a direction orthogonal to it. The refined definition of the squeezing parameter is therefore given by

$$\xi_q = \frac{\Delta J_{\perp}}{\sqrt{J/2}}. \quad (2.52)$$

where $J/2$ is the sum over all variances of individual spin $1/2$ systems and the orthogonal direction is defined such that $\Delta(\vec{n} \cdot \vec{J})$ is minimized [68].

Squeezing parameter definition by Wineland et al. Furthermore, another definition of the squeezing parameter is motivated by the improvement of signal-to-noise ratio in Ramsey-type spectroscopy [69] or equally by improvement of the phase sensitivity in Mach-Zehnder interferometers [70]. It is related to the previous definition ξ_q by Kitagawa and Ueda and defined by Wineland et al [69, 70] as

$$\xi_R \equiv \sqrt{J} \frac{\Delta J_{\perp}}{\sqrt{|\langle \vec{J} \rangle|/2}} = \frac{J}{\sqrt{|\langle \vec{J} \rangle|}} \xi_q \quad (2.53)$$

Squeezed states and entanglement in spin systems Note that a squeezed spin state is only given if there are correlations between individual spins. Therefore, as correlation is a necessary condition for squeezing, the detection of a squeezed state also implies correlation and moreover even entanglement between the spins such that a squeezed spin state also becomes a useful resource in quantum information processing [59, 60].

2.8.2 General Dynamics for Generation of Spin Squeezed States

Kitagawa and Ueda presented two exemplary mechanisms and Hamiltonians in order to instil Spin Squeezing in their landmark paper entitled "Squeezed Spin States" [58].

One-Axis Twisting Hamiltonian

The first standard Hamiltonian to induce Spin Squeezing is a simple quadratic Hamiltonian of the total angular momentum S_z with a free parameter χ .

$$H_{1a} = \chi S_z^2. \quad (2.54)$$

The total angular momentum is explicitly calculated as $S_z = \sum_i S_{z,i}$. In the following, we briefly review the time evolution of this Hamiltonian and look at the effects on the involved Uncertainties. As an example, we analyse the time evolution of this Hamiltonian for two qubits initially in a pure

2 Quantum State Engineering

superposition state $|+\rangle = 1/\sqrt{2}(|\uparrow\rangle + |\downarrow\rangle)$. For this case, we can calculate the analytical evolution as

$$|\Psi_1(t)\rangle = e^{i\chi S_z^2 t} |++\rangle = \frac{1}{2} (e^{i\chi} |\uparrow\uparrow\rangle + |\downarrow\uparrow\rangle + |\uparrow\downarrow\rangle + e^{i\chi} |\downarrow\downarrow\rangle). \quad (2.55)$$

From this time-dependent state we can then calculate a squeezing parameter according to equations (2.52) and (2.65). The evolution of this parameter is displayed in Figure 2.21.

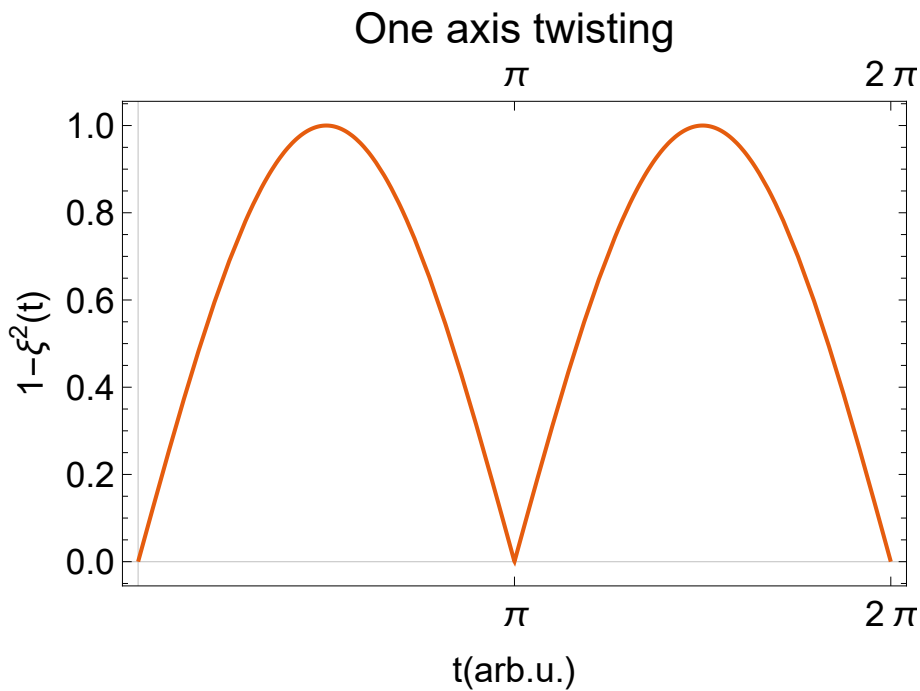


Figure 2.21: Time Evolution of the Squeezing Parameter ξ_R , calculated according to equation (2.65), in the case of the state in equation (2.55), stemming from a One-Axis Twisting Hamiltonian (2.54). Squeezing is plotted as $1 - \xi_R^2$ over time t in arbitrary units. The free parameter χ in the Hamiltonian is set to one. Note that higher values on the y-axis denote higher amounts of squeezing, as $\xi_R < 1$ indicates squeezing.

Moreover, in order to illustrate the effect of the evolution on the involved Uncertainties, we con-

struct and plot the overlap with a general reference state

$$|\Psi\rangle_{ref} = \left(\cos\left(\frac{\theta}{2}\right)|\downarrow\rangle + e^{i\phi} \sin\left(\frac{\theta}{2}\right)|\uparrow\rangle \right)^{\otimes 2}. \quad (2.56)$$

The overlap of the state in (2.55) and the reference state then illustrate the dynamics of the involved Uncertainties. The construction of the Quasiprobability Distribution (QPD) follows reference [58]. See Figure 2.22 for the evolved QPD from the one-axis twisting Hamiltonian.

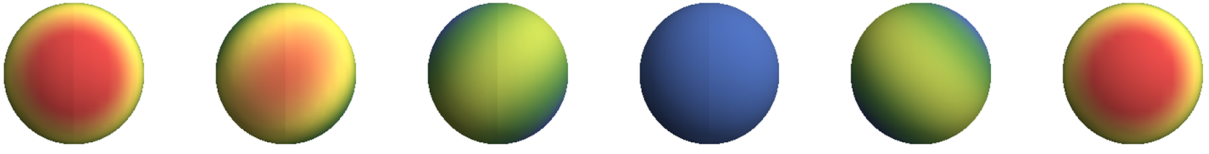


Figure 2.22: Evolved Quasiprobability Distribution constructed as overlap of the evolved state resulting from a One-Axis Twisting Hamiltonian for Spin Squeezing with the reference state in (2.56). The parameters θ and Φ then constitute the angles of a spherical plot, while weights (coloring) is given by the overlap $\left| \langle \Psi_{ref} | \Psi_1(t) \rangle \right|^2$, with $|\Psi_1(t)\rangle$ defined in equation (2.55). Red colour signifies an overlap close to one, while dark blue denotes zero. The parameter χ is set to one. The time evolution is to be read from left to right, beginning at $t = 0$ and ending at $t = 2\pi$. Note that the QPD is squeezed together (spheres 2 and 3), then twisted (sphere 5) and finally restored (last sphere). The Mathematica Code for this evolution is explicitly given in the Appendix in section A.2.3.

A final note on the effect of the One-Axis Twisting Hamiltonian and squeezing in general is the fact that entanglement is also persistent along with squeezing here. We can explicitly calculate the reduced density matrix of any one of the two qubits from state $|\Psi_1(t)\rangle$ from equation 2.55 as

$$Tr_1(|\Psi_1(t)\rangle \langle \Psi_1(t)|) = \begin{pmatrix} \frac{1}{2} & \frac{\cos t}{2} \\ \frac{\cos t}{2} & \frac{1}{2} \end{pmatrix}. \quad (2.57)$$

2 Quantum State Engineering

From this, we can further extract the entanglement Entropy

$$S(t) = \sum_i \lambda_i(t) \log_2 \lambda_i(t), \quad (2.58)$$

where λ_i are the Eigenvalues of the reduced density matrix above. The time-evolution of the Entanglement Entropy is given in Figure 2.23. As entanglement is clearly building up, we can thus confirm in this example the observation that Squeezing always implies pairwise entanglement [59].

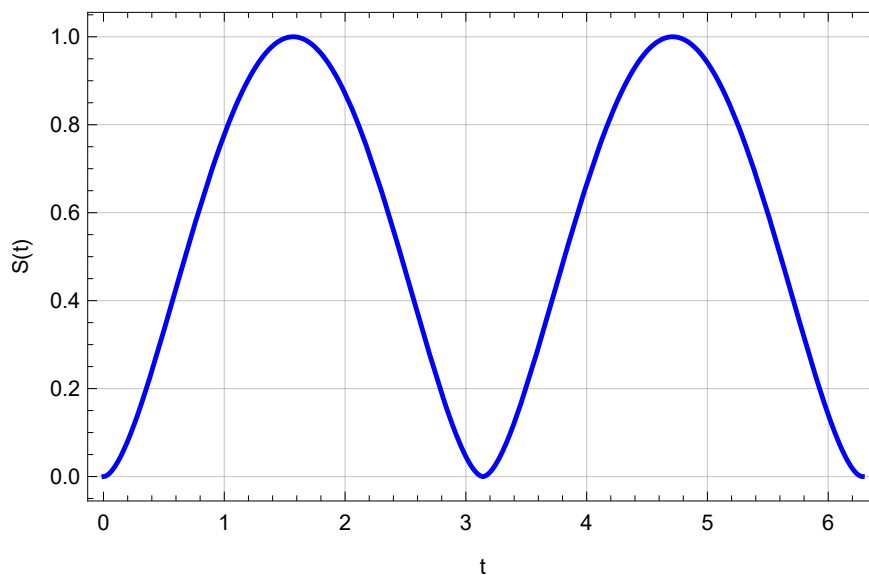


Figure 2.23: Entanglement among the Qubits subjected to a One-Axis Twisting Hamiltonian (2.54) over time is analysed by the measure of Entanglement Entropy $S(t)$, defined in (2.58). Clearly, the Entanglement Entropy rises and falls analogously to the Squeezing Parameter in Figure 2.21. Observe that Correlation is a necessary condition for Squeezing [58] and Squeezing in turn provably implies pairwise entanglement [59].

Two-Axes Countertwisting Hamiltonian

The second canonical Hamiltonian for Spin Squeezing brought forth by Kitagawa and Ueda [58] is the Two-Axes Countertwisting Hamiltonian

$$H_{2a} = \frac{\chi}{2i} (S_+^2 - S_-^2) \quad (2.59)$$

Where $S_{\pm} = S_x \pm iS_y$ is composed of the total angular momenta in x and y direction. We can furthermore analytically provide an explicit expression for a time evolved state in a two-qubit example as

$$\begin{aligned} |\Psi_2(t)\rangle &= e^{i\frac{\chi}{2i}(S_+^2 - S_-^2)t} |++\rangle \\ &= \frac{1}{2}(\sin(t\chi) + \cos(t\chi) |\downarrow\downarrow\rangle + |\downarrow\uparrow\rangle + |\uparrow\downarrow\rangle + \sin(t\chi) - \cos(t\chi) |\uparrow\uparrow\rangle) \end{aligned} \quad (2.60)$$

From this, we can plot the time evolution of the squeezing parameter ξ_R and the Entanglement Entropy $S(t)$ as before in Figures 2.21 and 2.23 for the case of the One-Axis Twisting Hamiltonian. We provide the analysis for the Two-Axes Countertwisting Hamiltonian in Figure 2.25. The Quasiprobability Distribution is also calculated analogously to Figure 2.22, with the overlap adjusted to $|\langle \Psi_{ref} | \Psi_2(t) \rangle|^2$.

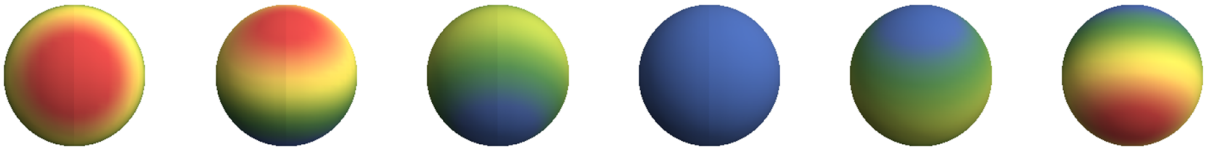


Figure 2.24: QPD of the exemplary state in equation (2.60), a superposition state evolved by a Two-Axis Countertwisting Hamiltonian. Here, the Quasiprobability Distribution is rather rotated around the sphere than visibly squeezed. For better visualisation of the effect, the timescale is set here from $t = 0$ (Leftmost sphere) to $t = 7\pi/4$ (Rightmost sphere).

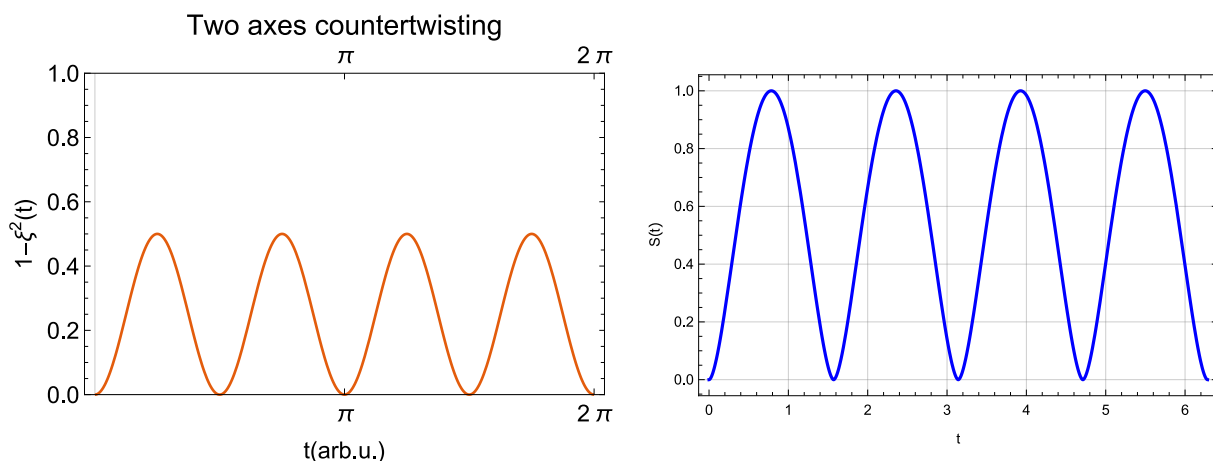


Figure 2.25: Evolution of the Spin Squeezing parameter $\xi(t)$ (left image) and the Entanglement Entropy $S(t)$ (right image) in a Two-Axes Countertwisting Hamiltonian two-qubit example. We note faster dynamics than in the comparable One-Axis Twisting example (Figure 2.21). Moreover, note that the scale in the case of the squeezing parameter is rescaled to the maximum of $1/2$. We thus observe less Squeezing, but still see maximal Entanglement Entropy, evolving analogously. The squeezing parameter $\widetilde{\xi}_{q,\text{gen}}$ is calculated according to equation (2.66), while interestingly, $\widetilde{\xi}_q$ calculated according to equation (2.65) yields no squeezing in this case, due to the involved assumptions.

Any Correlating Hamiltonian is a Candidate to instil Spin Squeezing

The close relation between Spin Squeezing and pairwise Entanglement has become clear from the previous discussions [59]. I want to stress here, that the creation of Spin Squeezed states – be it in an experimental or theoretical setting – by no means requires the involved Hamiltonians to be exactly, or even approximately described as the introduced One-Axis Twisting Hamiltonian or the Two-Axes Countertwisting Hamiltonian [6, 71]. Kitagawa and Ueda chose these Hamiltonians in their seminal paper [58] simply as exemplary Hamiltonians to induce correlations between spins. All that is required is a non-linear interaction beyond what is known as single-qubit gates today, in order to establish correlations among the spins [58]. The One-Axis Twisting Hamiltonian (2.54)

or the Two-Axes Countertwisting Hamiltonian (2.59) are simply somewhat obvious examples of non-linear Hamiltonians. Of course there are many other theoretical and experimental ways of correlating spins. As an example, we look at the time evolution of a simple z-z coupling Hamiltonian

$$H_{zz} = \sum_{i,j} J_{ij} S_i^z S_j^z \quad (2.61)$$

where J_{ij} is the matrix of couplings between the involved spins. The resulting squeezing parameter is analysed in Figure 2.26 for two different choices of spin numbers and different coupling geometries. This demonstrates that Spin Squeezing can not only result from the described canonical Hamiltonians, but also, for example, from simple two-qubit z-z interactions.

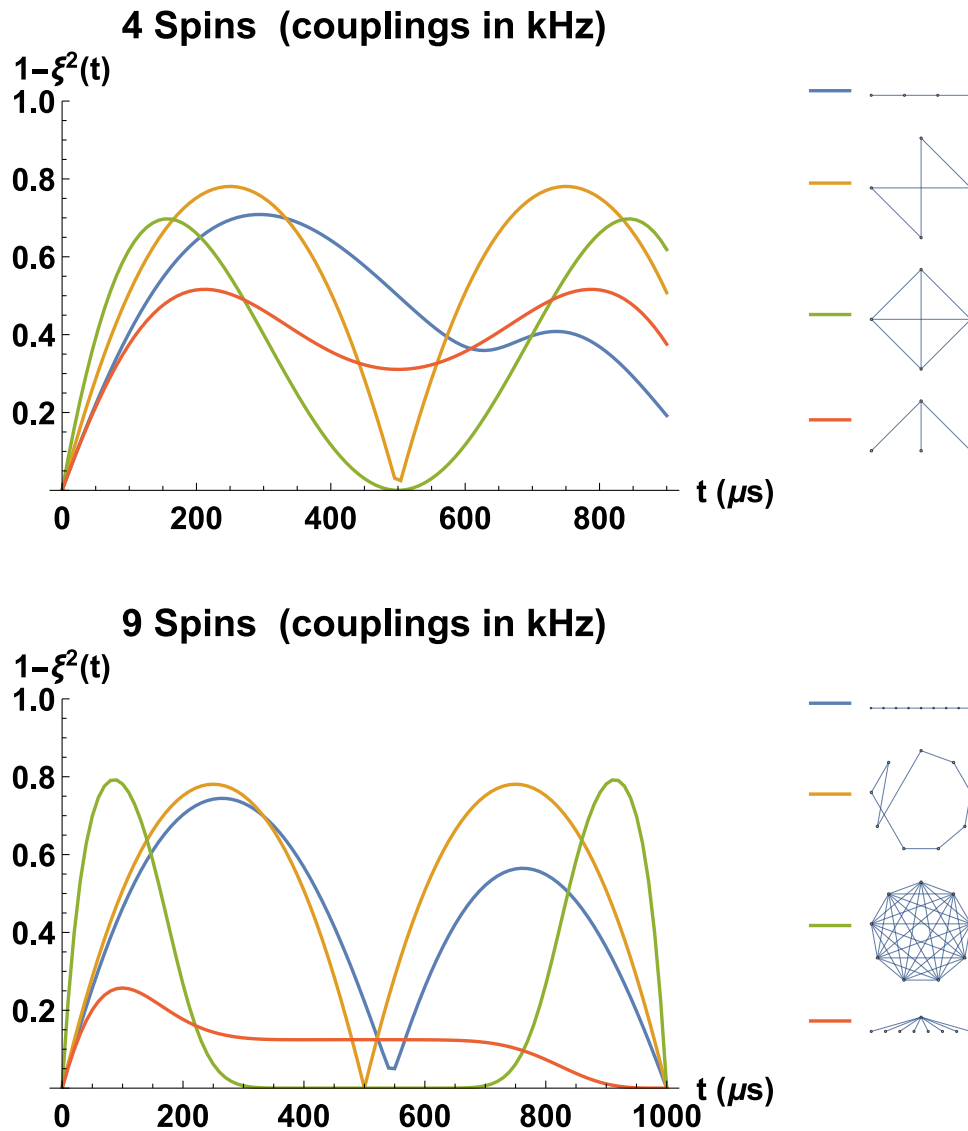


Figure 2.26: Evolution of the Squeezing Parameter $\tilde{\xi}_q$ (2.65) in the case of simple z-z coupling between spins in different coupling geometries, for the case of four spins (top) and nine spins (bottom). Four different coupling geometries are analysed, namely linear (blue curve), circular (orange curve), all-to-all (green curve) and Central Spin coupling (red curve), as indicated by the graphs in the Plot Legend. The coupling strength is fixed to 1kHz for each existing connection in the coupling graph. Squeezing is clearly persistent in all cases. For the higher number of spins (bottom plot), it is visible that a Central Spin geometry becomes less effective, while all-to-all couplings show highest squeezing after short evolution times.

2.8.3 Nuclear Spin Squeezed States in Diamond

Spin squeezing is of great interest for applications in quantum metrology and as a possible resource in quantum information. We develop a method to create a squeezed state of nuclear spins surrounding a nitrogen-vacancy defect in diamond. Recent results have shown that the sensitivity of diamond based magnetometers can approach the order of spin projection noise [27]. Sensitivity exceeding this standard quantum limit is demonstrated for direct phase accumulation in the nuclear spin register, even in the presence of decoherence. Furthermore, readout improvements of a phase imprinted on the nitrogen-vacancy electron spin directly are discussed. Here we propose spin squeezing of a well controllable system [72, 73] with low spin numbers ($n \sim 10$), namely a register of one ^{14}N and several ^{13}C nuclear spins contained in the modified diamond lattice around a nitrogen-vacancy (NV) defect at room temperature. This quantum register is particularly well controllable since nuclear spins with quantization axes parallel to the NV axis are preselected and aligned to an external magnetic field. Therefore, couplings between the electron spin and the nuclear spins are predominant in the z-direction parallel to the magnetic field and contributions in x or y direction can safely be neglected. Furthermore, direct interactions between the nuclear spins are negligible, leading to a central spin model. Rotations of individual nuclear spin states are stimulated via controlled application of external radio frequency fields and are resolvable in the fluorescence of the diamond vacancy by optically detected magnetic resonance (ODMR) [33]. The high degree of controllability presents an advantage for the realization of spin squeezing in solid-state systems against other proposals involving a high number of nitrogen-vacancy electron spins [6]. Moreover, as a recent development [25], the strength of each electron spin - nuclear spin interaction can be controlled in a co-moving coordinate frame such that it is possible to engineer a hyperfine interaction Hamiltonian between the electron and n nuclear spins with a uniform coupling strength J as

$$H_{int} = \sum_{k=1}^n JS_z I_z^{(k)}. \quad (2.62)$$

2 Quantum State Engineering

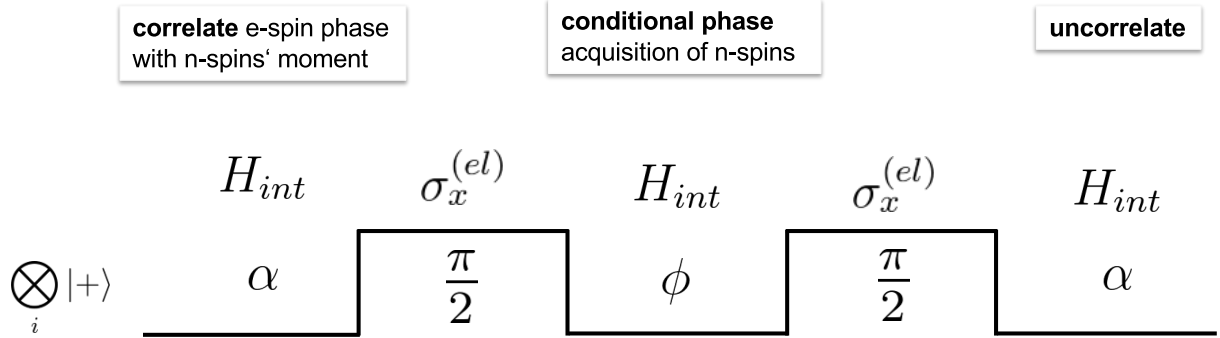


Figure 2.27: Sequence to create Spin Squeezing among nuclear spins in diamond. Starting from an initial superposition state of all involved spins, free evolutions of the interaction Hamiltonian (2.62) are followed by $\pi/2$ -pulses on the NV electron spin. Text above the individual free interaction Hamiltonian evolutions indicates their respective function.

Yet, no squeezing is observed in the subsystem of the nuclear spins after a simple time evolution of this Hamiltonian. Squeezing does however occur when additional rotations of the central electron spin are included. The time evolution operator of the sequence is given by

$$U = e^{-iH_{int}\alpha} e^{-\frac{i}{2}\sigma_x^{(el)}\frac{\pi}{2}} e^{-iH_{int}\phi} e^{-\frac{i}{2}\sigma_x^{(el)}\frac{\pi}{2}} e^{-iH_{int}\alpha}, \quad (2.63)$$

as further illustrated in Figure 2.27. The input state can be initialized by optical pumping with the electron spin and successive transfer of polarization to all n nuclear spins, followed by controlled radio-frequency pulses in x -direction such that the state after p iterations of the sequence is

$$|\Psi(t_p)\rangle = U^p \bigotimes_{i=1}^{n+1} \frac{|0\rangle_i + |1\rangle_i}{\sqrt{2}}. \quad (2.64)$$

Here, $|0\rangle$ and $|1\rangle$ denote the $m_s = 0$ and $m_s = -1$ state for the electron spin but $m_I = -1/2$ and $m_I = 1/2$ for the ^{13}C , as well as $m_I = 0$ and $m_I = 1$ in the case of the ^{14}N nuclear spin, respectively. ξ_q given by Kitagawa and Ueda (2.52) can then be calculated explicitly for the case $\langle I_y \rangle = \langle I_z \rangle = 0$, $\langle I_x \rangle \neq 0$ as [74]

$$\tilde{\xi}_q = \sqrt{\frac{2}{n} \left(\langle I_y^2 + I_z^2 \rangle - \sqrt{\langle I_y^2 - I_z^2 \rangle^2 + \langle \{I_y, I_z\} \rangle^2} \right)^{\frac{1}{2}}} \quad (2.65)$$

2.8 Squeezed Spin States

where $I_j = \sum_k \frac{1}{2} \sigma_j^{(k)}$ is the nuclear spins' collective angular momentum operator in the respective spatial direction. The curly brackets denote the anti-commutator, such that $\{A, B\} = AB + BA$. Squeezing occurs in the nuclear spin register when $\widetilde{\xi}_q < 1$.

Generally, while the definition of $\widetilde{\xi}_q$ as in equation (2.65) according to reference [74] is useful in certain contexts, the involved assumptions are a great restriction for a state resulting from a free evolution. Thus, following the calculation in [74], but dropping the previous assumption, such that $\langle I_x \rangle \neq 0$, $\langle I_y \rangle \neq 0$ and $\langle I_z \rangle \neq 0$ we arrive at a more general definition

$$\widetilde{\xi}_{q,\text{gen}} = \sqrt{\frac{2}{n} \left(\langle I_y^2 + I_z^2 \rangle - \langle I_y \rangle^2 - \langle I_z \rangle^2 - \sqrt{\left(\langle I_y^2 - I_z^2 \rangle + \langle I_y \rangle^2 - \langle I_z \rangle^2 \right)^2 + \left(\langle \{I_y, I_z\} \rangle - 2\langle I_y \rangle \langle I_z \rangle \right)^2} \right)^{\frac{1}{2}}}. \quad (2.66)$$

Working with this definition enables us to calculate a squeezing parameter directly from the expectation values of angular momentum operators without additional assumptions. A full model of the system shows a high amount of squeezing (i.e. a decrease of $\widetilde{\xi}_{q,\text{gen}}$) depending on the number of involved nuclear spins n when the free parameters α , ϕ and number of repetitions p (c.f. equation (2.64)) are optimized numerically (see Figure 2.30).

A similar optimization has been carried out for the measure of Squeezing ξ_R defined by Wineland (2.53), with more focus on metrological advantages [69, 70] as illustrated in Figure 2.31. A further comparison of the two different spin squeezing measures is given in Figure 2.32.

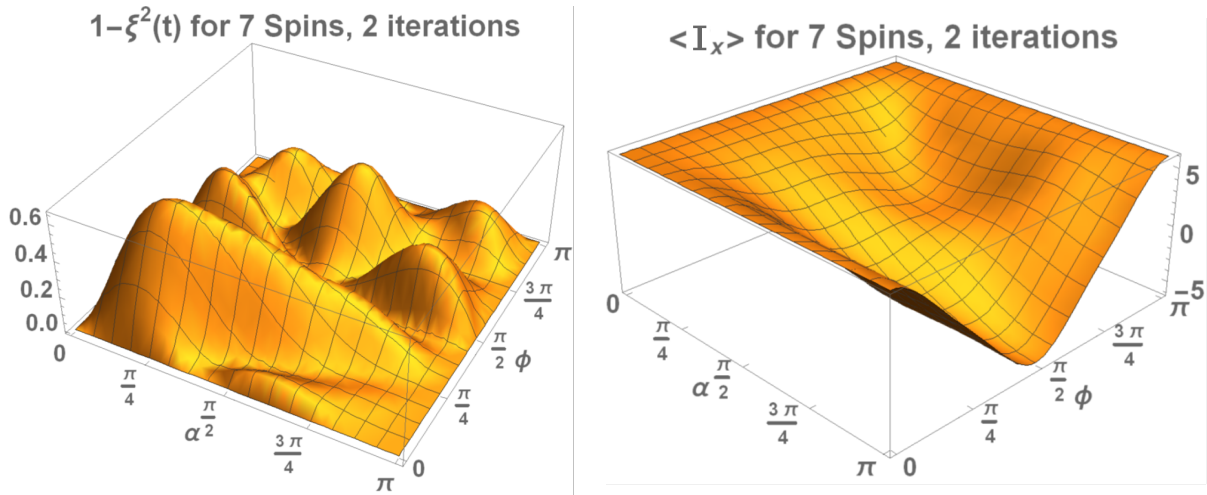


Figure 2.28: 3D Plots of Spin Squeezing (left image) among seven nuclear spins and the associated total angular momentum $\langle I_x \rangle$ expectation value (right image) under variation of both free parameters α and ϕ in two iterations of the sequence in Figure 2.27. A high amount of squeezing is observable already for small parameters α and ϕ , i.e. for short evolution times. However good experimental control of those parameters is necessary as the peaks are rather sharp. The expectation value $\langle I_x \rangle$ is importantly non-zero for regions of high squeezing. There is a trade-off between creation of spin squeezing and reduction of the readable signal $\langle I_x \rangle$ for some parameters, which motivates the definition of a different benefit factor in (2.72).

| nuclear spins | $1-\xi^2$ | Iterations | α | ϕ | ϕ/α |
|---------------|-----------|------------|----------|---------|---------------|
| 2 | 1. | 3 | 1.15199 | 4.30458 | 3.73665 |
| 3 | 0.666667 | 4 | 1.26306 | 3.14159 | 2.48729 |
| 4 | 0.927051 | 1 | 3.14159 | 1.5708 | 0.5 |
| 5 | 0.761036 | 5 | 0.428446 | 6.91633 | 16.1428 |
| 6 | 0.859479 | 7 | 5.75974 | 2.40068 | 0.416803 |
| 7 | 0.770855 | 5 | 0.409523 | 5.79337 | 14.1466 |
| 8 | 0.788919 | 8 | 6.53712 | 6.70496 | 1.02568 |
| 9 | 0.743739 | 4 | 12.1439 | 12.14 | 0.999674 |

Figure 2.29: Parameters obtained from numerical optimization for different numbers of nuclear spins involved in a Spin Squeezing sequence mediated by the central NV electron spin. All free parameters in equations (2.63) and (2.64) were numerically optimized under the constraints $p \in \mathbb{N}$ and $\{\alpha, \Phi\} \in (0, 4\pi)$. The resulting values are listed here and used for the plot in Figure 2.30.

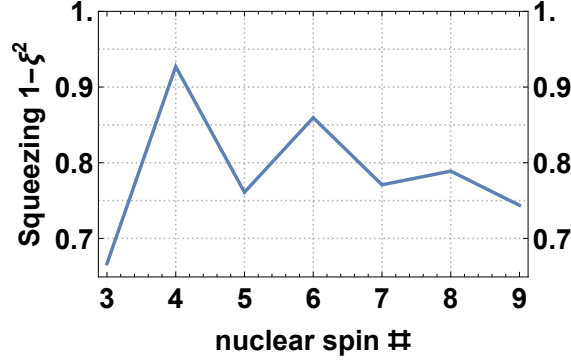


Figure 2.30: Optimized Squeezing over the number of involved nuclear spins, where all involved free parameters have been numerically optimized. Squeezing is calculated according to the generalized definition $\widetilde{\xi}_{q,\text{gen}}$ in equation (2.66). Observe that even numbers of involved spins are preferred, intuitively due to the strong relation between Squeezing and Pairwise Entanglement. Since the correlation is mediated by the central NV electron spin, the maximally achieved Squeezing drops with higher numbers of involved spins, as the ratio between one Central Spin and several nuclear spins decreases. Note that the exact ideal number of involved spins (here $n = 4$ in the non-trivial case) depends on the involved coupling strengths in a realistic scenario. The parameters resulting from numerical optimization are listed in Figure 2.29.

2 Quantum State Engineering

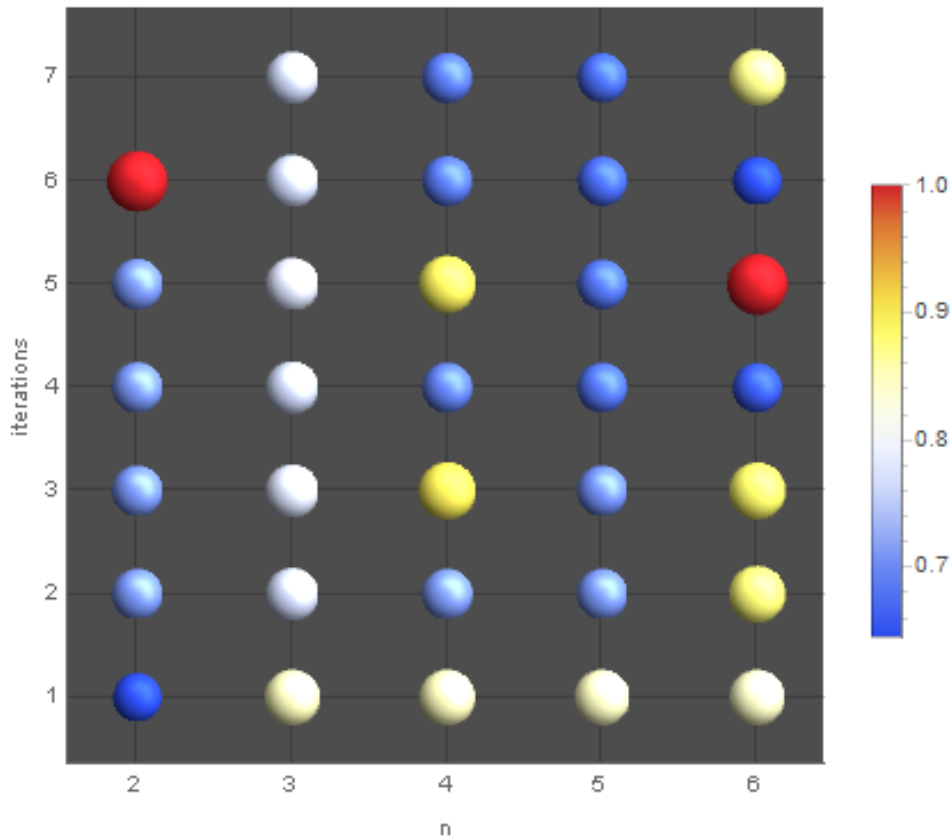


Figure 2.31: Results of numerical optimization within the Squeezing Scheme (2.63) when minimizing the Squeezing Parameter ξ_R defined by Wineland (2.53). Note that lower values (dark blue) indicate better Squeezing in this case, as opposed to higher values (red), which signify non-squeezed states. Note that the lowest parameters obtained stem from the trivial case $n = 2$ with $\xi_R = 0.645$ as well as $n = 6$ obtaining $\xi_R = 0.646$, using six iterations, like in the case of $n = 5$, where $\xi_R = 0.670$ was obtained. Using $n = 4$ spins and seven iterations, a minimal value of $\xi_R = 0.684$ results from the optimization. Note that the direction of Squeezing is completely free here, and is part of the optimization. Here, the previous trend of preferably even numbers of involved nuclear spins can not be fully confirmed. Moreover, it is interesting to observe how strongly the optimal squeezing can change with the number of iterations.

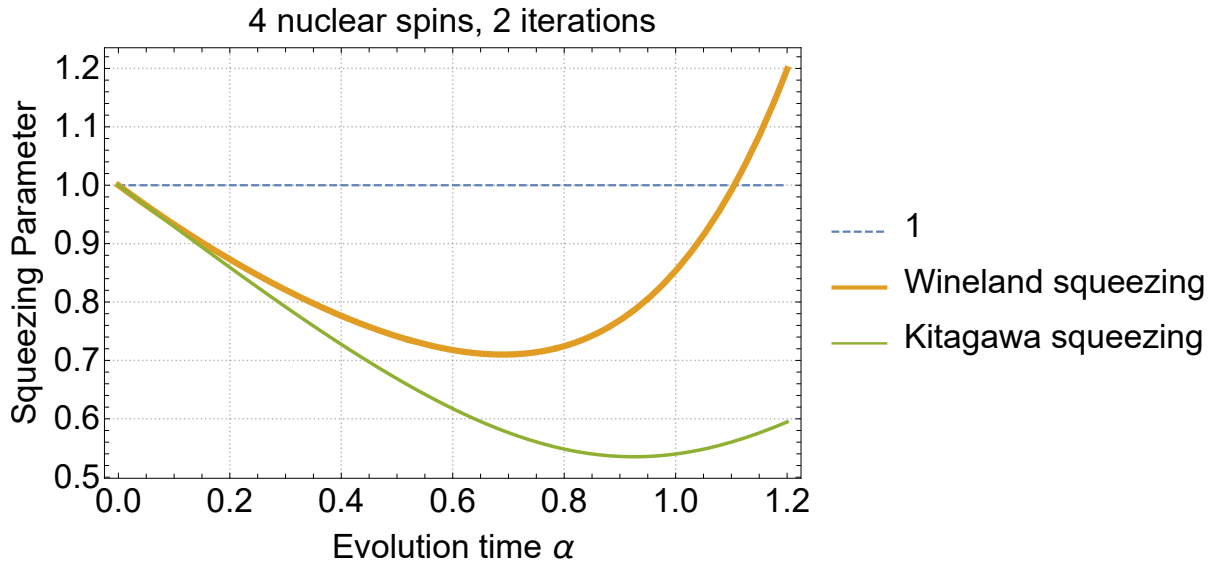


Figure 2.32: Direct comparison between the Squeezing Parameters ξ_R defined by Wineland (2.53) and ξ_q defined by Kitagawa and Ueda (2.52) in a specific numeric example ($n = 4$ spins, $p = 2$ iterations) following the introduced sequence in (2.63). Note that lower values indicate higher amounts of Squeezing. While all other parameters are fixed by numerical optimization, the parameter α of the first free evolution is varied. Even though the goal function of the optimization was the parameter ξ_R introduced by Wineland (orange curve), the parameter ξ_q by Kitagawa and Ueda (green curve) displays more squeezing. ξ_R by Wineland is thus a stricter measure of Squeezing in this case and could be preferable in a realistic setting.

2.8.4 The Squeezed Nuclear Spin Register as a Coprocessor for the Electron Spin Sensor

The squeezing sequence introduced above in (2.63) is here adapted and rewritten in terms of Quantum Gates in order to come closer to an experimental implementation of squeezing nuclear spins. In order to optimize the sensitivity of a single NV's electron spin to external fields, we propose to repeatedly map the phase collected by the electron spin onto the squeezed register of nuclear spins, followed by a collective readout. In order to map the phases to the nuclear spins, the electron is reinitialized once in state $|0\rangle$. A sequence of $C_nNOT_{el} - R_z^{(el)}(\tau) - C_nNOT_{el}$ then has the same effect as a single qubit z-rotation on the nuclear spin.

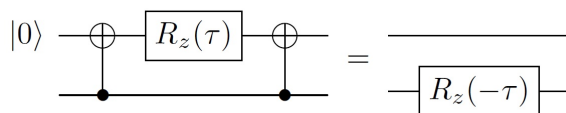


Figure 2.33: Quantum Circuit to illustrate the mapping of a phase collected by the electron spin onto a single nuclear spin. Using two CNOT gates with an intermediate phase collection on the NV electron spin is equal to mapping the inverse phase directly on the nuclear spin.

This equivalence also holds when the scheme is extended to several nuclear spins which are each subjected to the same sequence after a single reinitialization of the electron spin. Therefore, the operation on the nuclear spins is equal to

$$\bigotimes_k e^{i\sigma_z^{(k)}\phi} = e^{i\sum_k \sigma_z^{(k)}\phi} = e^{iI_z\phi}. \quad (2.67)$$

Where we have used $[\sigma_z^{(j)}, \sigma_z^{(k)}] = 0$. Consequently, the nuclear spins experience a collective rotation, if the phase ϕ is identical in each step as assumed above. In effect, the described operation thus yields a direct phase accumulation in the nuclear spin register

$$\tilde{\rho}_n(\phi) = e^{-iI_z\phi} \rho_n e^{iI_z\phi}. \quad (2.68)$$

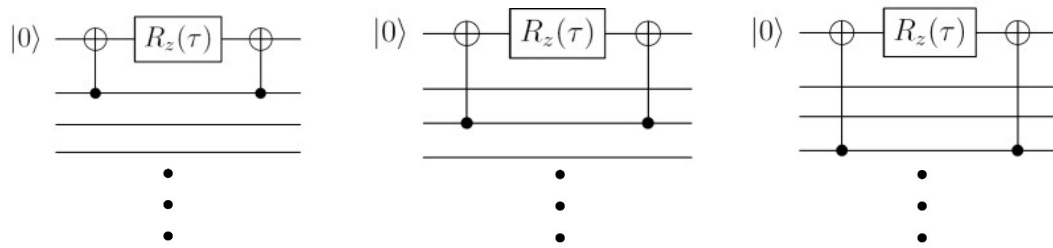


Figure 2.34: Sequential mapping of phases collected individually by the NV electron spin, onto nuclear spins. The individual mapping operations are done as in Figure 2.33. Here, the successive mapping on different nuclear spins is illustrated.

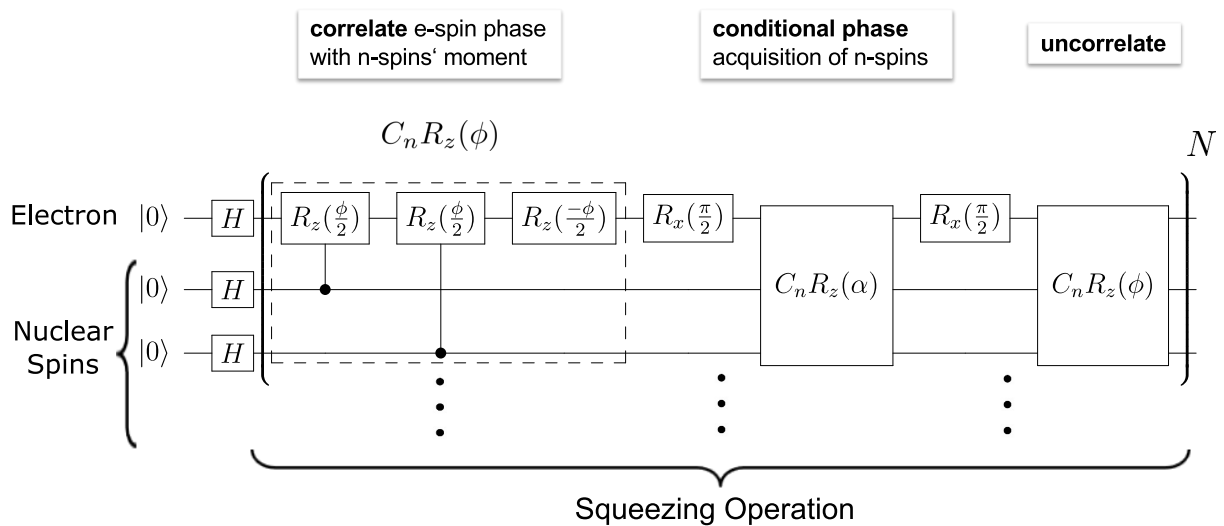


Figure 2.35: Proposed total operation in Quantum Gate notation for squeezing of nuclear spins surrounding an NV-Center. Note the similarities to the sequence before in Figure 2.27, including the commenting text for the collective operations, above the Quantum Circuit. The notation with experimentally realizable Quantum Gates aids in potential conduction of experiments.

2 Quantum State Engineering

A sensed phase is thus mapped sequentially to each individual nuclear spin. The different nuclear spins are correlated during the total operation, leading to a nuclear spin squeezed state. When measuring each individual nuclear spin state, a correlation between the nuclear spins is expected to be translated into a more precise measurement of the total inflicted phase ϕ .

Interferometric improvements are then canonically quantified by the sensitivity [45]

$$\delta\phi = \sqrt{\frac{1}{n} \frac{(\Delta I_z)^2}{(\partial_\phi \langle I_z \rangle)^2}}. \quad (2.69)$$

Here however, we first introduce an a priori benefit factor b which reflects the competition between the squeezing factor and the measurement signal available from the squeezed nuclear spins. We obtain the Signal to Noise Ratio (SNR)

$$\frac{S}{N_{sqzd}} = \frac{2 \langle I_x \rangle}{\xi \sqrt{N}} \quad (2.70)$$

We want to compare this SNR with the standard shot-noise limit [75]

$$\frac{S}{N_{std}} = \frac{2 \langle I_x \rangle}{\sqrt{N}} \xrightarrow{\langle I_x \rangle = \frac{N}{2}} \sqrt{N} \quad (2.71)$$

and define a benefit factor b that is one when reaching the shot-noise limit and greater than one for when going beyond such that we arrive at

$$b \equiv \frac{2 \langle I_x \rangle}{\xi N}. \quad (2.72)$$

When optimizing this factor numerically upon application of the introduced sequence, we see in Figure 2.36 an increase with increasing numbers of spins and can clearly demonstrate that surpassing the shot-noise-limit ($b = 1$) is possible.

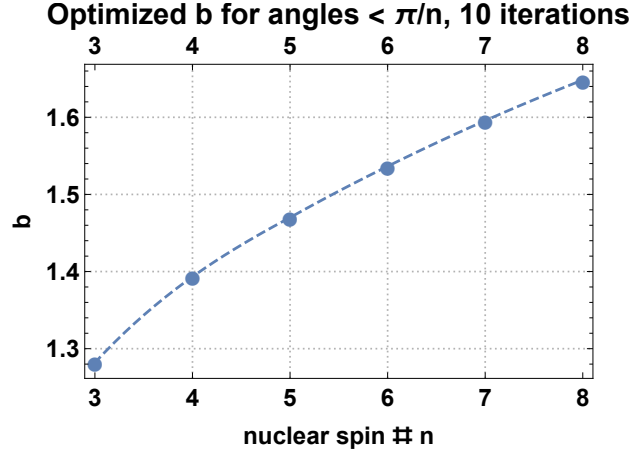


Figure 2.36: Numerical Optimization of the benefit factor b introduced in (2.72) for up to eight nuclear spins. The number of iterations is fixed to ten and the involved angles (evolution times) α and ϕ are chosen suitably small ($< \pi/n$) for experimental implementations. $b > 1$ indicates that sensing beyond the shot-noise limit is possible. The benefit factor is observed to increase with the number of involved nuclear spins.

2.8.5 Robustness of the Nuclear Spin Squeezed State against Decoherence

One of the central benefits of Spin Squeezed States is their stability under decoherence. Indeed, numerical calculations show a sensitivity beyond the shot-noise limit, even in the presence of decoherence (Figure 2.37). Since the coherence times of the nuclear spins are much longer ($\sim 1\text{ms}$) than those of the NV electron spin ($\sim 200\mu\text{s}$) [33], we can assume dephasing on the electron spin alone such that the density matrix of the composite system after preparation of the squeezed state becomes, in a simple dephasing model, decreasing the off-diagonal elements of the electron spin density matrix as

$$\rho(t) = \frac{1}{2} \begin{pmatrix} 1 & e^{-\gamma t} \\ e^{-\gamma t} & 1 \end{pmatrix} \otimes \rho_n. \quad (2.73)$$

2 Quantum State Engineering

In addition to the previous definition of sensitivity (2.69), for the presented experimental scenario of individually controllable nuclear spins, an experimentally more accessible [72] operator is instead defined as

$$O \equiv \bigotimes_k \sigma_x^{(k)} \neq \sum_k \sigma_x^{(k)} \quad (2.74)$$

such that the Sensitivity is redefined in terms of this operator, yielding

$$\delta\phi_O \equiv \frac{\Delta O}{\left| \frac{\partial \langle O \rangle}{\partial \phi} \right|}. \quad (2.75)$$

In a numerical simulation, this sensitivity is calculated for different values of the dephasing factor. Sensitivity beyond the shot-noise limit is demonstrated in Figure 2.37.

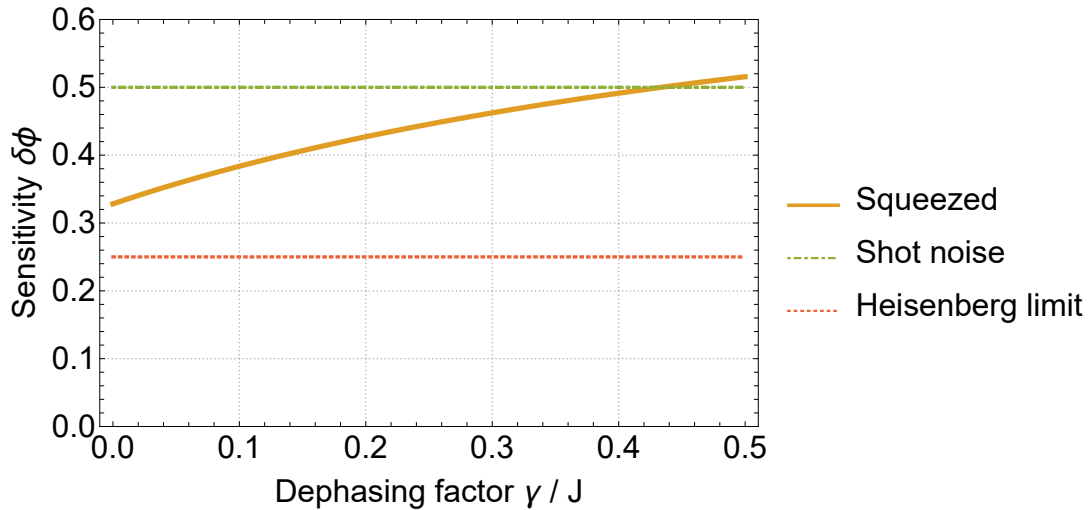


Figure 2.37: Sensitivity of a Nuclear Spin Squeezed state composed of $n = 4$ nuclear spins, compared to the shot-noise limit and the Heisenberg limit. The phase inflicted on the nuclear spins according to (2.68) is assumed as $\phi \approx \frac{2\pi}{5}$, while the evolution times are fixed to $\pi/2$ and π , respectively. Qualitatively, the shot-noise limit is clearly beaten, while for larger dephasing factors (γ defined in (2.73)), the sensitivity naturally starts to worsen such that the shot-noise limit may no longer be achieved.

2.8.6 Analytical Model of Nuclear Spin Squeezing in Fock Basis

Since the numerical model grows exponentially with the number of nuclear spins, it is beneficial to obtain an analytical model. We thus analyse the dynamics in the basis of Fock states, where m is the number of excitations in the given state, while n represents the number of involved spins, such that $n/2$ is the maximum number of excitations for a spin- $1/2$ system [76]. The operation on the nuclear spins can thus be written in terms of the excitations m such that

$$e^{if(I_z)t} \sum_{m=-n/2}^{n/2} c_m \left| \frac{n}{2}, m \right\rangle = \sum_{m=-n/2}^{n/2} e^{if(m)t} c_m \left| \frac{n}{2}, m \right\rangle \quad (2.76)$$

The prefactor c_m is generally fixed here as

$$c_m = \sqrt{\binom{n}{m + \frac{n}{2}}} \cdot 2^{-n}, \quad (2.77)$$

where the parentheses denote the binomial coefficient in this case. For $n=4$, the effect of the optimal sequence coincides with an interesting class of states given by $f(m)=|m|$, which even yields better squeezing than a quadratic Hamiltonian for low spin numbers. We define four different functions $f(m)$ of interest for the evolution in (2.76).

$$\begin{aligned} f_{|m|} &= |m| \\ f_{m,\text{linear}} &= m \\ e^{if_{m,\text{sequence}}} &= \frac{1}{2} \left(e^{imt} + 2i \cos(mt) - 1 \right) \\ f_{m,1a} &= m^2. \end{aligned} \quad (2.78)$$

Where $f_{|m|}$ is the described curious function agreeing with the results from evolution of the standard one-axis twisting Hamiltonian $f_{m,1a}$ as in (2.54) for small spin numbers. The function $f_{m,\text{sequence}}$ is constructed to reflect the effects of the introduced sequence, while $f_{m,\text{linear}}$ is just introduced for reference and does not induce squeezing. The results of a numerical simulation of the above functions for squeezing in the Fock basis are displayed in Figure 2.38. Moreover, in this framework,

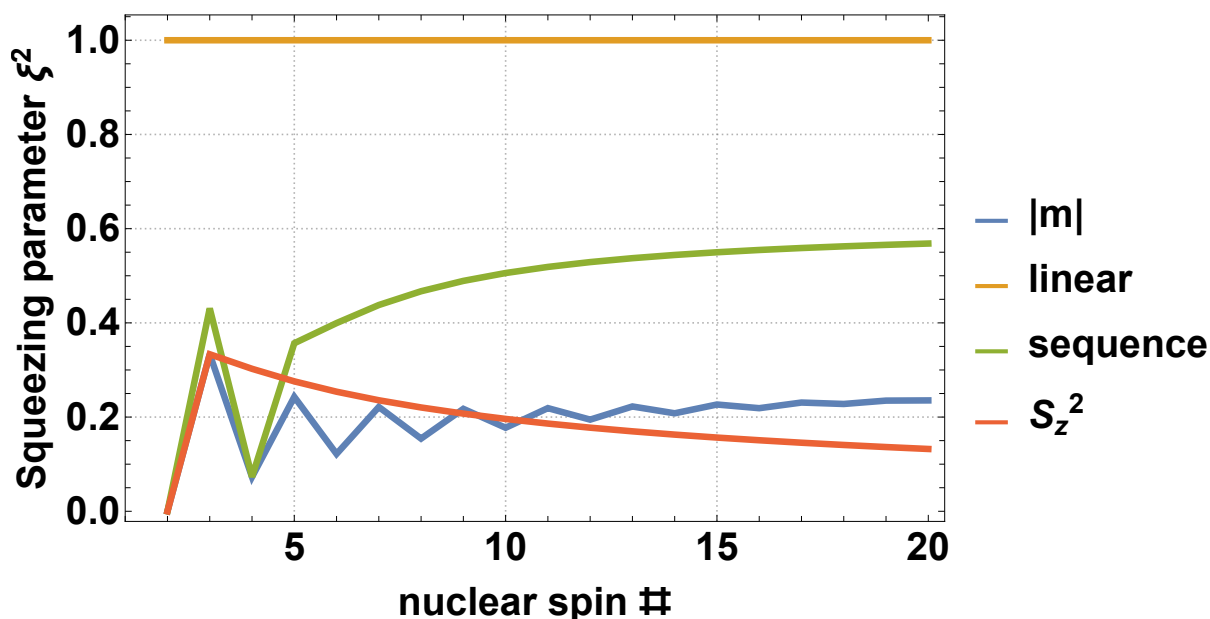


Figure 2.38: Comparison of different squeezing mechanism, as defined in (2.78) with analytical expression in a Fock basis for up to twenty spins. The time evolution is according to equation (2.77) with $n = 4$ nuclear spins and evolution times are numerically optimized in each case with the boundary condition $0 \leq t < \pi$ such that the squeezing parameter $\tilde{\xi}_q$ (2.65) is minimized. Note that for lower spin numbers, the sequence (green curve) and the exotic $|m\rangle$ interaction (blue curve) are advantageous, while the one-axis twisting Hamiltonian (S_z^2 , red curve) is preferable for higher spin numbers.

dephasing is introduced by

$$\rho \mapsto \sum_{m,m'} c_m c_{m'}^* e^{-\gamma|m-m'|} |m\rangle \langle m'| \quad (2.79)$$

and a comparison is made between a global maximally entangled state and a squeezed state stemming from the $f_{|m|}$ function introduced above, in terms of reachable sensitivity in Figure 2.39, compared to shot-noise limit and Heisenberg limit. Note that the fully entangled GHZ state [1] allows a sensitivity reaching the Heisenberg limit, as expected. An interesting literature observation at this point is that even scaling beyond the Heisenberg limit has been theorized [75].

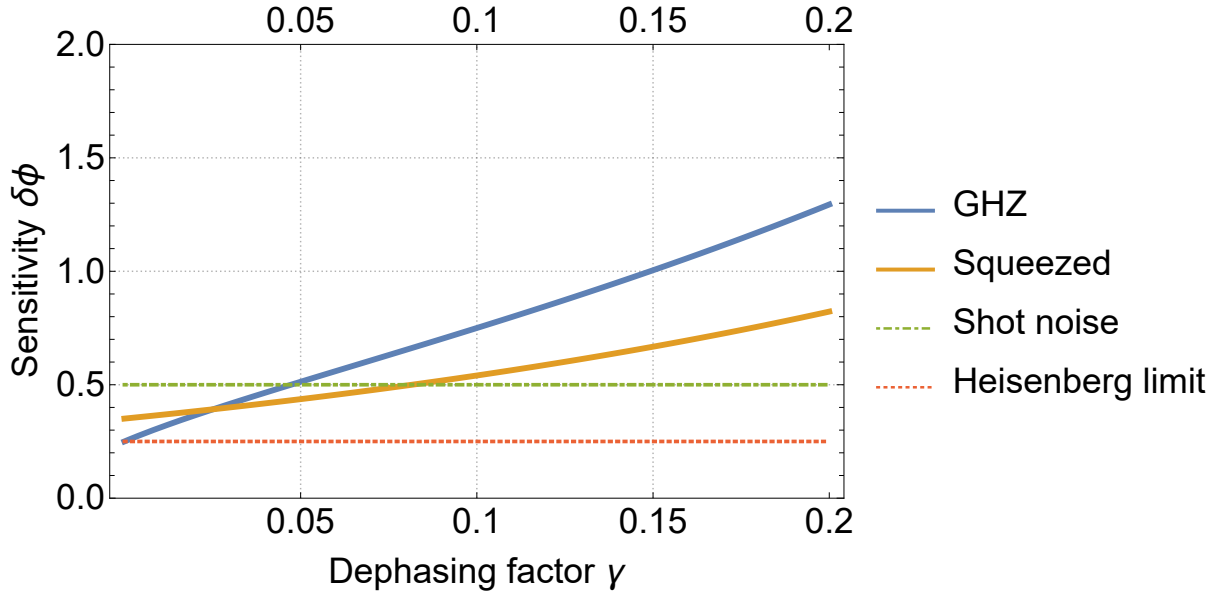


Figure 2.39: A GHZ state and a squeezed state are compared under dephasing by (2.79) in terms of the Sensitivity in (2.75). The great benefit of Squeezed States is visible here, namely the robustness against Decoherence, compared to otherwise preferable fully entangled state. The squeezed state is here created by the $f_{|m|}$ interaction from (2.76) and the inflicted phase is set to $\phi \approx \pi/4$. Note that the GHZ state (blue curve) starts at the Heisenberg limit, but is quickly outdone by the Squeezed State (orange curve), as the dephasing parameter γ rises.

2.8.7 Outlook and Possible Improvements for Nuclear Spin Squeezing

We have seen a proposal for a NV nuclear spin squeezed state at room temperature and found that sensitivity beyond the shot noise limit is possible, even in the presence of decoherence. An experimental realization has not yet been carried out presently, to my knowledge, but is possible due to short process times. Dynamical decoupling can further extend the coherence time T_2 [77]. Possible improvements of the performed simulations include scaling up nuclear spin and electron spin numbers with realistic parameters, accompanying a possible experiment. In particular, when coupling several NV electron spins, surrounded by nuclear spins as in Figure 2.40, for the pur-

2 Quantum State Engineering

pose of Sensing with the aid of Spin Squeezed Nuclear Spin states, collective improvements in sensitivity can be expected and theoretical questions can be answered. In particular, a surely very challenging – due to low-noise requirements in the experimental setup – but unquestionably impactful demonstration would be to examine sensitivity beyond the Heisenberg-limit by interacting probes [75, 78].

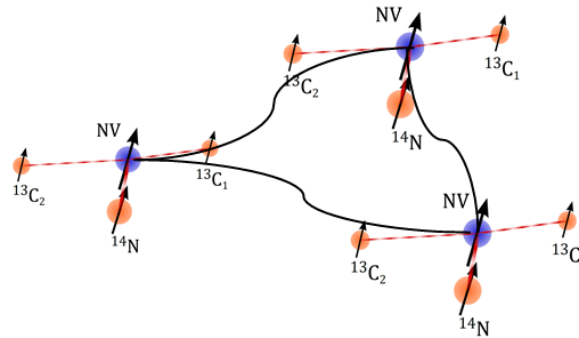


Figure 2.40: Illustration of the proposed coupled NV electron system with surrounding nuclear spins for Interferometry with nuclear spin squeezed states. While individual electron spins aided by nuclear spin states can reach sensitivities beyond the shot-noise limit and just short of the Heisenberg limit as in Figures 2.37 and 2.39, an even greater gain in sensitivity is possible by interacting probes [75, 78], combined with nuclear spin assisted sensing [4, 25].

2.8.8 Spin Squeezing with NV Ensembles

Due to the experimental accessibility, Nuclear Spin Squeezing of the nuclear spin entities surrounding an individual NV center was first introduced here. However, for more applicable sensing purposes such as sensing of magnetic fields [27] or electric fields [79, 80], it is preferable to use ensembles of NVs. Within such ensembles, NVs are not controlled individually, but collective operations by different geometries of wires for applying microwave control fields are possible [81]. In the following, a literature analysis and initial preparation of experiments for Spin Squeezing with

NV ensembles is therefore presented. In particular, a proposal paper by Cappellaro and Lukin [6] is examined and its potential implementation discussed, accompanied by additional simulations and work towards producing the right diamond sample to use for such experiments and sensitivity enhancements. In particular, given the daunting engineering work of noise reduction is suitably enabled, a further improvement of the subpicotesla sensitivity of a magnetic Quantum Sensor based on NVs reported by Wolf et al. in [27] is possible.

We begin by discussing the basic mechanism and requirements laid out in the proposal in [6]. Therein, in particular an implementation of the canonical One-Axis Twisting Hamiltonian (2.54) and the Two-Axis Countertwisting Hamiltonian (2.59) is sought. Let me stress again that – as outlined in Section 2.8.2, in [82] and briefly mentioned in [6] – while the introduced proposal mainly focuses on these particular Hamiltonians, any Hamiltonian describing the Correlation of several spins is in principle a good candidate in order to create Spin Squeezing. The main concept of the proposal in [6] is a mechanism to create Spin Squeezing by introducing a preferred direction within a three-dimensional dipolar coupling scenario involving the angular momenta of individual NV centers denoted as \vec{S} . This is done by using particular decoupling sequences in which the time evolution of one direction of the coupling (here the z-z interaction) is evolved slightly longer, by a time $\tau + \epsilon$, as highlighted in Figure 2.80. An approximate One-Axis Twisting Hamiltonian is then achieved as

$$H_{1a,H} = \epsilon H_{zz} + H_H \equiv \epsilon \sum_{l,j} d_{lj} S_{z,l} S_{z,j} + d_{lj} \vec{S}_l \cdot \vec{S}_j, \quad (2.80)$$

where d_{lj} are the dipolar coupling parameters among the spins and \vec{S} are the spin operators. In particular, following an earlier publication [83], a suitable collective subspace is chosen to ensure the creation of correlations while generally disordered couplings are present. Here, the subspace $m = N/2$ is chosen. So, the most significant term for the evolution of Spin Squeezing is the projection of the H_{zz} part of the Hamiltonian treated as a perturbation, onto this manifold.

$$\mathbf{P}_{N/2}(H_{zz}) = \frac{D}{N-1} \left(J_z^2 - \frac{N}{4} \mathbb{1} \right), \quad (2.81)$$

2 Quantum State Engineering

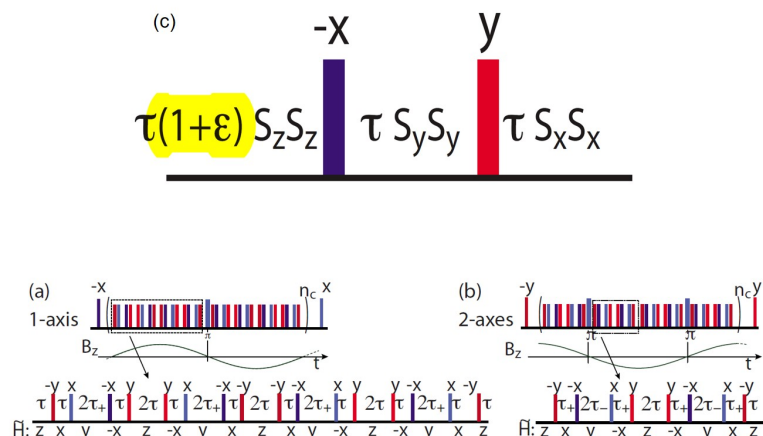


Figure 2.41: Decoupling sequences for Spin Squeezing of NV ensembles introduced by Cappellaro and Lukin in [6]. Images are directly adapted from [6]. Highlighting and arrangement mine. Note in particular the highlighted prolongation of the evolution time for one preferred coupling direction within the decoupling sequence in (c). τ_{\pm} in (a) and (b) qualitatively denotes the same time modification by $\tau \pm \epsilon$.

where N is the number of involved spins, J_z is the total angular momentum in z direction and D is the average dipolar coupling under the condition $D = \frac{1}{N} \sum_{l,j} d_{l,j} \gg 0$. Note that the factor $\frac{1}{4}$ is missing in [6]. This is by no means a severe mistake since the prefactor of the identity operator ($\mathbb{1}$) does not contribute to the dynamics. However the observation can be confirmed by explicitly calculating the part of the Hamiltonian with $J = N/2$ as

$$\begin{aligned}
 H_{zz} &= \sum_{j,l} d_{lj} S_{z,l} S_{z,j} = \sum_l \sum_{j \neq l} d_{lj} S_{z,l} S_{z,j} + \sum_{j=l} d_{lj} S_{z,l} S_{z,j} \\
 &= \frac{\sum_{j,l} d_{lj}}{N(N-1)} \sum_l S_{z,l} (J_z - S_{z,l}) + H_{(J \neq \frac{N}{2})} = \frac{D}{N-1} (J_z^2 - \frac{N}{4} \mathbb{1}) + H_{(J \neq \frac{N}{2})}.
 \end{aligned} \tag{2.82}$$

Having established the basic mechanism for squeezing NV spin ensembles, we now turn to the conditions for a successful implementation of this protocol. Firstly, since a projection to the $J = N/2$ subspace is considered to be the crucial part of the dynamics, a sufficient energy gap E_g between the associated energy level manifold to other manifolds is necessary, as illustrated in Figure 2.42

2.8 Squeezed Spin States

a) [83]. Additionally, in a realistic scenario, for dynamics to be rightly described by a dipolar coupling Hamiltonian as (2.80), dipolar couplings must be the dominating interaction and particularly, nuclear bath effects should be the dominating noise, which also signifies that a low number of P1 centers [33] should be present [6]. Very notably, the proposal also requires a rather low number of involved NV electron spins ($N \approx 10^2$) and a good conversion efficiency f of NV centers from single Nitrogen defects during fabrication, in order to reach suitable sensitivities [6]. This is illustrated in Figure 2.42 b).

As these conditions for a successful experiment are quite demanding, we further investigate what kind of diamond sample could fulfil the requirements.

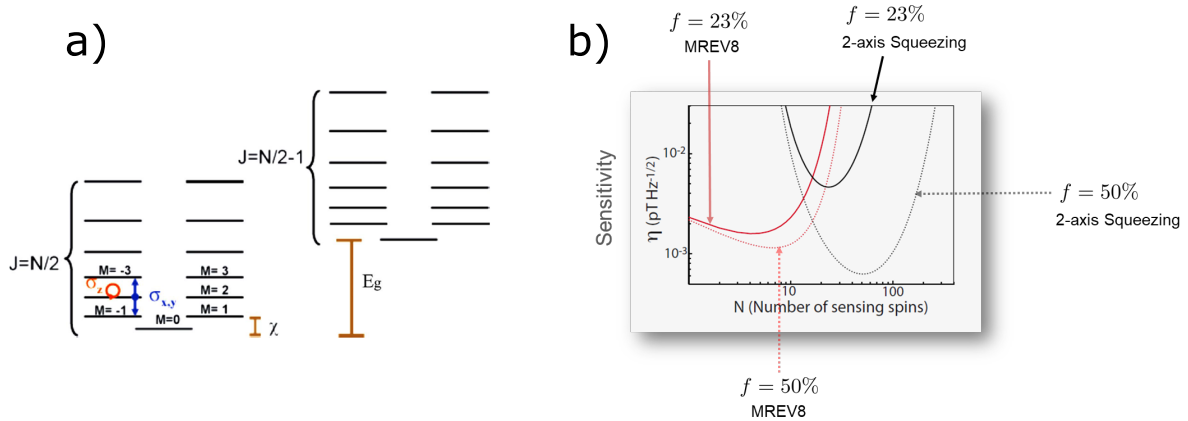


Figure 2.42: Conditions for Spin Squeezing with NV ensembles as proposed by Cappellaro and Lukin in [6]. The left image (a) is directly adapted from [83], referenced as well in [6], from which (b) is directly adapted with added comments. (a) displays the necessity of a suitable energy gap E_g between the energy level manifolds $J = N/2$ and $J = N/2 - 1$, for the projection in (2.81) to be the dominating term. On the right hand, (b) signifies reachable (preferably low) Sensitivity versus the number of sensing NV centers, which is notably small. Moreover, sensitivities for different decoupling sequences introduced in [6] are given, assuming different conversion efficiencies f during fabrication of NV centers, as specified in the added labels.

2.8.9 Diamond Samples and Coupling Geometries Suitable for NV Ensemble Spin Squeezing

Given the restraining conditions introduced in the previous section, we here elaborate on which constellations of NV ensembles are suitable for Spin Squeezing. While usual NV ensemble experiments involve a number of NV spins at the order of $N \approx 10^4 - 10^6$, a much smaller number of $N \approx 10^2$ is required here. This could be achieved by either addressing sub-regions of involved NV spins by sophisticated decoupling protocols, e.g. spins with uniform coupling frequencies, opening up a whole set of needed developments to obtain Spin Squeezing. Alternatively, a specific diamond sample could be fabricated in order to maximize the average dipole-dipole coupling D , as in equation (2.81) which can likely average out in a sample with randomly distributed NVs in terms of orientation and placement. While a random spin orientation is generally possible for the implementation of [6], a non-vanishing D is critical. Moreover, the energy gap E_g , see Figure 2.42, has to be maximized. While preferential growth [84] of NV centers is surely helpful for this requirement, sophisticated methods to place the involved NVs at certain lattice spaces may also be needed. In order to improve our understanding on the required coupling geometries and placements of the involved NV spins, we analyse possible coupling configurations arising for NVs in a diamond lattice in general. For this purpose, a simulation of the diamond lattice including NV centers in all possible orientations was carried out. Diamond unit cells were thus arranged in a spherical manner, in order to find regions of identical couplings, as in Figure 2.43, for increasing distances and thus the generally obtainable coupling frequencies can be calculated as displayed in Figure 2.44.

Preferable Geometries of NVs for Ensemble Spin Squeezing. We see from the obtained coupling frequencies between individual NVs in diamond that there is a diverse landscape of possible coupling frequencies, such that a carelessly chosen diamond sample would likely not fulfil the conditions for Spin Squeezing according to [6], especially the requirement for the total dipolar

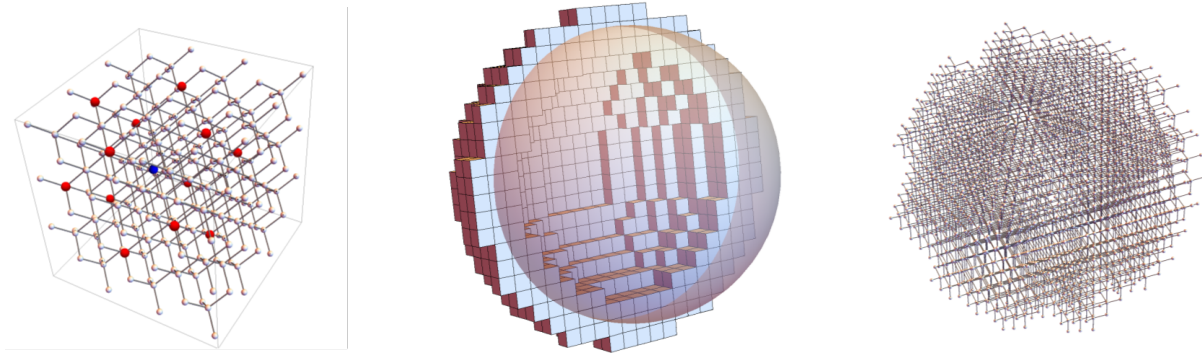


Figure 2.43: Schematic Illustration of the method used to calculate coupling frequencies between NV centers in diamond, with diamond unit cells arranged in a spherical manner. From left to right, a display of several diamond unit cells with one central NV center (blue) and several other possible NV sites (red), from which the occurring couplings are inferred. The middle image shows the “squaring of the sphere”, i.e. an approach to construct unit cells around a central NV in such a way that nearly identical couplings can be found in a certain radius. The right image shows a 3D-illustration of an approximately spherical diamond obtained from this method. Resulting coupling frequencies are shown in Figure 2.44.

coupling $D = \frac{1}{N} \sum_{l,j} d_{l,j} \gg 0$. Moreover, NVs generally appear in several different orientations within the diamond lattice, further cancelling out dipolar moments in three dimensions, illustrated in Figure 2.45. So, carefully engineered diamond samples featuring Quasi-2D-regions of NV electron spins are instead proposed, such as portrayed on the right side of Figure 2.45. A volume of $300\text{nm}^2 \cdot 10\text{nm}$ is proposed in [6] as a suitable size of such a sample, whose fabrication would require involved implantation techniques [85, 86]. Alternatively, instead of focusing on fabrication techniques, addressing sub-regions of spins would also be possible by external control, such as magnetic field gradients [30, 87].

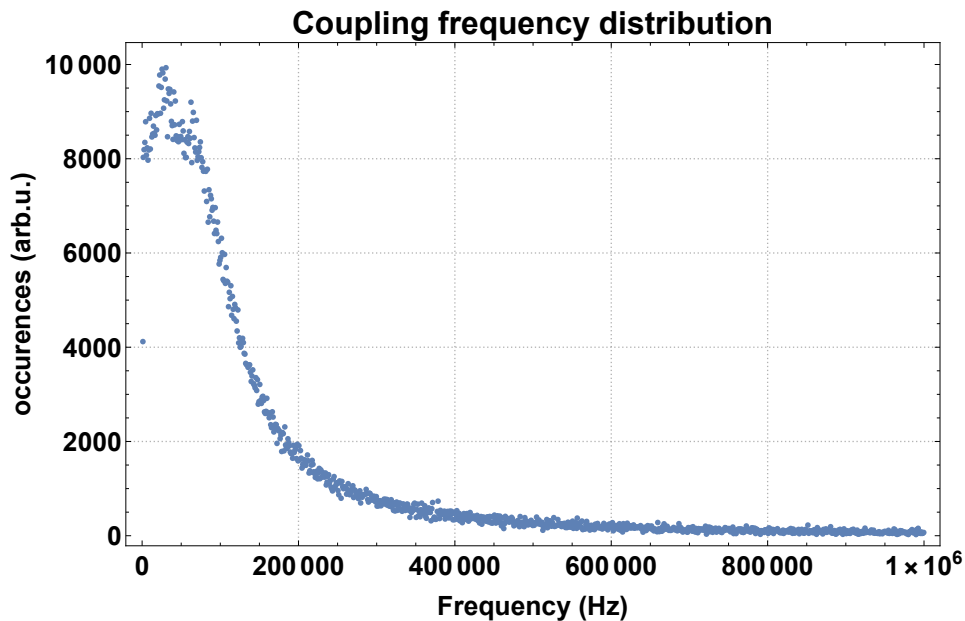


Figure 2.44: Possible occurrences of coupling frequencies within an ensemble of NV centers distributed in three dimensions, for all possible orientations and lattice sites in a distance of up to 1024 diamond unit cells from a central NV. Note especially the inhomogeneity of couplings for the involved discussion. Couplings are binned in this graph, such that the diversity of possible coupling frequencies is even underestimated. Extending the simulation beyond the calculated radius of up to 1024 diamond unit cells would result in a sharper peak of lower coupling frequencies.

Alternative Ways to achieve Spin Squeezing. Further alternatives to sophisticated fabrication or involved external control techniques include the transfer of already squeezed states. Initially inspired by a footnote in [58] (Footnote 14), several approaches to direct absorption of correlated states are finally listed here. Firstly, the collective absorption of squeezed light is possible, with the benefit that there is no need to transfer single photon information, as in previous low temperature experiments with NV centers [88]. Instead, the transfer of correlations between photons onto spins by collective absorption has already been demonstrated with atoms [61, 89, 90]. This should also be possible using NV centers, due to the presence of polarization-dependent transitions [91].

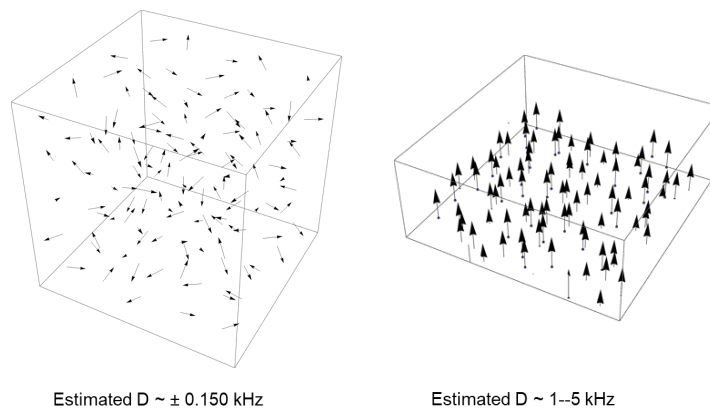


Figure 2.45: Exemplary three-dimensional geometries of NV Centers and resulting total dipolar coupling D as proposed for experiments to investigate possibilities of Spin Squeezing with NV ensembles. NV centers are randomly distributed within a cubic geometry with different NV orientations (left image) and in the described Quasi-2D-region within a three-dimensional sample (right image). Importantly, the total dipolar coupling is significantly higher in the Quasi-2D case, noted below the images.

While arbitrary polarization-squeezed states of light can be used, following the cited approaches, a more fundamental – and little-studied – alternative investigation would be to consider the effects of absorbing Phase-Amplitude Squeezed Light [92]. Moreover, absorption of squeezed microwaves is a possibility, as polarization-squeezing of microwave photon has been demonstrated [93, 94]. However a challenge here is that squeezed microwaves are usually obtained at mK temperatures. Further alternatives include Squeezing by controlled dissipation [92, 95, 96] or by a piezoactive layer [97]. Finally the perspective of involving nuclear spins in NV Spin Squeezing, either by actively using their individual couplings at low temperature, or by Squeezing the nuclear spin register through control of a single NV electron spin as introduced in the previous sections from 2.8.3, should not be forgotten.

2.9 Conclusion: Quantum State Engineering

Several concepts to create and make use of specific Quantum States were presented in this chapter. A method to create pairwise entangled states, generalizable to further states of interest by repeated projections of a Central Spin was introduced in Section 2.1. The possibility to even purify completely mixed states was highlighted (2.2) as well as the benefits in terms of Monogamy of Entanglement and Quantum Sensing enhancements resulting especially from pairwise entangled Singlet States (2.3). Varied coupling geometries with different dimensionalities of nuclear spins surrounding an NV Center in diamond were analysed (2.4) as well as methods to scale up simulations of these nuclear spins to large spin numbers (2.5). Existing and proposed experiments using the introduced method were briefly discussed (2.6), accompanied by applications to other physical systems such as Transmon qubits (2.7). Methods and theoretical preparations for future experiments implementing Spin Squeezing haven then been introduced (2.8), with particular focus on both Squeezing of nuclear spin states (2.8.3) and Spin Squeezing within NV ensembles (2.8.8). Particularly, Spin Squeezed States as a valuable resource in presence of Decoherence have been outlined (2.8.5).

There are thus several uncommon approaches beyond usual pulse sequences, in order to create correlated states, which can then be used as a resource in protocols for Quantum Sensing or Quantum Algorithms in general. While we have focused on Entangled States and Spin Squeezed States here, in the following we will also discuss more a more exotic version of entanglement called Bound Entanglement. The role of measurements has already played a role by using secondary effects such as measurement-back-action and induced Purification of previously mixed states by repeated Projections. We will continue on this path by examining the phenomenon of Quantum Contextuality and the possibility of an experimental observation thereof using NV-Centers. The overarching topic of the following chapter will be the use of high-dimensional quantum systems which enable the observation of said particularities of Quantum Information Processing.

3 Multiple Quantum levels or Qudits

“We always have had . . . a great deal of difficulty in understanding the world view that quantum mechanics represents . . . every new idea, it takes a generation or two until it becomes obvious that there’s no real problem. It has not yet become obvious to me that there’s no real problem. I cannot define the real problem, therefore I suspect there’s no real problem, but I’m not sure there’s no real problem.”

-Richard Feynman-

Qubits, i.e. quantum mechanical two-level systems, are surely the dominating quantum system used in modern Quantum Information Processing. However, besides the obvious increase of dimensionality for the resources of Superposition and Entanglement, higher-dimensional systems such as Qutrits (three-level systems) or generalized Qudits (n-level systems), also enable the observation of phenomena which are inaccessible in a single two-dimensional system. A single Qutrit enables measurements of the phenomenon of Quantum Contextuality [2] and fully entangling the Hilbert spaces of two Qutrits allows to observe so-called Bound Entanglement [51, 98], a curious kind of entanglement which can not be converted to regular entangled states. The fact that the NV center in diamond is a natural spin-1, i.e. a Qutrit, thus provides a somewhat hidden opportunity to observe fundamental quantum mechanical properties on the one hand, and could provide unexpected and largely unexplored resources for Quantum Information Processing on the other hand, since both Quantum Contextuality and Bound Entanglement have been shown to be useful in Quantum Technology for Certification and Security [8, 99], Heisenberg-limited Sensing [100]

3 Multiple Quantum levels or Qudits

and Entanglement Activation [98, 101], rather than just being interesting theoretical phenomena. Initially inspired by the paper “Quantumness of spin-1 states” [102], I conceived that the simple presence of three or more levels in a Quantum System may present a valuable resource for Quantum Information Processing and started the investigation presented in the following, on how this quantum resource can be beneficially used in the case of the natural Spin-1 systems occurring in NV-Centers.

3.1 Bound Entanglement

The definition of entanglement proves to be non-trivial for higher-dimensional quantum systems [20, 103], especially in the case of mixed quantum states, fulfilling $\text{Tr}(\rho^2) < 1$, where commonly used entanglement measures fail [103]. Bound Entanglement is a special kind of entanglement of mixed states, which can indeed not be converted (‘distilled’) to entanglement of pure states in singlet form [104]. In terms of physical relevance, the quantum system with minimal dimensionality in order to observe Bound Entanglement is the space of two Qutrits, i.e. a coupled Quantum System of two Spin-1 entities, as present in the case of NV-Centers. A further motivation for the experimental preparation of Bound Entangled states is the fact that, unlike early assumptions which deemed these states as useless for Quantum Technology, Bound Entanglement was found to be a useful Quantum Resource for several protocols in Quantum Information Processing [98, 105–108], while non-Distillability was found to be related to irreversibility in Thermodynamics [109, 110]. Significantly for the application to NV-Centers, Bound Entanglement has also been theoretically demonstrated to enable Quantum Sensing up to the Heisenberg-limit [100, 111].

The discussion in the following sections presents work towards an experimental observation of Bound Entanglement in a solid-state system. Bound Entanglement is related to the Peres-Horodecki criterion [112], also known as Positive Partial Transpose (PPT) criterion, as we will outline below.

To begin the revision of Bound entanglement, we define the notion of a partial transpose by

$$\rho^{T_B}(\rho) \equiv (\mathbb{1}_A \otimes T)(\rho), \quad (3.1)$$

where T is a transposition operator, solely acting on the subspace B of a combined density matrix $\rho \in \mathcal{H}_A \otimes \mathcal{H}_B$. For separable states, the partial transpose can also be obtained by partial tracing

$$\rho^{T_B}(\rho) \stackrel{\rho = \rho_A \otimes \rho_B}{=} \text{Tr}_B(\rho) \otimes (\text{Tr}_A(\rho))^T \quad (3.2)$$

Since the transposition preserves eigenvalues and as $\rho \geq 0$ is a condition on Eigenvalues of any physical density operator, it makes sense to investigate whether the density matrix of a subsystem is still physical after transposition. This motivates the Peres-Horodecki criterion [112]

$$(\rho = \rho_A \otimes \rho_B) \Rightarrow \underbrace{(\rho^{T_B}(\rho) \geq 0)}_{\text{PPT Criterion}}. \quad (3.3)$$

It is also indicated in (3.3) that separability implies satisfaction of the PPT criterion, following trivially from (3.2). For two-Qubit and Qubit-Qutrit states the logical implication in (3.3) can also be reversed, such that the PPT criterion is a sufficient condition for separability in this specific case. This does not hold for higher dimensions [104]. Instead, for two Qutrits and for density matrices of even higher dimensions, it has been shown that states exist which are inseparable despite the fact that they satisfy the PPT Criterion [104]. These states are called bound entangled states, since they can not be distilled, i.e. converted to pure entangled singlet states by local operations and classical communication (LOCC) [104].

In fact, while the PPT criterion is sufficient in order to prove that a state is bound entangled, if it is also non-separable, it is an open problem whether the converse is also true. It is currently not known whether there are bound-entangled states which are provably non-distillable, but possess a non-positive partial transpose (NPT) [113]. A further interesting observation is that, due to the fact that copies of a matrix ρ with positive Eigenvalues and positive partial transposes will still be

3 Multiple Quantum levels or Qudits

positive, such that the same properties of ρ are also maintained by

$$\rho^{\otimes N} = \underbrace{\rho \otimes \dots \otimes \rho}_N. \quad (3.4)$$

I.e., even N copies of a bound entangled state will remain bound entangled and are not distillable to pure entangled singlet states by LOCC [104]. We have thus established the concept of Bound Entanglement and move on towards criteria in order to measure and make use of this curious kind of entanglement.

3.2 Measuring Bound Entanglement in two-Qutrit Systems

In order to progress further towards an experimental implementation, criteria must be defined what kind of states can be considered Bound Entangled. While the Positive Partial Transposition is accessible after experimental reconstruction of a density matrix, a simple trial-and-error sampling of states obtained from density matrix tomography would not only be time-consuming but is also prone to systematic errors [56], caused by a bias due to the assumption of positive semi-definite density matrices a priori [114]. While this presents a general problem in density matrix tomography, it is especially significant in the case when positivity is the deciding criterion for Bound Entanglement. So, a family of target states to reach in experiments, which contain quantifiable amounts of Bound Entanglement were defined in [113]. Indeed, the publication in [113] is likely the first entanglement quantification for PPT-entangled states. The target states considered for the analysis of Bound Entanglement [113] are given for clarity in their explicit two-Qutrit matrix form

3.2 Measuring Bound Entanglement in two-Qutrit Systems

here as

$$\rho_{\text{target}}^{\diamond} = \frac{\mathbb{1}}{9} + \begin{pmatrix} \alpha & 0 & 0 & 0 & \beta & 0 & 0 & 0 & \beta \\ 0 & -\frac{\alpha}{2} - \gamma & 0 & 0 & 0 & 0 & 0 & 0 & 0 \\ 0 & 0 & \gamma - \frac{\alpha}{2} & 0 & 0 & 0 & 0 & 0 & 0 \\ 0 & 0 & 0 & \gamma - \frac{\alpha}{2} & 0 & 0 & 0 & 0 & 0 \\ \beta & 0 & 0 & 0 & \alpha & 0 & 0 & 0 & \beta \\ 0 & 0 & 0 & 0 & 0 & -\frac{\alpha}{2} - \gamma & 0 & 0 & 0 \\ 0 & 0 & 0 & 0 & 0 & 0 & -\frac{\alpha}{2} - \gamma & 0 & 0 \\ 0 & 0 & 0 & 0 & 0 & 0 & 0 & \gamma - \frac{\alpha}{2} & 0 \\ \beta & 0 & 0 & 0 & \beta & 0 & 0 & 0 & \alpha \end{pmatrix}, \quad (3.5)$$

where $\alpha, \beta, \gamma \in \mathbb{R}$ are free, real parameters which define Bound Entanglement according to [113]. Notice that there are only very few (six) off-diagonal elements consistent of the free parameter β . While it is very helpful to know what kind of states to aim for in experiments, engineering these particular states with a very limited protected subspace is experimentally hard. Conference discussions surrounding the proposal paper by Sentís [113] lead to a refined, experimentally more accessible joint publication targeted towards measurements with NV-Centers [114]. In particular the question which candidate states are most suitable in order to experimentally verify bound entanglement is addressed by introducing states that have a large enough distance to non-physical, distillable and separable states.

Here, a family of candidate states is introduced in a similar manner to (3.5) as

$$\rho = a |\phi_3\rangle\langle\phi_3| + b \sum_{k=0}^2 |k, k \oplus 1\rangle\langle k, k \oplus 1| + c \sum_{k=0}^2 |k, k \oplus 2\rangle\langle k, k \oplus 2| \quad (3.6)$$

with $|\phi_3\rangle = \sum_{k=0}^2 |kk\rangle / \sqrt{3}$, while $a, b, c \in \mathbb{R}$ are free parameters [114]. In order to specify the suitability of these states for robustness of bound entanglement detection in experiments, a ball of

3 Multiple Quantum levels or Qudits

states is introduced according to the Hilbert-Schmidt norm $\|X\|_2 = \sqrt{\text{Tr}(X^\dagger X)}$

$$\mathcal{B} \equiv \rho + rX \quad (3.7)$$

$$\forall X :: \|X\|_2 = \sqrt{\text{Tr}(X^\dagger X)} \leq 1,$$

with a real parameter $r \geq 0$ [114]. This enables to check the criteria of PPT (3.3), as well as to verify that the state is entangled at all, here by resorting to the measure of the Computable Cross Norm Criterion (CCNR), introduced by Gühne and Tóth in [115].

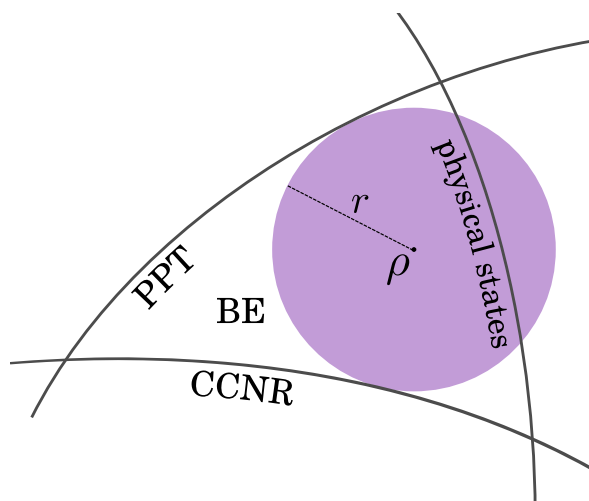


Figure 3.1: Illustration of the ball of states with radius r (3.7) in terms of the Hilbert-Schmidt norm $\|X\|_2 = \sqrt{\text{Tr}(X^\dagger X)}$, in order to identify bound-entangled states, starting from a well-defined family of states (3.6). PPT signifies the Positive Partial Transpose Criterion (3.3), which is sufficient to ensure bound entanglement (BE), as long as the states in question are entangled at all, as verified by the Computable Cross Norm Criterion (CCNR) [115] in this case. The third line symbolizes the physical states, fulfilling $\rho \geq 0$ and $\text{Tr}(\rho) = 1$, which is not assumed a priori. This concept is introduced in our publication in [114], in which the illustration also appears.

Experimental Scenarios for Bound Entanglement Measurements using NVs

Two-Qutrit scenarios necessary for the verification of bound entanglement with the families of candidate states introduced in (3.6) from [114] arise when considering the negatively charged NV^- , a natural spin 1 system, i.e. a solid state Qutrit [33]. Bipartite entanglement between two qutrits or subspaces thereof has been experimentally demonstrated in two scenarios: Firstly, two separate NV^- can be entangled by using either direct dipolar interaction at room temperature [116] or by indirect single-photon mediated entanglement swapping at cryogenic temperatures [117]. Secondly, the NV^- electronic spin 1 within the vacancy can be correlated with the nuclear spin of the adjacent Nitrogen atom. This entanglement is mediated by hyperfine or dipolar interaction and is routinely used in experiments [42]. While entanglement of qubit-subspaces is known, techniques have to be developed in order to entangle the full qutrit space and to produce specific mixed states. There are several approaches to producing mixed states with NVs, as presented in the following. For proof of concept, it is sufficient to statistically prepare different pure states and conclude that bound entanglement was present from the measurement data. However, especially if bound entanglement should be used as a resource, e.g. for entanglement activation [98, 101] or Heisenberg limited sensing [100], it is worthwhile to examine dynamics that lead to the specific target states. This can be done by entangling to ancillary qubits, namely C^{13} nuclear spins in the diamond lattice followed by suitable non-local gates [72] and tracing out of the ancillary spins. Repeated projections of the NV electron spin and subsequent controlled preparation of specific mixed states, stopping short of full Purification – similar to the methods introduced in section 2.1 – can also be engineered to fit the necessary target states [46]. Another possibility is to introduce controlled channels of decoherence by varying external fields such as the laser used for initialization and readout [118], the external magnetic field and the radio frequency and microwave pulses used for spin manipulation. In particular, established concepts to experimentally dissipate an NV electron state in a controlled manner include illumination by orange laser light in addition to the green laser used for excitation, in order to repolarize the NV or even change its charge state between NV^- and NV^0 [118].

3 Multiple Quantum levels or Qudits

We have thus introduced the phenomenon of Bound Entanglement [104], discussed its potential use in Quantum Technology in general [98, 105–108] as well as Quantum Sensing in particular [100, 111] and pointed towards the analysis of candidate states for experimental verification of Bound Entanglement, as presented in equations (3.5) and (3.6) from our joint publication with Sentís et al in [114]. This presents a step towards the first experimental verification of Bound Entanglement in a solid-state system as well as the further analysis and use of Bound Entanglement as a Quantum Resource. A similar particularity of Quantum Mechanics, in the sense that its measurement is only accessible if the involved Quantum Systems at least have the dimensionality of Qutrits, is presented by Quantum Contextuality.

3.3 Quantum Contextuality

“Each new generation of students learns quantum mechanics more easily than their teachers learned it. The students are growing more detached from prequantum pictures. [...] Quantum mechanics will be accepted by students from the beginning as a simple and natural way of thinking, because we shall all have grown used to it. By that time, if science progresses as we hope, we shall be ready for the next big jump into the unknown.”

-Freeman Dyson-

The phenomenon of Contextuality is the logical description of the notion of a context for certain questions or, as equivalently formulated later on, for measurements and was first conceived by Specker. Starting from very fundamental questions about logic and the relation between different commuting or non-commuting implications between simple logical sentences, he defined sets of exemplary questions, in which the answer depends on the order of questions asked [119, 120]. Moreover, he was concerned about the possibility of mutually exclusive questions, which can not be asked at the same time without influencing each other [119]. Quantum Mechanics turned out to be the perfect physical theory for observation of such questions. Indeed, together with Kochen, a formalisation of Contextuality in Quantum Mechanics was successful, resulting in the Kochen-Specker theorem [121], which interestingly requires at least three quantum levels, i.e. a Qutrit, in order to be demonstratable in principle. From these first theoretical concepts, Quantum Contextuality has since proven to be experimentally measurable in Quantum Technology [2, 7, 122–126] and was identified as a useful resource in Quantum Computation with Qubits [127]. Quantum Contextuality is even identified as a candidate for the specific Quantum Resource supplying the ‘magic’ for Quantum Computation [128], i.e. the ingredient within Quantum Mechanics that essentially causes Quantum Computers to outperform their classical counterparts.

Tests of Quantum Contextuality are however non-trivial in the sense that assumptions on the measurements involved have to be carefully stated and followed during measurements in order to deal

3 Multiple Quantum levels or Qudits

with several potential loopholes such as Finite Precision and Compatibility [8, 129–132]. Therefore, in the case of NV-Centers, it is especially useful to consider experiments with a reduced set of assumptions and involved quantum systems. Quantum Contextuality experiments using NV-Centers have already been performed using several separated entangled qubits [126]. However, it is desirable to reduce the number of involved spin entities by performing either two-Qutrit measurements [132] or even, in the spirit of the original Kochen-Specker theorem [133] and with a reduced set of assumptions, direct verification of Contextuality in a single, indivisible Qutrit system [2, 134]. While similar experiments using NV-Centers have been performed [135, 136], a loophole-free verification of Quantum Contextuality or further use of Contextuality as a Quantum Resource, such as for Certification of a QRNG, has not yet been demonstrated with this physical system.

3.3.1 The Peres-Mermin Square

The basic concept of Quantum Contextuality is most readily understood by considering collective measurements on a two-qubit system, as introduced by Peres and Mermin [137, 138]. Their seminal works in 1990 have led to a canonical set of operators which define different contexts, now known as the Peres-Mermin Square, see Figure 3.2. Each row and each column in this square represent operators that are jointly measured. This means that after a projective measurement, which keeps the resulting quantum state alive, the next operator in the same row or column, i.e. in the same context, is measured. In the example of the set of operators in last column of the Square, two spin-1/2 particles are jointly measured in z-, x- and y-direction. Indeed the order of measurements does not matter, since the joint operators are commuting. This is an important property, since it would be no surprise if the outcomes would depend on the order of measurements or on the context, if the associated operators were non-commuting. Now, in order to illustrate the effect of Quantum Contextuality against a classical, predetermined measurement outcome, Peres and Mermin introduced the following calculation. The individual measurement outcome for each operator

$$\left[\begin{array}{ccc} \sigma_z \otimes \mathbb{1} & \mathbb{1} \otimes \sigma_z & \sigma_z \otimes \sigma_z \\ \mathbb{1} \otimes \sigma_x & \sigma_x \otimes \mathbb{1} & \sigma_x \otimes \sigma_x \\ \sigma_z \otimes \sigma_x & \sigma_x \otimes \sigma_z & \sigma_y \otimes \sigma_y \end{array} \right]$$

Figure 3.2: The Peres-Mermin Square, defining sets of commuting operators in its rows and columns which are jointly measured in projective measurements and thus define contexts for a test of Quantum Contextuality. [120, 137, 138]

O in the Peres-Mermin Square is $\langle O \rangle = \pm 1$. The product of the measurement outcomes in each column or row is denoted as C_i and R_i , respectively. These measurement outcomes of each context consisting of the operator sets in rows and columns is then multiplied such that the parameter

$$\mathcal{P} = C_1 C_2 C_3 R_1 R_2 R_3 \quad (3.8)$$

is obtained. In classical determinism, in which the measurement outcome would have been defined a priori, this product would always have to be $P_{\text{classical}} = 1$, since each individual outcome is multiplied twice, in a row or column and the individual outcomes are $\langle O \rangle = \pm 1$. Instead, in Quantum Mechanics, the overall product of the expectation values is $P_{\text{quantum}} = -1$. This is due to the commutation and anti-commutation rules of the involved Pauli Matrices, leading to the product rule

$$\sigma_a \sigma_b = \delta_{ab} I + i \varepsilon_{abc} \sigma_c. \quad (3.9)$$

Applying this to all sets of operators defined in the Peres-Mermin square (Figure 3.2) shows that all rows and columns but the last column yield the identity $\mathbb{1}$ when multiplied, except for the last column which yields $-\mathbb{1}$. In essence, the phenomenon of Quantum Contextuality uses the property of Quantum Mechanics, that jointly measured operators will always project the measured quantum states into their joint Eigenbasis. Compare, for example, the joint basis states of row one, in matrix

3 Multiple Quantum levels or Qudits

notation

$$\text{Basis}(R_1) = \left\{ \begin{pmatrix} 1 \\ 0 \\ 0 \\ 0 \end{pmatrix}, \begin{pmatrix} 0 \\ 1 \\ 0 \\ 0 \end{pmatrix}, \begin{pmatrix} 0 \\ 0 \\ 1 \\ 0 \end{pmatrix}, \begin{pmatrix} 0 \\ 0 \\ 0 \\ 1 \end{pmatrix} \right\}, \quad (3.10)$$

to the basis of the last column

$$\text{Basis}(C_3) = \left\{ \begin{pmatrix} -1 \\ 0 \\ 0 \\ 1 \end{pmatrix}, \begin{pmatrix} 0 \\ 1 \\ 1 \\ 0 \end{pmatrix}, \begin{pmatrix} 1 \\ 0 \\ 0 \\ 1 \end{pmatrix}, \begin{pmatrix} 0 \\ -1 \\ 1 \\ 0 \end{pmatrix} \right\}. \quad (3.11)$$

The joint operator $ZZ = \sigma_z \otimes \sigma_z$ appears in both contexts, and the listed basis vectors in both cases are Eigenstates of this operator ZZ . The state resulting from a projective measurement of ZZ is thus projected into one of the basis sets in question by the other operators in the respective context. This simple observation forms the basis of Quantum Contextuality, but has profound implications for Quantum Technology [127, 128].

3.4 The KCBS inequality

Applied to a Spin-1 or three-level-system, a comparatively simple way was found for a test of Quantum Contextuality by Klyachko, Can, Binicioğlu and Shumovsky in 2008 [2]. The inequality found reduces the problem to the projective measurement of five operators, projectors corresponding to five pairwise orthogonal states which can be graphically represented in a pentagram as in the figure below. These operators are binary in the sense that the outcomes of a measurement are limited to the values $\{-1, 1\}$. The resulting inequality was subsequently named KCBS-inequality after the authors and has the simple form: [7]

$$\langle A_1 A_2 \rangle + \langle A_2 A_3 \rangle + \langle A_3 A_4 \rangle + \langle A_4 A_5 \rangle + \langle A_5 A_1 \rangle \geq -3 \quad (3.12)$$

3.4 The KCBS inequality

It is easy to verify the classical bound on the right hand side of (3.12), when assigning fixed classical values to individual operators combined with minimising the sum on the left hand side.

The operators are defined as

$$A_i = 2 |l_i\rangle \langle l_i| - \mathbb{1} \quad (3.13)$$

where the projectors

$$P_{1,i} = |l_i\rangle \langle l_i| , P_{2,i} = \mathbb{1} - |l_i\rangle \langle l_i| \quad (3.14)$$

are defined implicitly and associated with the measurement outcomes +1 and -1, respectively. The operators have the (cyclic) property:

$$\langle l_i | l_{i+1} \rangle = 0 \Rightarrow [A_i, A_{i+1}] = 0 \quad (3.15)$$

such that subsequent measurements always commute, which is a necessary requirement for any test of Contextuality. Remember that the essence of Contextuality is a dependence on the order in which operators are measured, which is already trivially given when operators are non-commuting. Here, the notion of a context is given by the pairs of observables in the KCBS-inequality (3.12), where each operator is included in two different contexts.

3 Multiple Quantum levels or Qudits

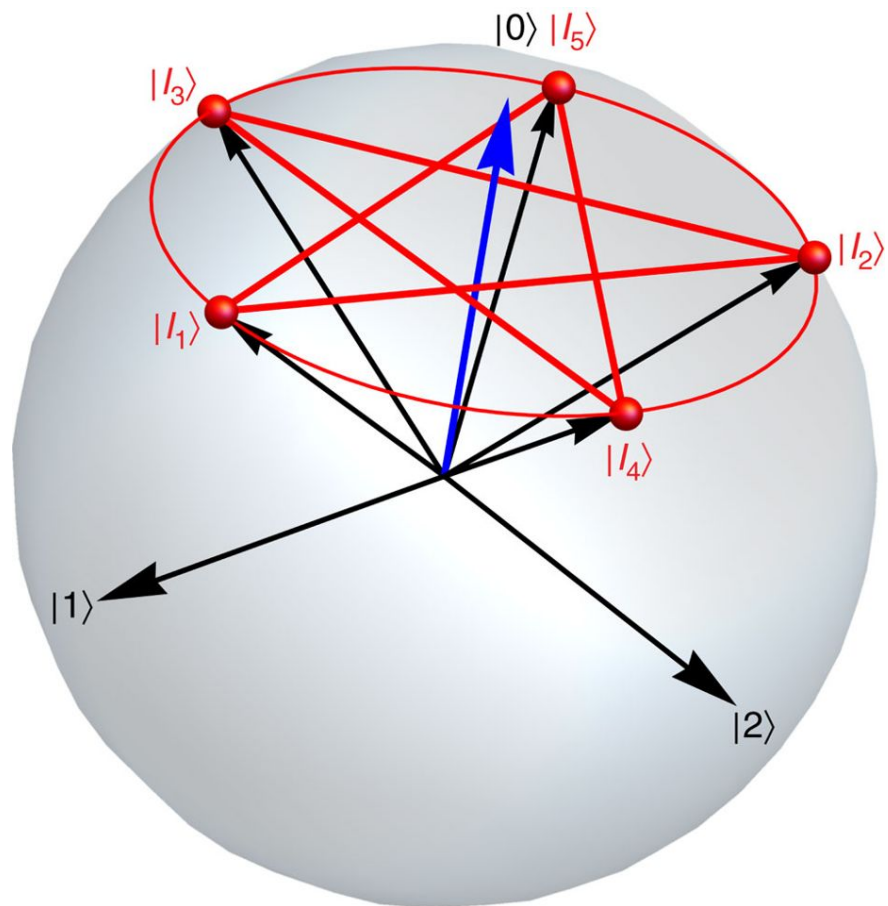


Figure 3.3: KCBS pentagram. The states $|i\rangle$ in the equations above form a pentagram when connecting pairwise orthogonal states. The corresponding observables build up the KCBS inequality as in equation (3.14). Illustration adapted from Jerger et al [7].

3.5 Experimental KCBS Inequality Violation

For practical Quantum Technology applications, in particular for the certification of Quantum Random numbers, it is of interest to use inequalities that are particularly simple in their conception. Therefore, more profound approaches such as state-independent inequalities [139] or inequalities using qudits of higher dimensions are less suitable than the KCBS inequality, which utilizes the minimal system possible to demonstrate Contextuality, namely a qutrit. Experimental demonstrations of the violation of this inequality by quantum mechanics have recently been shown using superconducting qubits [7, 140], single ions [141] and single photons [125]. Here, a realization with NV centers is proposed and tailored to the technological possibilities and challenges specific to this quantum system.

3.5.1 Proposal for an Implementation with NV centers

Besides the novelty of a loophole-free realization with NV centers – as opposed to previous related experiments [135, 136] – the main motivation to realize another experimental KCBS inequality violation is the vision to construct a certified Quantum Random Number Generator. Unlike other systems which have to operate at cryogenic temperatures (superconducting qubits) or at high vacuum (trapped ions), the NV can be operated at ambient conditions. Therefore, a practical and economical certified Quantum Random Number Generator is feasible. In comparison to other approaches, technological challenges are reduced and a single portable solution can be produced as opposed to approaches which rely on no-signalling and certification by Bell-like inequalities [142]. The specific steps and requirements for an implementation are described below.

3 Multiple Quantum levels or Qudits

Possible NV Setups for KCBS Inequality Violations

There are two basic requirements for a violation of the KCBS inequality:

1. Good experimental control of a three-level-system
2. The ability to perform projective measurements.

Both of these criteria can be satisfied when performing experiments with Nitrogen-Vacancy centers. There are two obvious possibilities to perform such a measurement, either at room temperature or in a low temperature setup.

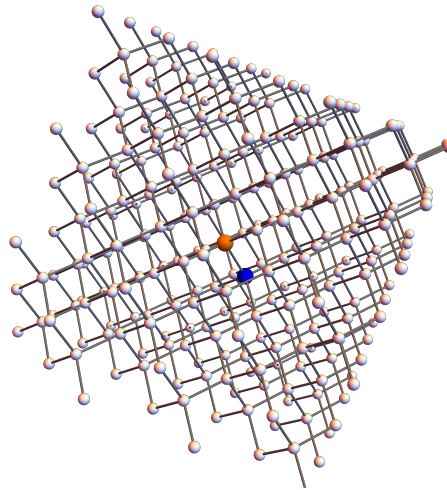


Figure 3.4: An NV^- center consisting of two spin-1 entities in a modified diamond lattice, namely the inherent electron spin of the Vacancy (blue), as well as the adjacent ^{14}N nuclear spin (orange); both spins can in principle be used for KCBS inequality violations by projective readouts.

Low Temperature Electron Single-Shot Readout It is possible to use the NV^- 's inherent electron spin 1 directly for projective readouts. With the help of a solid immersion lens and low temperature operation, the detected fluorescence and the coherence properties are controllable

3.5 Experimental KCBS Inequality Violation

as demonstrated by Robledo et al [143]. At room temperature, the necessary levels can not be resolved or addressed individually. A great advantage of using the NV's electron spin directly, however, is the conceptual advantage of using a natural spin 1 system, without further assumptions and qudit constructions.

Nuclear Spin Single-Shot Readout The preferred possibility, in terms of engineering overhead, is to make use of the NV center's inherent ^{14}N nuclear spin at room temperature. It has the desired property of the nuclear spin $I = 1$ and thus represents a qutrit or three-level system. Moreover, projective readout has been demonstrated as single-shot readout of the ^{14}N nuclear spin. The NV's inherent electron spin is used for readout and initialisation purposes through its coupling to the nuclear spin in a now standard procedure described in detail in a landmark paper by Neumann et al [42]. In the following, we assume this experimental situation for the measurement procedure.

3.5.2 The Problem of Maintaining Coherence in Quantum Measurements

One condition of projective measurements is that the sum of projection operators is the identity, also known as the completeness relation [41]

$$\sum_m M_m M_m^\dagger = \mathbb{1} \quad (3.16)$$

As the Kochen-Specker theorem demands at least three levels of the involved quantum system, the requirements in this case are either three one-dimensional projectors or one one-dimensional projector accompanied by a two-dimensional projector. For illustration, if we denote the involved levels as $| -1 \rangle, | 0 \rangle, | 1 \rangle$, a one-dimensional projector projects into exactly one of these levels as

$$P_1 = | 0 \rangle \langle 0 | \quad (3.17)$$

3 Multiple Quantum levels or Qudits

while a two-dimensional projector projects into the remaining two-dimensional subspace as

$$P_2 = |-1\rangle\langle -1| + |1\rangle\langle 1|. \quad (3.18)$$

Fundamental Treatment of the Coherence Question

A question of relevance for the measurement of a KCBS Inequality violation is whether it is possible in practice to implement a two-dimensional projector. To understand the discussed problem, consider the effect of a successful projection on the density matrix. If the projection is successful, i.e. $\langle\Psi|P_1|\Psi\rangle = \langle P_1\rangle = 1$, the resulting state will surely be exactly the eigenstate of the projector, here $|\Psi_{res}\rangle = |0\rangle$ and equivalently $\rho_{res} = |0\rangle\langle 0|$. In matrix notation this means that

$$\rho = \begin{pmatrix} R & * & * \\ * & R & * \\ * & * & R \end{pmatrix} \xrightarrow{\langle P_1\rangle=1} \begin{pmatrix} 0 & 0 & 0 \\ 0 & 1 & 0 \\ 0 & 0 & 0 \end{pmatrix} = \rho_{res} \quad (3.19)$$

Here, $R \in \mathbb{R}$ are real numbers, while $* \in \mathbb{C}$ are complex numbers. Obviously, the conditions $Tr(\rho) = 1$ and $\rho \geq 0$ still need to be fulfilled for the density matrices [41]. The crucial question is now, what effect the projection has in the case $\langle P_1\rangle = 0$, i.e. when the projection is not successful. Long before the possibility of experimental quantum mechanical measurements, this was also discussed as a Gedankenexperiment and fundamental question by von Neumann and Lüders who maintained two opposing views [47, 144]. Von Neumann was convinced that no coherence can be preserved after a measurement, i.e.

$$\rho = \begin{pmatrix} R & * & * \\ * & R & * \\ * & * & R \end{pmatrix} \xrightarrow[\text{von Neumann}]{\langle P_1\rangle=0} \begin{pmatrix} R & 0 & 0 \\ 0 & 0 & 0 \\ 0 & 0 & R \end{pmatrix} = \rho_{res}. \quad (3.20)$$

Note that the resulting density matrix is mixed and has no off-diagonal entries. This means that any superposition or coherence between the remaining levels $|-1\rangle$ and $|1\rangle$ is lost. In the case of

a projective measurement that maintains coherence, as promoted by Lüders [144], the effect is as follows

$$\rho = \begin{pmatrix} R & * & * \\ * & R & * \\ * & * & R \end{pmatrix} \xrightarrow[\text{Lüders}]{\langle P_1 \rangle = 0} \begin{pmatrix} R & 0 & * \\ 0 & 0 & 0 \\ * & 0 & R \end{pmatrix} = \rho_{res}. \quad (3.21)$$

Observe that the only entries vanishing are the ones associated to the eigenstate of the projector, $|0\rangle$, while the remaining subspace is left intact. Off-diagonal elements are still present and superposition between the remaining levels is thus preserved. While the preservation of these coherences was assumed necessary in some experiments [7], indeed the measurement of a subspace with reduced dimensionality is also sufficient [8,145], as independently verified in the following.

3.5.3 Measurement of One-dimensional projectors

In an actual measurement, it is very hard not to destroy off-diagonal elements of the system's density matrix when a projective measurement is performed. In the case of NV centers, a sequence of repeated interaction of the NV spin with green Laser light, accompanied by two-qubit gates, is necessary in order to perform one single-shot measurement of a nuclear spin [42]. Since the NV spin is brought up to its excited state in each readout, it introduces decoherence, even on the nuclear spin it is coupled to by dipole-dipole interaction. Therefore, a measurement resulting in a density matrix as in equation (3.21) seems impossible and was identified as an initial crucial problem in experimental KCBS inequality violation with NVs. It was understood that 2-dimensional projectors like P_2 in equation (3.18) could not be implemented successfully, which would pose a threat to the implementation of the KCBS inequality as a whole.

However, as initially pointed out by M. Kleinmann in private correspondence, it is sufficient to measure one-dimensional projection operators, as we will confirm in the following, directly from the inequality. By equations (3.13) and (3.14), each operator can be written solely in terms of the

3 Multiple Quantum levels or Qudits

one-dimensional projector as

$$A_i = 2P_{1,i} - \mathbb{1}. \quad (3.22)$$

Plugging this in to the KCBS inequality

$$\langle A_1 A_2 \rangle + \langle A_2 A_3 \rangle + \langle A_3 A_4 \rangle + \langle A_4 A_5 \rangle + \langle A_5 A_1 \rangle \geq -3 \quad (3.23)$$

yields an inequality in terms of one-dimensional projectors as

$$P_{1,1}P_{1,2} + P_{1,2}P_{1,3} + P_{1,3}P_{1,4} + P_{1,4}P_{1,5} + P_{1,5}P_{1,1} - \left(\sum_{i=1}^5 P_{1,i}^2 \right) \leq -2 \cdot \mathbb{1} \quad (3.24)$$

$$\Leftrightarrow \sum_{i=1, j=(i+1 \bmod 5)}^5 P_{1,i}P_{1,j} - \sum_{i=1}^5 P_{1,i} \leq -2 \cdot \mathbb{1} \quad (3.25)$$

Mathematically, this inequality is completely identical to the KCBS inequality, with the added benefit that it only contains the one-dimensional projectors $P_{1,i}$. We used $P_{1,i}^2 = P_{1,i}$, as for any projector. However, it can be useful in experiments to measure the same projector twice, in order to compare with the measurements of other contexts, especially in terms of repeatability of the individual measurements. Moreover, the positive terms on the left of the equations above should ideally be zero. This is obvious since the projectors project to pairwise orthogonal states, easy to see when the equation is again rewritten as

$$\sum_{i=1, j=(i+1 \bmod 5)}^5 |l_i\rangle \underbrace{\langle l_i | l_j \rangle}_{= 0 \text{ (ideally)}} \langle l_j| - \sum_{i=1}^5 |l_i\rangle \langle l_i| \leq -2 \cdot \mathbb{1}. \quad (3.26)$$

However, this mathematically vanishing overlap should necessarily be verified in experiments since it depends on the preparation and readout fidelity of the involved states.

In summary, this already provides an experimental concept on how to measure the violation of a KCBS inequality on an NV setup, by only measuring one-dimensional projectors according to equation (3.25). However, we will look at more details of the implementation and the involved unitary operations in particular in the following section.

3.5.4 Operations and Measurements to violate the KCBS inequality

In order to measure operators in different contexts, it has to be stressed that the operations have to be separate and measurements need to be projective. I.e., the qutrit states should not be destroyed during the measurement and the involved unitary operations should be seen as completely separate, withstanding the obvious temptation to combine two adjacent unitaries into one, as for example U^\dagger and V in the figure below. The most important point here is to avoid the loopholes of compatibility

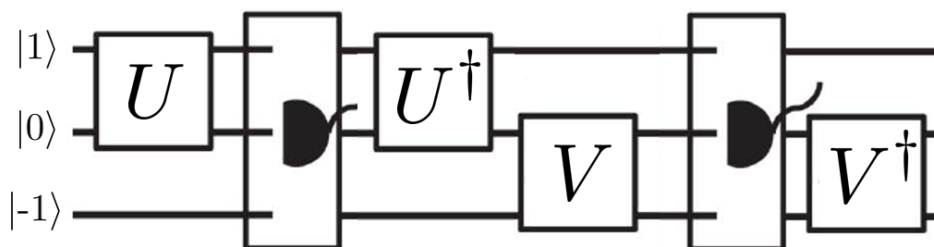


Figure 3.5: General procedure for a measurement of operators U and V in one context. Note that U^\dagger and V should not be combined in order to guarantee individual-existence. Also note that any rotation is reversed after the projective measurement to restart from the original basis. Illustration based on reference [8], modified.

and individual-existence, which would render the contextuality test useless as a whole, if its basic assumptions are not fulfilled [7]. Compatibility means that jointly measured operators always have to commute, which is diluted by experimental imperfections, leading to fundamental theoretical questions [146]. Individual-existence requires the projections to be meaningful as individual measurements, thus they are required to be completely separate from other measurements [7].

Necessary Unitary Operations

In order to realize the proposed experiment, it is surely helpful to have the required unitary operations ready at hand. In known implementations, two ways are presented to implement the

3 Multiple Quantum levels or Qudits

necessary unitary gates. While Jerger et al [7] optimize the problem numerically and find five suitable pentagram states, a careful analysis of Um et al [8] revealed fundamental theoretical problems concerning the involved states.

Unitary Operations according to Jerger et al

One possible choice of pentagram states is well defined in the reference of Jerger et al [7]. Each operation U_i is composed of two primitive rotations R_y^{01} and R_y^{12} which represent rotations in y -direction between two of the three involved levels. The operators are not explicitly defined in the publication but were reconstructed from the notation and verified in calculations as

$$R_y^{01} = \begin{pmatrix} \cos \phi_y & -\sin \phi_y & 0 \\ \sin \phi_y & \cos \phi_y & 0 \\ 0 & 0 & 1 \end{pmatrix}, \quad R_y^{12} = \begin{pmatrix} 1 & 0 & 0 \\ 0 & \cos \phi_y & -\sin \phi_y \\ 0 & \sin \phi_y & \cos \phi_y \end{pmatrix}. \quad (3.27)$$

The explicit construction of the involved unitaries is given in the figure below for completeness. Note that the numerically optimized rotation angle in R_y^{01} can be reconstructed by minimizing the pairwise overlap of the pentagram states to zero. Each pentagram state results from its respective unitary, applied to the basis state $|0\rangle$ which equals the vector $(1\ 0\ 0)^T$ in our matrix notation. It is easy to verify that the implicitly defined states do not overlap and are linearly independent, thus form a proper set of pairwise orthogonal qutrit states. The primitives in (3.27) are in general not hard to implement experimentally, since they only require transitions between two levels.

3.5 Experimental KCBS Inequality Violation

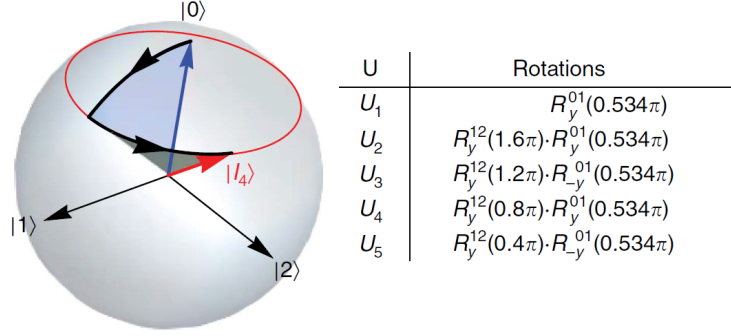


Figure 3.6: Explicit construction of the involved unitaries U_1 to U_5 in Jerger et al [7]. The image on the left shows the composed trajectory of the unitary U_4 as an example, which maps the basis state $|0\rangle$ to the fourth pentagram state.

Alternative Operations in Um et al

The following operations are suggested as primitives in Um et al [8], as they evolve naturally from Rabi oscillations in the trapped-ion context

$$\begin{aligned}
 R_1(\theta_1, \phi_1) &= \begin{pmatrix} \cos\left(\frac{\theta_1}{2}\right) & 0 & -ie^{i(\phi_1 + \frac{\pi}{2})} \sin\left(\frac{\theta_1}{2}\right) \\ 0 & 1 & 0 \\ -ie^{-i(\phi_1 + \frac{\pi}{2})} \sin\left(\frac{\theta_1}{2}\right) & 0 & \cos\left(\frac{\theta_1}{2}\right) \end{pmatrix}, \\
 R_2(\theta_2, \phi_2) &= \begin{pmatrix} 1 & 0 & 0 \\ 0 & \cos\left(\frac{\theta_2}{2}\right) & -ie^{i(\phi_2 + \frac{\pi}{2})} \sin\left(\frac{\theta_2}{2}\right) \\ 0 & -ie^{-i(\phi_2 + \frac{\pi}{2})} \sin\left(\frac{\theta_2}{2}\right) & \cos\left(\frac{\theta_2}{2}\right) \end{pmatrix}
 \end{aligned} \tag{3.28}$$

Note that the definition of R_2 is slightly different from the publication in [8], since a sign mistake therein would render it non-unitary. The actual operations used for the pentagram states set $\phi_i = 0$, thus effectively getting unitaries very similar to (3.27) as

$$R_1(\gamma, 0) = \begin{pmatrix} \cos\left(\frac{\gamma}{2}\right) & 0 & \sin\left(\frac{\gamma}{2}\right) \\ 0 & 1 & 0 \\ -\sin\left(\frac{\gamma}{2}\right) & 0 & \cos\left(\frac{\gamma}{2}\right) \end{pmatrix}, \quad R_2(\gamma, 0) = \begin{pmatrix} 1 & 0 & 0 \\ 0 & \cos\left(\frac{\gamma}{2}\right) & \sin\left(\frac{\gamma}{2}\right) \\ 0 & -\sin\left(\frac{\gamma}{2}\right) & \cos\left(\frac{\gamma}{2}\right) \end{pmatrix}. \tag{3.29}$$

3 Multiple Quantum levels or Qudits

Here, the angle of rotation is fixed as $\gamma = 51.83^\circ \approx 0.288\pi$. This angle is interestingly close to $\cos^{-1}(1/\phi)$, with the Golden Ratio $\phi = \frac{1}{2}(\sqrt{5} + 1)$. However, there is no justification for this particular choice of angle in the publication, there is also no relation to the angle used by Jerger et al [7], as above in Figure 3.6. The choice of pentagram states is summed up for clarity in Table 3.1. During careful analysis of the paper in reference [8], I noted a substantial notational or

| Pentagram state | (rotated) Basis state |
|-----------------|---|
| $ v_1\rangle$ | $ 1\rangle$ |
| $ v_2\rangle$ | $ 2\rangle$ |
| $ v_3\rangle$ | $R_1(\gamma, 0) 1\rangle$ |
| $ v_4\rangle$ | $R_2(\gamma, 0) 2\rangle$ |
| $ v_5\rangle$ | $R_1(\gamma, 0)R_1(\gamma, 0) 1\rangle$ |
| $ v'_1\rangle$ | $R_2(\gamma, 0)R_2(\gamma, 0) 2\rangle$ |

Table 3.1: Pentagram states used by Um et al [8] for an experimental test of Contextuality by KCBS-inequality violation. Note that an additional state $|v'_1\rangle$ is introduced for experimental convenience. Moreover this choice of pentagram states can not be recommended due to overlaps inconsistent with the assumptions of Contextuality, as described below.

operational problem in the definition of these pentagram states. From the matrix notation of the paper, it becomes obvious that $|1\rangle \equiv (0\ 0\ 1)^T$ and $|2\rangle \equiv (0\ 1\ 0)^T$. However, with this choice of basis states, it is easy to verify that pentagram states $|v_2\rangle$ and $|v_3\rangle$ show non-zero overlap and are thus not pairwise orthogonal as required. Therefore, all possible choices of initial basis states were analysed in the table in Figure 3.7, including all their pairwise overlaps, i.e. the dot product of neighbouring states. The last column of the table in Figure 3.7 shows these overlaps as elements of an overlap vector, including the cyclic overlap of $|v'_1\rangle$ and $|v_1\rangle$. This vector should indeed be composed of zeroes, as in the third row of the table, in order to guarantee the required properties for the involved pentagram states, especially the commutativity of the associated operators. However, this is not the case, even for any choice of basis states, except in row three. Here however, the set

3.5 Experimental KCBS Inequality Violation

| $ \nu_1\rangle$ | $ \nu_2\rangle$ | $ \nu_3\rangle$ | $ \nu_4\rangle$ | $ \nu_5\rangle$ | $ \nu_{i'}\rangle$ | $\{\nu_i \cdot \nu_{(i+1)}\}$ |
|---|---|--|--|--|--|--|
| $\begin{pmatrix} 1 \\ 0 \\ 0 \end{pmatrix}$ | $\begin{pmatrix} 0 \\ 1 \\ 0 \end{pmatrix}$ | $\begin{pmatrix} 0.899443 \\ 0 \\ -0.437037 \end{pmatrix}$ | $\begin{pmatrix} 0 \\ 0.899443 \\ -0.437037 \end{pmatrix}$ | $\begin{pmatrix} 0.617997 \\ 0 \\ -0.786181 \end{pmatrix}$ | $\begin{pmatrix} 0 \\ 0.617997 \\ -0.786181 \end{pmatrix}$ | $\begin{pmatrix} 0 \\ 0 \\ 0.191002 \\ 0.34359 \\ 0.61808 \\ 0 \\ 0 \end{pmatrix}$ |
| $\begin{pmatrix} 1 \\ 0 \\ 0 \end{pmatrix}$ | $\begin{pmatrix} 0 \\ 0 \\ 1 \end{pmatrix}$ | $\begin{pmatrix} 0.899443 \\ 0 \\ -0.437037 \end{pmatrix}$ | $\begin{pmatrix} 0 \\ 0.437037 \\ 0.899443 \end{pmatrix}$ | $\begin{pmatrix} 0.617997 \\ 0 \\ -0.786181 \end{pmatrix}$ | $\begin{pmatrix} 0 \\ 0.786181 \\ 0.617997 \end{pmatrix}$ | $\begin{pmatrix} 0 \\ -0.437037 \\ -0.39309 \\ -0.707125 \\ -0.485857 \\ 0 \\ 0 \end{pmatrix}$ |
| $\begin{pmatrix} 0 \\ 1 \\ 0 \end{pmatrix}$ | $\begin{pmatrix} 1 \\ 0 \\ 0 \end{pmatrix}$ | $\begin{pmatrix} 0 \\ 1 \\ 0 \end{pmatrix}$ | $\begin{pmatrix} 1 \\ 0 \\ 0 \end{pmatrix}$ | $\begin{pmatrix} 0 \\ 1 \\ 0 \end{pmatrix}$ | $\begin{pmatrix} 1 \\ 0 \\ 0 \end{pmatrix}$ | $\begin{pmatrix} 0 \\ 0 \\ 0 \\ 0 \\ 0 \\ 0 \\ 0 \end{pmatrix}$ |
| $\begin{pmatrix} 0 \\ 1 \\ 0 \end{pmatrix}$ | $\begin{pmatrix} 0 \\ 0 \\ 1 \end{pmatrix}$ | $\begin{pmatrix} 0 \\ 1 \\ 0 \end{pmatrix}$ | $\begin{pmatrix} 0 \\ 0.437037 \\ 0.899443 \end{pmatrix}$ | $\begin{pmatrix} 0 \\ 1 \\ 0 \end{pmatrix}$ | $\begin{pmatrix} 0 \\ 0.786181 \\ 0.617997 \end{pmatrix}$ | $\begin{pmatrix} 0 \\ 0 \\ 0.437037 \\ 0.437037 \\ 0.786181 \\ 0.786181 \\ 0 \end{pmatrix}$ |
| $\begin{pmatrix} 0 \\ 0 \\ 1 \end{pmatrix}$ | $\begin{pmatrix} 1 \\ 0 \\ 0 \end{pmatrix}$ | $\begin{pmatrix} 0.437037 \\ 0 \\ 0.899443 \end{pmatrix}$ | $\begin{pmatrix} 1 \\ 0 \\ 0 \end{pmatrix}$ | $\begin{pmatrix} 0.786181 \\ 0 \\ 0.617997 \end{pmatrix}$ | $\begin{pmatrix} 1 \\ 0 \\ 0 \end{pmatrix}$ | $\begin{pmatrix} 0 \\ 0.437037 \\ 0.437037 \\ 0.786181 \\ 0.786181 \\ 0 \\ 0 \end{pmatrix}$ |
| $\begin{pmatrix} 0 \\ 0 \\ 1 \end{pmatrix}$ | $\begin{pmatrix} 0 \\ 1 \\ 0 \end{pmatrix}$ | $\begin{pmatrix} 0.437037 \\ 0 \\ 0.899443 \end{pmatrix}$ | $\begin{pmatrix} 0 \\ 0.899443 \\ -0.437037 \end{pmatrix}$ | $\begin{pmatrix} 0.786181 \\ 0 \\ 0.617997 \end{pmatrix}$ | $\begin{pmatrix} 0 \\ 0.617997 \\ -0.786181 \end{pmatrix}$ | $\begin{pmatrix} 0 \\ 0 \\ -0.39309 \\ -0.270088 \\ -0.485857 \\ -0.786181 \\ 0 \end{pmatrix}$ |

Figure 3.7: All possible choices of pentagram states according the operations described in Um et al [8]. Overlaps are shown as elements of the vector in the last column and are found to be largely non-vanishing. The non-orthogonality of pentagram states poses a vital thread to the results obtained in the publication or at least suggests notation errors therein.

of basis states suffers from the problem of linear dependence, in this case even identity of the basis states, e.g. $|\nu_1\rangle = |\nu_3\rangle = |\nu_5\rangle$. This is of course also fatal for the test of Contextuality, since the associated operators then only form two different Contexts, instead of different Contexts for each pair, as required. No viable set of pentagram states could be constructed from the definitions in Um et al [8], according to equation (3.29) and Table 3.1.

Corrigendum of Um et al

During the course of writing of this thesis, the findings above were confirmed by the authors of reference [8]. Moreover a new approach focusing on Random Number Expansion was published at the time of writing [145]. The authors have since published a Corrigendum of [8], in which several fundamental notational mistakes were admitted [11]. In particular, the basis states outlined above in Table 3.1 were corrected as in Table 3.2. Moreover, the angle γ was corrected to $\tilde{\gamma} = 103.68^\circ$.

| Pentagram state | (rotated) Basis state |
|-----------------|---|
| $ v_1\rangle$ | $ 1\rangle$ |
| $ v_2\rangle$ | $ 2\rangle$ |
| $ v_3\rangle$ | $R_1^{-1}(\tilde{\gamma}, 0) 1\rangle$ |
| $ v_4\rangle$ | $R_1^{-1}(\tilde{\gamma}, 0)R_2(\tilde{\gamma}, 0) 2\rangle$ |
| $ v_5\rangle$ | $R_1^{-1}(\tilde{\gamma}, 0)R_2^{-1}(\tilde{\gamma}, 0)R_1^{-1}(\tilde{\gamma}, 0) 1\rangle$ |
| $ v'_1\rangle$ | $R_1^{-1}(\tilde{\gamma}, 0)R_2^{-1}(\tilde{\gamma}, 0)R_1^{-1}(\tilde{\gamma}, 0)R_2(\tilde{\gamma}, 0) 2\rangle$ |

Table 3.2: A corrected set of Pentagram states, published by Um et al in [11]. The matrix operations are defined as before in equation (3.29). Note that the angle γ is also corrected. Consequently, it was confirmed that the original publication in Scientific Reports [8] contained fundamental notational errors and can not be followed in future experiments. It is instead recommended to consider the Corrigendum in [11] or the correct implementation by Jerger [7].

In order to avoid mistakes in an experimental implementation, instead of following the original publication by Um et al. [8, 11], it is recommended to use the set of operations in Jerger et al. [7] as described above in subsection 3.5.4 and summarized in Figure 3.6.

In Summary, the concept of Quantum Contextuality was presented (Section 3.3), with a focus on experimental verification in a single indivisible Spin-1 system by the KCBS inequality (3.4). Moreover, the possibility to reduce this Inequality to measurements of 1-dimensional projectors,

3.5 Experimental KCBS Inequality Violation

see Equation (3.25), was introduced in Section 3.5.3. Comparable experiments using trapped ions and superconducting Qutrit were analysed (Section 3.5.4) in order to present the operations and measurements necessary for future experiments demonstrating and further using the resource of Quantum Contextuality.

3.6 Conclusion: Qudits

Motivated by the special properties of Spin-1 Quantum Systems [102], such as naturally occurring in the NV-Center in diamond and its inherent ^{14}N nuclear spin, two applications making use of this higher dimensionality, compared to commonly used Qubits, were proposed. Bound Entanglement was identified as an insufficiently demonstrated phenomenon of Quantum Mechanics, with recent results enabling its detection in the two-Qutrit case (Section 3.2). Moreover, theoretically established protocols making use of the resource of Bound Entanglement in Quantum Information Processing [105–108] and Quantum Sensing up to the Heisenberg-limit in particular [100, 111] were pointed out, such that the steps presented towards experimental implementations with NV-Centers may constitute valuable resources for future developments. In the case of Quantum Contextuality (Section 3.3), measures for experimental verification are better established than in the case of Bound Entanglement, such that several experiments have already been performed in optical, superconducting and trapped ion systems [7, 123, 125, 126, 145]. However, subtleties such as the avoidance of several loopholes [122, 132] and memory assumptions [147] were pointed out along with the benefits of using a well-controllable naturally occurring Spin-1 system such as the NV-Center in diamond. Preparation towards an experimental implementation using this physical system were thus presented in Sections 3.5ff. One of the possible applications of Quantum Contextuality as a resource, due to Inequalities such as the KCBS Inequality (Section 3.4), is the certification of Quantum Random Number Generation, which indeed presents the topic of the following chapter.

4 Quantum Random Number Generation

“Quantum mechanics is certainly imposing. But an inner voice tells me that it is not yet the real thing. The theory says a lot, but does not really bring us any closer to the secret of the "old one."

I, at any rate, am convinced that He does not throw dice.”

- Albert Einstein -

“You ought not to speak for what Providence can or can not do.”

- Niels Bohr -

In the Digital Age of Smartphones, Social Networks, Big Data, Cryptocurrencies, Industry 4.0 and the Internet of Things, Cryptography has developed from a profession of secret agencies, specialists and scientists to a field of high relevance for our daily lives and work. Digital data is everywhere, even in our pockets, and is often considered private or of special value to the holder. It is thus very relevant to consider new ways of encryption and secure communication. Quantum Technology promises to deliver new securities through Quantum Key Distribution and Quantum Random Number Generation. On the other hand, Shor’s algorithm famously proves that common prime number factoring algorithms can be broken with a fully-fledged Quantum Computer at hand [148]. Here, we focus on random numbers which are a crucial resource for classical encryption. Since any algorithm is per se deterministic, a random seed is always required to offer true protection against eavesdroppers. Recent studies have shown that the supply of random numbers with low entropy is a very effective attack on encryption, since the complexity of an attack

4 Quantum Random Number Generation

is dramatically reduced [149, 150]. Moreover, common classical, so-called True Random Number Generators (TRNG) suffer from inherent problems since the promised Randomness is often just based on ignorance of the underlying physics of a hardware Random Number Generator or is even provably deterministic as in the case of computer-based Pseudo Random Number Generators (PRNG) [151]. Unlike any such system governed by classical physics, Quantum Mechanics on the other hand promises indeed that – even with full knowledge of the underlying physics – the measurement results will be probabilistic and therefore yield random numbers with high entropy.

4.1 Certified Quantum Random Number Generation

Different experimental approaches, mainly in Quantum Optics, have been used as Quantum Random Number Generators (QRNG) [152–159]. However, one important drawback remains: It is difficult to prove that the specific implementation really corresponds to the modelled quantum random number generation. It has to be shown that quantum effects truly are the only source of randomness in the system, even in continuous operation and beyond any reasonable doubt. This leads back to the fundamental discussion in Quantum Mechanics, whether the seemingly probabilistic behaviour is actually governed by latent deterministic mechanisms called Hidden Variables. If this possibility can not be excluded for a particular system, QRNG are rightfully named device-dependent [160]. On the other hand, a violation of Bell-like classical inequalities offer the possibility of device-independent Quantum Random Number Generation [142, 161].

4.1.1 Quantum Indeterminism and Bell-like Inequalities

Albert Einstein famously assumed that the laws of physics should not be governed by randomness, illustrating his point by considering games of dice a non-godly behaviour [162]. This assumption lead physicists to look for a hidden mechanism or hidden variables explaining the phenomena of

4.1 Certified Quantum Random Number Generation

Quantum Mechanics, including superpositions and particularly entanglement [163]. However, it was shown decades later that classical inequalities based on the assumptions of hidden variables and an assignment of values prior to measurement can be violated by quantum mechanics [164]. Within the limitations of our understanding this indeed favours the interpretation that there is an inherently random aspect in Quantum Mechanics.

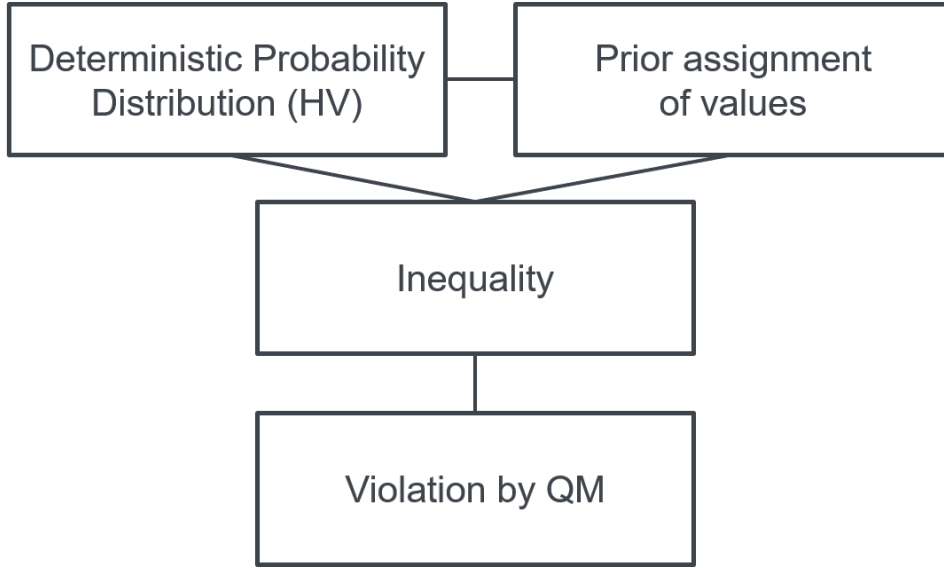


Figure 4.1: Schematic illustration of a Bell-like inequality violation based on deterministic assumptions and a priori assignment of values.

In order to illustrate the concept of Bell-like inequalities let us briefly review the basic concept of the CHSH inequality by Clauser, Horne, Shimony and Holt [165].

Let a, a', b and b' be real variable with a fixed (a priori) assignment that allows them to take exclusively the values -1 or $+1$.

$$\{a, a', b, b'\} \in \{-1, 1\}. \quad (4.1)$$

Then, it can be easily verified that the following (classical) inequality holds

$$\langle ab \rangle + \langle ab' \rangle + \langle a'b' \rangle - \langle a'b \rangle \leq 2. \quad (4.2)$$

4 Quantum Random Number Generation

However, in Quantum Mechanics we can define the following measurement operators on an entangled state $|\varphi^+\rangle$

$$\hat{A} = \sigma_x, \hat{A}' = \sigma_z, \hat{B} = \frac{\sigma_x - \sigma_z}{\sqrt{2}}, \hat{B}' = \frac{\sigma_x + \sigma_z}{\sqrt{2}}, |\varphi^+\rangle = \frac{|00\rangle + |11\rangle}{\sqrt{2}} \quad (4.3)$$

which leads to the expectation values

$$\langle \varphi^+ | \hat{A} \hat{B} | \varphi^+ \rangle = \langle AB \rangle = \langle AB' \rangle = \langle A'B' \rangle = -\langle A'B \rangle = \frac{1}{\sqrt{2}} \quad (4.4)$$

and therefore yields a violation of the classical inequality (4.2) by

$$\langle AB \rangle + \langle AB' \rangle + \langle A'B' \rangle - \langle A'B \rangle = 2\sqrt{2}. \quad (4.5)$$

This shows that such a Bell-like inequality can easily be set up and violated in theory. In practice, however, the situation is much more delicate. A number of landmark experiments have shown violations of Bell-like inequalities [166, 167]. However, a great difficulty arises with the ambition to convince any sceptic that all the assumptions involved in the experiment have indeed been addressed. Several loopholes have been identified, namely the loopholes in detection (fair sampling), communication (non-signalling), rotational invariance, coincidence, memory, nonrecurrence, free choice of detector orientations [168, 169]. Moreover, a sceptic can pose the argument that the exclusion of a certain deterministic model does not exclude all possible deterministic models (cf. [170]) and refer to a general theory-loophole, indicating that our understanding and interpretation of Quantum Mechanics is still subject to future change. There are indeed currently unanswered fundamental questions such as the quantization of Gravity, the possibility of extra dimensions or the hierarchy problem, a missing Grand Unified Theory and diverging integrals of Quantum Field Theory which lead to theories beyond the Standard Model of particle physics, such as Supersymmetry and String Theory. For practical purposes, however it is safe until the next big shift of paradigms to work with the common understanding of Quantum Mechanics. Yet it is difficult enough to engineer any practically useful Quantum Random Number Generator that violates a Bell-like inequality beyond reasonable doubt. In optics, experiments that rightfully close the communication loophole either require extremely fast time-resolution or devices that extend

over large distances (up to kilometers) to ensure no classical signals nullifying the effects of the involved Quantum channels can be transmitted between different parties. Moreover, the rates at which random numbers are produced are extremely low in such experiments [168]. It is therefore desirable to find alternative approaches to Certified Quantum Random Number Generation, which circumvents some of these challenges. A novel approach based on a solid-state spin system and certification by Quantum Contextuality will be examined in the following.

4.2 Quantum Random Number Generation Certified by Quantum Contextuality

In principle, the proposed violation of a KCBS-inequality, as from Section 3.4 offers the possibility of generating Random Numbers certified by an Inequality ensuring the Quantum nature of the underlying process. Similar experiments have been carried out using trapped ions or effective optical Qutrits, aiming at Quantum Random Number Generation certified by Quantum Contextuality [8, 140, 145]. The theoretical foundation of QRNG Certification by Quantum Contextuality [171] however is less established than in the case of the more commonly used Certification by Bell-inequalities [172, 173]. A central advantage of Contextuality-certified QRNG on the other hand is the avoidance of the famous Locality Loophole present in any Certification based on Bell-Inequalities [174]. While the Locality Loophole has been shown to be in principle avoidable by experiments [168, 169], it presents a huge challenge in engineering a QRNG device based on Bell-Inequalities as optimizing the size of such a device and the related time-resolution in order to demonstrate non-signalling is difficult. Quantum Contextuality on the other hand, can be demonstrated on a single indivisible Quantum System [2]. Detection presents a possible loophole in both cases, as the Certification depends on fair sampling and efficiency of the involved detectors [8, 168, 169]. A number of specific loopholes need to be addressed in the case of Certification by Quantum Contextuality. In particular, the Compatibility loophole concerns the fact that

4 Quantum Random Number Generation

operators in each context have to commute, which has to be demonstrated separately in experiments [129, 132, 175]. This is related to the effect of Finite Precision, i.e. the observation that both the orthogonality of states and the statistical uncertainty on measurement results is never perfect in experiments, which presents an existential threat to the basic assumptions of Quantum Contextuality [131], but several approaches to overcome this loophole have been presented [176, 177]. Moreover, the individual-existence loophole [7, 178] is relevant, as a verification of Quantum Contextuality requires joint measurements, the existence of a meaningful operational definition of an individual measurement has to be ensured [7]. Finally, it has to be ensured that no classical memory is influencing the measurement results, since Contextuality effects can be simulated classically by the use of external memory [130, 179]. It is debatable whether this presents an additional loophole since simulation of Bell-Inequality violation is also possible when allowing for classical signalling [168].

For practical purposes, random bits related to the KCBS inequality can be extracted from the experiment presented above, section 3.4, by following the min-entropy extraction presented by Um et al [8]. Therein, the original KCBS inequality (3.12) is rewritten in terms of a measurable expectation value L in terms of conditional probabilities on the agreement of measurement outcomes such as [8]

$$L \equiv \sum_{i, a_i, a_j} (p(a_i = a_{i+1} | A_i A_{i+1})) - p(a_i \neq a_{i+1} | A_i A_{i+1}) \leq 3, \quad (4.6)$$

according to their definition of measurement configurations A_i with possible results $a_i = \pm 1$. This is then related to a min-Entropy of the kind [8]

$$\mathcal{H}_\infty = -p(A_i) \log_2(\max_{a_i} p(a_i | A_i)), \quad (4.7)$$

such that the entropy is minimized in terms of the possible measurement outcomes. The approach in [8] should be taken cum grano salis due to notational mistakes, as specified in Section 3.5.4 and in the Corrigendum published [11]. Moreover, bounds obtained in [8] are based on the theoretical reference by Pioronio [173], which however is based on Bell-Inequalities rather than the required

4.3 The NV-Center as Single-Photon Emitter for QRNG

analysis based on Quantum Contextuality, with a different set of assumptions and possible loopholes. However, an analysis similar to the conditional probabilities and entropies presented above should be followed as in [160, 173]. A renewed attempt of obtaining secure bounds in terms of Randomness Expansion by the same authors as [8] is presented in [145]. Obtainable entropies are then, as also attempted in [8], based on the underlying properties of Quantum Physics rather than being based on mere analysis of the random output, which is an important step towards Certification [160, 173].

In essence, experimental violation of the KCBS inequality as proposed in Section 3.4ff thus offers the potential for Certification of Random Numbers. A number of subtleties and potential loopholes [180] have been listed and compared to the Bell-Inequality case. While the underlying theory needs to be solidified [171, 172], the necessity to avoid the Locality Loophole for Bell Inequalities favours QRNGs certified by Quantum Contextuality for practical applications, due to reduced engineering requirements and applicability in single, irreducible quantum systems [8, 140]. In the following, another Ansatz towards Quantum Certification of Random Numbers, based on single photons emitted from NVs, will be presented.

4.3 The NV-Center as Single-Photon Emitter for Quantum Random Number Generation

Making use of the NV Center's property to be able to emit single photons, the implementation of a canonical Quantum Random Number Generator (QRNG) of single photons impinging is possible. While single photons impinging on a beam splitter are often described as a basic example in discussions of QRNG [152, 153, 181], surprisingly few examples of such systems are experimentally implemented in the literature [182–184], using spontaneous parametric down-conversion and integrated optics. The reason for the rarity of implementations is likely due to the experimental

4 Quantum Random Number Generation

challenges involved [185], including the need for a stable single-photon source, for which the NV Center in diamond is very well suitable [186], even enabling a 24/7 operation as a single-photon source at ambient conditions [187].

In comparison to the OPO-Ansatz presented in section 4.4, a QRNG based on single photons from an NV Center presents a clearer picture in terms of the quantum origin of Randomness, at first sight. On the other hand, random number generation by a period-doubling fibre-feedback OPO is shown to have exceptionally advantageous unambiguity and requires no post-processing per se [10]. Moreover, a more detailed analysis of the quantum origin of the randomness from a single-photon experiment, yields several challenges. Cauchy-Schwarz inequalities do present clear measures for non-classicality in terms of phase-amplitude relations, or photon numbers [188]. However, in order to properly use this quantum resource, the experimental measurements should include photon number statistics experiments such as optical homodyne detection [189]. If, on the other hand, path information is used like in the case of the standard beam splitter experiment, certification of quantum random numbers would necessitate cross-correlation detection [190] or, in the case of using time-arrival information as for anti-bunching [191], temporal Bell inequalities such as Leggett-Garg inequalities should be used [192, 193] in order to demonstrate the quantumness of the mechanism for the output of random numbers. Here, a unique Ansatz is developed instead, in an aim to work towards certification of random numbers by a single-photon experiment. The setup consists of the NV-Center as a single photon source, a beam splitter and two APDs registering the arrival of photons at the respective location, displayed in Figure 4.2.

A first naive approach to implement a quantum random number generator is to process the recorded time stamps simply by taking the time-ordered sequence of detected clicks. We associate the reflected detected photons with the outcome **1** and the other one with the outcome **0**. Consequently, all clicks are interpreted as random bits. This procedure exhibits a number of problems: The experimentally observed bias of a higher count rate on one detector (about 20%) affects the balance

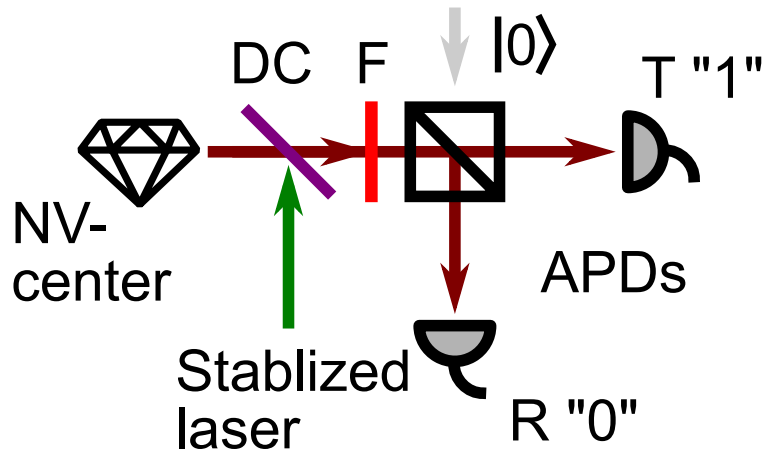


Figure 4.2: Experimental Setup for Random Number Generation with single photons originating from a NV-Center, by using a beam splitter with detectors on each path. Image adapted from our publication in [187].

of the bits. Furthermore, the Avalanche Photodiode (APD) dead time and the APD's afterpulsing issues will influence the independence of bits. The given dead time on the order of 45 ns influences a fraction of the recorded bits only. The raw data, from which the existence of a bias can be observed without difficulty, is depicted in Figure 4.3.

A very simple scheme of unbiasing a biased random bit sequence is the so-called von Neumann-unbiasing procedure [194]. In this procedure, the bits are collected into non-overlapping tuples and only such tuples with a bit flip ($\mathbf{1,0}$ and $\mathbf{0,1}$) are counted as $\mathbf{1}$ or alternatively as $\mathbf{0}$; other sequences ($\mathbf{0,0}$ and $\mathbf{1,1}$) are ignored. The resulting bit sequence is unbiased, simply since the probability of $\mathbf{1}$ can be associated with p and therefore, the counter-probability (of $\mathbf{0}$) will be $1 - p$. Thus, the joint probability of $\mathbf{1, 0}$ is $p \times (1 - p)$, being equal to the probability for $\mathbf{0, 1}$, which is $(1 - p) \times p$. Higher-order unbiasing schemes of this procedure are also reported in the literature [195] which can even extract more random bits per input bit. The von Neumann procedure reduces the amount of random bits. To which extend the random bit stream is reduced depends on the bias, and in the limes, a quarter of the tuples will generate a random bit. From n bits, consequently, only $n/4$ bits can be extracted. With a bias δ , this equation changes to $(p - \delta)(1 - p + \delta)$. The resulting bit stream

4 Quantum Random Number Generation

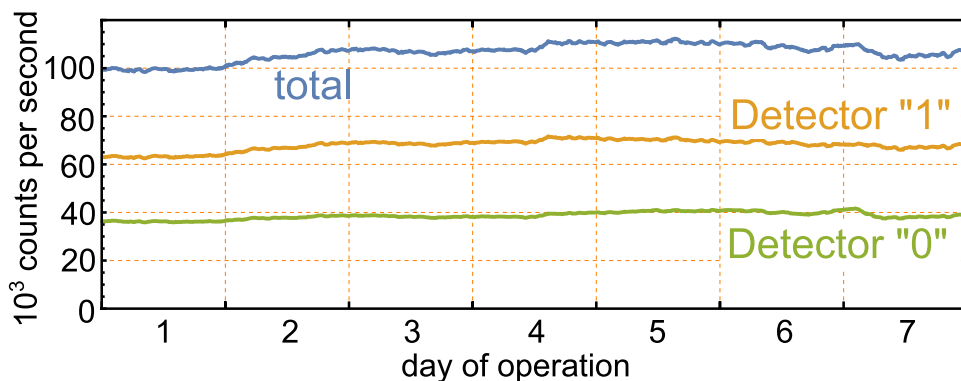


Figure 4.3: Experimental data (in thousand counts per second) recorded of the single-photon QRNG based on an NV-Center in a 24/7 operation at ambient conditions. A bias towards Detector “1” (orange curve) is clearly visible. Image adapted from our publication in [187].

is now unbiased but might still contain some memory effects. The described unbiasing procedure is comparable to the recording of anti-bunching. Whereas we utilize time-ordered tuples of bits to derive a next bit in the von Neumann procedure, we intrinsically determine reordered bit tuples in the anti-bunching. Then these bits are equally balanced around zero time delay. While many papers examine the theoretical background of anti-bunching [191, 196] it is considered instructive to list the necessary steps to experimentally analyse **anti-bunching**:

1. Register a click in one detector, e.g. detector “0”, record the time-stamp.
2. Measure the time until a click is registered in the other detector, e.g. detector “1”
3. Create a histogram by binning the time-axis and record number of events per bin
4. Obtain from the data a correlation-function

$$g^{(2)}(\tau) = \frac{\langle I_1(t)I_2(t + \tau) \rangle}{\langle I_1(t) \rangle \langle I_2(t) \rangle}, \quad (4.8)$$

which essentially correlates the expectation value to detect a photon after a time $t + \tau$ when a previous photon has been detected at time t .

4.3 The NV-Center as Single-Photon Emitter for QRNG

5. $g^{(2)}(0) < 1$ indicates non-classical light [191], while $g^{(2)}(0) < 1/2$ moreover confirms the single-photon nature of the light source [187, 196].

Performing such anti-bunching measurements firstly confirmed the non-classicality and the single-photon nature in the presented NV experiment [187]. Moreover, the output bits stemming from the associated measurements were filtered according to the correlation function. This means that only bits for which the non-classical nature of the light impinging on the beam-splitter was confirmed was post-selected, as indicated in Figure 4.4. While this surely asserts the quantum nature of the QRNG based on single-photons from NV-Centers, it is an interesting open question whether filtering according to anti-bunching measurements can lead to Certified Quantum Random Number Generation [142]. As discussed in the introduction of this section, anti-bunching presents a statement about temporal correlation, requiring loophole-free temporal Bell Inequalities to make qualitative statements about certification of the randomness involved [192]. As the output bits are essentially measured depending on the path taken, a deeper analysis of the path-information including cross-correlation measurements or homodyne detection could present a promising endeavour towards Certified Quantum Random Number Generation [189, 190]. A further optical experiment producing random numbers, in which quantum effects play a significant role, is discussed below.

4 Quantum Random Number Generation

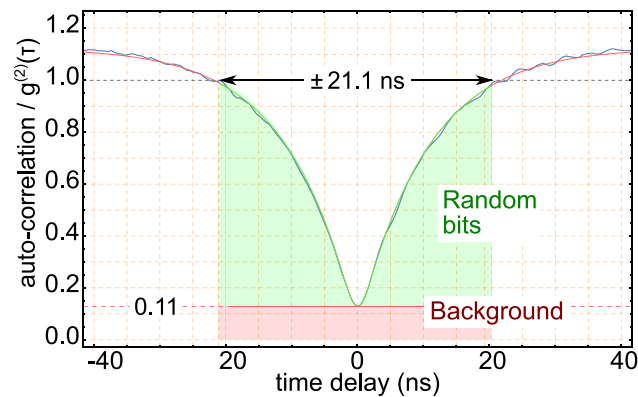


Figure 4.4: Correlation data obtained from the NV-Center based single-photon Random Number Generator. Only measurement outcomes satisfying the non-classicality bound $g^{(2)}(\tau) < 1$ are chosen as random bits. Anti-bunching is therefore shown and used as a physical mechanism to post-process the data in such a way that only bits relating to quantum effects are chosen. The single-photon nature is also demonstrated, with the bound $g^{(2)}(\tau) < 0.5$ clearly violated. This represents a further, stricter bound by which random bits could be filtered. The illustration is adapted from our publication in [187].

4.4 Unambiguous Quantum Random Number Generation by Optical Parametric Oscillators

A very common problem in random number generation is that raw data is usually biased towards one of the possible outcomes, such that post-processing of the data is necessary. An advantage of Optical Parametric Oscillators (OPOs), in particular when operated in the period-doubling state, as opposed to the more common degenerate operation [197, 198], is that the measurement outcomes are very well-defined, unambiguous and it is even possible to obtain random numbers from the raw data that can be considered unbiased for all practical purposes [10]. Due to the fast rates of possible measurements and the accessibility of quantum mechanical effects, optical processes are favourable for quantum random number generation in general. However, e.g. in the case of single photon random number generation, there are several disadvantageous effects such as

dead time or unequal efficiencies of detectors, beam splitter imperfections, time measurement imprecisions [185] and rate limitations by the saturation of single-photon detectors [199]. Even the most canonical classical random number generator, a coin, suffers the possibility of landing on the side, which represents an ambiguous measurement that has to be ignored for the purpose of randomness generation. The fact that random number generation by period-doubling OPOs can be regarded as unambiguous and unbiased thus presents a very subtle and applicable advantage towards other Random Number Generators (RNGs), especially since post-processing algorithms in RNGs also open back doors for cryptographical attacks [150].

4.4.1 The Optical Parametric Oscillator and Period Doubling

The basic, simplified working principle of an OPO involves a pulsed pump laser impinging on a gain crystal, within an optical cavity consisting of said gain crystal and a decoupler enabling variable output. Here, a polarizing beam splitter is used as decoupler [10]. For period-doubling, it is moreover necessary to include a non-linear element. This is in the present case constituted by a non-linear feedback fibre, resulting in a fibre-feedback OPO (also denoted as ffOPO). Period-doubling (P2-cycle) means that in the equilibrium state achieved, only every second pulse is identical in energy within a pulse train. It is experimentally very challenging to prepare an OPO in a P2-cycle such that the presented Random Number Generation protocol is understood to be the first application of an OPO using period-doubling [10]. Here, the described setup is further enriched by an optical chopper which provides the possibility for the system to randomly alternate between two different equilibrium states by interrupting and resetting the resonator, and a reference signal, obtained by halving the pump laser frequency, see Figure 4.5.

4 Quantum Random Number Generation

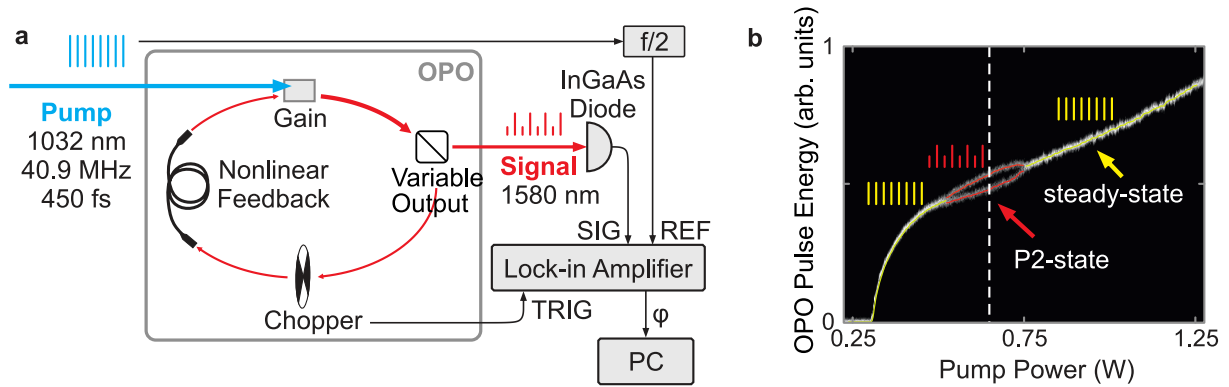


Figure 4.5: Simplified schematic illustration of a Period-Doubling Fibre-Feedback Optical Parametric Oscillator (OPO), featuring the experimental setup used (a) and a description of period-doubling (P2-state) by plotting Pulse Energy of the equilibrated OPO against Power of the pump laser (b). Image directly adapted from our publication in [10].

4.4.2 Unambiguous all-optical Random Number Generation with OPOs

Random numbers are generated from the period-doubling OPO in the following manner. While the OPO is off or blocked by the Chopper, there is no equilibrated state of pulse trains showing a clear repetitive pattern. During the transient process, the OPO pulse train builds up and may reach two different states within the P2-cycle. In the equilibrated state, the pulse train displays alternating pulse energies of high (H) and low (L) energy. In comparison with the reference signal, which is obtained by halving the frequency of the pump laser, the high-energy pulses (H) of the equilibrated P2-cycle can either be in phase or out of phase. When the OPO signal and the reference are measured to be in phase, the outcome is interpreted as random number **1**. Instead, if there is a phase difference of π , or equally the OPO low-energy pulse (L) and the reference signal are in phase, the measurement result is interpreted as number **0** instead. See Figure 4.6 for an illustration of the method to obtain random numbers from the OPO. Uncertainties on the phase measurement are negligible, as the two possible outcomes are separated by more than 400 standard deviations

4.4 Unambiguous QRNG by Optical Parametric Oscillators

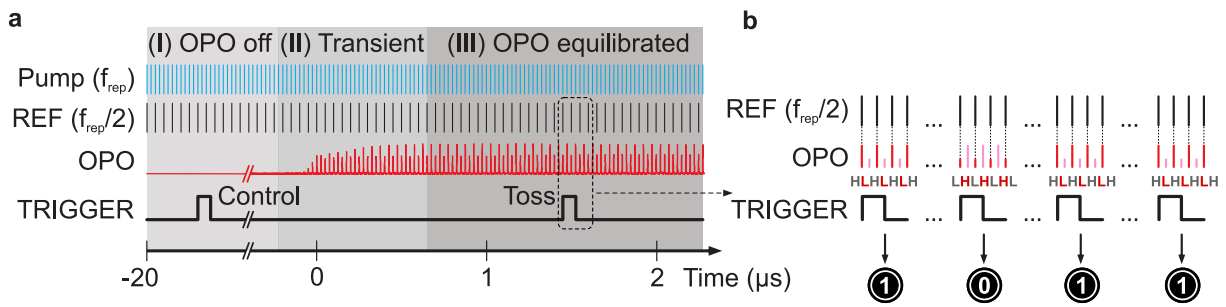


Figure 4.6: Transient process for Equilibration of a Period-Doubling Fibre-Feedback OPO (a) and method to obtain random numbers (b) by comparison of the OPO pulse-train with a reference signal. Image directly adapted from our publication in [10].

[10]. This renders the described OPO very suitable for random number generation and presents the reason for the featured Unambiguity. Moreover, the unprocessed data obtained directly from measurements displays no bias, i.e. the probabilities to obtain **0** or **1** can be considered equal [10], which builds the foundation of the positive outcomes of the randomness analysis in the following section.

4.5 Analysis of Random Numbers

“Anyone who considers arithmetical methods of producing random digits is, of course, in a state of sin.”

- John von Neumann -

Whenever random numbers are obtained, it is necessary to perform checks on the quality and the underlying mechanism of the RNG involved, in order to demonstrate that the obtained numbers can be considered random. Indeed, Randomness is a rather fundamental concept related to Predictability, Determinism and even the limits of the Scientific Method in general [142]. Every test of Randomness therefore is only valuable when the involved assumptions are clearly stated, which may in turn limit the applicability of the random numbers involved, such that ideally, Randomness is not qualified or certified by the numbers that are output, but by the physical system in question and the underlying mechanism which produces those numbers [160]. It is common to use standard randomness tests such as the NIST test suite [200]. However, these test are initially designed for algorithmic pseudo-random number generators and provide no sufficient proof of randomness [10, 201]. Indeed, it is impossible to search all possible patterns occurring in strings of random numbers, such that any test may miss a pattern and indeed, many numbers created from deterministic algorithms or even real numbers such as π or e do pass most of these test [10, 142]. In the case of the presented OPO, a complete a priori analysis of the involved entropies as in [160] was not feasible due to the complexity of the system and the open questions concerning proofs of the origin of randomness as discussed in [10]. In brief, the generation of single photons by spontaneous parametric down-conversion in the non-linear gain crystal present in the cavity plays a significant role in the transient process of the described OPO, along with cavity losses [10]. However, the qualitative contribution of these processes to the build-up of the period-doubling state is still under investigation [10] and expression of this state in terms of density matrices could not be readily obtained. Instead, an analysis of the output from $N \approx 2.25 \cdot 10^8$ measurements is presented, which

does not follow the presented standard tests, but examines Feller's Coin Tossing Constants [9] and conditional entropies obtained from sub-sequences of the measurement results [10, 185].

4.5.1 Feller's Coin Tossing Constants

A routine check on the output of a RNG is the balance between **0** and **1**, which ideally occur with identical probability. This analysis can be extended to tuples, as in the case of the conditional entropy analysis performed later on. Yet, it is desirable to analyse tuples of higher order, enabled e.g. by the Coin Tossing Constants introduced by Feller [9]. The basic idea behind this concept is to analyse whether patterns of subsequent identical outcomes such as $\underbrace{\mathbf{00} \dots \mathbf{0}}_k$ do occur, and to which order k . The probability for such sequences of k consecutive heads (or tails) to **not** appear in n independent tosses of a fair coin, is denoted as $p(n, k)$. In formal terms and specified to the problem at hand in a calculable way, we define the event $\mathbf{E}_{n,k}$ and the associated probability as

$$\mathbf{E}_{k,n} :: k \text{ consecutive } \mathbf{1}\text{s appear in } n \text{ independent outcomes of a fair RNG.} \quad (4.9)$$

$$p(n, k) \equiv p(\overline{\mathbf{E}_{k,n}}). \quad (4.10)$$

The bar over $\overline{\mathbf{E}_{k,n}}$ denotes negation of this event. For completeness, n is the size of the analysed (sub-)sample of measurement outcomes and k is the length of the consecutive sequence in question, as specified. These probabilities are calculated from the raw measurement data and compared to the ideal Feller's constants α_k given by the smallest positive real root of the polynomial [9]

$$x^{k+1} - 2^{k+1}(x - 1) = 0 \quad (4.11)$$

where k a priori is a general order parameter. The constant β_k is defined in terms of α_k and k as [9]

$$\beta_k \equiv 2 - \alpha_k / (k + 1 - k\alpha_k). \quad (4.12)$$

The relation between $p(n, k)$ and the coin tossing constants is

$$\lim_{n \rightarrow \infty} p(n, k) \alpha_k^{n+1} = \beta_k, \quad (4.13)$$

4 Quantum Random Number Generation

in the limit of an infinite sample size. For large n , this expression also yields an approximation

$$p(n, k) \approx \beta_k \alpha_k^{-(n+1)}. \quad (4.14)$$

It is possible to avoid the need of numerically solving the roots of the polynomial in (4.11), since $p(n, k)$ as defined in (4.13) can also be calculated explicitly with the use of generalized Fibonacci numbers from [202]

$$p(n, k) = \frac{F_{n+k}^{(k)}}{2^n} \quad (4.15)$$

where $F_{n+k}^{(k)}$ is the $(n + k) - th$ element of the k -step Fibonacci sequence. These general Fibonacci numbers extend the more commonly known notion of standard Fibonacci numbers in the sense that a number of k entries are summed up to obtain the next number in the sequence as opposed to the usual definition, where $k_{\text{standard}} \equiv 2$ is fixed, see Figure 4.7. Note that the notation $p(n, k) = \tilde{F}_{n+2}^{(k)}/2^n$ is also present in the literature, with the difference to (4.15) being the index $(n + 2)$ instead of $(n + k)$. This applies when the first element is $\tilde{F}_0^{(k)} \equiv 1$. For the calculations used here, the leading zeros $F_0^{(k)} \equiv 0$ are included in the definition [10].

| | | | | | | | | | | | | | | | | | | | | | | |
|------|---|---|---|---|---|----|----|----|-----|-----|-----|------|------|------|------|-------|-------|-------|--------|--------|--------|---------|
| k=2 | 1 | 1 | 2 | 3 | 5 | 8 | 13 | 21 | 34 | 55 | 89 | 144 | 233 | 377 | 610 | 987 | 1597 | 2584 | 4181 | 6765 | 10946 | 17711 |
| k=3 | 1 | 1 | 2 | 4 | 7 | 13 | 24 | 44 | 81 | 149 | 274 | 504 | 927 | 1705 | 3136 | 5768 | 10609 | 19513 | 35890 | 66012 | 121415 | 223317 |
| k=4 | 1 | 1 | 2 | 4 | 8 | 15 | 29 | 56 | 108 | 208 | 401 | 773 | 1490 | 2872 | 5536 | 10671 | 20569 | 39648 | 76424 | 147312 | 283953 | 547337 |
| k=5 | 1 | 1 | 2 | 4 | 8 | 16 | 31 | 61 | 120 | 236 | 464 | 912 | 1793 | 3525 | 6930 | 13624 | 26784 | 52656 | 103519 | 203513 | 400096 | 786568 |
| k=6 | 1 | 1 | 2 | 4 | 8 | 16 | 32 | 63 | 125 | 248 | 492 | 976 | 1936 | 3840 | 7617 | 15109 | 29979 | 59448 | 117920 | 233904 | 463968 | 928319 |
| k=7 | 1 | 1 | 2 | 4 | 8 | 16 | 32 | 64 | 127 | 253 | 504 | 1004 | 2000 | 3984 | 7936 | 15808 | 31489 | 62725 | 124946 | 248888 | 495776 | 987568 |
| k=8 | 1 | 1 | 2 | 4 | 8 | 16 | 32 | 64 | 128 | 255 | 509 | 1016 | 2028 | 4048 | 8080 | 16128 | 32192 | 64256 | 128257 | 256005 | 510994 | 1019960 |
| k=9 | 1 | 1 | 2 | 4 | 8 | 16 | 32 | 64 | 128 | 256 | 511 | 1021 | 2040 | 4076 | 8144 | 16272 | 32512 | 64960 | 129792 | 259328 | 518145 | 1035269 |
| k=10 | 1 | 1 | 2 | 4 | 8 | 16 | 32 | 64 | 128 | 256 | 512 | 1023 | 2045 | 4088 | 8172 | 16336 | 32656 | 65280 | 130496 | 260864 | 521472 | 1042432 |
| k=11 | 1 | 1 | 2 | 4 | 8 | 16 | 32 | 64 | 128 | 256 | 512 | 1024 | 2047 | 4093 | 8184 | 16364 | 32720 | 65424 | 130816 | 261568 | 523008 | 1045760 |
| k=12 | 1 | 1 | 2 | 4 | 8 | 16 | 32 | 64 | 128 | 256 | 512 | 1024 | 2048 | 4095 | 8189 | 16376 | 32748 | 65488 | 130960 | 261888 | 523712 | 1047296 |
| k=13 | 1 | 1 | 2 | 4 | 8 | 16 | 32 | 64 | 128 | 256 | 512 | 1024 | 2048 | 4096 | 8191 | 16381 | 32760 | 65516 | 131024 | 262032 | 524032 | 1048000 |
| k=14 | 1 | 1 | 2 | 4 | 8 | 16 | 32 | 64 | 128 | 256 | 512 | 1024 | 2048 | 4096 | 8192 | 16383 | 32765 | 65528 | 131052 | 262096 | 524176 | 1048320 |
| k=15 | 1 | 1 | 2 | 4 | 8 | 16 | 32 | 64 | 128 | 256 | 512 | 1024 | 2048 | 4096 | 8192 | 16384 | 32767 | 65533 | 131064 | 262124 | 524240 | 1048464 |
| k=16 | 1 | 1 | 2 | 4 | 8 | 16 | 32 | 64 | 128 | 256 | 512 | 1024 | 2048 | 4096 | 8192 | 16384 | 32768 | 65535 | 131069 | 262136 | 524268 | 1048528 |
| k=17 | 1 | 1 | 2 | 4 | 8 | 16 | 32 | 64 | 128 | 256 | 512 | 1024 | 2048 | 4096 | 8192 | 16384 | 32768 | 65536 | 131071 | 262141 | 524280 | 1048556 |
| k=18 | 1 | 1 | 2 | 4 | 8 | 16 | 32 | 64 | 128 | 256 | 512 | 1024 | 2048 | 4096 | 8192 | 16384 | 32768 | 65536 | 131072 | 262143 | 524285 | 1048568 |
| k=19 | 1 | 1 | 2 | 4 | 8 | 16 | 32 | 64 | 128 | 256 | 512 | 1024 | 2048 | 4096 | 8192 | 16384 | 32768 | 65536 | 131072 | 262144 | 524287 | 1048573 |
| k=20 | 1 | 1 | 2 | 4 | 8 | 16 | 32 | 64 | 128 | 256 | 512 | 1024 | 2048 | 4096 | 8192 | 16384 | 32768 | 65536 | 131072 | 262144 | 524288 | 1048575 |

Figure 4.7: Generalized Fibonacci numbers $F_{n+k}^{(k)}$ used in (4.15) to calculate the probabilities associated to Feller's Coin Tossing Constants [9], displayed up to order $k = 20$. Order parameters are listed in the first column, while the rows present the first 21 entries of each k -step Fibonacci sequence. Leading zeroes are not included. Note that each number is obtained by summing the previous k elements. For higher orders, the sequences naturally tend to include more powers of 2, highlighted in red colour.

4.5 Analysis of Random Numbers

The probabilities $p(n, k)$ are thus calculated with the use of generalized Fibonacci numbers (4.15) or from the approximation presented by Feller (4.14). The difference between both methods is negligible, as demonstrated in the Supplementary Material of [10], for large enough sample sizes. In order to find a good balance between non-vanishing probabilities $p(n, k)$ for low numbers of k , resulting in non-zero expectation values of occurrences in the sample of $N \approx 2.25 \cdot 10^8$ (c.f. Table 4.1), and the possibility to make qualitative and calculable statement for higher orders, a sub-sample size of $n = 400$ is chosen for the analysis of sequences occurring. This means that among the $N = 224,919,337$ bits analysed, all possible sequences of length $n = 400$, including overlaps are searched for sequences such as $\underbrace{\mathbf{11} \dots \mathbf{1}}_k$. The number of occurrence Ω of substrings in which such a sequence is **not** found, is counted and compared to the ideal value resulting from

$$\Omega_{ideal} = p(n, k) \cdot N, \quad (4.16)$$

see Table 4.1. From the actual number of occurrences in the data, a value

$$\tilde{p}_0(n, k) = \frac{\Omega_{real}}{N} \quad (4.17)$$

can be inferred. From this, according to equations (4.12) and (4.14), the Coin Tossing Constants α can be obtained, as done in Table 4.2, where the outcome is also compared to the ideal Coin Tossing Constants. Note that the mere counting of occurrences in overlapping strings of $n = 400$ bits within the whole sample of $N \approx 2.25 \cdot 10^8$ is extensive in terms of RAM and CPU, such that the calculations for each order k lasted between 4h and 5h using 20 CPU cores on an IBM Server System x3850 X5 4x 8C Xeon X7560 2,26GHz 128GB. The obtained occurrences are in very good agreement with the the ideal numbers calculated from Feller's Coin Tossing Constants. This is especially visible from the fraction of the observed and expected numbers in the last column of Table 4.1, in which the difference to unity is less than $2 \cdot 10^{-3}$ in all cases from $k > 5$ and continues to decrease. The raw and unprocessed measurement data can thus reproduce the expected behaviour following the principles introduced by Feller [9] and it was shown that indeed Feller's Coin Tossing Constants can be reproduced to very good accuracy, which is remarkable. However, on the critical

4 Quantum Random Number Generation

side, one may ask whether this passed test has any fundamental difference to the statistical standard tests commonly used on random numbers [200]. These tests were heavily criticized in [10] and elsewhere [142]. However they have in common with the presented method that very specific patterns are searched and analysed, while other patterns may be missed. Yet, the retrieval of Feller's Coin Tossing Constants [9] represents a way to make statements about tuples of high order within a sequence of random numbers.

| k | $p(n,k)$ | Expected occurrences | Occurrences in data | data/expected |
|----|--------------------------|----------------------|---------------------|---------------|
| 2 | 1.7846×10^{-37} | 0 | 0 | - |
| 3 | 3.1894×10^{-15} | 0 | 0 | - |
| 4 | 4.2602×10^{-7} | 96 | 131 | 1.36458 |
| 5 | 0.00109933 | 247260 | 247909 | 1.00262 |
| 6 | 0.0382887 | 8611853 | 8602356 | 0.998897 |
| 7 | 0.203962 | 45874935 | 45822724 | 0.998862 |
| 8 | 0.457264 | 102847303 | 102947552 | 1.00097 |
| 9 | 0.678849 | 152685938 | 152710004 | 1.00016 |
| 10 | 0.824992 | 185556222 | 185490825 | 0.999648 |
| 11 | 0.908715 | 204387118 | 204276752 | 0.99946 |
| 12 | 0.95344 | 214446648 | 214336752 | 0.999488 |
| 13 | 0.976518 | 219637428 | 219591262 | 0.99979 |
| 14 | 0.988224 | 222270275 | 222294422 | 1.00011 |
| 15 | 0.994111 | 223594365 | 223598120 | 1.00002 |

Table 4.1: The ideal probabilities $p(n, k)$ related to Feller's Coin Tossing Constants, and occurrences of associated sequences in the measurement data from the OPO operated as a Random Number Generator. The expected occurrences are calculated according to equation (4.16). Within a number of $N = 224919337 \approx 2.25 \cdot 10^8$ random bits, all occurring substrings of length $n = 400$ were searched for sequences of identical outcomes of length k . This length of the substrings is chosen in order to obtain non-vanishing probabilities, from which the extracted Coin Tossing Constants are calculated, see Table 4.2. This analysis is also performed in the Supplementary Material of [10].

| k | $\alpha_{\text{ideal}} - 1$ | $\alpha_{\text{extracted}} - 1$ | Relative change |
|-----|-----------------------------|---------------------------------|------------------------------|
| 2 | $2.36067977 \times 10^{-1}$ | – | – |
| 3 | $8.73780254 \times 10^{-2}$ | – | – |
| 4 | $3.75801274 \times 10^{-2}$ | $3.67635407 \times 10^{-2}$ | $2.17292158 \times 10^{-2}$ |
| 5 | $1.73207833 \times 10^{-2}$ | $1.73140575 \times 10^{-2}$ | $3.88306337 \times 10^{-4}$ |
| 6 | $8.27651672 \times 10^{-3}$ | $8.27932857 \times 10^{-3}$ | $-3.39738506 \times 10^{-4}$ |
| 7 | $4.03411036 \times 10^{-3}$ | $4.03700659 \times 10^{-3}$ | $-7.17936380 \times 10^{-4}$ |
| 8 | $1.98835585 \times 10^{-3}$ | $1.98587729 \times 10^{-3}$ | $1.24653524 \times 10^{-3}$ |
| 9 | $9.86236573 \times 10^{-4}$ | $9.85835060 \times 10^{-4}$ | $4.07116415 \times 10^{-4}$ |
| 10 | $4.90924534 \times 10^{-4}$ | $4.91824333 \times 10^{-4}$ | $-1.83286681 \times 10^{-3}$ |
| 11 | $2.44858952 \times 10^{-4}$ | $2.46240818 \times 10^{-4}$ | $-5.64351724 \times 10^{-3}$ |
| 12 | $1.22264478 \times 10^{-4}$ | $1.23579053 \times 10^{-4}$ | $-1.07518985 \times 10^{-2}$ |
| 13 | $6.10873757 \times 10^{-5}$ | $6.16278254 \times 10^{-5}$ | $-8.84715938 \times 10^{-3}$ |
| 14 | $3.05315574 \times 10^{-5}$ | $3.02515619 \times 10^{-5}$ | $9.17068859 \times 10^{-3}$ |
| 15 | $1.52625157 \times 10^{-5}$ | $1.52191234 \times 10^{-5}$ | $2.84306455 \times 10^{-3}$ |

Table 4.2: Feller’s Coin Tossing Constants (second column) compared to the constants extracted from measurement data provided by the OPO experiment (third column). The extracted Coin Tossing Constants are calculated from the data in Table 4.1. The reason why no Coin Tossing Constants could be inferred for $k < 4$ can also be seen in Table 4.1, namely no occurrences of the sequences in question were detected due to the vanishing associated probabilities. Note that this table differs from the one presented in the publication in [10]. Portrayed are the Coin Tossing Constants α subtracted with one, i.e. $\alpha - 1$. The relative change, calculated by $\frac{\alpha_{\text{ideal}} - \alpha_{\text{extracted}}}{\alpha_{\text{ideal}} - 1}$, is significantly lower than the relative change presented in the paper [10], which is calculated directly from the Coin Tossing Constants without subtraction. In [10], a scaling of the relative change in terms of \sqrt{N} is speculated, which can not be confirmed by the above analysis. Yet, the extracted Coin Tossing Constants are in good agreement with the ideal case.

4.5.2 Conditional Entropy Analysis of Random Numbers

Further tests were performed on the numbers output by the OPO experiment [10], in order to obtain conditional entropies from the data. These entropies are based on conditional probabilities defined in terms of joint probability and single probability by

$$p(x|y) = \frac{p(x \wedge y)}{p(y)}, \quad (4.18)$$

where the wedge “ \wedge ” represents the logical AND operator. Here, we define conditional entropies and associated conditional probabilities by events

$$\begin{aligned} \mathbf{E}_0(i) &:: \text{ the } i\text{-th bit is } \mathbf{0} \\ \mathbf{E}_0(i+1) &:: \text{ the } (i+1)\text{-th bit is } \mathbf{0} \end{aligned} \quad (4.19)$$

such that the conditional probability to obtain a $\mathbf{0}$ on the $(i+1)$ – *th* bit of a string of bits in the case when a $\mathbf{0}$ is already obtained on bit i reads as

$$p_i(\mathbf{0}|\mathbf{0}) \equiv p(\mathbf{E}_0(i+1) | \mathbf{E}_0(i)) = \frac{p(\mathbf{E}_0(i+1) \wedge \mathbf{E}_0(i))}{p(\mathbf{E}_0(i))}. \quad (4.20)$$

So, the conditional Shannon entropy in this case can be written down in the following exemplary manner.

$$\begin{aligned} \mathcal{H}_{Sh}(\mathbf{E}_0 | \mathbf{E}_1) &= \sum_i p(\mathbf{E}_1(i)) \cdot \mathcal{H}_{Sh}(\mathbf{E}_0 | \mathbf{E}_1(i)) \\ &= - \sum_i p(\mathbf{E}_1(i)) \cdot p(\mathbf{E}_0(i+1) | \mathbf{E}_1(i)) \cdot \log_2(p(\mathbf{E}_0(i+1) | \mathbf{E}_1(i))). \end{aligned} \quad (4.21)$$

Here, when the events \mathbf{E} are given without index, a unification is implicitly assumed such as $\mathbf{E}_0 \equiv \bigcup_i \mathbf{E}_0(i)$. Definitions for other tuple combinations of $\mathbf{0}$ and $\mathbf{1}$ are equally defined. A similar unification over the whole set of bits is implied when defining conditional probabilities for the overall sequence as

$$\begin{aligned} p(\mathbf{0}|\mathbf{0}) &\equiv \sum_i^{n-1} \frac{p_i(\mathbf{0}|\mathbf{0})}{n-1} = \frac{p(\mathbf{0} \wedge \mathbf{0})}{p(\mathbf{0})} \\ &\equiv \frac{\Omega(\mathbf{0} \wedge \mathbf{0})}{\Omega(\mathbf{0} \wedge \mathbf{0}) + \Omega(\mathbf{0} \wedge \mathbf{1}) + \Omega(\mathbf{1} \wedge \mathbf{0}) + \Omega(\mathbf{1} \wedge \mathbf{1})} / \frac{\Omega(\mathbf{0})}{\Omega(\mathbf{0}) + \Omega(\mathbf{1})} \end{aligned} \quad (4.22)$$

Note that at most, $(n - 1)$ tuples can occur within a sequence. Ω denotes occurrences of tuples within the overall sequence such that

$$\Omega(\mathbf{0} \wedge \mathbf{0}) \equiv \sum_{i=1} (\mathbf{E}_0(i + 1) \wedge \mathbf{E}_0(i)), \quad (4.23)$$

where the sum is taken over the boolean outcomes of the AND operation (\wedge), in the sense that true = 1 and false = 0. In simple terms, this just counts how many tuples of $\mathbf{0}$ s are found in the sequence, such that the conditional probabilities and entropies are easily calculable. In that sense, the Shannon entropy defined by events in (4.21) can be rewritten in terms of conditional probabilities of the overall sequence of bits

$$\mathcal{H}_{Sh} = - \sum_{y \in \{\mathbf{0}, \mathbf{1}\}} p(y) \sum_{x \in \{\mathbf{0}, \mathbf{1}\}} p(x|y) \log_2 p(x|y). \quad (4.24)$$

In an equal manner, the min Entropy \mathcal{H}_∞ is defined in terms of probabilities obtained from the data. In difference to the Shannon entropy, there is no summation over all possible conditional probability terms, but the maximal conditional probability is selected by

$$\mathcal{H}_\infty = - \log_2 \left[\sum_{y=\mathbf{0}}^{\mathbf{1}} p(y) \max_{x \in \{\mathbf{0}, \mathbf{1}\}} \{p(x|y)\} \right]. \quad (4.25)$$

Applying the above definitions on sub-samples of the overall sequence containing $N = 224919337 \approx 2.2 \cdot 10^8$ bits results in the plot given in Figure 4.8. Note that a few subtleties have to be considered when calculating the conditional entropies. So, the sample size N has to be even, such that the ideal case $p(\mathbf{0}) = p(\mathbf{1})$ is possible to be inferred from the data. Equally $p(\mathbf{0}|\mathbf{0}) = \dots = p(\mathbf{1}|\mathbf{1})$ is only possible to obtain when N is divisible by four [10]. It was initially intended to calculate the entropies for all possible permutations of overlapping sub-sequences of the overall measurement data, however with the IBM Server System available, this calculation was estimated to yield a total calculation time of approximately 2400 years of CPU time. This calculation was thus perceived to be beyond the scope of this PhD thesis. Instead, the sub-sample chosen in each calculation is simply given by the first N bits.

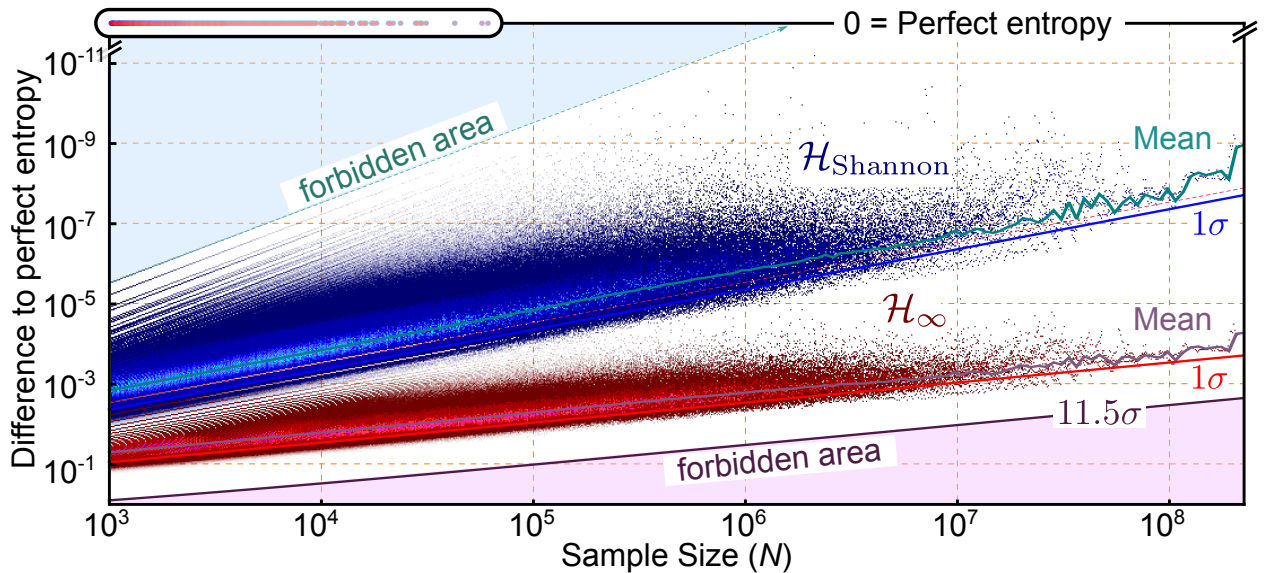


Figure 4.8: Shannon Entropies and Min Entropies calculated from the sequence of random bits produced by our OPO experiment in [10]. Indeed, the difference to perfect entropy, i.e. $(1 - \mathcal{H})$ is displayed over the length N of the respective sample sequence taken from the overall $N_{max} \approx 2.25 \cdot 10^8$ measurement results. The “forbidden areas” are obtained a priori by analysing the effect of one bit-flip from a perfectly distributed bit sequence (upper, light blue area) and the bound of 11.5σ (lower, light red area) is obtained by error propagation from a perfect distribution in the Supplementary Material of [10]. The inset on the upper left corner shows that a few sequences with lower sample sizes show perfect entropy, i.e. the single bit probabilities such as $p(\mathbf{0})$ and the conditional tuple probabilities such as $p(\mathbf{0}|\mathbf{1})$ are all equally likely to occur. This plot is also provided in our publication in [10].

Note that, as in the case of Feller's Coin Tossing Constants obtained in the previous section 4.5.1, this analysis of Conditional Entropies represents a test of patterns within the overall sequence of random bits. The test for Conditional Entropies is basically a search of tuples of bits occurring within the overall data from measurements. In this sense, this analysis is not fundamentally different to the statistical tests within the NIST test suite [200]. However, the entropies obtained show a clear scaling behaviour and reach remarkably high values. The most significant feature of the presented analysis is the fact that some bounds for the entropies in question can be obtained a priori, as seen in Figure 4.8, by analysing the effect of single bit-flips and realistic bounds as in the Supplementary Material of [10]. However, for future attempts to quantify Randomness, it would be desirable to obtain a different kind of conditional entropies a priori, namely entropies that can be inferred directly from the underlying physical processes and assumptions such as presented by Frauchinger, Renner and Troyer in [160].

4.6 Conclusion: QRNG

Three different approaches for generation of random numbers due to an underlying quantum mechanical process were presented. Steps towards rigorous Certification by Quantum Contextuality (Section 4.2), in particular by the KCBS-Inequality, introduced in Section 3.4, were given. While experiments aiming at such a certified Random Number Generation were presented [8, 140, 145], the need to solidify the underlying assumptions and implications was pointed out. In the case of the canonical single-photon beam-splitter QRNG experiment (Section 4.3), of which surprisingly few implementations were previously found, the quantum nature of the random numbers in question was confirmed by an Anti-Bunching analysis. Measurement results are filtered according to their correlation properties, which ensures Quantumness, but as of yet presents work towards a consistent Certification. In the case of the period-doubling Optical Parametric Oscillator (OPO) (Section 4.4), the quantum origin of the random output is harder to prove, even though spontaneous parametric down-conversion, as well as gain and loss processes within the optical cavity are identified as relevant processes. However, the raw bits stemming from OPO-measurements, without further post-processing, were confirmed to be very well suitable for Random Number Generation. They display excellent properties in terms of Unambiguity, are bias-free and were moreover found to perform in an excellent manner by an analysis of Feller's Coin Tossing Constants (Section 4.5.1) and Conditional Entropies (Section 4.5.2) obtained from the output. The inherent randomness in Quantum Mechanics was thus used, applied to different physical systems and settings, as a resource to certify the quality of the underlying physical process for Random Number Generation. This is impossible to obtain from any other non-probabilistic or (seemingly) chaotic physical process, underlining the unparalleled usefulness of Quantum Resources for future technological developments.

Appendix

*“The Quantum Universe has a quotation from me in every chapter
— but it’s a damn good book anyway.”*

-Richard Feynman-

A.1 Non-unitary Sum of two Unitaries

This section shows that the sum of two unitaries is non-unitary in almost all cases. This result is used in section 2.2.3, where the purification of spins surrounding a repeatedly projected central spin is discussed. Let

$$U = \frac{U_1 + U_2}{2}, \quad (\text{A.26})$$

where the division by two is necessary in order for the sum to be unitary, even for the trivial example $U_1 = U_2$. Then

$$\begin{aligned} U^\dagger U &= \frac{1}{4} (U_1 + U_2)(U_1 + U_2)^\dagger \\ &= \frac{\mathbb{1} + U_1 U_2^\dagger + U_2 U_1^\dagger + \mathbb{1}}{4} = \frac{\mathbb{1}}{2} + \frac{U_1 U_2^\dagger + U_2 U_1^\dagger}{4}. \end{aligned} \quad (\text{A.27})$$

This implies that the condition

$$U_1 U_2^\dagger + (U_1 U_2^\dagger)^\dagger \stackrel{!}{=} 2 \cdot \mathbb{1} \quad (\text{A.28})$$

A Appendix

must be fulfilled in order to satisfy the unitarity requirements $\det(U) = 1$ as well as $UU^\dagger = \mathbb{1}$. Obviously the trivial solution is

$$(U_1 = U_2) \Rightarrow \left(U_1 U_2^\dagger + (U_1 U_2^\dagger)^\dagger = 2 \cdot \mathbb{1} \right) \quad (\text{A.29})$$

whereas the other direction of equivalence, i.e. (A.28) $\stackrel{?}{\Rightarrow} (U_1 = U_2)$, remains open at this point. Considering the individual terms we can observe that

$$(U_1 U_2^\dagger = \mathbb{1}) \Rightarrow (U_1 = U_2) \quad (\text{A.30})$$

but we can not strictly draw this conclusion for the sum of both terms. However, (A.28) is surely a very strong constraint which is, at most, only fulfilled by a small class of matrices, such that we can conclude that the sum of two unitaries is non-unitary in almost all cases.

A.2 Selected Mathematica Code

Some examples of Mathematica Code of Simulations and Illustrations are provided here for possible use by future researchers.

A.2.1 Correlation of Twenty Spins by Repetitive Measurements of a Central Spin

The code below was used for the simulation of the Purification method introduced [46], here focused on the possibility to establish correlations among up to twenty spins, see Section 2.5.4.

Listing A.1: Mathematica Code for Correlation of twenty spins by repetitive measurements of a central spin

```

1 nuclearSpinsN = 20;
2 initState = N@1/Sqrt[2] {1, 1};
3 couplings = 20*N@Chop@Table[{d, 0, 1}/Norm[{d, 0, 1}]^4, {d,.1, 10, .1}][[;;, nuclearSpinsN]];
4 \[Omega] = 23.; \[Tau] = 0.3025;
5 reps = 23; repspartition = 16;
6 HplusSingleQubit = Table[Sum[couplings[[i,j]]*PauliMatrix[j]/2, {j,3}] + \[Omega] PauliMatrix[3]/2, {i,
   nuclearSpinsN}];
7 HminusSingleQubit = Table[Sum[-couplings[[i,j]]*PauliMatrix[j]/2, {j,3}] + \[Omega] PauliMatrix[3]/2, {i,
   nuclearSpinsN}];
8 UplusSingleQubit = MatrixExp[I # \[Tau]] & /@HplusSingleQubit;
9 UminusSingleQubit = MatrixExp[I # \[Tau]] & /@HminusSingleQubit;
10 DateObject[]
11 {timing, totalState} = Sum[{t[j], res} = AbsoluteTiming[ParallelSum[KroneckerProduct @@ Table[(Dot
   @@ (PadLeft[IntegerDigits[i, 2], reps] /. {1 -> UplusSingleQubit[[k]], 0 -> UminusSingleQubit[[k]]))].
   initState, {k,nuclearSpinsN}],{i,j*2^repspartition + 1, (j + 1)*2^repspartition }]]; {t[j], res}, {j, 0, 2^
   reps/2^repspartition - 1}];
12 timeConvert[timing]
13 totalState = Flatten[totalState];
14 totalState = totalState /Norm[totalState];
15 filePathName = NotebookDirectory[] <> "/data/" <> FileName[NotebookFileName[]] <> "-" <>
   IntegerString[nuclearSpinsN] <> "QubitState_freq" <> StringReplace[ToString[\[Omega]], "." -> ","] <> "
   time" <> StringReplace[ToString[\[Tau]], "." -> ","] <> "reps" <> IntegerString[reps] <> ".mx";
16 DumpSave[filePathName, totalState];

```

A.2.2 Purification Measurement Scheme Illustration

The following generates the Illustration of our Purification Measurement scheme, introduced above in Section 2.2.1. In particular the implementation of the Lemniscate of Geronon for general coordi-

A Appendix

nates of selected spin pairs may be of interest (Lines 24,25 below).

Listing A.2: Code for 3D figure of measurement scheme

```

1 newcone=Graphics3D[{EdgeForm[None],Opacity[.5],Glow[Green],Green,Specularity[1],newconeRegion=
    Cone[{{1.75,0,-.8},{-5.5,0,-.8}},.4],RegionFunction->Function[{x,y,z},z>-1]],Boxed->False,PlotRange
    ->{{-1,1},{-1,1},{-1,1}}];
2 focusedLaser=ParametricPlot3D[RotationMatrix[Theta,1,0,0].{x,0,.1x^2+.3} +{0,0,-.8},{x,-1.6,1.6},{[
    Theta],0,2[Pi]],Boxed->False,Mesh->None,Axes->False,PlotStyle->Directive[Opacity[.5],Glow[
    Green],Green,Specularity[1]]];
3 cube=Graphics3D[{Black,Opacity[.2],EdgeForm[None],Cuboid[{-1,-1,-1.2},{1,1,-.005}]]];
4 p=Polygon[{{-1,-1,0},{1,-1,0},{1,1,0},{-1,1,0}}];
5 plane=Graphics3D[{EdgeForm[None],Black,Opacity[.3],p,Boxed->False];
6 arrow=Graphics3D[{Lighter@Blue,Arrowheads[0.06],Arrow[Tube[{{0,0,-1.1},{0,0,-.5}},0.02]],Boxed->False];
7 pcords={{-0.56608,-0.594118,0.},{-0.536717,0.649914,0.},{-0.507535,-0.130824,0.},
8 {+0.173559,-0.624683,0.},{0.130172,0.685553,0.},{0.333096,0.0370521,0.},
9 {0.445469,-0.296539,0.},{-0.170616,0.102843,0.},{0.737797,-0.743911,0.},
10 {0.757756,-0.489728,0.}};
11 points=Graphics3D[{Orange,Specularity[.2],Ball[pcords,.05]};
12 connectionLines=Graphics3D[{Blue,Opacity[.35],Dashed,Thick,Line[Table[{{0,0,-.5},pcords[[i]]},{i,Length[
    pcords]}]]];
13 x1Photon=-.2(*+.27*);x2Photon=x1Photon+.4;zPhoton=-1.35;
14 beziercords={{x1Photon,0,zPhoton},{Mean[{x1Photon,x2Photon}],0,zPhoton+.2},{Mean[{x1Photon,x2Photon
    }],0,zPhoton-.2},{x2Photon,0,zPhoton}};
15 photonwiggle=Graphics3D[{Red,Thickness[.01],(*Arrow[*]BezierCurve[beziercords][*,-.1])(*BezierCurve
    [#+{0,0,0.15}&/@beziercords],BezierCurve[#+{0,0,-0.15}&/@beziercords]*),Boxed->False];
16 xa=-1.2;xb=-1.7;
17 newPhotonWiggle=Graphics3D[{Red,Thickness[.003],BezierCurve[Table[ {.15*Sin[50/Abs[xb-xa]]*(x-Mean[{
    xa,xb}])]*E^-((x-Mean[{xa,xb}])*5*1/Abs[xb-xa])^2,0,x},{x,Min[xa,xb],Max[xa,xb],Abs[xb-xa]/100}]]],
    Axes->True];
18 r=.3;xDetect=0;zDetect=-1.75;
19 semiSphere=ImplicitRegion[(x-xDetect)^2+y^2+(z-zDetect)^2<=r^2&&(z-zDetect)<=0,{x,y,z}];
20 detector=Show[RegionPlot3D[semiSphere,Boxed->False],Graphics3D[{Thickness[.01],Line[{{xDetect,0,
    zDetect-r},{xDetect,0,zDetect-2r}]]},Boxed->False];

```

```

21 measureBox=Graphics3D[{Darker@Green,Cylinder[{v={0,-.21,zDetect-2r-.2},v+{0,.01,0}},.1],Black,Opacity
    [.65],EdgeForm[Black],Cuboid[{-.2,-.2,zDetect-2r-.4},{.2,.2,zDetect-2r}]];
22 allSpins=GatherBy[Table[{pcords[[i]],Min@Table[Norm[pcords[[i]]-pcords[[j]]],{j,Delete[Table[k,{k,Length[
    pcords]],i]}]},{i,Length[pcords]},Last];obviousPairs=Select[allSpins,Length[#]==2&];remainigPairs=
    GatherBy[Table[{#[[i]],Min@Table[Norm[#[[i]]-#[[j]]],{j,Delete[Table[k,{k,Length[#]}],i]}]},{i,Length[#]}]&
    @Flatten[Complement[allSpins,obviousPairs][[All,All,1]],1],Last];
23 lines=Graphics3D[{Dashed,Line[{#[[1,1]],#[[2,1]]]&/@obviousPairs,Table[Line[{#[[i]],#[[i+1]]],{i,1,Length
    [#],2}]&[remainigPairs]],Boxed->False];
24 paraFunc=ParametricPlot3D[Norm[#1-#2]/1.2 RotationMatrix[{{1,0,0},#1-#2}].{Cos[t]/(1+Sin[t]^2),(Cos[t]
    Sin[t]/(1+Sin[t]^2),0)+Mean[{#1,#2}],{t,-\[Pi],\[Pi]},PlotStyle->Directive[Glow@Orange,Tube[.01]],
    PlotRange->All]&;
25 graphic=Show[detector,focusedLaser,plane,cube,arrow,points,paraFunc@@@obviousPairs[[All,All,1]],
    paraFunc@@@remainigPairs[[All,All,1]],(*connectionLines,*)newPhotonWiggle,measureBox,
    RotationAction->"Clip",PlotRange->{{-1.75,1.75},{-1,1},{.1,zDetect-2r-.4}},ImageSize->Large,
    ViewPoint->{0.184966,-3,1.3},ImageResolution->1000]

```

A.2.3 Spin Squeezing Uncertainty Spherical Plot

This code snippet generates the spherical illustrations of Quasi-Probability Distributions used for Spin Squeezed states in Section 2.8.2.

Listing A.3: Mathematica Code for Squeezing Uncertainty Plots, here using a One-Axis Twisting Hamiltonian.

```
1 spinsN = 2;
2 referenceState = KroneckerProduct@@Table[{Cos[\[Theta]/2], E^(I \[Phi]) Sin[\[Theta]/2]}, {i, spinsN}] //
   Flatten;
3 oneaxisState = Normalize[{E^(I t ), 1, 1, E^(I t )}];
4 overlap = Abs[oneaxisState.referenceState]^2;
5 ParallelTable [Quiet[overlapFunc = Inactive[Function][{x, y, z}, ColorData["DarkRainbow", TransformedField["
   Spherical" -> "Cartesian", overlap /. t -> a, {r, \[Theta], \[Phi]} -> {x, y, z }]]]];
6 SphericalPlot3D[1, {theta, 0, Pi}, {phi, 0, 2 \[Pi]}, ColorFunction -> Activate[overlapFunc],
   ColorFunctionScaling -> False, PlotPoints -> 50, Boxed -> False, Axes -> False, SphericalRegion
   -> True, ViewPoint -> {1.7, 0, 0}, ImageSize -> 200, Mesh -> None], {a, 0, 2 \[Pi], (2 \[Pi])/8}]
```

Acknowledgements

“Knowledge is in the end based on Acknowledgement.”

- Ludwig Wittgenstein -

Professor Dr Jörg Wrachtrup for the engaged Supervision of my studies through all ups and downs and indeed for all opportunities enabled, including the possibility to conduct PhD studies at the PI3.

Dr Durga Dasari for his invaluable guidance and support, especially for the joint work on Indirect Sensing and Purification [4,46]. His engagement at the PI3 was a significant turning point for the success of my PhD studies.

Professor Dr Stefanie Barz and Professor Dr Eric Lutz for taking up the roles as Examination Chairman and Second Advisor for this thesis.

Dr Phillip Neumann for sharing his expertise many times during my PhD and for joint work, in particular on the topics of Spin Squeezing and Quantum Sensing.

Dr Ilja Gerhardt not only for his infectious excitement for Randomness and joint work leading to papers [10, 187] and patents, but also for his kind invitation to Zürich and for pointing me to an extremely lively Contextuality workshop (Solstice of Foundations) at ETH Zürich.

Dr Friedemann Reinhardt for important initial academic advice and support at the PI3.

A Acknowledgements

Dr Matthias Pfender, Dr Sebastian Zaiser, Dr Nabeel Aslam, Dr Thomas Oeckinghaus, Dr Roland Nagy, Dr Thomas Wolf, Dr Thomas Häberle, Dr Andreas Brunner, Dr Dominik Schmid-Lorch, Marwa Garsi, Dr Florestan Ziem, Dr Ali Momen Zadeh, Sina Burk, Dr Helmut Fedder, Julia Michl and Ingmar Jakobi for insights into NV theory, experiments and techniques and for sharing their academic expertise.

Dr Florian Kaiser for a – sometimes simultaneous – superposition of Science, Sports, (Quantum) Information sharing and great support.

Professor Otfried Gühne, Dr Matthias Kleinmann and Dr Gael Sentís for very stimulating discussions, support and joint work [114] in the areas of Quantum Contextuality and Bound Entanglement, among many other topics in Quantum Theory. The kind invitation to Siegen as an academic guest was very memorable.

Professor Paola Cappellaro for sharing her expertise in Spin Squeezing, for important academic advice during a critical phase of my studies and for her kind invitation to the Massachusetts Institute of Technology (MIT)

Professor Renato Renner for incredibly profound discussions on Quantum Randomness and Quantum Contextuality during the Solstice of Foundations conference he managed in Zürich.

Professor Carlos Meriles for kindly hosting several members of our institute during a memorable academic exchange in New York City.

Dr Jan Sperling for sharing his very impressive knowledge on multipartite Quantum Entanglement theory as well as giving important guidance towards the certification of QRNG using single photons.

Professor Jiangfeng Du for his interest in our Faraday Discussion paper on Purification [4] and stimulating exchanges with our institute.

Dr Tobias Steinle for initiating the joint work on the OPO-RNG [10] during our continued regular lunch meetings, for many great exchanges and support.

Professor Harald Giessen for the joint work between PI4 and PI3 leading to the OPO-RNG publication [10] despite all sportive rivalry.

Professor Simon Kochen not only for his legacy concerning the Kochen-Specker theorem, but also for his notable presence at the Solstice of Foundations workshop in Zürich, for a memorable picture and a lunch invitation, though I regrettably failed to grasp the Context.

Dr Gonzalo Álvarez and Analia Zwick for a great exchange on Localization.

Dr Andreas Döring for inspring exchanges on fundamental quantum physics.

Prof. Dr. Tommaso Calarco for sharing insights into Quantum Technology, fuelling my interest in Quantum Random Number generation. I also benefited greatly from his management surrounding the EU Quantum Flagship initiative and related conferences.

Dr Andrew Aird for advice in a critical phase of my PhD.

Nikolas Abt, Kevin Kleinbeck and Cedric Sommer for growing from students to teachers and for great and very helpful support with teaching activities.

Helmut Frasch, Sven Bodenstedt, Stefan Jesenski and Philipp Konzelmann for the joy of seeing former Quantum Information Processing students thrive at the institute.

All members of PI3 for a very memorable time, for being good colleagues and for mostly accepting me as I am.

Dr Durga Dasari, Dr Vadim Vorobev, Dr Tobias Steinle, Dr Florian Kaiser for providing initial feedback on this thesis.

Thomas Oeckinghaus for being the best office mate and for being a valuable ‘battle buddy’ when finishing the thesis.

A Acknowledgements

My colleagues at IBM and previously at Daimler – including the late Dr. Hintennach – for enabling an exciting transition from research to applied Quantum Technology.

The Dr. Karl Eisele and Elisabeth Eisele Foundation is appreciated for continued support from a pathbreaking prize in high-school up to a PhD scholarship.

The Wilhelm and Else Heraeus Foundation for funding and enabling the conferences “Discrete and Analogue Quantum Simulators”, “Quantum Correlations beyond Entanglement” and “Scalable Architectures for Quantum Simulation” that I loved participating in.

My parents and my family for who they are and for their support and care.

My wife Deborah for her continuous support, sacrifices and love in these years and indeed for becoming my wife during this time. Our son Gabriel is also appreciated for having to let his dad go for scientific adventures and writing.

Finally I wish to thank our Creator whose works I believe to study.

Publications and Patents

Publications

- Johannes N. Greiner, Durga Bhaktavatsala Rao Dasari, Philipp Neumann and Jörg Wrachtrup. Indirect Quantum Sensors: Improving the Sensitivity in Characterizing Very Weakly Coupled Spins. *Faraday Discussions*, 2015,184,163-171, July 2015. [4]
- Johannes N. Greiner, Durga Bhaktavatsala Rao Dasari, and Jörg Wrachtrup. Purification of an Unpolarized Spin Ensemble into Entangled Singlet Pairs. *Scientific Reports*, 7(1):529, April 2017. [46]
- Tobias Steinle*, Johannes N. Greiner*, Jörg Wrachtrup, Harald Giessen, and Ilja Gerhardt. Unbiased All-Optical Random-Number Generator. *Physical Review X* 7, 041050, November 2017. [10]
- S. C. Ndlovu, A. Marais, P. T. Shabangu, L. Noto, N. E. Engelbrecht, S. Matshawule, G. Jackson, A. Mboniyiryivuze, S. Zongo, Z. Dhunny, J. Greiner and S. Ramjatan. Diversity of participant representation within the 66th Lindau Nobel Laureate Meeting. *S Afr J Sci.* 2018;114(3/4), April 2018. [203]

*These authors contributed equally

A Publications and Patents

- Gael Sentís, Johannes N. Greiner, Jiangwei Shang, Matthias Kleinmann, and Jens Siewert. Bound Entangled States Fit for Experimental Verification. *Quantum* 2, 113, December 2018. [114]
- Xing Chen, Johannes N. Greiner, Jörg Wrachtrup, and Ilja Gerhardt. Single Photon Randomness based on a Defect Center in Diamond. *Scientific Reports* 9, 18474, December 2019. [187]

News and Views Articles with Reference to our Work

- David Abergel, Random numbers: A Quantum Coin Toss. *Nature Physics* 14, 7, January 2018. [204]
- David F. P. Pile. Optical Coin Toss. *Nature Photonics* 12, 58, January 2018. [205]

Patents and Inventions

- Tobias Steinle, Johannes N. Greiner, Jörg Wrachtrup, Harald Giessen, and Ilja Gerhardt. Apparatus and Method for Generating At Least One Random Number, Use of an Optical Parametric Oscillator. International Patent Application Number: EP2017/001268, October 2017
- Johannes Greiner, Sebastian Zaiser, Matthias Pfender, Philipp Neumann, Ilja Gerhardt, Matthias Kleinmann and Jörg Wrachtrup. Zertifizierter Quantenzufallsgenerator auf Diamantbasis. Erfindungsmeldung Universität Stuttgart, Dezember 2017
- Johannes N. Greiner, Ilja Gerhardt, and Jörg Wrachtrup. Erzeugung von Zufallszahlen durch pfadabhängige Detektion von Einzelphotonen mit nachgewiesenem Einzelphotonencharakter aus einer einzelnen Fehlstelle in einem Festkörper. Erfindungsmeldung Universität Stuttgart, September 2017

A Publications and Patents

Bibliography

- [1] Daniel M. Greenberger, Michael A. Horne, Abner Shimony, and Anton Zeilinger. Bell's theorem without inequalities. *American Journal of Physics*, 58(12):1131–1143, December 1990. doi:10.1119/1.16243. [cited on pp. 9 and 120]
- [2] Alexander A. Klyachko, M. Ali Can, Sinem Binicioğlu, and Alexander S. Shumovsky. Simple Test for Hidden Variables in Spin-1 Systems. *Physical Review Letters*, 101(2):020403, July 2008. doi:10.1103/PhysRevLett.101.020403. [cited on pp. 9, 131, 139, 140, 142, and 163]
- [3] T. H. Taminiau, J. J. T. Wagenaar, T. van der Sar, F. Jelezko, V. V. Dobrovitski, and R. Hanson. Detection and Control of Individual Nuclear Spins Using a Weakly Coupled Electron Spin. *Physical Review Letters*, 109(13):137602, September 2012. doi:10.1103/PhysRevLett.109.137602. [cited on pp. 17, 35, 36, 38, and 39]
- [4] Johannes N. Greiner, D. D. Bhaktavatsala Rao, Philipp Neumann, and Jörg Wrachtrup. Indirect quantum sensors: improving the sensitivity in characterizing very weakly coupled spins. *Faraday Discussions*, September 2015. doi:10.1039/C5FD00116A. [cited on pp. 17, 31, 33, 35, 36, 37, 39, 41, 43, 45, 46, 53, 122, 191, 192, and 195]
- [5] D. D. Bhaktavatsala Rao, Sen Yang, Stefan Jesenski, Emre Tekin, Florian Kaiser, and Jörg Wrachtrup. Observation of nonclassical measurement statistics induced by a coherent spin

Bibliography

- environment. *Physical Review A*, 100(2):022307, August 2019. doi : 10.1103/PhysRevA.100.022307. [cited on pp. 19, 31, 33, 90, 91, and 92]
- [6] P. Cappellaro and M. D. Lukin. Quantum correlation in disordered spin systems: Applications to magnetic sensing. *Physical Review A*, 80(3):032311, September 2009. doi : 10.1103/PhysRevA.80.032311. [cited on pp. 22, 57, 96, 104, 107, 123, 124, 125, 126, and 127]
- [7] Markus Jerger, Yarema Reshitnyk, Markus Oppliger, Anton Potočnik, Mintu Mondal, Andreas Wallraff, Kenneth Goodenough, Stephanie Wehner, Kristinn Juliusson, Nathan K. Langford, and Arkady Fedorov. Contextuality without nonlocality in a superconducting quantum system. *Nature Communications*, 7, October 2016. doi : 10.1038/ncomms12930. [cited on pp. 23, 139, 142, 144, 145, 149, 151, 152, 153, 154, 156, 158, and 164]
- [8] Mark Um, Xiang Zhang, Junhua Zhang, Ye Wang, Shen Yangchao, D. L. Deng, Lu-Ming Duan, and Kihwan Kim. Experimental Certification of Random Numbers via Quantum Contextuality. *Scientific Reports*, 3, April 2013. doi : 10.1038/srep01627. [cited on pp. 23, 25, 131, 140, 149, 151, 152, 153, 154, 155, 156, 163, 164, 165, and 184]
- [9] William Feller. *An introduction to probability theory and its applications. Vol. 1.* Wiley series in probability and mathematical statistics. Wiley, S.I., 3. ed., rev. print., [nachdr.] edition, 2009. OCLC: 837266385. [cited on pp. 23, 175, 176, 177, and 178]
- [10] Tobias Steinle, Johannes N. Greiner, Jörg Wrachtrup, Harald Giessen, and Ilja Gerhardt. Unbiased All-Optical Random-Number Generator. *Physical Review X*, 7(4):041050, November 2017. doi : 10.1103/PhysRevX.7.041050. [cited on pp. 23, 166, 170, 171, 172, 173, 174, 175, 176, 177, 178, 179, 180, 181, 182, 183, 191, 193, and 195]
- [11] Mark Um, Xiang Zhang, Junhua Zhang, Ye Wang, Yangchao Shen, D.-L. Deng, Lu-Ming Duan, and Kihwan Kim. Corrigendum: Experimental Certification of Random Numbers

- via Quantum Contextuality. *Scientific Reports*, 8:46927, February 2018. doi:10.1038/srep46927. [cited on pp. 25, 156, and 164]
- [12] J. Aasi et al. Enhanced sensitivity of the LIGO gravitational wave detector by using squeezed states of light. *Nature Photonics*, 7(8):613, August 2013. doi:10.1038/nphoton.2013.177. [cited on pp. 27 and 57]
- [13] Boris Korzh, Charles Ci Wen Lim, Raphael Houlmann, Nicolas Gisin, Ming Jun Li, Daniel Nolan, Bruno Sanguinetti, Rob Thew, and Hugo Zbinden. Provably secure and practical quantum key distribution over 307 km of optical fibre. *Nature Photonics*, 9(3):163–168, March 2015. doi:10.1038/nphoton.2014.327. [cited on p. 28]
- [14] Sheng-Kai Liao, Wen-Qi Cai, Wei-Yue Liu, Liang Zhang, Yang Li, Ji-Gang Ren, Juan Yin, Qi Shen, Yuan Cao, Zheng-Ping Li, Feng-Zhi Li, Xia-Wei Chen, Li-Hua Sun, Jian-Jun Jia, Jin-Cai Wu, Xiao-Jun Jiang, Jian-Feng Wang, Yong-Mei Huang, Qiang Wang, Yi-Lin Zhou, Lei Deng, Tao Xi, Lu Ma, Tai Hu, Qiang Zhang, Yu-Ao Chen, Nai-Le Liu, Xiang-Bin Wang, Zhen-Cai Zhu, Chao-Yang Lu, Rong Shu, Cheng-Zhi Peng, Jian-Yu Wang, and Jian-Wei Pan. Satellite-to-ground quantum key distribution. *Nature*, 549(7670):43–47, September 2017. doi:10.1038/nature23655. [cited on p. 28]
- [15] Jacob D. Biamonte and Peter J. Love. Realizable Hamiltonians for universal adiabatic quantum computers. *Physical Review A*, 78(1):012352, July 2008. doi:10.1103/PhysRevA.78.012352. [cited on p. 28]
- [16] A. D. Córcoles, A. Kandala, A. Javadi-Abhari, D. T. McClure, A. W. Cross, K. Temme, P. D. Nation, M. Steffen, and J. M. Gambetta. Challenges and Opportunities of Near-Term Quantum Computing Systems. *Proceedings of the IEEE*, pages 1–15, 2019. doi:10.1109/JPROC.2019.2954005. [cited on pp. 28 and 93]
- [17] K. Wright, K. M. Beck, S. Debnath, J. M. Amini, Y. Nam, N. Grzesiak, J.-S. Chen, N. C. Pienti, M. Chmielewski, C. Collins, K. M. Hudek, J. Mizrahi, J. D. Wong-

Bibliography

- Campos, S. Allen, J. Apisdorf, P. Solomon, M. Williams, A. M. Ducore, A. Blinov, S. M. Kreikemeier, V. Chaplin, M. Keesan, C. Monroe, and J. Kim. Benchmarking an 11-qubit quantum computer. *Nature Communications*, 10(1):1–6, November 2019. doi:10.1038/s41467-019-13534-2. [cited on p. 28]
- [18] Frank Arute, John M. Martinis, et al. Quantum supremacy using a programmable superconducting processor. *Nature*, 574(7779):505–510, October 2019. doi:10.1038/s41586-019-1666-5. [cited on pp. 28 and 31]
- [19] Szilárd Szalay. Multipartite entanglement measures. *Physical Review A*, 92(4), October 2015. arXiv: 1503.06071. doi:10.1103/PhysRevA.92.042329. [cited on p. 29]
- [20] J. Sperling and W. Vogel. Multipartite Entanglement Witnesses. *Physical Review Letters*, 111(11):110503, September 2013. doi:10.1103/PhysRevLett.111.110503. [cited on pp. 29 and 132]
- [21] Otfried Gühne, Géza Tóth, and Hans J. Briegel. Multipartite entanglement in spin chains. *New Journal of Physics*, 7(1):229, 2005. doi:10.1088/1367-2630/7/1/229. [cited on p. 29]
- [22] A. Döring and C. J. Isham. A topos foundation for theories of physics: II. Daseinisation and the liberation of quantum theory. *Journal of Mathematical Physics*, 49(5):053516, May 2008. doi:10.1063/1.2883742. [cited on p. 29]
- [23] Edwin Pednault, John A. Gunnels, Giacomo Nannicini, Lior Horesh, and Robert Wisniewski. Leveraging Secondary Storage to Simulate Deep 54-qubit Sycamore Circuits. October 2019. [cited on p. 31]
- [24] C.L. Degen, F. Reinhard, and P. Cappellaro. Quantum sensing. *Reviews of Modern Physics*, 89(3):035002, July 2017. doi:10.1103/RevModPhys.89.035002. [cited on p. 31]

- [25] Sebastian Zaiser, Torsten Rendler, Ingmar Jakobi, Thomas Wolf, Sang-Yun Lee, Samuel Wagner, Ville Bergholm, Thomas Schulte-Herbrüggen, Philipp Neumann, and Jörg Wrachtrup. Enhancing quantum sensing sensitivity by a quantum memory. *Nature Communications*, 7:12279, August 2016. doi:10.1038/ncomms12279. [cited on pp. 31, 33, 38, 107, and 122]
- [26] P. Cappellaro, J. Emerson, N. Boulant, C. Ramanathan, S. Lloyd, and D. G. Cory. Entanglement Assisted Metrology. *Physical Review Letters*, 94(2):020502, January 2005. doi:10.1103/PhysRevLett.94.020502. [cited on p. 31]
- [27] Thomas Wolf, Philipp Neumann, Kazuo Nakamura, Hitoshi Sumiya, Takeshi Ohshima, Junichi Isoya, and Jörg Wrachtrup. Subpicotesla Diamond Magnetometry. *Physical Review X*, 5(4):041001, 2015. doi:10.1103/PhysRevX.5.041001. [cited on pp. 31, 107, 122, and 123]
- [28] Jörg Wrachtrup and Amit Finkler. Single spin magnetic resonance. *Journal of Magnetic Resonance*, 269:225–236, August 2016. doi:10.1016/j.jmr.2016.06.017. [cited on p. 31]
- [29] Lukas Schlipf, Thomas Oeckinghaus, Kebiao Xu, Durga Bhaktavatsala Rao Dasari, Andrea Zappe, Felipe Fávoro de Oliveira, Bastian Kern, Mykhailo Azarkh, Malte Drescher, Markus Ternes, Klaus Kern, Jörg Wrachtrup, and Amit Finkler. A molecular quantum spin network controlled by a single qubit. *Science Advances*, 3(8):e1701116, August 2017. doi:10.1126/sciadv.1701116. [cited on pp. 31 and 35]
- [30] S. Bodenstedt, I. Jakobi, J. Michl, I. Gerhardt, P. Neumann, and J. Wrachtrup. Nanoscale Spin Manipulation with Pulsed Magnetic Gradient Fields from a Hard Disc Drive Writer. *Nano Letters*, 18(9):5389–5395, September 2018. doi:10.1021/acs.nanolett.8b01387. [cited on pp. 31 and 127]

Bibliography

- [31] Ashok Ajoy and Paola Cappellaro. Stable three-axis nuclear-spin gyroscope in diamond. *Physical Review A*, 86(6):062104, December 2012. doi : 10.1103/PhysRevA.86.062104. [cited on p. 31]
- [32] J.-C. Jaskula, K. Saha, A. Ajoy, D.J. Twitchen, M. Markham, and P. Cappellaro. Cross-Sensor Feedback Stabilization of an Emulated Quantum Spin Gyroscope. *Physical Review Applied*, 11(5):054010, May 2019. doi : 10.1103/PhysRevApplied.11.054010. [cited on p. 31]
- [33] Marcus W. Doherty, Neil B. Manson, Paul Delaney, Fedor Jelezko, Jörg Wrachtrup, and Lloyd C. L. Hollenberg. The nitrogen-vacancy colour centre in diamond. *Physics Reports*, 528(1):1–45, July 2013. doi : 10.1016/j.physrep.2013.02.001. [cited on pp. 32, 34, 35, 42, 44, 49, 50, 51, 60, 107, 117, 125, and 137]
- [34] P. C. Maurer, G. Kucsko, C. Latta, L. Jiang, N. Y. Yao, S. D. Bennett, F. Pastawski, D. Hunger, N. Chisholm, M. Markham, D. J. Twitchen, J. I. Cirac, and M. D. Lukin. Room-Temperature Quantum Bit Memory Exceeding One Second. *Science*, 336(6086):1283–1286, June 2012. doi : 10.1126/science.1220513. [cited on p. 32]
- [35] F. Jelezko, T. Gaebel, I. Popa, M. Domhan, A. Gruber, and J. Wrachtrup. Observation of Coherent Oscillation of a Single Nuclear Spin and Realization of a Two-Qubit Conditional Quantum Gate. *Physical Review Letters*, 93(13):130501, September 2004. doi : 10.1103/PhysRevLett.93.130501. [cited on p. 32]
- [36] Abdelghani Laraoui, Florian Dolde, Christian Burk, Friedemann Reinhard, Jörg Wrachtrup, and Carlos A. Meriles. High-resolution correlation spectroscopy of ^{13}C spins near a nitrogen-vacancy centre in diamond. *Nature Communications*, 4:1651, April 2013. doi : 10.1038/ncomms2685. [cited on pp. 32 and 38]
- [37] F. Shagieva, S. Zaiser, P. Neumann, D. B. R. Dasari, R. Stöhr, A. Denisenko, R. Reuter, C. A. Meriles, and J. Wrachtrup. Microwave-Assisted Cross-Polarization of Nuclear Spin

- Ensembles from Optically Pumped Nitrogen-Vacancy Centers in Diamond. *Nano Letters*, 18(6):3731–3737, June 2018. doi:10.1021/acs.nanolett.8b00925. [cited on p. 35]
- [38] Jianming Cai, Alex Retzker, Fedor Jelezko, and Martin B. Plenio. A large-scale quantum simulator on a diamond surface at room temperature. *Nature Physics*, 9(3):168–173, 2013. doi:10.1038/nphys2519. [cited on p. 35]
- [39] H. J. Mamin, M. Kim, M. H. Sherwood, C. T. Rettner, K. Ohno, D. D. Awschalom, and D. Rugar. Nanoscale Nuclear Magnetic Resonance with a Nitrogen-Vacancy Spin Sensor. *Science*, 339(6119):557–560, February 2013. doi:10.1126/science.1231540. [cited on p. 38]
- [40] Johannes Greiner. *Bell Measurement and Quantum Teleportation using Entangled Single Spins in Nitrogen-Vacancy Diamond Defects*. Bachelor’s Thesis, University of Stuttgart, 2011. URL: <http://homepage.cem.itesm.mx/jose.luis.gomez/quantum/baateleportation.pdf>. [cited on pp. 40 and 57]
- [41] Michael A. Nielsen and Isaac L. Chuang. *Quantum Computation and Quantum Information*. Cambridge University Press, October 2000. [cited on pp. 42, 45, 47, 48, 81, 147, and 148]
- [42] Philipp Neumann, Johannes Beck, Matthias Steiner, Florian Rempp, Helmut Fedder, Philip R. Hemmer, Jörg Wrachtrup, and Fedor Jelezko. Single-Shot Readout of a Single Nuclear Spin. *Science*, 329(5991):542–544, July 2010. doi:10.1126/science.1189075. [cited on pp. 44, 137, 147, and 149]
- [43] E. Togan, Y. Chu, A. Imamoglu, and M. D. Lukin. Laser cooling and real-time measurement of the nuclear spin environment of a solid-state qubit. *Nature*, 478(7370):497–501, 2011. doi:10.1038/nature10528. [cited on pp. 51, 60, and 90]
- [44] W. Pfaff, B. J. Hensen, H. Bernien, S. B. van Dam, M. S. Blok, T. H. Taminiau, M. J. Tiggelman, R. N. Schouten, M. Markham, D. J. Twitchen, and R. Hanson. Unconditional

Bibliography

- quantum teleportation between distant solid-state quantum bits. *Science*, 345(6196):532–535, August 2014. doi:10.1126/science.1253512. [cited on p. 57]
- [45] S. F. Huelga, C. Macchiavello, T. Pellizzari, A. K. Ekert, M. B. Plenio, and J. I. Cirac. Improvement of Frequency Standards with Quantum Entanglement. *Physical Review Letters*, 79(20):3865–3868, November 1997. doi:10.1103/PhysRevLett.79.3865. [cited on pp. 57, 96, and 116]
- [46] Johannes N. Greiner, Durga Bhaktavatsala Rao Dasari, and Jörg Wrachtrup. Purification of an unpolarized spin ensemble into entangled singlet pairs. *Scientific Reports*, 7(1):529, April 2017. doi:10.1038/s41598-017-00603-z. [cited on pp. 57, 60, 61, 62, 63, 68, 70, 71, 72, 73, 74, 78, 79, 91, 92, 137, 186, 191, and 195]
- [47] G. Lüders. Concerning the state-change due to the measurement process. *Annalen der Physik*, 15(9):663–670, September 2006. doi:10.1002/andp.200610207. [cited on pp. 58 and 148]
- [48] Hiromichi Nakazato, Tomoko Takazawa, and Kazuya Yuasa. Purification through Zeno-Like Measurements. *Physical Review Letters*, 90(6):060401, February 2003. doi:10.1103/PhysRevLett.90.060401. [cited on pp. 58, 66, and 78]
- [49] Iñigo Urizar-Lanz, Philipp Hyllus, Iñigo Luis Egusquiza, Morgan W. Mitchell, and Géza Tóth. Macroscopic singlet states for gradient magnetometry. *Physical Review A*, 88(1):013626, July 2013. doi:10.1103/PhysRevA.88.013626. [cited on pp. 70 and 93]
- [50] Brijesh Kumar. Quantum spin models with exact dimer ground states. *Physical Review B*, 66(2):024406, June 2002. doi:10.1103/PhysRevB.66.024406. [cited on pp. 70 and 93]
- [51] Ryszard Horodecki, Paweł Horodecki, Michał Horodecki, and Karol Horodecki. Quantum entanglement. *Reviews of Modern Physics*, 81(2):865–942, June 2009. doi:10.1103/RevModPhys.81.865. [cited on pp. 72 and 131]

- [52] Wojciech H. Zurek. Decoherence and the Transition from Quantum to Classical. *Physics Today*, 44(10):36–44, 1991. doi:10.1063/1.881293. [cited on p. 72]
- [53] William K. Wootters. Entanglement of Formation of an Arbitrary State of Two Qubits. *Physical Review Letters*, 80(10):2245–2248, March 1998. doi:10.1103/PhysRevLett.80.2245. [cited on p. 74]
- [54] Richard A. Brualdi. *Introductory combinatorics*. Pearson/Prentice Hall, Upper Saddle River, N.J, 5th ed edition, 2010. OCLC: ocn245024866. [cited on p. 79]
- [55] James L. Hein. *Discrete mathematics*. Jones and Bartlett Publishers, Boston, 2nd ed edition, 2003. [cited on p. 79]
- [56] Christian Schwemmer, Lukas Knips, Daniel Richart, Harald Weinfurter, Tobias Moroder, Matthias Kleinmann, and Otfried Gühne. Systematic Errors in Current Quantum State Tomography Tools. *Physical Review Letters*, 114(8):080403, February 2015. doi:10.1103/PhysRevLett.114.080403. [cited on pp. 93 and 134]
- [57] Iagoba Apellaniz, Matthias Kleinmann, Otfried Gühne, and Géza Tóth. Optimal witnessing of the quantum Fisher information with few measurements. *Physical Review A*, 95(3):032330, March 2017. doi:10.1103/PhysRevA.95.032330. [cited on p. 93]
- [58] Masahiro Kitagawa and Masahito Ueda. Squeezed spin states. *Physical Review A*, 47(6):5138–5143, June 1993. doi:10.1103/PhysRevA.47.5138. [cited on pp. 96, 98, 99, 101, 102, 103, 104, and 128]
- [59] Xiaoguang Wang and Barry C. Sanders. Spin squeezing and pairwise entanglement for symmetric multiqubit states. *Physical Review A*, 68(1):012101, July 2003. doi:10.1103/PhysRevA.68.012101. [cited on pp. 96, 99, 102, and 104]
- [60] N. Killoran, M. Cramer, and M. B. Plenio. Extracting Entanglement from Identical Particles.

Bibliography

- Physical Review Letters*, 112(15):150501, April 2014. doi:10.1103/PhysRevLett.112.150501. [cited on pp. 96 and 99]
- [61] J. Hald, J. L. Sørensen, C. Schori, and E. S. Polzik. Spin Squeezed Atoms: A Macroscopic Entangled Ensemble Created by Light. *Physical Review Letters*, 83(7):1319–1322, August 1999. doi:10.1103/PhysRevLett.83.1319. [cited on pp. 96 and 128]
- [62] R. J. Sewell, M. Koschorreck, M. Napolitano, B. Dubost, N. Behbood, and M. W. Mitchell. Magnetic Sensitivity Beyond the Projection Noise Limit by Spin Squeezing. *Physical Review Letters*, 109(25):253605, December 2012. doi:10.1103/PhysRevLett.109.253605. [cited on p. 96]
- [63] T. Fernholz, H. Krauter, K. Jensen, J. F. Sherson, A. S. Sørensen, and E. S. Polzik. Spin Squeezing of Atomic Ensembles via Nuclear-Electronic Spin Entanglement. *Physical Review Letters*, 101(7):073601, August 2008. doi:10.1103/PhysRevLett.101.073601. [cited on p. 96]
- [64] Jian Ma, Xiaoguang Wang, C. P. Sun, and Franco Nori. Quantum spin squeezing. *Physics Reports*, 509(2–3):89–165, December 2011. doi:10.1016/j.physrep.2011.08.003. [cited on p. 96]
- [65] M. Vengalattore, J. M. Higbie, S. R. Leslie, J. Guzman, L. E. Sadler, and D. M. Stamper-Kurn. High-Resolution Magnetometry with a Spinor Bose-Einstein Condensate. *Physical Review Letters*, 98(20):200801, 2007. doi:10.1103/PhysRevLett.98.200801. [cited on p. 96]
- [66] C. Gross, T. Zibold, E. Nicklas, J. Estève, and M. K. Oberthaler. Nonlinear atom interferometer surpasses classical precision limit. *Nature*, 464(7292):1165–1169, April 2010. doi:10.1038/nature08919. [cited on p. 96]
- [67] A. R. Usha Devi, Xiaoguang Wang, and B. C. Sanders. Spin Squeezing Criterion with Local

- Unitary Invariance. *Quantum Information Processing*, 2(3):207–220, June 2003. doi:10.1023/B:QINP.00000004125.12489.f4. [cited on p. 96]
- [68] Özgür E. Müstecaplıoğlu, M. Zhang, and L. You. Spin squeezing and entanglement in spinor condensates. *Physical Review A*, 66(3):033611, September 2002. doi:10.1103/PhysRevA.66.033611. [cited on pp. 97 and 98]
- [69] D. J. Wineland, J. J. Bollinger, W. M. Itano, F. L. Moore, and D. J. Heinzen. Spin squeezing and reduced quantum noise in spectroscopy. *Physical Review A*, 46(11):R6797–R6800, December 1992. doi:10.1103/PhysRevA.46.R6797. [cited on pp. 99 and 109]
- [70] D. J. Wineland, J. J. Bollinger, W. M. Itano, and D. J. Heinzen. Squeezed atomic states and projection noise in spectroscopy. *Physical Review A*, 50(1):67–88, July 1994. doi:10.1103/PhysRevA.50.67. [cited on pp. 99 and 109]
- [71] Anders S. Sørensen and Klaus Mølmer. Entanglement and Extreme Spin Squeezing. *Physical Review Letters*, 86(20):4431–4434, 2001. doi:10.1103/PhysRevLett.86.4431. [cited on p. 104]
- [72] G. Waldherr, Y. Wang, S. Zaiser, M. Jamali, T. Schulte-Herbrüggen, H. Abe, T. Ohshima, J. Isoya, J. F. Du, P. Neumann, and J. Wrachtrup. Quantum error correction in a solid-state hybrid spin register. *Nature*, 506(7487):204–207, February 2014. doi:10.1038/nature12919. [cited on pp. 107, 118, and 137]
- [73] P. Neumann, N. Mizuochi, F. Rempp, P. Hemmer, H. Watanabe, S. Yamasaki, V. Jacques, T. Gaebel, F. Jelezko, and J. Wrachtrup. Multipartite Entanglement Among Single Spins in Diamond. *Science*, 320(5881):1326–1329, June 2008. doi:10.1126/science.1157233. [cited on p. 107]
- [74] G. R. Jin and C. K. Law. Relationship between spin squeezing and single-particle coherence in two-component Bose-Einstein condensates with Josephson coupling. *Physical Review A*,

Bibliography

- 78(6):063620, December 2008. doi:10.1103/PhysRevA.78.063620. [cited on pp. 108 and 109]
- [75] M. Napolitano, M. Koschorreck, B. Dubost, N. Behbood, R. J. Sewell, and M. W. Mitchell. Interaction-based quantum metrology showing scaling beyond the Heisenberg limit. *Nature*, 471(7339):486–489, March 2011. doi:10.1038/nature09778. [cited on pp. 116, 120, and 122]
- [76] Emi Yukawa, G. J. Milburn, C. A. Holmes, Masahito Ueda, and Kae Nemoto. Precision measurements using squeezed spin states via two-axis countertwisting interactions. *Physical Review A*, 90(6):062132, 2014. doi:10.1103/PhysRevA.90.062132. [cited on p. 119]
- [77] G. de Lange, Z. H. Wang, D. Ristè, V. V. Dobrovitski, and R. Hanson. Universal Dynamical Decoupling of a Single Solid-State Spin from a Spin Bath. *Science*, 330(6000):60–63, October 2010. doi:10.1126/science.1192739. [cited on p. 121]
- [78] Sergio Boixo, Steven T. Flammia, Carlton M. Caves, and JM Geremia. Generalized Limits for Single-Parameter Quantum Estimation. *Physical Review Letters*, 98(9):090401, February 2007. doi:10.1103/PhysRevLett.98.090401. [cited on p. 122]
- [79] Julia Michl, Jakob Steiner, Andrej Denisenko, André Bülau, André Zimmermann, Kazuo Nakamura, Hitoshi Sumiya, Shinobu Onoda, Philipp Neumann, Junichi Isoya, and Jörg Wrachtrup. Robust and Accurate Electric Field Sensing with Solid State Spin Ensembles. *Nano Letters*, 19(8):4904–4910, August 2019. doi:10.1021/acs.nanolett.9b00900. [cited on p. 122]
- [80] Florian Dolde, Marcus W. Doherty, Julia Michl, Ingmar Jakobi, Boris Naydenov, Sebastien Pezzagna, Jan Meijer, Philipp Neumann, Fedor Jelezko, Neil B. Manson, and Jörg Wrachtrup. Nanoscale Detection of a Single Fundamental Charge in Ambient Conditions

- Using the NV- Center in Diamond. *Physical Review Letters*, 112(9):097603, March 2014. doi:10.1103/PhysRevLett.112.097603. [cited on p. 122]
- [81] F. Ziem, M. Garsi, H. Fedder, and J. Wrachtrup. Quantitative nanoscale MRI with a wide field of view. *Scientific Reports*, 9(1):1–9, August 2019. doi:10.1038/s41598-019-47084-w. [cited on p. 122]
- [82] Anders S. Sørensen and Klaus Mølmer. Entanglement and Extreme Spin Squeezing. *Physical Review Letters*, 86(20):4431–4434, May 2001. doi:10.1103/PhysRevLett.86.4431. [cited on p. 123]
- [83] A. M. Rey, L. Jiang, M. Fleischhauer, E. Demler, and M. D. Lukin. Many-body protected entanglement generation in interacting spin systems. *Physical Review A*, 77(5):052305, May 2008. doi:10.1103/PhysRevA.77.052305. [cited on pp. 123 and 125]
- [84] Julia Michl, Tokuyuki Teraji, Sebastian Zaiser, Ingmar Jakobi, Gerald Waldherr, Florian Dolde, Philipp Neumann, Marcus W. Doherty, Neil B. Manson, Junichi Isoya, and Jörg Wrachtrup. Perfect alignment and preferential orientation of nitrogen-vacancy centers during chemical vapor deposition diamond growth on (111) surfaces. *Applied Physics Letters*, 104(10):102407, March 2014. doi:10.1063/1.4868128. [cited on p. 126]
- [85] S. Pezzagna, D. Rogalla, H.-W. Becker, I. Jakobi, F. Dolde, B. Naydenov, J. Wrachtrup, F. Jelezko, C. Trautmann, and J. Meijer. Creation of colour centres in diamond by collimated ion-implantation through nano-channels in mica. *physica status solidi (a)*, 208(9):2017–2022, 2011. doi:10.1002/pssa.201100455. [cited on p. 127]
- [86] S. Ali Momenzadeh, Felipe Fávoro de Oliveira, Philipp Neumann, D. D. Bhaktavatsala Rao, Andrej Denisenko, Morteza Amjadi, Zhiqin Chu, Sen Yang, Neil B. Manson, Marcus W. Doherty, and Jörg Wrachtrup. Thin Circular Diamond Membrane with Embedded Nitrogen-Vacancy Centers for Hybrid Spin-Mechanical Quantum Systems. *Physical Review Applied*, 6(2):024026, August 2016. doi:10.1103/PhysRevApplied.6.024026. [cited on p. 127]

Bibliography

- [87] Meghana Raghunandan, Jörg Wrachtrup, and Hendrik Weimer. High-Density Quantum Sensing with Dissipative First Order Transitions. *Physical Review Letters*, 120(15):150501, April 2018. doi : 10.1103/PhysRevLett.120.150501. [cited on p. 127]
- [88] Sen Yang, Ya Wang, D. D. Bhaktavatsala Rao, Thai Hien Tran, Ali S. Momenzadeh, M. Markham, D. J. Twitchen, Ping Wang, Wen Yang, Rainer Stöhr, Philipp Neumann, Hideo Kosaka, and Jörg Wrachtrup. High-fidelity transfer and storage of photon states in a single nuclear spin. *Nature Photonics*, 10(8):507–511, August 2016. doi : 10.1038/nphoton.2016.103. [cited on p. 128]
- [89] A. Kuzmich, Klaus Mølmer, and E. S. Polzik. Spin Squeezing in an Ensemble of Atoms Illuminated with Squeezed Light. *Physical Review Letters*, 79(24):4782–4785, December 1997. doi : 10.1103/PhysRevLett.79.4782. [cited on p. 128]
- [90] J. Hald and E. S. Polzik. Mapping a quantum state of light onto atoms. *Journal of Optics B: Quantum and Semiclassical Optics*, 3(1):S83, February 2001. doi : 10.1088/1464-4266/3/1/365. [cited on p. 128]
- [91] Thiago P. Mayer Alegre, Charles Santori, Gilberto Medeiros-Ribeiro, and Raymond G. Beusoleil. Polarization-selective excitation of nitrogen vacancy centers in diamond. *Physical Review B*, 76(16):165205, October 2007. doi : 10.1103/PhysRevB.76.165205. [cited on p. 128]
- [92] Andreas Kronwald, Florian Marquardt, and Aashish A. Clerk. Dissipative optomechanical squeezing of light. *New Journal of Physics*, 16(6):063058, June 2014. doi : 10.1088/1367-2630/16/6/063058. [cited on p. 129]
- [93] David Vitali, Shabir Barzanjeh, Mehdi Abdi, Paolo Tombesi, and Gerard J. Milburn. A Reversible Optical to Microwave Quantum Interface. In *Research in Optical Sciences*, OSA Technical Digest, page QM3A.6. Optical Society of America, March 2012. doi : 10.1364/QIM.2012.QM3A.6. [cited on p. 129]

- [94] C. Eichler, D. Bozyigit, C. Lang, M. Baur, L. Steffen, J. M. Fink, S. Filipp, and A. Wallraff. Observation of Two-Mode Squeezing in the Microwave Frequency Domain. *Physical Review Letters*, 107(11):113601, September 2011. doi:10.1103/PhysRevLett.107.113601. [cited on p. 129]
- [95] Shane Dooley, Emi Yukawa, Yuichiro Matsuzaki, George C. Knee, William J. Munro, and Kae Nemoto. A hybrid-systems approach to spin squeezing using a highly dissipative ancillary system. *New Journal of Physics*, 18(5):053011, May 2016. doi:10.1088/1367-2630/18/5/053011. [cited on p. 129]
- [96] D.D. Bhaktavatsala Rao, S. Ali Momenzadeh, and Jörg Wrachtrup. Heralded Control of Mechanical Motion by Single Spins. *Physical Review Letters*, 117(7), August 2016. doi:10.1103/PhysRevLett.117.077203. [cited on p. 129]
- [97] Jianming Cai, Fedor Jelezko, and Martin B. Plenio. Hybrid sensors based on colour centres in diamond and piezoactive layers. *Nature Communications*, 5, June 2014. doi:10.1038/ncomms5065. [cited on p. 129]
- [98] Paweł Horodecki, Michał Horodecki, and Ryszard Horodecki. Bound entanglement can be activated. *Physical review letters*, 82(5):1056, 1999. doi:10.1103/PhysRevLett.82.1056. [cited on pp. 131, 132, 137, and 138]
- [99] Karol Horodecki, Michał Horodecki, Paweł Horodecki, Ryszard Horodecki, Marcin Pawłowski, and Mohamed Bourennane. Contextuality offers device-independent security. *arXiv:1006.0468 [quant-ph]*, June 2010. URL: <http://arxiv.org/abs/1006.0468>. [cited on p. 131]
- [100] Ł. Czekaj, A. Przysiężna, M. Horodecki, and P. Horodecki. Quantum metrology: Heisenberg limit with bound entanglement. *Physical Review A*, 92(6):062303, 2015. doi:10.1103/PhysRevA.92.062303. [cited on pp. 131, 132, 137, 138, and 158]

Bibliography

- [101] Fumihiko Kaneda, Ryosuke Shimizu, Satoshi Ishizaka, Yasuyoshi Mitsuori, Hideo Kosaka, and Keiichi Edamatsu. Experimental Activation of Bound Entanglement. *Physical Review Letters*, 109(4), July 2012. doi : [10.1103/PhysRevLett.109.040501](https://doi.org/10.1103/PhysRevLett.109.040501). [cited on pp. 132 and 137]
- [102] Fabian Bohnet-Waldraff, D. Braun, and O. Giraud. Quantumness of spin-1 states. *Physical Review A*, 93(1):012104, January 2016. doi : [10.1103/PhysRevA.93.012104](https://doi.org/10.1103/PhysRevA.93.012104). [cited on pp. 132 and 158]
- [103] Szilárd Szalay. Multipartite entanglement measures. *Physical Review A*, 92(4):042329, October 2015. doi : [10.1103/PhysRevA.92.042329](https://doi.org/10.1103/PhysRevA.92.042329). [cited on p. 132]
- [104] Michał Horodecki, Paweł Horodecki, and Ryszard Horodecki. Mixed-State Entanglement and Distillation: Is there a “Bound” Entanglement in Nature? *Physical Review Letters*, 80(24):5239–5242, June 1998. doi : [10.1103/PhysRevLett.80.5239](https://doi.org/10.1103/PhysRevLett.80.5239). [cited on pp. 132, 133, 134, and 138]
- [105] Lluís Masanes. All Bipartite Entangled States Are Useful for Information Processing. *Physical Review Letters*, 96(15):150501, April 2006. doi : [10.1103/PhysRevLett.96.150501](https://doi.org/10.1103/PhysRevLett.96.150501). [cited on pp. 132, 138, and 158]
- [106] Karol Horodecki, Michał Horodecki, Paweł Horodecki, and Jonathan Oppenheim. Secure Key from Bound Entanglement. *Physical Review Letters*, 94(16):160502, April 2005. doi : [10.1103/PhysRevLett.94.160502](https://doi.org/10.1103/PhysRevLett.94.160502). [cited on pp. 132, 138, and 158]
- [107] Tobias Moroder, Oleg Gittsovich, Marcus Huber, and Otfried Gühne. Steering Bound Entangled States: A Counterexample to the Stronger Peres Conjecture. *Physical Review Letters*, 113(5):050404, August 2014. doi : [10.1103/PhysRevLett.113.050404](https://doi.org/10.1103/PhysRevLett.113.050404). [cited on pp. 132, 138, and 158]

- [108] Tamás Vértesi and Nicolas Brunner. Disproving the Peres conjecture by showing Bell non-locality from bound entanglement. *Nature Communications*, 5(1):1–5, November 2014. doi:10.1038/ncomms6297. [cited on pp. 132, 138, and 158]
- [109] Fernando G. S. L. Brandao and Martin B. Plenio. Entanglement Theory and the Second Law of Thermodynamics. *Nature Physics*, 4(11):873–877, October 2008. arXiv:0810.2319 [quant-ph]. doi:10.1038/nphys1100. [cited on p. 132]
- [110] Michał Horodecki, Jonathan Oppenheim, and Ryszard Horodecki. Are the Laws of Entanglement Theory Thermodynamical? *Physical Review Letters*, 89(24):240403, November 2002. doi:10.1103/PhysRevLett.89.240403. [cited on p. 132]
- [111] Géza Tóth and Tamás Vértesi. Quantum States with a Positive Partial Transpose are Useful for Metrology. *Physical Review Letters*, 120(2):020506, January 2018. doi:10.1103/PhysRevLett.120.020506. [cited on pp. 132, 138, and 158]
- [112] Asher Peres. Separability Criterion for Density Matrices. *Physical Review Letters*, 77(8):1413–1415, August 1996. doi:10.1103/PhysRevLett.77.1413. [cited on pp. 132 and 133]
- [113] Gael Sentís, Christopher Eltschka, and Jens Siewert. Quantitative bound entanglement in two-qutrit states. *Physical Review A*, 94(2):020302, August 2016. doi:10.1103/PhysRevA.94.020302. [cited on pp. 133, 134, and 135]
- [114] Gael Sentís, Johannes N. Greiner, Jiangwei Shang, Jens Siewert, and Matthias Kleinmann. Bound entangled states fit for robust experimental verification. *Quantum*, 2:113, December 2018. doi:10.22331/q-2018-12-18-113. [cited on pp. 134, 135, 136, 137, 138, 192, and 196]
- [115] Otfried Gühne and Géza Tóth. Entanglement detection. *Physics Reports*, 474(1):1–75, April 2009. doi:10.1016/j.physrep.2009.02.004. [cited on p. 136]

Bibliography

- [116] F. Dolde, I. Jakobi, B. Naydenov, N. Zhao, S. Pezzagna, C. Trautmann, J. Meijer, P. Neumann, F. Jelezko, and J. Wrachtrup. Room-temperature entanglement between single defect spins in diamond. *Nature Physics*, 9(3):139–143, March 2013. doi : 10.1038/nphys2545. [cited on p. 137]
- [117] H. Bernien, B. Hensen, W. Pfaff, G. Koolstra, M. S. Blok, L. Robledo, T. H. Taminiau, M. Markham, D. J. Twitchen, L. Childress, and R. Hanson. Heralded entanglement between solid-state qubits separated by three metres. *Nature*, 497(7447):86–90, 2013. doi : 10.1038/nature12016. [cited on p. 137]
- [118] Matthias Pfender, Nabeel Aslam, Hitoshi Sumiya, Shinobu Onoda, Philipp Neumann, Junichi Isoya, Carlos A. Meriles, and Jörg Wrachtrup. Nonvolatile nuclear spin memory enables sensor-unlimited nanoscale spectroscopy of small spin clusters. *Nature Communications*, 8(1):834, October 2017. doi : 10.1038/s41467-017-00964-z. [cited on p. 137]
- [119] Ernst Specker. Die Logik nicht gleichzeitig entscheidbarer Aussagen. *Dialectica*, 14(2-3):239–246, 1960. doi : 10.1111/j.1746-8361.1960.tb00422.x. [cited on p. 139]
- [120] Otfried Gühne and Matthias Kleinmann. Auf den Kontext kommt es an. *Physik Journal*, 12(2):25, 2013. [cited on pp. 139 and 141]
- [121] E. Specker Simon Kochen. The Problem of Hidden Variables in Quantum Mechanics. *Indiana University Mathematics Journal*, 17(1):59–87, 1968. [cited on p. 139]
- [122] Adán Cabello. Simple method for experimentally testing any form of quantum contextuality. *Physical Review A*, 93(3):032102, 2016. doi : 10.1103/PhysRevA.93.032102. [cited on pp. 139 and 158]
- [123] Radek Lapkiewicz, Peizhe Li, Christoph Schaeff, Nathan K. Langford, Sven Ramelow, Marcin Wieśniak, and Anton Zeilinger. Experimental non-classicality of an indivisible quantum system. *Nature*, 474(7352):490–493, June 2011. doi : 10.1038/nature10119. [cited on pp. 139 and 158]

- [124] Alley Hameedi, Armin Tavakoli, Breno Marques, and Mohamed Bourennane. Communication Games Reveal Preparation Contextuality. *Physical Review Letters*, 119(22):220402, November 2017. doi:10.1103/PhysRevLett.119.220402. [cited on p. 139]
- [125] Andrea Crespi, Marco Bentivegna, Ioannis Pitsios, Davide Rusca, Davide Poderini, Gonzalo Carvacho, Vincenzo D’Ambrosio, Adán Cabello, Fabio Sciarrino, and Roberto Osellame. Single-Photon Quantum Contextuality on a Chip. *ACS Photonics*, 4(11):2807–2812, November 2017. doi:10.1021/acsp Photonics.7b00793. [cited on pp. 139, 145, and 158]
- [126] S. B. van Dam, J. Cramer, T. H. Taminiiau, and R. Hanson. Multipartite Entanglement Generation and Contextuality Tests Using Nondestructive Three-Qubit Parity Measurements. *Physical Review Letters*, 123(5):050401, July 2019. doi:10.1103/PhysRevLett.123.050401. [cited on pp. 139, 140, and 158]
- [127] Juan Bermejo-Vega, Nicolas Delfosse, Dan E. Browne, Cihan Okay, and Robert Raussendorf. Contextuality as a Resource for Models of Quantum Computation with Qubits. *Physical Review Letters*, 119(12):120505, September 2017. doi:10.1103/PhysRevLett.119.120505. [cited on pp. 139 and 142]
- [128] Mark Howard, Joel Wallman, Victor Veitch, and Joseph Emerson. Contextuality supplies the ‘magic’ for quantum computation. *Nature*, 510(7505):351–355, June 2014. doi:10.1038/nature13460. [cited on pp. 139 and 142]
- [129] Xiao-Min Hu, Jiang-Shan Chen, Bi-Heng Liu, Yu Guo, Yun-Feng Huang, Zong-Quan Zhou, Yong-Jian Han, Chuan-Feng Li, and Guang-Can Guo. Experimental Test of Compatibility-Loophole-Free Contextuality with Spatially Separated Entangled Qutrits. *Physical Review Letters*, 117(17):170403, 2016. doi:10.1103/PhysRevLett.117.170403. [cited on pp. 140 and 164]

Bibliography

- [130] Matthias Kleinmann, Otfried Gühne, José R. Portillo, Jan-Åke Larsson, and Adán Cabello. Memory cost of quantum contextuality. *New Journal of Physics*, 13(11):113011, 2011. doi:10.1088/1367-2630/13/11/113011. [cited on pp. 140 and 164]
- [131] David A. Meyer. Finite Precision Measurement Nullifies the Kochen-Specker Theorem. *Physical Review Letters*, 83(19):3751–3754, November 1999. doi:10.1103/PhysRevLett.83.3751. [cited on pp. 140 and 164]
- [132] Adán Cabello and Marcelo Terra Cunha. Proposal of a Two-Qutrit Contextuality Test Free of the Finite Precision and Compatibility Loopholes. *Physical Review Letters*, 106(19):190401, 2011. doi:10.1103/PhysRevLett.106.190401. [cited on pp. 140, 158, and 164]
- [133] Simon Kochen and E. P. Specker. The Problem of Hidden Variables in Quantum Mechanics. In C. A. Hooker, editor, *The Logico-Algebraic Approach to Quantum Mechanics*, number 5a in The University of Western Ontario Series in Philosophy of Science, pages 293–328. Springer Netherlands, 1975. doi:10.1007/978-94-010-1795-4_17. [cited on p. 140]
- [134] Radek Lapkiewicz, Peizhe Li, Christoph Schaeff, Nathan K. Langford, Sven Ramelow, Marcin Wieśniak, and Anton Zeilinger. Experimental non-classicality of an indivisible quantum system. *Nature*, 474(7352):490–493, June 2011. doi:10.1038/nature10119. [cited on p. 140]
- [135] Richard E. George, Lucio M. Robledo, Owen J. E. Maroney, Machiel S. Blok, Hannes Bernien, Matthew L. Markham, Daniel J. Twitchen, John J. L. Morton, G. Andrew D. Briggs, and Ronald Hanson. Opening up three quantum boxes causes classically undetectable wavefunction collapse. *Proceedings of the National Academy of Sciences*, 110(10):3777–3781, March 2013. doi:10.1073/pnas.1208374110. [cited on pp. 140 and 145]

- [136] Xi Kong, Mingjun Shi, Mengqi Wang, Fazhan Shi, Pengfei Wang, Fei Kong, Pu Huang, Qi Zhang, Wenchao Ma, Hongwei Chen, Chenyong Ju, Mingliang Tian, Changkui Duan, Sixia Yu, and Jiangfeng Du. Experimental test of non-classicality of quantum mechanics using an individual atomic solid-state quantum system. *arXiv:1602.02455 [quant-ph]*, February 2016. URL: <http://arxiv.org/abs/1602.02455>. [cited on pp. 140 and 145]
- [137] Asher Peres. Incompatible results of quantum measurements. *Physics Letters A*, 151(3):107–108, December 1990. doi:10.1016/0375-9601(90)90172-K. [cited on pp. 140 and 141]
- [138] N. David Mermin. Simple unified form for the major no-hidden-variables theorems. *Physical Review Letters*, 65(27):3373–3376, December 1990. doi:10.1103/PhysRevLett.65.3373. [cited on pp. 140 and 141]
- [139] Sixia Yu and C. H. Oh. State-Independent Proof of Kochen-Specker Theorem with 13 Rays. *Physical Review Letters*, 108(3):030402, January 2012. doi:10.1103/PhysRevLett.108.030402. [cited on p. 145]
- [140] Anatoly Kulikov, Markus Jerger, Anton Potočnik, Andreas Wallraff, and Arkady Fedorov. Realization of a Quantum Random Generator Certified with the Kochen-Specker Theorem. *Physical Review Letters*, 119(24):240501, December 2017. doi:10.1103/PhysRevLett.119.240501. [cited on pp. 145, 163, 165, and 184]
- [141] F. M. Leupold, M. Malinowski, C. Zhang, V. Negnevitsky, A. Cabello, J. Alonso, and J. P. Home. Sustained State-Independent Quantum Contextual Correlations from a Single Ion. *Physical Review Letters*, 120(18):180401, May 2018. doi:10.1103/PhysRevLett.120.180401. [cited on p. 145]
- [142] Antonio Acín and Lluís Masanes. Certified randomness in quantum physics. *Nature*, 540(7632):213–219, 2016. doi:10.1038/nature20119. [cited on pp. 145, 160, 169, 174, and 178]

Bibliography

- [143] Lucio Robledo, Lilian Childress, Hannes Bernien, Bas Hensen, Paul F. A. Alkemade, and Ronald Hanson. High-fidelity projective read-out of a solid-state spin quantum register. *Nature*, 477(7366):574–578, September 2011. doi:10.1038/nature10401. [cited on p. 147]
- [144] Gerhart Lüders. Über die Zustandsänderung durch den Meßprozeß. *Annalen der Physik*, 443(5-8):322–328, January 1950. doi:10.1002/andp.19504430510. [cited on pp. 148 and 149]
- [145] Mark Um, Qi Zhao, Junhua Zhang, Pengfei Wang, Ye Wang, Mu Qiao, Hongyi Zhou, Xiongfeng Ma, and Kihwan Kim. Randomness Expansion Secured by Quantum Contextuality. *Physical Review Applied*, 13(3):034077, March 2020. doi:10.1103/PhysRevApplied.13.034077. [cited on pp. 149, 156, 158, 163, 165, and 184]
- [146] Andreas Winter. What does an experimental test of quantum contextuality prove or disprove? *Journal of Physics A: Mathematical and Theoretical*, 47(42):424031, 2014. doi:10.1088/1751-8113/47/42/424031. [cited on p. 151]
- [147] Matthias Kleinmann, Costantino Budroni, Jan-Åke Larsson, Otfried Gühne, and Adán Cabello. Optimal Inequalities for State-Independent Contextuality. *Physical Review Letters*, 109(25):250402, 2012. doi:10.1103/PhysRevLett.109.250402. [cited on p. 158]
- [148] P. Shor. Polynomial-Time Algorithms for Prime Factorization and Discrete Logarithms on a Quantum Computer. *SIAM Journal on Computing*, 26(5):1484–1509, October 1997. doi:10.1137/S0097539795293172. [cited on p. 159]
- [149] Arjen K. Lenstra, James P. Hughes, Maxime Augier, Joppe W. Bos, Thorsten Kleinjung, and Christophe Wachter. Ron was wrong, Whit is right. Technical Report 064, 2012. URL: <https://eprint.iacr.org/2012/064>. [cited on p. 160]
- [150] Georg T. Becker, Francesco Regazzoni, Christof Paar, and Wayne P. Burleson. Stealthy Dopant-Level Hardware Trojans. In *Cryptographic Hardware and Embedded Systems -*

- CHES 2013*, Lecture Notes in Computer Science, pages 197–214. Springer, Berlin, Heidelberg, August 2013. doi:10.1007/978-3-642-40349-1_12. [cited on pp. 160 and 171]
- [151] Mario Stipčević and Çetin Kaya Koç. True Random Number Generators. In Çetin Kaya Koç, editor, *Open Problems in Mathematics and Computational Science*, pages 275–315. Springer International Publishing, 2014. doi:10.1007/978-3-319-10683-0_12. [cited on p. 160]
- [152] Miguel Herrero-Collantes and Juan Carlos Garcia-Escartin. Quantum random number generators. *Reviews of Modern Physics*, 89(1):015004, February 2017. doi:10.1103/RevModPhys.89.015004. [cited on pp. 160 and 165]
- [153] Xiongfeng Ma, Xiao Yuan, Zhu Cao, Bing Qi, and Zhen Zhang. Quantum random number generation. *npj Quantum Information*, 2:npjqi201621, June 2016. doi:10.1038/npjqi.2016.21. [cited on pp. 160 and 165]
- [154] Christian Gabriel, Christoffer Wittmann, Denis Sych, Ruifang Dong, Wolfgang Maurer, Ulrik L. Andersen, Christoph Marquardt, and Gerd Leuchs. A generator for unique quantum random numbers based on vacuum states. *Nature Photonics*, 4(10):711–715, October 2010. doi:10.1038/nphoton.2010.197. [cited on p. 160]
- [155] Bruno Sanguinetti, Anthony Martin, Hugo Zbinden, and Nicolas Gisin. Quantum Random Number Generation on a Mobile Phone. *Physical Review X*, 4(3):031056, September 2014. doi:10.1103/PhysRevX.4.031056. [cited on p. 160]
- [156] André Stefanov, Nicolas Gisin, Olivier Guinnard, Laurent Guinnard, and Hugo Zbinden. Optical quantum random number generator. *Journal of Modern Optics*, 47(4):595–598, March 2000. doi:10.1080/09500340008233380. [cited on p. 160]
- [157] Thomas Jennewein, Ulrich Achleitner, Gregor Weihs, Harald Weinfurter, and Anton Zeilinger. A fast and compact quantum random number generator. *Review of Scientific Instruments*, 71(4):1675–1680, April 2000. doi:10.1063/1.1150518. [cited on p. 160]

Bibliography

- [158] Harald Fürst, Henning Weier, Sebastian Nauerth, Davide G. Marangon, Christian Kurtsiefer, and Harald Weinfurter. High speed optical quantum random number generation. *Optics Express*, 18(12):13029–13037, June 2010. doi:10.1364/OE.18.013029. [cited on p. 160]
- [159] Yicheng Shi, Brenda Chng, and Christian Kurtsiefer. Random numbers from vacuum fluctuations. *Applied Physics Letters*, 109(4):041101, July 2016. doi:10.1063/1.4959887. [cited on p. 160]
- [160] Daniela Frauchiger, Renato Renner, and Matthias Troyer. True randomness from realistic quantum devices. *arXiv:1311.4547 [quant-ph]*, November 2013. URL: <http://arxiv.org/abs/1311.4547>. [cited on pp. 160, 165, 174, and 183]
- [161] S. Pironio, A. Acín, S. Massar, A. Boyer de la Giroday, D. N. Matsukevich, P. Maunz, S. Olmschenk, D. Hayes, L. Luo, T. A. Manning, and C. Monroe. Random numbers certified by Bell’s theorem. *Nature*, 464(7291):1021–1024, April 2010. doi:10.1038/nature09008. [cited on p. 160]
- [162] Albert Einstein, Max Born, and Hedwig Born. *The Born-Einstein letters: correspondence between Albert Einstein and Max and Hedwig Born from 1916-1955, with commentaries by Max Born*. Macmillan, 1971. [cited on p. 160]
- [163] Albert Einstein, Boris Podolsky, and Nathan Rosen. Can quantum-mechanical description of physical reality be considered complete? *Physical review*, 47(10):777, 1935. [cited on p. 161]
- [164] John S. Bell. On the einstein-podolsky-rosen paradox. *Physics*, 1(3):195–200, 1964. URL: <http://philoscience.unibe.ch/documents/TexteHS10/bell1964epr.pdf>. [cited on p. 161]

- [165] John F. Clauser, Michael A. Horne, Abner Shimony, and Richard A. Holt. Proposed Experiment to Test Local Hidden-Variable Theories. *Physical Review Letters*, 23(15):880–884, 1969. doi:10.1103/PhysRevLett.23.880. [cited on p. 161]
- [166] Stuart J. Freedman and John F. Clauser. Experimental Test of Local Hidden-Variable Theories. *Physical Review Letters*, 28(14):938–941, April 1972. doi:10.1103/PhysRevLett.28.938. [cited on p. 162]
- [167] Alain Aspect, Philippe Grangier, and Gérard Roger. Experimental Tests of Realistic Local Theories via Bell’s Theorem. *Physical Review Letters*, 47(7):460–463, August 1981. doi:10.1103/PhysRevLett.47.460. [cited on p. 162]
- [168] B. Hensen, H. Bernien, A. E. Dréau, A. Reiserer, N. Kalb, M. S. Blok, J. Ruitenberg, R. F. L. Vermeulen, R. N. Schouten, C. Abellán, W. Amaya, V. Pruneri, M. W. Mitchell, M. Markham, D. J. Twitchen, D. Elkouss, S. Wehner, T. H. Taminiau, and R. Hanson. Loophole-free Bell inequality violation using electron spins separated by 1.3 kilometres. *Nature*, 526(7575):682–686, 2015. doi:10.1038/nature15759. [cited on pp. 162, 163, and 164]
- [169] Marissa Giustina, Marijn A. M. Versteegh, Sören Wengerowsky, Johannes Handsteiner, Armin Hochrainer, Kevin Phelan, Fabian Steinlechner, Johannes Kofler, Jan-Åke Larsson, Carlos Abellán, Waldimar Amaya, Valerio Pruneri, Morgan W. Mitchell, Jörn Beyer, Thomas Gerrits, Adriana E. Lita, Lynden K. Shalm, Sae Woo Nam, Thomas Scheidl, Rupert Ursin, Bernhard Wittmann, and Anton Zeilinger. Significant-Loophole-Free Test of Bell’s Theorem with Entangled Photons. *Physical Review Letters*, 115(25):250401, December 2015. doi:10.1103/PhysRevLett.115.250401. [cited on pp. 162 and 163]
- [170] Jochen Szangolies, Matthias Kleinmann, and Otfried Gühne. Tests against noncontextual models with measurement disturbances. *Physical Review A*, 87(5):050101, May 2013. doi:10.1103/PhysRevA.87.050101. [cited on p. 162]

Bibliography

- [171] Alastair A. Abbott, Cristian S. Calude, Jonathan Conder, and Karl Svozil. Strong Kochen-Specker theorem and incomputability of quantum randomness. *Physical Review A*, 86(6):062109, 2012. doi : 10.1103/PhysRevA.86.062109. [cited on pp. 163 and 165]
- [172] S. Pironio, A. Acín, S. Massar, A. Boyer de la Giroday, D. N. Matsukevich, P. Maunz, S. Olmschenk, D. Hayes, L. Luo, T. A. Manning, and C. Monroe. Random numbers certified by Bell’s theorem. *Nature*, 464(7291):1021–1024, April 2010. doi : 10.1038/nature09008. [cited on pp. 163 and 165]
- [173] Stefano Pironio and Serge Massar. Security of practical private randomness generation. *Physical Review A*, 87(1):012336, January 2013. doi : 10.1103/PhysRevA.87.012336. [cited on pp. 163, 164, and 165]
- [174] Nicolas Brunner, Daniel Cavalcanti, Stefano Pironio, Valerio Scarani, and Stephanie Wehner. Bell nonlocality. *Reviews of Modern Physics*, 86(2):419–478, April 2014. doi : 10.1103/RevModPhys.86.419. [cited on p. 163]
- [175] Otfried Gühne, Matthias Kleinmann, Adán Cabello, Jan-Åke Larsson, Gerhard Kirchmair, Florian Zähringer, Rene Gerritsma, and Christian F. Roos. Compatibility and noncontextuality for sequential measurements. *Physical Review A*, 81(2):022121, February 2010. doi : 10.1103/PhysRevA.81.022121. [cited on p. 164]
- [176] N. David Mermin. A Kochen-Specker Theorem for Imprecisely Specified Measurement. December 1999. URL: <https://arxiv.org/abs/quant-ph/9912081v1>. [cited on p. 164]
- [177] Adán Cabello. Finite-precision measurement does not nullify the Kochen-Specker theorem. *Physical Review A*, 65(5):052101, April 2002. doi : 10.1103/PhysRevA.65.052101. [cited on p. 164]
- [178] Mauricio Arias, Gustavo Cañas, Esteban S. Gómez, Johanna F. Barra, Guilherme B. Xavier, Gustavo Lima, Vincenzo D’Ambrosio, Flavio Baccari, Fabio Sciarrino, and Adán Cabello.

- Testing noncontextuality inequalities that are building blocks of quantum correlations. *Physical Review A*, 92(3):032126, September 2015. doi:10.1103/PhysRevA.92.032126. [cited on p. 164]
- [179] Gabriel Fagundes and Matthias Kleinmann. Memory cost for simulating all quantum correlations from the Peres–Mermin scenario. *Journal of Physics A: Mathematical and Theoretical*, 50(32):325302, July 2017. doi:10.1088/1751-8121/aa7ab3. [cited on p. 164]
- [180] Adán Cabello, Elias Amslem, Kate Blanchfield, Mohamed Bourennane, and Ingemar Bengtsson. Proposed experiments of qutrit state-independent contextuality and two-qutrit contextuality-based nonlocality. *Physical Review A*, 85(3):032108, 2012. doi:10.1103/PhysRevA.85.032108. [cited on p. 165]
- [181] M. Stipčević and B. Medved Rogina. Quantum random number generator based on photonic emission in semiconductors. *Review of Scientific Instruments*, 78(4):045104, April 2007. doi:10.1063/1.2720728. [cited on p. 165]
- [182] Markus Gräfe, René Heilmann, Armando Perez-Leija, Robert Keil, Felix Dreisow, Matthias Heinrich, Hector Moya-Cessa, Stefan Nolte, Demetrios N. Christodoulides, and Alexander Szameit. On-chip generation of high-order single-photon W-states. *Nature Photonics*, 8(10):791–795, October 2014. doi:10.1038/nphoton.2014.204. [cited on p. 165]
- [183] David Branning and Matthew Bermudez. Testing quantum randomness in single-photon polarization measurements with the NIST test suite. *JOSA B*, 27(8):1594–1602, August 2010. doi:10.1364/JOSAB.27.001594. [cited on p. 165]
- [184] Patrick Bronner, Andreas Strunz, Christine Silberhorn, and Jan-Peter Meyn. Demonstrating quantum random with single photons. *European Journal of Physics*, 30(5):1189–1200, August 2009. doi:10.1088/0143-0807/30/5/026. [cited on p. 165]
- [185] Lukas Oberreiter and Ilja Gerhardt. Light on a beam splitter: More randomness with single

Bibliography

- photons. *Laser & Photonics Reviews*, 10(1):108–115, January 2016. doi:10.1002/lpor.201500165. [cited on pp. 166, 171, and 175]
- [186] A. Gruber, A. Dräbenstedt, C. Tietz, L. Fleury, J. Wrachtrup, and C. von Borczyskowski. Scanning Confocal Optical Microscopy and Magnetic Resonance on Single Defect Centers. *Science*, 276(5321):2012–2014, June 1997. doi:10.1126/science.276.5321.2012. [cited on p. 166]
- [187] Xing Chen, Johannes N. Greiner, Jörg Wrachtrup, and Ilja Gerhardt. Single Photon Randomness based on a Defect Center in Diamond. *Scientific Reports*, 9(1):18474, December 2019. doi:10.1038/s41598-019-54594-0. [cited on pp. 166, 167, 168, 169, 170, 191, and 196]
- [188] Igor V. Volovich. Cauchy–Schwarz inequality-based criteria for the non-classicality of sub-Poisson and antibunched light. *Physics Letters A*, 380(1):56–58, January 2016. doi:10.1016/j.physleta.2015.09.011. [cited on p. 166]
- [189] M. Avenhaus, H. B. Coldenstrodt-Ronge, K. Laiho, W. Mauerer, I. A. Walmsley, and C. Silberhorn. Photon Number Statistics of Multimode Parametric Down-Conversion. *Physical Review Letters*, 101(5):053601, August 2008. doi:10.1103/PhysRevLett.101.053601. [cited on pp. 166 and 169]
- [190] E. P. Menzel, R. Di Candia, F. Deppe, P. Eder, L. Zhong, M. Ihmig, M. Haerberlein, A. Baust, E. Hoffmann, D. Ballester, K. Inomata, T. Yamamoto, Y. Nakamura, E. Solano, A. Marx, and R. Gross. Path Entanglement of Continuous-Variable Quantum Microwaves. *Physical Review Letters*, 109(25), December 2012. arXiv: 1210.4413. doi:10.1103/PhysRevLett.109.250502. [cited on pp. 166 and 169]
- [191] X. T. Zou and L. Mandel. Photon-antibunching and sub-Poissonian photon statistics. *Physical Review A*, 41(1):475–476, January 1990. doi:10.1103/PhysRevA.41.475. [cited on pp. 166, 168, and 169]

- [192] A. J. Leggett, S. Chakravarty, A. T. Dorsey, Matthew P. A. Fisher, Anupam Garg, and W. Zwerger. Dynamics of the dissipative two-state system. *Reviews of Modern Physics*, 59(1):1–85, January 1987. doi:10.1103/RevModPhys.59.1. [cited on pp. 166 and 169]
- [193] G. Waldherr, P. Neumann, S. F. Huelga, F. Jelezko, and J. Wrachtrup. Violation of a Temporal Bell Inequality for Single Spins in a Diamond Defect Center. *Physical Review Letters*, 107(9):090401, August 2011. doi:10.1103/PhysRevLett.107.090401. [cited on p. 166]
- [194] John Von Neumann. Various techniques used in connection with random digits. *Appl. Math Ser*, 12(36-38):5, 1951. [cited on p. 167]
- [195] Yuval Peres. Iterating Von Neumann’s Procedure for Extracting Random Bits. *The Annals of Statistics*, 20(1):590–597, March 1992. doi:10.1214/aos/1176348543. [cited on p. 167]
- [196] N. Mizuochi, T. Makino, H. Kato, D. Takeuchi, M. Ogura, H. Okushi, M. Nothaft, P. Neumann, A. Gali, F. Jelezko, J. Wrachtrup, and S. Yamasaki. Electrically driven single-photon source at room temperature in diamond. *Nature Photonics*, 6(5):299–303, May 2012. doi:10.1038/nphoton.2012.75. [cited on pp. 168 and 169]
- [197] Yoshitomo Okawachi, Mengjie Yu, Kevin Luke, Daniel O. Carvalho, Michal Lipson, and Alexander L. Gaeta. Quantum random number generator using a microresonator-based Kerr oscillator. *Optics Letters*, 41(18):4194–4197, September 2016. doi:10.1364/OL.41.004194. [cited on p. 170]
- [198] Alireza Marandi, Nick C. Leindecker, Konstantin L. Vodopyanov, and Robert L. Byer. All-optical quantum random bit generation from intrinsically binary phase of parametric oscillators. *Optics Express*, 20(17):19322–19330, August 2012. doi:10.1364/OE.20.019322. [cited on p. 170]

Bibliography

- [199] Robert H. Hadfield. Single-photon detectors for optical quantum information applications. *Nature Photonics*, 3(12):696–705, December 2009. doi:10.1038/nphoton.2009.230. [cited on p. 171]
- [200] Lawrence Bassham, Andrew Rukhin, Juan Soto, James Nechvatal, Miles Smid, Elaine Barker, Stefan Leigh, Mark Levenson, Mark Vangel, David Banks, N. Heckert, and James Dray. A Statistical Test Suite for Random and Pseudorandom Number Generators for Cryptographic Applications. Technical Report NIST Special Publication (SP) 800-22 Rev. 1a, National Institute of Standards and Technology, April 2010. doi:https://doi.org/10.6028/NIST.SP.800-22r1a. [cited on pp. 174, 178, and 183]
- [201] Cristian S. Calude. *Information and Randomness: An Algorithmic Perspective*. Springer Science & Business Media, March 2013. [cited on p. 174]
- [202] Mark Finkelstein and Robert Whitley. Fibonacci Numbers in Coin Tossing Sequences. *Fibonacci Quarterly*, 16(6), 1978. URL: <http://escholarship.org/uc/item/9nx172g1>. [cited on p. 176]
- [203] Sphumelele C. Ndlovu, Adriana Marais, Promise T. Shabangu, Luyanda L. Noto, Johannes N. Greiner, Nicholas E. Engelbrecht, and Asma Z. Dhunny. Diversity of participant representation within the 66th Lindau Nobel Laureate Meeting. *South African Journal of Science*, 114(3/4):4–4, March 2018. doi:10.17159/sajs.2018/a0263. [cited on p. 195]
- [204] David Abergel. Random numbers: A quantum coin toss. *Nature Physics*, 14(1):7, 2018. doi:10.1038/nphys4342. [cited on p. 196]
- [205] David F. P. Pile. Optical coin toss. *Nature Photonics*, 12(2):58, February 2018. doi:10.1038/s41566-018-0102-y. [cited on p. 196]

Bibliography

*“As far as quantum field theory is concerned, a human being
or the center of a star isn’t all that different from empty space.”*

-Sean Carroll-

As advocated by the University of Stuttgart in the regulations for Dissertations, a brief Academic Curriculum Vitae is included. A Professional CV is found at [LinkedIn: Johannes N. Greiner](#).

Curriculum Vitae

Doctor Rerum Naturalium in Physics (Jan 2014 – May 2020)

University: University of Stuttgart.

Thesis: “Algorithms and Resources for Quantum Technology,
Sensing and Random Number Generation.”

Supervision: Prof. Dr. Jörg Wrachtrup, Dr. Durga Dasari.

Master of Science in Theoretical Physics (Sept 2012 – Oct 2013)

University: King’s College London (KCL).

Thesis: “Entanglement and Decoherence in Many-Body Quantum Models.”

Supervision: Dr. Benjamin Doyon.

Bachelor of Science in Physics (Oct 2008 – Oct 2011)

University: University of Stuttgart.

Thesis: “Bell Measurement and Quantum Teleportation using
Entangled Single Spins in Nitrogen-Vacancy Diamond Defects.”

Supervision: Prof. Dr. Jörg Wrachtrup, Dr. Florian Rempp.